Phase transitions and surface growth in nonequilibrium lattice models

vorgelegt von

M. Sc.

Thomas Michael Martynec

ORCID: 0000-0001-5736-6108

an der Fakultät II – Mathematik und Naturwissenschaften
der Technischen Universität Berlin
zur Erlangung des akademischen Grades

DOKTOR DER NATURWISSENSCHAFTEN

Dr.rer.nat.

genehmigte Dissertation

PROMOTIONSAUSSCHUSS:

Vorsitzender: Prof. Dr. Michael Lehmann

Gutachterin: Prof. Dr. Sabine H. L. Klapp

Gutachter: Prof. Dr. Martin Oettel

Tag der wissenschaftlichen Aussprache: 10.03.2021

Berlin 2021

Acknowledgement

First, I want to thank my supervisor Sabine Klapp for giving me the opportunity to work în her group and allowing me to develop own ideas, work independently and autonomously. Further, I would like to thank Stefan Kowarik for introducing me to the exciting field of machine learning. Moreover I want to thank Sarah Loos for the enjoyable collaboration on thermodynamic projects. I would like to thank my colleagues Sascha, Alex, Mohsen, Gaurav, Guo-Jun, Nima, Henning and Sarah for fruitful discussions, the many joyful activities outside the academic context and the pleasant atmosphere that we always had within the group during coffee, lunch and dinner breaks. I thank Henning Reinken and Sarah Loos for their ideas, comments and the valuable feedback on this thesis. Furthermore, I would also like to thank the CRC 951 for providing financial support over the last few years. Lastly, I want to thank Gabriele and Edith Martynec for always supporting me in any situation.

List of publications

The results presented in this thesis are mainly based on the following publications and preprints

• Thomas Martynec and Sabine H. L. Klapp
Impact of anisotropic interactions on nonequilibrium cluster growth at surfaces
Phys. Rev. E **98** 042801 (2018)

• Thomas Martynec and Sabine H. L. Klapp
Modeling of nonequilibrium surface growth by a limited-mobility model with distributed diffusion length
Phys. Rev. E **100** 033307 (2019)

• Thomas Martynec, Sabine H. L. Klapp and Sarah A. M. Loos
Entropy production at criticality in a nonequilibrium Potts model
New J. Phys. **22** 093069 (2020)

• Thomas Martynec, Christos Karapanagiotis, Sabine H. L. Klapp and Stefan Kowarik
Prediction of energetics in nucleation and non-equilibrium growth using machine learning
submitted (2020)

Abstract

In this thesis, we investigate two paradigmatic lattice systems far from thermal equilibrium by means of particle-based computer simulations. The first model we study mimics surface growth through vacuum deposition techniques like physical vapor deposition and molecular beam epitaxy which are used for the industrial fabrication of thin films. A thorough knowledge of the dynamical behavior of particles which are deposited during the growth procedure is essential to optimize the quality of thin film semiconductor devices. The second model that we investigate is a nonequilibrium spin system which we analyze at criticality in order to deepen our understanding of nonequilibrium phase transitions.
Using kinetic Monte Carlo simulations, we investigate nonequilibrium surface growth in a generic model with anisotropic interactions among spherically shaped particles. The interaction anisotropy is characterized by a control parameter that measures the ratio of interaction energy along the two lattice directions. The simplicity of the model allows to systematically study the effect and interplay between interaction anisotropy, the binding energy and the deposition rate on the shapes and the fractal dimension of clusters. We find that the growing clusters exhibit power-law scaling with universal growth exponents. We also identify a growth condition-dependent critical cluster length that indicates a transition from one-dimensional to self-similar two-dimensional cluster growth. Moreover, the cluster properties depend markedly on the critical cluster size in the isotropic reference system.
Further, we develop a model for surface growth with limited mobility of deposited particles. Limited mobility models highly reduce the computational effort compared to simulation setups that include diffusion processes for all adatoms in the topmost layer at any time of the growth simulation. Our model is based on the stochastic transition rules of the Das Sarma-Tamborena model but differs from the latter via a variable diffusion length which mimics diffusional fluctuations. The analysis of surface morphologies reveals that diffusional fluctuations, which are usually neglected in limited mobility models, are essential to produce surface structures that are, at arbitrary growth conditions, indistinguishable from those obtained from growth simulations with full diffusion models.
Another aspect of this thesis concerns the question of the applicability of machine learning techniques in the field of nonequilibrium surface growth. In particular, we aim to obtain the microscopic energy barriers, which determine the rates of the adatom diffusion processes, from static snapshots of surface morphologies in the submonolayer growth regime. To this end, we trained a convolutional neural network on clean and noisy snapshots by means of supervised learning. We find that the convolutional neural network can predict the values of the underlying diffusion and binding energies with high precision in a large

parameter space.

Moreover, we study thermodynamic properties of surface growth by calculating the entropy production rate of a growth model which includes deposition, diffusion and desorption of particles. Our main result here is that the model in presence of a substrate is always in thermal equilibrium when it is in the bound phase where the surface height fluctuates around zero.

In addition to that, we study a nonequilibrium version of the q-state vector Potts model which is driven out of equilibrium by coupling the spins to two heat baths at different temperatures. We investigate the critical behavior at a second-order and an infinite-order phase transition. For the second-order transition, we find that the universality class remains the same as in equilibrium. Interestingly, the derivative of the entropy production rate rate with respect to temperature diverges with a power-law at the critical point, but displays a non-universal critical exponent. The latter depends on the temperature difference between the heat baths, i.e., the strength of driving. For the infinite-order transition, the derivative of the entropy production rate exhibits a maximum in the disordered phase, similar to the specific heat. However, in contrast to the specific heat, the maximum of the derivative of the entropy production rate grows with increasing temperature difference between the heat baths.

Zusammenfassung

In dieser Arbeit werden zwei paradigmatische Systeme mit diskretem Phasenraum mittels teilchenbasierter Computersimulationen untersucht. Das erste Modell dient dem Zweck das Nichtgleichgewichtswachstum kristalliner Dünnschichtstrukturen mittels Verfahren der physikalischen Gasphasenabscheidung wie der Molekularstrahlepitaxie zu simulieren. Eine Hauptanwendung dieses Verfahrens ist die Fertigung von monokristallinen Halbleiterstrukturen mit herausragenden elektronischen und optischen Eigenschaften. Ein vertieftes Verständnis des dynamischen und kollektiven Verhaltens der Atome und Moleküle welche während des Wachstumsprozeses durch einen gerichteten Molekularstrahls auf ein Substrat aufgedampft werden ist substantiell, um die bestmöegliche Qualität und Funktionalität zu erzielen. Das zweite hier betrachtete Modell ist ein aus dem Gleichgewicht getriebenes Spinsystem, welches wir in der Nähe des kritischen Punkts untersuchen. Dies dient dem Zwecks unser grundlegendes Verständnis vom physikalischen Verhalten von Nichtgleichgewichtssystemen an Phasenübergaengen zu vertiefen.

Mittels kinetischer Monte-Carlo Simulationen untersuchen wir zunächst das Oberflächenwachstumsverhalten in einem generischen Modellsystem in welchem sphärische, anisotrop wechselwirkende Teilchen auf ein Substrat aufgedampt werden. Die Stärke der Wechselwirkungsanisotropie entlang der zwei Achsen des zweidimensionalen Substrates ist der Kontrollparameter. Die Einfachheit des Modellsystems ermöglicht eine systematische Untersuchung des Einflusses der Wechselbeziehung zwischen dem Grad der Anisotropie, der Stärke der Bindungsenergie und dem Wert der Adsorptionsrate auf Form und fraktale Dimension der entstehenden Cluster. Es stellt sich heraus, dass das Clusterwachstum einem Potenzverhalten mit universellen Wachstumsexponenten genügt. Desweiteren haben wir eine kritische Clusterlänge identifiziert. Diese gibt an ab welcher Länge das ursprünglich eindimensionale Clusterwachstum in einen selbstähnlichen zweidimensionalen Wachstumsmodus übergeht. Wir konnten nachweisen, dass die Wachstumseigenschaften der Cluster insbesondere von der kritischen Clustergrösse des zugehörigen anisotropen Referenzsystems abhängen.

Desweiteren diskutieren wir in dieser Arbeit Wachstumsmodelle mit begrenzter Teilchenmobilität der adsorbierten Teilchen, sogenannte “Limited-mobility”-Modelle. Solche Modelle reduzieren den Rechenaufwand in erheblichem Maße gegenüber “full diffusion”-Modellen, in welchen jedes Teilchen in der obersten Schicht des wachsenden Kristalls zu jedem Zeitschritt einen Diffusionsprozess durchführen kann. Unser Modell unterliegt den Übergangsraten des Das Sarma-Tamborena-Modells, unterscheidet sich von diesem jedoch

durch eine variable Diffusionslänge. Dadurch kann unser Modell Fluktuationen in der Diffusionslänge von Adsorbaten, welche in stochastischen Wachstumsprozessen zwangsläufig vorhanden sind, imitieren. Für gewöhnlich werden diese in “Limited-mobility”-Modellen vernachlässigt. Es stellt sich jedoch heraus, dass diese essenziell sind um Oberflächenstrukturen zu erzeugen die ununterscheidbar von jenen sind welche mittels “full diffusion” Modellen erzeugt wurden.
Ein weiterer Aspekt dieser Arbeit betrifft die Anwendbarkeit und Nützlichkeit von Machine Learning Algorithmen auf dem Gebiet des Oberflächenwachstums fern vom thermischen Gleichgewicht. Ziel unserer Untersuchungen ist es die mikroskopischen Energiebarrieren, welche die Diffusionsraten von Adatomen bestimmen, anhand von Bildern der gewachsenen Oberflächenstruktur zu bestimmen. Zu diesem Zweck haben wir ein “Convolutional Neural Network” mittels überwachtem Lernen von unverrauschten und verrauschten Bildern von Oberflächenstrukturen trainiert. Es zeigt sich, dass das trainierte neuronale Netzwerk die zugrundeliegenden Diffusions- und Bindungsenergien sehr präzise bestimmen kann. Wir hoffen, dass diese Strategie zukünftig genutzt werden kann um aus experimentellen Bildern mikroskopische Energiebarrieren zu extrahieren.
Darüber analysieren wir in dieser Arbeit thermodynamische Eigenschaften von Wachstumsprozessen. Diesbezüglich berechnen wir die Entropieproduktionsrate eines Wachstumsmodells in welchem neben der Adsorption und Diffusion auch die Desorption von Teilchen möglich ist. Dabei zeigt sich, dass das System in Anwesenheit eines starren Substrats in der gebundenen Phase stets ein thermodynamisches Gleichgewicht erreicht. In diesem Zustand fluktuiert die Oberfläche des Kristalls um den Nullpunkt. Zusätzlich haben wir eine Variante des q-state Potts Modells untersucht welches durch Kopplung der Spins an zwei Wärmebäder unterschiedlicher Temperaturen aus dem thermischen Gleichgewicht getrieben wird. Wir haben das kritische Verhalten des Systems an Phasenübergängen zweiter und unendlicher Ordnung untersucht. Es stellt sich heraus, dass das kritische Verhalten an Übergängen zweiter Ordnung ununterscheidbar vom entsprechenden Gleichgewichtssystem ist, sodass die Universalitätsklasse nicht von der eingeführten Temperaturdifferenz geändert wird. Die Ableitung der Entropieproduktionsrate nach der Temperatur weist am kritischen Punkt Potenzverhalten mit einem nicht universellen kritischen Exponenten auf. Dieser hängt explizit von der Temperaturdifferenz der zwei Wärmebäder ab. Am Phasenübergang unendlicher Ordnung zeigt die Änderung der Entropieproduktionsrate ein Maximum in der ungeordneten Phase in gleichem Maße wie die spezifische Wärme. Im Gegensatz zu dieser wächst das Maximum der Änderung der Entropieproduktionsrate mit steigender Temperaturdifferenz der zwei Wärmebäder.

Contents

1 Introduction

Order or disorder on the microscale make the same substance or material appear as a hard solid, a flowing liquid or an airy gas. It is the structural arrangement of the microscopic degrees of freedom that determines the physical state of matter and thereby also the properties of any substance, material and technological device not only on the microbut also on the macroscale. Unraveling properties of the various phases of matter and understanding the physical behavior of systems undergoing transitions between them is one of the central research subjects of statistical physics. Examples include the classical phases like gas, liquid, solid and plasma, as well as glassy, magnetic or liquid crystal states together with low-temperature phases like the superfluid phase, Bose–Einstein and Fermionic condensates [1–3]. Besides this classification, more specific details like the precise crystal structure, the lattice constant as well as the question which elements and molecules are involved further determine properties of the different phases of matter. A thorough knowledge of the diverse properties of phases in equilibrium and out of equilibrium is important in numerous research fields ranging from physics, chemistry, biology, engineering and materials science up to the industrial sector. In this thesis, we investigate the phase behavior of nonequilibrium spin systems and analyze their critical properties in order to deepen our understanding of nonequilibrium phase transitions. Moreover, this thesis is concerned with nonequilibrium surface growth phenomena. In particular, we investigate the emergence of a solid phase via self-assembly of particles in a discrete growth model that is tempted to mimic nonequilibrium surface growth through vacuum deposition techniques like physical vapor deposition and molecular beam epitaxy.

General remarks on phase transitions: As one part of this thesis is concerned with phase transitions, let us introduce to this topic by shortly discussing a classical textbook example which makes clear how material properties depend on the state of the microscopic degrees of freedom. Figure 1.1 illustrates two different phases of the magnetic moments that can be found in ferromagnetic materials like iron, cobalt, nickel and alloys or compounds [4, 5]. At high temperatures, the spatially localized magnetic moments, i.e., the spins, are (quasi) statistically independent from each other as thermal noise dominates over their interaction forces. Accordingly, individual spins randomly occupy one of the two possible spin configurations (they either point up or down, thus, they exhibit a discrete symmetry). In this spin-disordered paramagnetic phase, the macroscopic magnetization is zero. If the temperature, which acts as control parameter, is decreased below the material-dependent, so-called Curie temperature, this symmetry gets spontaneously broken, as the

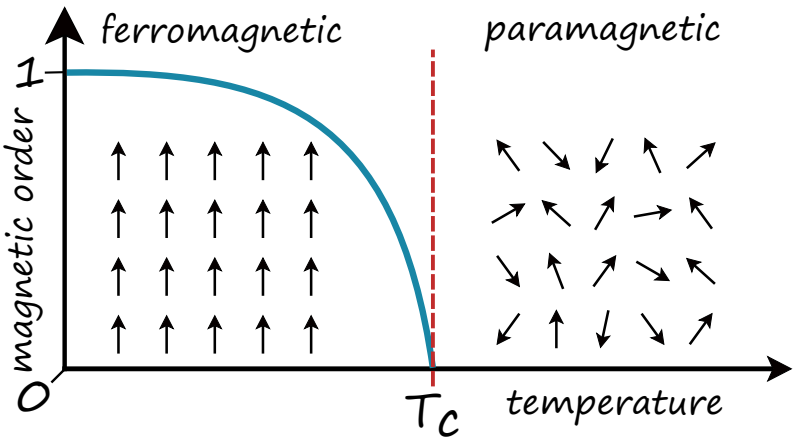

Fig. 1.1: Illustration of a continuous (second-order) phase transition in a lattice-based spin model where each spin is located at a fixed position. At temperatures T below the critical temperature T_c, the spins point in the same direction. In this state, the system is said to be in the spin-ordered ferromagnetic phase which is characterized by a measurable magnetization. This is quantified by the magnetic order parameter which takes the value 1 in the ordered phase. As the temperature is increased above T_c, the order gets slowly vanishes until it is completely destroyed by thermal fluctuations for $T \geq T_c$. At T_c the system undergoes a phase transition. The magnetization vanishes since the spins point in random directions. The order parameter takes the value 0 in the spin-disordered paramagnetic phase.

spins suddenly align parallel to each other as shown in Fig. 1.1. This symmetry breaking is associated with the emergence of magnetic domains and a measurable magnetization. The system is now in a spin-ordered ferromagnetic phase where (within magnetic domains) the spins point, on average, in the same direction. From this specific example, we can see a generic phenomenon, that is, various properties of the very same substance or material can drastically change as it undergoes a transition from one phase of matter to another as an appropriate control parameter is varied across a system-dependent critical point. Of particular interest in this context is the behavior of systems in the vicinity of phase transitions which crucially depends on the order of the phase transition [6, 7].

Fundamentals of nonequilibrium surface growth: Next to phase transitions, this thesis is concerned with numerical investigations of growth phenomena, which represent examples for the emergence of complex structures out of interacting simple agents. Each piece of matter found in the solid state has originally been formed by accumulation of individual atoms and molecules via some sort of growth process. Crystal growth phenomena represent an important research topic in statistical physics [8–13]. Growth processes are omnipresent in nature and crucial for the industrial fabrication of thin film devices with highly specialized properties [14–19]. For the fabrication of crystalline materials by means of epitaxy techniques like physical and chemical vapor deposition [20–24], pulsed laser deposition [25–27] or molecular beam epitaxy (MBE) [28, 29], it is important to achieve a thorough understanding of the morphological evolution of the solid phase. The latter is formed from a spatially confined lattice gas created through deposition of particles from a beam that is directed onto a crystalline substrate. In particular, not only the specific

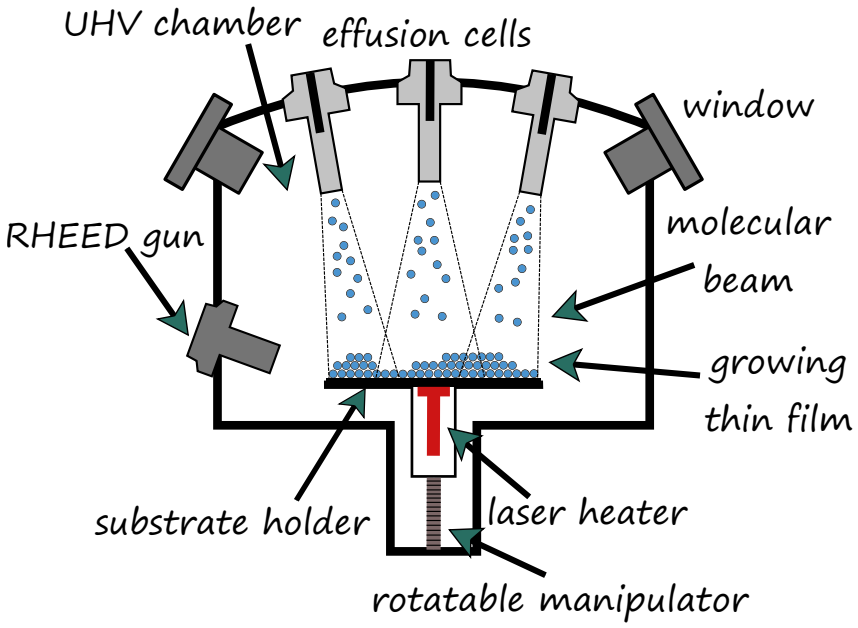

Fig. 1.2: Illustration of a basic experimental setup for thin film growth via MBE which takes place in an ultra-high vacuum chamber. After sublimation of solid materials in effusion cells, a particle beam is directed onto a rotatable substrate which is kept at a constant temperature. The thin film structure grows via adsorption of deposited particles. Once adsorbed, particles diffuse on the substrate, participate in cluster nucleation events or attach to existing clusters. These processes affect the morphology, and thus, the quality of the growing thin film. A reflection high-energy electron diffraction gun is used to monitor the thin film growth process.

geometrical arrangement and the sort of deposited atoms or molecules crucially determine the properties of the growing crystal. Additionally, also the substrate temperature, the adatom flux rate, the defect density and the nucleation density may have an impact on the crystal morphology, and thereby affect the quality and functionality of nano-structured thin film devices like solar cells [30–32], (organic) light-emitting diodes [33, 34], field-effect transistors [35–37] or quantum wires and quantum dots [38–40].

During crystal growth by means of MBE, which we mimic in this thesis with a particle-based model, solid atomic or molecular structures are heated in Knudsen effusion cells under ultra-high vacuum conditions until they sublime. A simple experimental setup for MBE growth is shown in Fig. 1.2. The evaporated particles form a beam which is directed onto a solid substrate (that is kept at a fixed temperature) where they are adsorbed. From a theoretical point of view, diffusion of individual adatoms on the crystalline substrate is modeled via thermally activated Arrhenius-type hopping processes. The deposited particles form a two-dimensional lattice gas from which the solid thin film emerges through nucleation and growth of clusters via attachment of diffusing adatoms to boundary sites of existing clusters. It is therefore essential to comprehend the mechanisms and microscopic details of the lattice gas phase in order to control the morphological evolution of the solid phase. In other words, MBE is a technique that involves two phases of matter which exhibit drastically different properties. From the initial gas phase, a self-assembled solid

phase emerges. Growth processes pose a challenging problem for statistical mechanics and we are still far from a complete understanding. Since the emerging solid state can be probed by scanning tunneling or atomic force microscopy, it is possible to validate theoretical predictions of growth processes with experimental results at atomic resolution. This allows to gain a deeper understanding of the actual mechanisms that control the growth of crystalline materials [12, 41, 42].

The study of material properties like magnetization and the fabrication of thin films by epitaxial growth are only two of many examples where a detailed knowledge of phases and the behavior at transitions between them is essential. In epidemiology, the percolation threshold (where a mathematical social network undergoes a transition from an unconnected to a fully connected phase where all nodes of a graph are linked with each other) is crucial for understanding the spreading of diseases on a regional, nationwide and global scale [43–46]. From studying Susceptible-Infectious-Recovered (SIR) networks it is known that the timing and magnitude of interventions within the unconnected phase are essential to prevent the system from undergoing a transition to the connected phase, where a network spanning cluster emerges that results in uncontrolled disease spreading. Thus, knowing details of the phase behavior of social networks is crucial to understand how different factors can help to mitigate the spreading of diseases like the ebola or the SARS-CoV-2 virus [47–49]. Moreover, even in the context of living, biological matter, concepts from statistical physics are applied to understand swarming and flocking of bacteria, birds or fish that arises from collective behavior of energy consuming entities [149, 190].

The examples just mentioned include equilibrium systems as well as nonequilibrium systems. When it comes to a theoretical description of physical systems, this distinction becomes very important because our physical understanding of nonequilibrium systems is not as profound as it is for systems in a state of thermal equilibrium.

Fundamentals of statistical mechanics: For matter in thermal equilibrium, statistical mechanics provides elaborated theoretical concepts that successfully explain the underlying mechanisms which determine the properties of physical systems in various different phases. In particular, it connects the underlying dynamical laws which govern the behavior of individual constituents of matter on the microscale with thermodynamic laws that provide phenomenological rules on the macroscale. In this regard, a key property of any equilibrium systems is detailed balance, which poses a condition on state occupation and transition probabilities, independent of the system's microscopic details. Furthermore, also the fluctuations of various quantities around the equilibrium point are known to fulfill universally valid fluctuation theorems. This is discussed in the framework of stochastic thermodynamics [50–52].

Further, in thermal equilibrium fundamental connections between symmetries of the principles that govern the collective behavior of the microscopic degrees of freedom and the properties of different phases and phase transitions of the macroscopic system are well known. A prominent example of such a connection is the Mermin-Wagner theorem. It states that in one- and two-dimensional systems with short-range interactions and continuous rotational symmetry of the microscopic degrees of freedom, long-range ordered phases can not emerge in the presence of thermal fluctuations, i.e., at finite temperatures [53–56] . Indeed, the validity of the Mermin-Wagner theorem has been experimentally demonstrated for many one- and two-dimensional systems [57–60].

Moreover, the connection between the underlying symmetries and the collective behavior of the microscopic degrees of freedom also plays a fundamental role in the characterization of phase transitions. In general, phase transitions can be divided in two main classes [61–65]. On the one hand, there are phase transitions where the state of the system changes in a discontinuous way. On the other hand, there are transitions where the state changes continuously. In this case, the correlation length of the microscopic degrees of freedom that undergo a transition from one phase to another diverge at the critical point. For this second type (which we will focus on in this thesis), the connection between underlying symmetries and collective behavior is described within the framework of universality. The latter is a further important concept provided by statistical mechanics that helps to deepen our understanding of systems in the vicinity of critical points of continuous phase transitions. It is based on the observation that large classes of systems share certain properties which are independent of the microscopic details of the respective systems. More precisely, different systems may behave identical regarding the scaling behavior of certain quantities in the vicinity of a continuous phase transition. Thus they are said to belong to the same universality class. In 1971 Kadanoff pointed out that *"all phase transition problems can be divided into a small number of different classes depending upon the dimensionality of the system and the symmetries of the order state. Within each class, all phase transitions have identical behavior in the critical region, only the names of the variables are changed.*" The main ingredients that determine the universality class of a system are symmetries and conservation laws. Additionally, detailed balance and fluctuation relations impose strong constraints on equilibrium systems that enhance the robustness of universality classes. The concept of universality is well established for equilibrium systems and various robust universality classes have been discovered during the last decades [66–71]. In this regard, especially worth mentioning due to it's simplicity and widespread applicability is the Ising universality class which, among other cases, describes the ferromagnetic transition in the Ising model. In this thesis we analyze the q-state Potts model and a variant of the XY model under equilibrium and nonequilibrium conditions to investigate how irreversibility affects the critical behavior.

While the general connections between symmetries and the microscopic degrees of freedom just mentioned are well understood and explain various natural occurring phenomena, we

must acknowledge that they are based on the assumption of thermal equilibrium. However, under real-world conditions, systems are in fact often found to be in nonequilibrium. Nonequilibrium statistical mechanics deals with the properties of irreversible processes where thermodynamic notions like entropy and temperature are not directly available. Further, detailed balance is broken and the equilibrium fluctuation relations are not guaranteed to hold. The lack of these constraints allows for more variability in the systems dynamics and in the phase behavior [72–76]. An example for a nonequilbrium phase transition is motility-induced phase separation between a dense and dilute fluid phase, which occurs in two-dimensional active matter systems with continuous symmetry and would hence not be allowed in thermal equilibrium as stated by the Mermin-Wagner theorem. Further, the driving may, or may not, affect the corresponding critical exponents [73–75]. Being in a nonequilibrium state gives rise to more freedom for the behavior in the vicinity of phase transitions and may weaken the robustness of universality [73, 74]. However, there are also cases where driving a system out of thermal equilibrium does not affect the critical behavior and does therefore not change the universality class of the system [73, 74]. In fact, it is often *a priori* not clear which symmetries are affected by driving a system out of thermal equilibrium. For example, it has recently been shown that the motility-induced phase separation in the Vicsek Model lies in the equilibrium Ising universality class with conservative Kawasaki spin dynamics [77]. This means that the scaling properties of the collective behavior of active particles undergoing a gas-liquid phase separation behave at criticality indistinguishably from the equilibrium Ising model undergoing a transition from a spin-disordered paramagnetic to a spin-ordered ferromagnetic phase.

Goals of this thesis: In this thesis, we aim to deepen the understanding of phases and phase transitions under nonequilibrium conditions by studying suitable example systems. In particular, we numerically investigate two, rather generic stochastic lattice-based systems and address questions regarding the behavior of these systems far from thermal equilibrium. The first model is a discrete growth model designed to mimic nonequilibrium surface growth. More precisely, we study the homoepitaxial growth of stable crystal structures from a lattice gas phase by means of kinetic Monte-Carlo simulations and address different questions that will be outlined in the following. The second model is a nonequilibrium variant of the q-state vector Potts spin model that is investigated at criticality. In the following paragraphs, we will give a short overview of the specific models and the research questions addressed. More detailed background information on the various topics is given in the later chapters of this thesis.

The first question we address is the impact of anisotropic interactions on nonequilibrium cluster growth. While tuning the properties of inorganic semiconductor devices is often limited to doping [78–81], thin film devices made of conjugated organic molecules (COMs) are much more variable compared to inorganic devices due to the nearly inexhaustible number of synthesizeable conjugated systems [82–85]. COMs often exhibit a complex

geometrical structure and an anisotropic interaction potential. The morphology of crystals consisting of COMs is crucial for properties and the performance of organic thin film devices since the electron transport and charge carrier mobility strongly depend on the precise configuration of the molecules in the solid state [86–88]. Therefore, it is essential to understand the nonequilibrium growth behavior of the emerging solid state consisting of anisotropically interacting constituents. Computational studies have shown that it is very challenging to simulate the growth process with elongated, anisotropically interacting particles [89–94]. To nevertheless investigate the impact of anisotropic interactions on nonequilibrium growth we use a most reduced setup. Specifically, by means of kinetic Monte-Carlo simulations we study a growth model where the shape of deposited particles is isotropic and only the interactions between them are anisotropic [95]. We aim to understand the formation and properties of stable crystal structures.

Despite the enormous computational resources that are available, numerical growth studies are often limited to relatively small system sizes and a rather low number of deposited layers. Therefore, one is often operating in the transient regime where the surface roughness has not yet reached a steady state. To deepen our fundamental understanding of surface growth it is essential to unravel the universality class of nonequilibrium growth processes. In order to obtain the critical exponents, one has to reach the saturation regime of the surface roughness for systems with increasing sizes. However, the onset of saturation scales with system size. This explains why particle-based simulations are computationally expensive. To tackle this problem, we have constructed a model with limited particle mobility which drastically reduces the simulation times compared to conventional full-diffusion kinetic Monte-Carlo growth simulations [96]. In particular, the model mimics the surface dynamics during growth in such a way that at each simulation step, one particle gets adsorbed and performs exactly one diffusional move. Our model is based on the stochastic transition rules of the Das Sarma-Tamborena model [97, 98] but differs from the latter via a variable diffusion length which is chosen from a Gaussian distribution to mimic diffusional fluctuations. The model is constructed to imitate low-temperature surface growth by means of MBE. We compare the resulting surface morphologies in the sub- and multilayer growth regime to those obtained from kinetic Monte-Carlo simulations, and use the limited-mobility model to calculate the critical exponents. In particular, it turns out that diffusional fluctuations, which are usually neglected in limited mobility models, are essential to produce surface structures that are indistinguishable from those obtained from simulations of full diffusion surface growth models.

Controlled growth of crystalline thin films from the gas phase of novel materials is a crucial ingredient for device manufacturing and rapid prototyping of advanced materials. However, it is challenging to achieve the desired material quality as device applications have specific requirements regarding grain size and shape, defect densities, and film roughness. On the atomic scale, thin film growth kinetics is governed by only a few stochastic processes including the deposition of adatoms from the evaporator or from a

chemical precursor gas, and diffusion of adatoms on the crystal surface. The complexity of growth stems from the fact that diffusion of adatoms is not independent from each other but highly correlated as they can form islands and crystal nuclei that hinder further movement. Machine learning is playing an increasing role in the discovery of novel materials [99–106] and may facilitate growth of highest quality crystals and thin films. In this thesis, we study how neural networks can predict optimum processing parameters in a multi-dimensional processing parameter space [107]. We perform kinetic Monte-Carlo simulations of sub-monolayer growth to generate a training data set for a convolutional neural network that consists of surface snapshots in the submonolayer growth regime. We demonstrate that the convolutional neural network can predict the values of the underlying energy barriers that determine the diffusion processes of the adatom lattice gas particles. Moreover, the convolutional neural network can also make correct predictions of the underlying energy barriers for images with noise and lower than atomic scale resolution. We expect our machine learning method to be of use for fundamental studies of growth kinetics and for a faster optimization of epitaxially grown materials.

Finally, we turn to a thermodynamic investigation of discrete systems far from thermal equilibrium. In particular, we investigate the applicability of the entropy production as tool to specifically characterize nonequilibrium phase transitions in the same manner as critical quantities. As mentioned earlier, it is often not clear how driving a system out of thermal equilibrium affects it's critical behavior. Earlier research has shown that, in principle, it is possible to typify nonequilibrium phase transitions in a similar way to equilibrium systems, for instance, by the use of the same order parameter and the same critical quantities as in equilibrium systems [73, 74]. However, such a classification often hides the irreversible character of the dynamics as well as the impact on properties of the phase transition [108–111]. This motivates us to consider the behavior of nonequilibrium measures at the critical point, in addition to the usual critical quantities [112]. In particular, we consider the behavior of the entropy production rate at criticality. This quantity is zero in the equilibrium case and strictly positive in nonequilibrium systems where it directly quantifies the distance from equilibrium. We first consider a simple one-dimensional growth model with adsorption, diffusion and desorption of particles in presence of a hard substrate at zero height. This allows us to define two phases, a bound phase where the interface is pinned to the substrate and a growing phase where the crystal grows and the interface thus detaches from the substrate. We study the behavior of the entropy production rate in the bound phase, the growing phase and in the vicinity of the transition between these two phases. Then, we turn away from surface growth and consider nonequilibrium phase transitions in a spin system in detail. For this purpose, we study an Ising-like spin system under nonequilibrium conditions. Specifically, by coupling a q-state vector Potts model to two heat baths at different temperatures, we drive the system out of equilibrium and study the effect of irreversible dynamics on the critical behavior.

1.1 Outline of the thesis

We close this introduction by giving a brief overview of the structure of this thesis. The first part of this thesis provides an introduction to the theoretical and methodological background. In particular, Chapter 2 introduces the concepts of Markov chains, including the technique of Monte-Carlo and event-driven kinetic Monte-Carlo simulations. There, we also give the main details of the simulations and models used in this thesis. Chapter 3 introduces the fundamental concepts of stochastic thermodynamics for discrete systems. We specifically focus on the formulation of the entropy production rate used later in Chapter 8 and Chapter 9 where it's applicability as tool to characterize phase transitions is investigated. Chapter 4, which is the last part of the theoretical foundations, concerns the introduction of critical behavior and universality. We will pay special attention to the concept of universality in the context of both, phase transitions and surface growth. The next part of this thesis presents our numerical results. We begin with discussing the results for surface growth of particles with anisotropic interactions in Chapter 5. In Chapter 6, we present the limited-mobility model with variable diffusion length where we compare the morphology of grown structures with those obtained from full diffusion kinetic Monte-Carlo simulations. Moreover, we determine the universality class of our simplified growth model. In the following Chapter 7, we discuss the applicability of machine learning methods to determine the microscopic energy barriers that determine the morphological evolution during nonequilibrium surface growth. Finally, in Chapter 8 we turn to stochastic thermodynamics of nonequilibrium surface growth. We calculate the entropy production rate in a one-dimensional growth model which includes the processes of adsorption, diffusion and desorption. In Chapter 9, we investigate the entropy production rate in the vicinity of phase transitions in nonequilibrium spin systems. Finally, we end with Chapter 10 where we summarize our results and propose some ideas for future investigations.

2 Fundamentals of Markov chains and simulation details

This chapter is concerned with Markov chains and simulation details of the lattice-based models which are investigated in this thesis. After introducing the fundamentals of discrete Markov chains and Markov chain Monte-Carlo methods, we discuss classical spin systems and simulation details. In particular, we explain single particle and cluster Monte-Carlo algorithms. The end of the chapter is concerned with surface growth simulations. We explain coarse-graining in surface growth and the event-driven kinetic Monte-Carlo simulation method.

2.1 Fundamentals of discrete Markov Chains

Markov chain representation of stochastic models: In a nutshell, Markov chains represent a class of stochastic models which describe a sequence of transitions (events) $\mu \to \nu$ between microstates, μ, ν, of the underlying (physical) model for which the probability of each occurring event, i.e., the transition $\mu \to \nu$ from μ to ν, depends only on the state, μ, occupied in that precise instant of time when the transition event takes place. The transition event $\mu \to \nu$ is explicitly independent of the history of previously occupied states. Therefore, the probability for state transitions $\mu \to \nu$ are events satisfying the Markov property. Therefore, they are also referred to as "memoryless" processes since they do not depend in any form on the past, i.e., the history of previously occupied states. There exist many examples of real-world processes in physics, chemistry, biology economics and finance or information and computer science where Markov chains are applied as statistical models to mimic their dynamics [113–119]. In particular, all lattice-based stochastic models considered and investigated in this thesis have in common that they represent examples of such history-independent Markov Chains whose dynamical evolution depends solely on the currently occupied state μ, i.e., they have no memory of the past. Accordingly, any form of time-delay, a feature of non-Markovian systems, is not of relevance in this thesis. However, we want to point out that the investigation of non-Markovian systems with time-delay is a timely topic in statistical physics [120–123]. For example, time-delay could be included in the nonequilibrium Potts model which is investigated in in C. 9. Time-delay is known to cause and stabilize periodic solutions [120, 124]. It would be interesting to check whether a stable, periodically oscillating nonequilibrium phase emerges in the Potts model in presence of time-delay. Moreover, it is well known that (lattice-based)

spin systems are suitable to model social dynamics where time-delay plays an important role [125–127]. So far, effects of time-delays in the dynamics of social systems have hardly been analyzed and it would be interesting to study the effect of time-delay in this context.

On the level of stochastic modeling, a Markov Chain can be described as a stochastic sequence (also called stochastic path or trajectory)

$$\mathbf{X}(N) = (X_1 = \mu, X_2 = \nu, ..., X_{N-1} = \eta, X_N = \gamma), \tag{2.1}$$

consisting of an, in principal, arbitrary number N of transitions between different microstates, $\mu, \nu, \eta, \gamma \in \Omega$ of the underlying stochastic system. Here, Ω is the countable set of all possible microstates. This set is also called the probability state space of the respective Markov Chain. At each time step $t = 1, 2, ...N$, the system state X_t is one element from Ω, i.e., the system is occupying a state of the state space, $X_t \in \Omega$. In general, Ω can contain anything that may be the outcome of a random experiment. Perhaps the simplest example for a Markov Chain is the repetitive tossing of a coin. In this particular case, the probability state space, $\Omega = \{H, T\}$, only contains head, H and tail, T, i.e., the two sides of the coin form the probability state space Ω. An exemplary stochastic path consisting of a random sequence of H and T may be given by $\mathbf{X}(N = 5) = (X_1 = T, X_2 = H, X_3 = H, X_4 = T, X_5 = H)$. This sequence begins in state $X_1 = T$ and ends in $X_5 = H$ after the coin has been flipped $N = 5$ times in total. Playing dice and counting the number of eyes after each throw or picking a random card from a stack containing a certain number of cards are further examples of Markov chains which exhibit a discrete and countable probability state space Ω. Throughout this chapter, we use the notation $X_t \in \Omega$ in order to denote (micro)states of a stochastic system that the system occupies at time steps $t = 1, 2, ..., N$ during it's dynamical evolution.

The Markov property: On a mathematical level, the just mentioned Markov property states that the conditional probability to find a stochastic system at time step $t + 1$ in state X_{t+1} only depends on the state X_t occupied at time step t and is thus totally independent of all previously occupied states X_k ($k = 1, 2, 3, ..., t - 1$). Consequently, $\mathcal{P}(X_{t+1})$ does not depend on the history of the system, which means that for all $t > 1$, the Markov property reads

$$\mathcal{P}\left(X_{t+1}|X_t, X_{t-1}, ..., X_1\right) = \mathcal{P}\left(X_{t+1}|X_t\right). \tag{2.2}$$

This conditional probability corresponds to the transition rate for the state transition $X_t = \mu \to X_{t+1} = \nu$ (here, we randomly picked the states $\mu, \nu \in \Omega$ in order to denote the states the system is occupying at time t and $t + 1$). For stochastic systems obeying the Markov property, this transition rate for the state transition $\mu \to \nu$ can be written as

$$w_{\nu\mu} = \mathcal{P}\left(X_{t+1} = \nu|X_t = \mu\right). \tag{2.3}$$

For Markov chains which exhibit a discrete and finite, i.e., countable, state space Ω, whose dimension $\dim(\Omega) = \mathcal{N}$ corresponds to the total number $\mathcal{N}$ of states, one can introduce the transition rate matrix $\underline{\mathbf{W}}$ (often also referred to as infinitesimal generator matrix or intensity matrix). The latter is a $\mathcal{N} \times \mathcal{N}$ matrix which contains the rates of all state transitions $w_{\nu\mu}$ that are possible in the respective stochastic system under consideration. The diagonal elements $w_{\mu\mu}$ of a transition rate matrix $\underline{\mathbf{W}}$ are defined such that they contain all possible transition from state μ to any other state ν of the system. In other words, they correspond to the total outgoing rate to escape from state μ. This can be written as

$$w_{\mu\mu} = -\sum_{\nu \neq \mu} w_{\nu\mu}. \tag{2.4}$$

As a consequence, all rows of the transition rate matrix $\underline{\mathbf{W}}$ sum up to zero, i.e., $\sum_\nu w_{\nu\mu} = 0$ for all states $\mu \in \Omega$ of the system. This is a necessary conditions for a transition rate matrix. Additionally, a properly defined transition rate matrix $\underline{\mathbf{W}}$ requires that all transition rates are non-negative, i.e., $w_{\nu\mu} \geq 0$ for all $\mu \neq \nu$, and thus, $-w_{\mu\mu} \geq 0$ holds for all diagonal elements $w_{\mu\mu}$ of $\underline{\mathbf{W}}$. In fact, negative transition rates would physically make no sense at all. In this thesis, we only consider (physical) stochastic models with time-independent transition rates, i.e., $\mathrm{d}w_{\nu\mu}/\mathrm{d}t = 0$ for all states $\mu, \nu \in \Omega$. As a consequence, the transition rate matrix is a time-independent, stationary matrix $\underline{\mathbf{W}}(t) = \underline{\mathbf{W}}$. Let us now define a (probability) state vector of a (physical) stochastic system

$$\mathbf{P} = [p(\omega_1), p(\omega_2), ..., p(\omega_{\mathcal{N}-1}), p(\omega_{\mathcal{N}})] = [p_1, p_2, ..., p_{\mathcal{N}-1}, p_{\mathcal{N}}]. \tag{2.5}$$

This vector contains the normalized occupation probabilities $\sum_{i=1}^{\mathcal{N}} p(\omega_i) = \sum_{i=1}^{\mathcal{N}} p_i = 1$ of all discrete (micro)states ω_i of the probability state space $\Omega = \{\omega_1, \omega_2, ..., \omega_{\mathcal{N}}\}$. Specifically, $\sum_{i=1}^{\mathcal{N}} p_i = 1$ holds always, i.e., we assume probability conservation in all the systems studied in this thesis. In order to simplify the notation, we here denote the states of the system as ω_i, or just i and the corresponding occupation probabilities as $p(\omega_i) = p_i$. This notation for states is interchangeable with the otherwise used notation $\mu, \nu \in \Omega$ which is a convenient way to denote state transitions $\mu \to \nu$. the transition rate matrix $\underline{\mathbf{W}}$ can be used to model the dynamical evolution of time-independent Markov systems. The time-evolution of any configuration $\mathbf{P}(t)$ of a stochastic system is determined by $\underline{\mathbf{W}}$ via a Markovian master equation (ME)

$$\frac{\mathrm{d}}{\mathrm{d}t}\mathbf{P}(t) = \dot{\mathbf{P}}(t) = \underline{\mathbf{W}}\mathbf{P}(t). \tag{2.6}$$

If the system is prepared in a random initial configuration $\mathbf{P}(t = 0)$, it will relax towards the steady state (stationary) distribution $\mathbf{P} = \lim_{t\to\infty} \mathbf{P}(t)$ of the system under the dynamics governed by the transition rate matrix $\underline{\mathbf{W}}$. Accordingly, one gets $\underline{\mathbf{W}}\mathbf{P} = 0$ if the generator matrix $\underline{\mathbf{W}}$ is applied to $\mathbf{P}$. The steady state configuration $\mathbf{P}$ can simply be obtained by diagonalizing the generator matrix $\underline{\mathbf{W}}$. Specifically, $\mathbf{P}$ corresponds to the left eigenvector $\mathbf{v}$ of $\underline{\mathbf{W}}$ belonging to the eigenvalue $\lambda = 0$ which fulfills $\underline{\mathbf{W}}\mathbf{v} = \lambda\mathbf{v} = 0$ [113, 114]. Coming from the state vector $\mathbf{P}$ and taking a closer look at the occupation probability p_μ of a

specific state $\mu \in \Omega$, one finds that the time-dependent change of its occupation probability is also governed by a Markovian ME of the form

$$\dot{p}_\mu = \sum_\nu \left(p_\nu w_{\mu\nu} - p_\mu w_{\nu\mu} \right). \tag{2.7}$$

Here, $p_\nu w_{\mu\nu}$ corresponds to the total incoming flow into state μ from all states $\nu \neq \mu$ with $w_{\mu\nu} > 0$, while $p_\mu w_{\nu\mu}$ is the total outgoing flow from state μ to any state $\nu \neq \mu$ for which $w_{\nu\mu} > 0$. In particular, if $\dot{p}_\mu = 0$ for all states $\mu \in \Omega$, the system is in a stationary state (SS) with time-independent state vector $\mathbf{P}$ which is characterized by $\partial_t \mathbf{P} = \dot{\mathbf{P}} = 0$. In the following, we will shortly discuss ergodicity and then come to the conditions which must be met for a Markovian system in order to reach a steady state.

Ergodicity in discrete systems: Next to being "memoryless", ergodicity is another important feature of the Markovian (equilibrium and nonequilibrium) systems that we analyze in the context of this thesis. This is particularly relevant when it comes to the investigation of entropy production in nonequilibrium systems as it is the case in C. 9 and C. 8. The reason for this is that entropy production can only be properly defined if for any transition (or event) $\mu \to \nu$ with transition rate $w_{\nu\mu} > 0$, also the backward transition $\nu \to \mu$ is possible, i.e., is characterized by a non-vanishing transition rate $w_{\mu\nu} > 0$. Ergodicity and irreversibility are not the same thing, however, they are both important when it comes to calculating the entropy production in stochastic systems, i.e., quantifying their distance from thermal equilibrium. Therefore, we will briefly discuss necessary conditions that need to be met in a Markovian system in order to be ergodic. In general, a Markov Chain is said to be ergodic if all states μ, ν of Ω are aperiodic and positive recurrent [113, 114]. The period of a state μ is defined as the largest integer d fulfilling

$$d = gcd \left\{ n > 0 : \mathcal{P}(X_t = \mu | X_0 = \mu) > 0 \right\}, \tag{2.8}$$

where *gcd* is the greatest common divisor. If $d = 1$, state μ is called aperiodic, whereas states with $d > 1$ are denoted as periodic states. If all states $\mu \in \Omega$ are aperiodic, then the undrlying Markov Chain is aperiodic. In addition to aperiodicity, the property of recurrency (or persistency) is an essential prerequisite for a Markov Chain to be ergodic. In this sense, a state μ is recurrent, if along a stochastic path $\mathbf{X}(N)$ of length N the system that is found in state μ at time step t, i.e., $X_t = \mu$, will definitely return (with probability 1) to the very same state μ at some later time. The step t_{hit} when the system first comes back to state μ is called the hitting time. In other words, state μ is recurrent if it exhibits a finite hitting time $t_{\text{hit}} < \infty$. In other words, the system is able to explore the whole state (and phase) space Ω such that transitions from any state μ to any other state ν take place through a loop consisting of a finite number of state transitions. Consequently, not all states μ, ν have to be directly connected via a single transition $\mu \to \nu$, i.e., $w_{\nu\mu} = w_{\mu\nu} = 0$ is allowed, but they merely have to be connected via some sequence $\mathbf{X}(N) = (X_1 = \mu, ..., X_N = \nu)$ of finite length $N < \infty$.

Reversibility and detailed balance: Let us now discuss under which conditions a Markov process is reversible or irreversible, which is closely connected to the question whether the system is in thermal equilibrium or not. To this end, we consider the detailed balance condition. This condition is of immediate importance to formulate a consistent framework for nonequilibrium systems [50–52].

A Markov process is called reversible if it satisfies the detailed balance (DB) condition (also called the detailed balance equation), which is defined as

$$p_\mu w_{\nu\mu} = p_\nu w_{\mu\nu}, \tag{2.9}$$

for all transitions between any pair of states, $\mu, \nu \in \Omega$. Physically, Eq. (2.9) states that the probability to change (per time step) from state μ to state ν (due to the transition $\mu \to \nu$) and vice versa (due to the reversed process $\nu \to \mu$) are equal. One can easily understand why DB ensures reversibility of a Markovian system. If Eq. (2.9) holds, the forward state transition, $\mu \to \nu$, and the corresponding backward transition, $\nu \to \mu$, balance, and thus, the system does not change with time, i.e., the probability state vector is time-independent $\dot{\mathbf{P}} = 0$. Interestingly, it can be shown that this means that one can not decipher whether a shown movie of a system fulfilling Eq. (2.9) is played forward or backwards [52, 128, 129]. In particular, Eq. (2.9) further implies that the *flow of probability*

$$J_\nu = \sum_{\mu \in \Omega} p_\mu w_{\nu\mu} - p_\nu w_{\mu\nu} \tag{2.10}$$

nullifies for all states of the system. We note that DB implies that the system is in a steady state, as readily follows by inserting Eq. (2.10) into the Master equation (2.7). If DB holds for any state, the system is in thermal equilibrium. However, there is also the possibility hat $J_\nu \neq 0$ for some states $\nu \in \Omega$. Under certain conditions the system may still be found in a steady state, however, in a nonequilibrium one, i.e., in a nonequilibrium steady state (NESS) [130–132].

It is often convenient to describe the system which is investigated in terms of a connectivity graph consisting of nodes (which represent the states of the system) which can be connected by a finite number of edges. Specifically, an edge connecting nodes, i.e. the states of the system, μ and ν implies that a transition between these two states is possible. If the edge is pointing from state μ to ν, i.e., $\mu \to \nu$, the transition rate is denoted as $w_{\nu\mu}$. The backwards transition is denoted as $w_{\mu\nu}$. If two states μ, ν are not directly connected, i.e., a transition between these states is not possible, then we do not draw edges between those nodes since $w_{\nu\mu} = w_{\mu\nu} = 0$. If the system is ergodic, then any state can be reached through a loop of multiple state transitions, even if some nodes are not connected by edges. An example for a connectivity graph consisting of three nodes μ, ν, σ with corresponding state transitions is shown in Fig. 2.1.

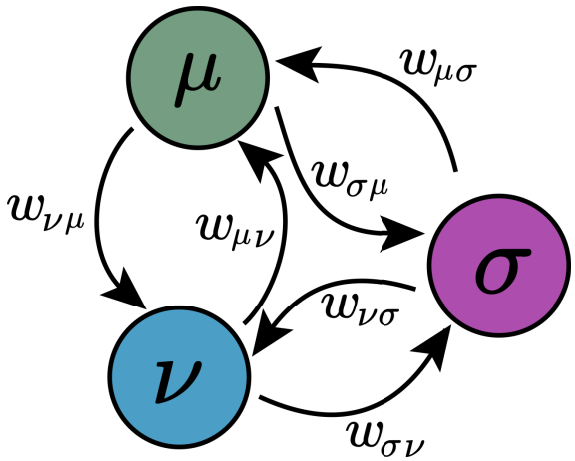

Fig. 2.1: Connectivity graph for a small system consisting of three discrete states, μ, ν and σ. Nodes, which represent the states of the system, are given by circles. The arrows which connect the nodes are called edges and they represent transitions between nodes. The transition rate for jumping from state μ to ν is denoted by $w_{\nu\mu}$. If $w_{\nu\mu} > 0$, then the system can directly jump from node μ to ν. Otherwise, if $w_{\nu\mu} = 0$, the transition $\mu \to \nu$ is not possible. If $w_{\nu\mu} > 0$ and $w_{\mu\nu} > 0$, the transition is reversible, whereas if $w_{\nu\mu} > 0$ and $w_{\mu\nu} = 0$, the transition is irreversible.

To give an explicit example, the nodes in Fig. 2.1 could represent the microstates of the spin models discussed in C 9. In that particular case, each node corresponds to a unique arrangement of spins on a d-dimensional lattice of lateral length L, containing L^2 spins in total. Edges between pairs of nodes are present if node (state) ν can be reached from node (state) μ (and/or vice versa) by changing the orientation, i.e., the state, of a single spin on the lattice. Such a single spin-flip process occurs with transition rate $w_{\nu\mu}$ (or $w_{\mu\nu}$ for the backward process) whose precise value depends on details of the system. The edges in the generic connectivity graph shown in Fig. 2.1 indicate that a direct transition between the states which are connected by an edge is possible. Of course, the general picture of the connectivity graph could also represent a different system. Important is just that nodes represent the states of the system and edges correspond to direct transitions between nodes.

2.2 Markov Chain Monte-Carlo methods

In order to simulate the dynamical evolution of Markovian systems, one typically uses Markov chain Monte-Carlo (MCMC) methods. The latter represent popular methods to obtain information about probability distributions without the need to know all mathematical details of the distribution. MCMC algorithms are appropriate to sample states, e.g., the microstates $\mu \in \Omega$ of discrete models, from a probability distribution $P(\mu)$, taking into account the Markov property. In particular, MCMC algorithms use continuous random variables to estimate properties of a certain distribution by examining random samples from the distribution. Concerning physical systems, one constructs a Markov chain such that the

probability p_μ to sample configuration μ of the underlying model is given by the Boltzmann distribution, i.e., $p_\mu \sim \exp(E_\mu/k_{\mathrm{b}}T)$ (where E_μ is the energy of configuration/microstate μ). The application of MCMCs to a physical system which is initially prepared in a random state μ at the beginning of the simulation will lead to a relaxation of the system towards its steady state probability distribution $P(\mu)$. There exist a variety of different MCMC algorithms in the literature [115, 117, 133]. Details of the algorithms used to model the dynamical evolution of spin systems are given in Sec. 2.3. Specifically, there we discuss the two most commonly used MCMC algorithms for lattice spin systems. These are, the Metropolis and the Glauber algorithm. Additionally, we shortly mention the Wolff and the Swendsen-Wang algorithm as examples for cluster update algorithms. The advantage of these algorithms is that they do not suffer from critical slowing down in the vicinity of phase transitions [134–136]. Unlike the spin models, we are particularly interested in the time-evolution of systems when it comes to investigating nonequilibrium surface growth. To this end, we use the kinetic Monte-Carlo (KMC) method. This algorithm allows to explicitly simulate the time evolution of stochastic processes. It is particularly useful when it comes to simulating the dynamical evolution of growing surfaces. The KMC method is introduced in Sec. 2.4.3.

2.3 Classical spin systems and simulation details

We begin the following section with a brief historical introduction to spin systems in the context of physics and then discuss examples where else these simply models are applied in order to describe collective phenomena. Moreover, we explain in detail the classical spin systems which are used in this thesis and sketch their exact solutions. The end of this section is concerned with numerical solutions of spin systems. Specifically, we discuss the most suitable algorithms which are frequently used to model the dynamics of spin systems.

2.3.1 Historical notes and fundamentals of spin systems

Spin systems and ferromagnetism on the microscale: Spin systems have been first introduced as simple models to study magnetism in solids on a fundamental, microscopic level. The latter represents a class of physical phenomena associated with electric charges [2, 65, 137, 138]. It exists in various different forms, involving single-particle as well as complex many-body effects. The spin systems considered in this thesis are simple mathematical models whose original purpose was to explain the phenomenon of ferromagnetism in solids. This form of magnetism is the strongest and most common manifestation of magnetism that we encounter in everyday life. The characteristic feature of ferromagnetic materials is the presence of an intrinsic magnetic field if the ambient temperature T is below some critical, material-specific value T_c (also known as Curie temperature). If the

temperature is increased above T_c, the internal magnetic field vanishes and the material behaves like a paramagnet as it was first discovered by Pierre Curie in 1895 [139]. This means that there occurs a transition from a magnetized phase to an unmagnetized phase at the critical temperature T_c which goes along with some dramatic internal changes of properties. It was a long-standing problem what exactly is happening inside a ferromagnetic substance on the microscale and how the change of system properties at T_c can be physically and mathematically described. This question is directed related to the topic of critical phenomena and universality which we discuss in C. 4.

It is well-established that any form of magnetism is a pure quantum mechanical effect as stated by the Bohr–van Leeuwen theorem [138, 140, 141]. The thermal average magnetization of an isolated system, i.e., no external fields are applied and rotations of the system are forbidden, vanishes when only tools from classical and statistical mechanics are applied. In this sense, ferromagnetism arises due to two fundamental quantum mechanical principles: First, it requires the concept of the quantum mechanical spin, a form of angular momentum which is carried by elementary particles that is responsible for their intrinsic magnetic dipole moment. Second, it is due to the Pauli exclusion principle [2, 138, 142] which states that in any atom it is not allowed for two or more fermions, i.e., spin $1/2$-particles, to have a set of identical quantum numbers. In other words, this means that it is forbidden for more than one fermion to occupy the same quantum state. Using these two concepts one can explain the emergence of ferromagnetism in certain materials. An essential prerequisite for ferromagnetism in solids are atoms with unpaired electrons such that their electron magnetic moments do not cancel out. As a consequence, such atoms carry a magnetic moment which can be interpreted as tiny magnet. The fact that crystalline materials are characterized by an ordered arrangement of atoms, ions or molecules, justifies the simplified mathematical perception of treating the magnetic moments as vectors on discrete positions of a rigid lattice. These spatially localized spins can point in a uniform direction mediated by the so-called exchange interaction [143, 144]. The latter is a quantum mechanical effect that explains the reduction of the potential energy of a spin ordered state in solids compared to a spin disordered state and it is responsible for the emergence of ferromagnetism in certain substances like iron, cobalt and nickel.

As suggested by Dirac [144], the critical features of the exchange interaction can be mimicked on a coarse-grained level by considering neighboring fermions as simply having their spin momenta coupled by a potential J in such a way that the exchange interaction Hamiltonian between two neighboring spins $\mathbf{s}_i$ and $\mathbf{s}_j$ which are located at discrete and equidistant lattice positions i and j can be written as $-2J\mathbf{s}_i\mathbf{s}_j$. This simple representation of magnetic systems has made a major contribution to understand ferromagnetism on a fundamental level. It also played a central role for the general theoretical understanding of phase transitions, critical behavior and universality are important topics within this thesis, especially concerning the content of C. 4, C. 9 and C. 6. Moreover, it served as inspiration

to introduce similar lattice models which are convenient to represent different physical systems outside the context of magnetism. For example, similar models are applied in the context of sociophysics where they are used model opinion formation, i.e., complex collective phenomena in societies [145]. An exemplary system is the majority vote model which has been intensively studied in the last two decades and is still investigated in various forms [146, 147]. Moreover, simple lattice-based spin systems are also applied in active matter physics. In this context, there exist models which describe the collective motion of swarms. Interestingly, despite their simplicity, they show the emergent phenomenon of motility induced phase separation [65, 148, 149]. Also in the context of surface growth, lattice-based models which are similar to the early spin systems are nowadays used to model the dynamical evolution of a growing surface. In particular, using lattice-based models, this is investigated in C. 5, C. 6, C. 7 and C. 8.

Mathematical representation of classical lattice-based spin models: So far we introduced the most simple form of interaction between spins, which is given by $\sim J\mathbf{s}_i\mathbf{s}_j$, but did not further specify any properties of this kind of interaction. The latter strongly depends on the question of whether one considers a classical or a quantum mechanical system. Without exception, solely classical systems are considered in this thesis. As a consequence, we restrict ourselves to a classical representation of spins $\mathbf{s}_i$ as specified further below in this section. A spin is represented by a n-dimensional vector that is interacting with neighboring spins, i.e., neighboring n-dimensional vectors, through a coupling constant of strength J. The sign of this coupling constant determines the ground-state spin configuration which corresponds to the configuration that minimizes the potential energy, $E = \langle\mathcal{H}\rangle$, of a system consisting of many interacting spins (where $\mathcal{H}$ is the Hamiltonian of the system). If the exchange constant is positive, $J > 0$, coupled spins prefer to align parallel to each other and thereby minimize E. In this case, spins are said to be ferromagnetically coupled and the ground state corresponds to a configuration where all spins $\mathbf{s}_i$ point in the same spatial direction. Conversely, if $J < 0$, interacting spins are antiferromagnetically coupled and they favor to align anti-parallel to each other in order to minimize the potential energy E of the system. Considering a many-body system consisting of spins $\mathbf{s}_i$ and $\mathbf{s}_j$ which are located on equidistant positions i, j of a discrete d-dimensional lattice of not further specified geometry leads us to the following general Hamiltonian for classical spin systems with nearest-neighbor interactions

$$\mathcal{H} = \frac{1}{2}(-2J\sum_{\langle ij\rangle}\mathbf{s}_i\mathbf{s}_j) + \sum_i h_i\mathbf{s}_i = -J\sum_{\langle ij\rangle}\mathbf{s}_i\mathbf{s}_j + \sum_i h_i\mathbf{s}_i. \tag{2.11}$$

In this equation, the pre-factor $1/2$ accounts for double counting in the sum that runs over all spatially neighboring spins $\mathbf{s}_i$ and $\mathbf{s}_j$, as indicted by $\langle ij\rangle$. This means that spins only interact with each other if they are spatially adjacent on the lattice. The second term models an externally applied magnetic field of strength h_i which acts locally on each lattice site i. This field may be random on all sites i, oscillating with a certain frequency or equal and constant on all lattice sites. Again, we did not specify any properties of the spins $\mathbf{s}_i$ and

$\mathbf{s}_j$ and we also did not give any details concerning their geometrical arrangement. Basically, we only wrote down the simplest form of a Hamiltonian which accounts for interacting n-dimensional spins $\mathbf{s}_i$ and $\mathbf{s}_j$ on a lattice of some dimension d and geometry. We restrict ourselves to $d \leq 3$ and $n \leq 3$. To avoid misunderstandings, we again want to point out that d refers to the spatial dimension of the lattice on which the spins $\mathbf{s}_i$ are located, whereas n, which is also called the order-parameter symmetry number, corresponds to the spatial dimension of the spins.

Let us now discuss the structure of the spins $\mathbf{s}_i$ in more detail. Without any exception, spins in this thesis are represented by n-dimensional unit vectors in the real coordinate space, $\mathbf{s}_i \in \mathcal{R}^n$, with $\sum_n |\mathbf{s}_i^n| = 1$. Accordingly, spins with $n = 1$ can only take the values, $\mathbf{s}_i = 1$ and $\mathbf{s}_i = -1$, i.e., they can solely point parallel or antiparallel along the x-axis, which is the only axis of the one-dimensional coordinate space $\mathcal{R}^1 = (x)$. Nevertheless, such one-dimensional spins can be arranged on a lattice with $d \geq 1$. For example, they can be arranged on square, hexagonal, triangular ($d = 2$) or cubic lattices ($d = 3$). The lattice dimension d and geometry can have an enormous impact on the collective ordering dynamics of the system and its critical behavior in the vicinity of phase transitions as discussed in detail in C 4.

In the literature, there exist many different variants of classical (as well as quantum mechanical) spin systems which are distinguished from each other by the sign and range of the coupling constant J, e.g., also non-adjacent spins can be coupled (with the same or a different coupling strength), their lattice geometry, d, and the spin dimension n. Additionally, their exist one further important attribute that can strongly affect the collective ordering behavior and the scaling properties of the system. This additional attribute corresponds to the parameter q which determines the rotational degrees of freedom of spins in the coordinate space $\mathcal{R}^n$. The question is whether the n-dimensional spins are allowed to rotate continuously, and thus can point in any direction within the given space, $\mathcal{R}^n$, or if they are restricted to a limited number of discrete directions. This is regulated by the parameter q, which is an integer that sets the number of possible states, i.e., orientations, a single spin $\mathbf{s}_i$ can take in its n-dimensional coordinate space. Specifically, for $n = 2$ (we only consider $n = 1$ and $n = 2$), the parameter q determines the allowed, uniformly distributed angles

$$\theta_i = (2\pi a)/q, \tag{2.12}$$

the spins can take within the unit circle. In this equation, $a \in [0, q-1]$ is an integer with maximum value $a = q - 1$ which determines the pointing direction, i.e., the angle θ_i, of a spin $\mathbf{s}_i$ that is located at lattice position i. The possible spin orientations for some exemplary values of q (where $n = 2$) are shown in Fig. 2.2.

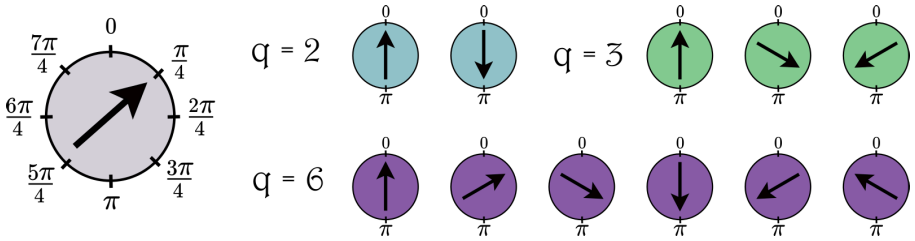

Fig. 2.2: Illustration of the possible spin configurations s_i, i.e., the allowed orientations of spins $\theta_i = (2\pi a)/q$ (where $a \in [0, q-1]$ is an integer with maximum value $q-1$) with spin dimension $n = 2$ for three values of q indicated by three different colors. The spins can be found in each of the q uniformly distributed states within the unit circle in the $x-y$ plane. Specifically, this means that the length of spins is unity in any o the q configurations.

For the trivial example $n = 1$, one finds that q can not be chosen freely and $q = 2$ is the maximum value. Consequently, for $q = 2$, only the states parallel, $\mathbf{s}_i = 1$, and anti-parallel, $\mathbf{s}_i = -1$, to the x-axis are possible. This setup is known as the Ising Model which will be discussed in detail in Sec. (2.3.2). More complex are the cases $n \geq 2$ where q can be any positive integer. For example, if one considers $n = 2$, it is possible to take $q = 2$ and thereby recover the Ising model. However, also $q > 2$ is possible because spins are also allowed to point along the y-axis. For the case $n = 2$ and $q \to \infty$, the spins are represented by two-dimensional unit vectors, $\mathbf{s}_i = (x, y)$, which can rotate freely within the $x-y$-plane, i.e., $\theta \in (0, 2\pi]$. This setup is known as the classical XY model and will be discussed in the next section Sec. 2.3.2. Just for completeness we mention the scenarios $n = 0$ and $n = 3$ which correspond to the self-avoiding random walk [150] and the classical Heisenberg model [151], respectively. Though they are important and have been intensively studied, they are not investigated in this thesis.

In summary, the coupling constant J, the lattice dimension d, the spin dimension n, the external field h and the number of possible (discrete) spin configurations q together with the geometry of the lattice form a fundamental set of parameters (J, d, n, h, q) that determines various properties of spin models, their critical behavior and the corresponding universality class (see C. 4 and C. 9). However, we want to point out that their exist much more adjusting screws which can affect the collective behavior of many-body spin systems. For example, some sites i could be empty as it is the case in the dilute Ising model [152], the strength J of the coupling constant can be non-uniform (e.g., the directed Ising model [153]) or the spins may be coupld to several heat baths at different temperatures. The last two examples are investigated in this thesis in C. 9 and in the outlook. Moreover, also the choice of the spin-update algorithm plays a crucial role for the dynamical evolution of the system. Usually, one uses MCMC algorithms to model the dynamics of lattice-based spin systems [115]. The latter being a class of algorithms which sample states from an appropriate probability distribution as discussed in Sec. 2.3.3. By constructing a Markov chain that has the desired distribution as its equilibrium distribution, one can obtain a sample of the distribution by recording states from the chain via an appropriate algorithm. Two of the most frequently used MCMC methods are the Metropolis algorithm and the

Glauber dynamics. They are distinguished from each other by the acceptance rate for spin flips as shown in more detail in Sec. 2.3.3. In order to model the dynamics of a spin system by one of these two algorithms, it is crucial to couple the spins to a heat bath at temperature T. This temperature acts as control parameter. The temperature T has an impact on the acceptance probability of spin flips and thereby controls the degree of spin order in the system. Heat baths which are kept at a temperature T are essential constituents for the dynamics of many-body spin systems. They will be discussed in some more detail in Sec. (2.3.2).

2.3.2 Classical lattice-based spin models

In this section we discuss the very basics of the microscopic details of the lattice-based spin models which are investigated in this thesis. The models are distinguished from each other by the order-parameter symmetry number n and the parameter q which determines the number of directions in which the spins can point. We limit ourselves to $n = 1$ and $n = 2$ and only consider one-dimensional ($d = 1$) and two-dimensional ($d = 2$) square lattices.

The Ising model: The Ising model was first introduced by Lenz in 1920 [154, 155] based on the assumption that the elementary magnetic moments, i.e. the spins $\mathbf{s}_i$, in solids do not freely rotate in space, but instead only change their direction by turning around by $180°$, a process which is also referred to as Umklapp Prozess. This means that spins, which are located on discrete lattice positions i, can only be found in one of two distinct states, $\mathbf{s}_i \in [-1, 1]$, corresponding to one configuration pointing parallel along the x-axis and one pointing antiparallel along x. In line with the categorization of spin systems as discussed above in Sec. 2.3.1, the Ising model is a spin system with $n = 1$, $q = 2$, and consequently, $\theta_i = 0$ or $\theta_i = \pi$. Since $n = 1$ for the Ising model, we can replace the vector notation for the spins $\mathbf{s}_i \equiv s_i$ and write the Hamiltonian of the system with nearest-neighbor coupling as

$$\mathcal{H} = -J \sum_{\langle ij \rangle} s_i s_j + \sum_i h_i s_i. \tag{2.13}$$

In this equation, the sums run over all lattice sites, J represents the coupling constant between nearest-neighbor (NN) spins s_i and s_j which mimics the mutual interaction and h_i models an externally applied transversal magnetic field as in the general Hamiltonian which we introduced in Eq. (2.11). For ferromagnetic coupling, $J = 1$, the ground-state configuration corresponds to a maximally ordered state, i.e., all spins point in the same direction (i.e., all spins point either up, $s_i = 1$ or down, $s_i = -1$) and consequently, the order parameter, i.e., the magnetization $m = |1/L^d \sum_i s_i|$ (where d refers to the spatial dimension of the lattice), is maximized, $m = 1$. Since the spins are coupled to a heat bath at temperature T, thermal fluctuations can destroy the spin ordered state. These fluctuations are responsible for a phase transition to an unmagnetized state, $m = 0$, if the temperature T is increased above the critical temperature T_c which, for the two-

dimensional Ising model on a square lattice, is given by $T_c = 2.269$. In the following we discuss the one- and two-dimensional Ising model in more detail. Specifically, we sketch the analytical calculation to determine the critical temperature T_c where the system undergoes an order-disorder phase transition and thereby show that the one-dimensional version of the model does not have a spin ordered phase.

The one-dimensional Ising model: The Ising model in one spatial dimension, $d = 1$, with nearest-neighbor coupling and periodic boundary conditions (PBC) was first solved analytically by Ising in 1925 [156]. In this lattice dimension, the system is also referred to as Ising chain. It does not exhibit a stable spin ordered phase. Thus, it does not exhibit a order-disorder phase transition upon lowering the temperature T. In other words, there is no critical temperature T_c. Despite the apparent simplicity of spin models, analytic solutions are often involved or even impossible to obtain. Therefore, we here use the opportunity to sketch the general solution of the exactly solvable Ising model (where an uniform transverse field $hi \neq 0$ may be present) via the transfer matrix method [155, 157, 158]. To this end, let us consider a one-dimensional lattice configuration consisting of L equidistant sites i which are occupied by spins, $s_i \in [-1, 1]$. Due to the imposed PBC, $s_{L+1} = s_1$. Since we consider a canonical ensemble, the probability to find the system, which is kept at temperature T, in microstate μ with energy E_μ is given by the Boltzmann-Gibbs measure

$$p_\mu(T) = \frac{1}{Z}\exp\left(-E_\mu/T\right), \tag{2.14}$$

where $Z = \sum_\mu \exp\left(-E_\mu/T\right)$ is the canonical partition function which normalizes the Boltzmann distribution. In particular, Z is important because it relates the microscopic properties of the system (that constitute the energy E_μ of each microstate μ) to macroscopic thermodynamic quantities like the Helmholtz free energy

$$F = -\frac{1}{L}k_\mathrm{b}T\ln(Z). \tag{2.15}$$

The partition function of the one-dimensional Ising model (i.e., the Ising chain) with inverse temperature $\beta = 1/T$ reads

$$Z = \sum_\mu \exp\left(-\beta E_\mu\right) = \sum_{\{s_i\}} \exp\left[-\beta E\left(s_1, s_2, ...s_{L-1}, s_L\right)\right], \tag{2.16}$$

where $\sum_{\{s_i\}} = \sum_{s_1=-1}^{1}\sum_{s_2=-1}^{1}...\sum_{s_L=-1}^{1}$ means that the sum in Eq. (2.16) runs over all 2^L microstates, i.e., all possible configurations of spins on the lattice. Note that each individual configuration $(s_1, s_2, ..., s_{L-1}, s_L)$ of spins simply corresponds to exactly one microstate μ of the system which is assigned the energy $E(s_1, s_2, ..., s_{L-1}, s_L) = E_\mu$. The energy of the bond between s_i and s_{i+1} reads

$$E(s_i, s_{i+1}) = Js_is_{i+1} + \frac{h}{2}\left(s_i + s_{i+1}\right). \tag{2.17}$$

Consequently, the energy of a particular microstate μ corresponds to $E_\mu = E(s_1, s_2) + E(s_2, s_3) + ... + E(s_{L-1}, s_L) + E(s_L, s_1)$. In the next step we have to rewrite the Hamiltonian as sum over bonds and factor the Boltzmann weights to pairwise factors

$$Z = \sum_{s_1}\sum_{s_2}...\sum_{s_{L-1}}\sum_{s_L}\prod_{i=1}^{L}\exp\Bigg\{\beta\underbrace{\left[Js_is_{i+1} + \frac{h}{2}(s_i + s_{i+1})\right]}_{E(s_i,s_{i+1})}\Bigg\}. \tag{2.18}$$

At this point, we introduce the transfer matrix elements for spatially neighboring spins s_i and s_{i+1}

$$t_{s_i,s_{i+1}} = \exp\left[\beta E(s_i, s_{i+1})\right] = \exp\left\{\beta\left[Js_is_{i+1} + \frac{h}{2}(s_i + s_{i+1})\right]\right\}. \tag{2.19}$$

Specifically, since for the Ising model both spins, s_i and s_{i+1} can be found in state $s_i = 1$ or $s_i = -1$, there are the following four two spin configurations: $(1.)$ $s_i = s_{i+1} = 1$, $(2.)$ $s_i = s_{i+1} = -1$, $(3.)$ $s_i = 1, s_{i+1} = -1$, $(4.)$ $s_i = -1, s_{i+1} = 1$. As a consequence, the transfer matrix $\underline{\mathbf{t}}_{s_i,s_{i+1}}$ is a 2×2 matrix containing these four configurations,

$$\underline{\mathbf{t}}_{s_is_{i+1}} = \begin{pmatrix} t_{1,1} & t_{1,-1} \\ t_{-1,1} & t_{-1,-1} \end{pmatrix} = \begin{pmatrix} \exp\left[\beta E(1,1)\right] & \exp\left[\beta E(1,-1)\right] \\ \exp\left[\beta E(-1,1)\right] & \exp\left[\beta E(-1,-1)\right] \end{pmatrix}.$$

At this point, we can rewrite the partion function and express it in terms of transfer matrices

$$Z = \sum_{s_1}\sum_{s_2}...\sum_{s_L}\underline{\mathbf{t}}_{s_1s_2}\underline{\mathbf{t}}_{s_2s_3}...\underline{\mathbf{t}}_{s_{L-1}s_L}\underline{\mathbf{t}}_{s_Ls_1}. \tag{2.20}$$

A close inspection of this equation and the corresponding transfer matrices reveals that for each bond between neighboring spins s_i and s_{i+1}, two transfer matrices share one index. This can be seen by considering $\underline{\mathbf{t}}_{s_1s_2}$ and $\underline{\mathbf{t}}_{s_2s_3}$. Here, the second spin, s_2, is shared since it is part of both transfer matrices. Thus, the sum over s_2 in the expression for Z can be rewritten as multiplication

$$\sum_{s_2}\underline{\mathbf{t}}_{s_1s_2}\underline{\mathbf{t}}_{s_2s_3} = (\underline{\mathbf{t}}\cdot\underline{\mathbf{t}})_{s_1s_3} = \underline{\mathbf{t}}^2_{s_1s_3}. \tag{2.21}$$

As we see, the second index, s_2, vanishes if we perform the corresponding sum over this site. By repeating this procedure for all sums in Eq. (2.20), we arrive at

$$\sum_{s_1}(\underline{\mathbf{t}}\cdot\underline{\mathbf{t}}\cdot\underline{\mathbf{t}}\cdot...\cdot\underline{\mathbf{t}}\cdot\underline{\mathbf{t}})_{s_1s_1} = \sum_{s_1}(\underline{\mathbf{t}}^L)_{s_1s_1} \equiv \mathrm{Tr}[\underline{\mathbf{t}}^L]. \tag{2.22}$$

The partition function Z can be written as the trace of $\underline{\mathbf{t}}_{s_1s_1}$ to the power of the number of bonds which is equal to L, the number of spins. This rewriting procedure of Z is useful since we now can apply basic linear algebra to simplify the trace in Eq. (2.22). After

diagonalizing the transfer matrix, $\underline{\mathbf{t}} = S^{-1}\Lambda S$, we can make use of the cyclic property of the trace,

$$Z = \mathrm{Tr}[\underline{\mathbf{t}}^L] = \mathrm{Tr}[S^{-1}\Lambda S S^{-1}\Lambda S ... S^{-1}\Lambda S] = \mathrm{Tr}[S^{-1}\Lambda^L S] = \mathrm{Tr}[\Lambda^N] = \lambda_1^L + \lambda_2^L. \quad (2.23)$$

Thereby, we end up with a simple expression for the partition function Z which reveals that it can be expressed by the two eigenvalues $\lambda_1 \geq \lambda_2$. These eigenvalues satisfy the characteristic equation

$$\lambda^2 - \mathrm{Tr}[\underline{\mathbf{t}}]\lambda + \mathrm{Det}[\underline{\mathbf{t}}] = 0 \quad (2.24)$$

of the transfer matrix $\underline{\mathbf{t}}$. Finally, this brings us to the following solution for the two eigenvalues,

$$\lambda_{1,2} = \exp(\beta J)\left[\cosh(\beta h) \pm \sqrt{\sinh(\beta h) + \exp(-4\beta J)}\right]. \quad (2.25)$$

By going to the thermodynamic limit, i.e. $L \to \infty$, and making use of $\lambda_1 \geq \lambda_2$, we can approximately express the partition function Z according to

$$\lim_{L\to\infty} Z \approx \lambda_1^L = \exp(L\beta J)\left[\cosh(\beta h) + \sqrt{\sinh(\beta h) + \exp(-4\beta J)}\right]^L, \quad (2.26)$$

which is the final form of the partition function. Equation (2.26) can be used to calculate various quantities. For example the free energy F of the system is given by

$$F = -J - kT\ln\left[\cosh(\beta h) + \sqrt{\sinh(\beta h) + \exp(-4\beta J)}\right]. \quad (2.27)$$

From the free energy, the ensemble average absolute magnetization m of the system can be calculated according to

$$m = -\frac{\partial F}{\partial h} = \frac{\sinh(\beta h)}{\sqrt{\sinh^2(\beta h) + \exp(-4\beta J)}}. \quad (2.28)$$

By switching off the external field, $h \to 0$, the spontaneous magnetization vanishes, i.e., $m \to 0$. This means that there is no stable ferromagnetic phase in the system when there is no external field applied. As a consequence, there is no phase transition in the one-dimensional version of the Ising model in absence of an externally applied transverse magnetic field.

The two-dimensional Ising model: Here, we shortly sketch the solution of the two-dimensional Ising model based on the transfer matrix method [157, 159, 160] which was already used to solve the one-dimensional version in the previous paragraph. In contrast to the Ising chain, the model with nearest-neighbor coupling in two spatial dimensions, $d = 2$, exhibits a stable ferromagnetic phase at low temperatures even in the absence of an external magnetic field h. Considering a square lattice of lateral length L, the two-dimensional Ising model can be interpreted as succession of L one-dimensional

rows of length L. Each row $r = 1, 2, ..., L$ has the same 2^L configurations as the one-dimensional Ising chain of length L. The spin configuration of row r can be written as $\phi_r = (s_1, s_2, ..., s_{L-1}, s_L)$. The next step is to write transfer matrices for neighboring rows. This is a quite cumbersome procedure which we will not show here. As for the one-dimensional case, the partition function becomes a consecutive product of transfer matrices. Finally, in the limit $L \to \infty$, the partition function of the two-dimensional Ising model with $h = 0$ can be written as

$$\lim_{L\to\infty} = \ln\left[2\cosh\left(2\beta J\right)\right] + \frac{1}{2\pi}\int_0^\pi \mathrm{d}\vartheta \ln\left[\frac{1}{2}\left(1 + \sqrt{1 - \kappa^2 \sin^2(\vartheta)}\right)\right], \tag{2.29}$$

where $\theta = (2\sinh(2\beta J))/(\cosh(2\beta J))$. The ferromagnetic phase emerges as T is decreased below the critical temperature T_c. The critical temperature can be expressed in closed form according to Onsager's solution of the model [160]

$$T_c = \frac{2J}{\ln(1 + \sqrt{2})}. \tag{2.30}$$

In numerical simulations of the Ising model, the order-disorder phase transition corresponds to the crossing point of the fourth-order Binder cumulant U_4 for different system sizes L (see Sec. 2.3.3 for details where U_4 for system sizes from $L = 16$ to $L = 32$ is plotted together with exact value $T_c = 2.269$). At the critical point T_c, the system undergoes a continuous (second-order) phase transition. The model shows critical behavior in the vicinity of T_c and the corresponding critical exponents represent the equilibrium Ising universality class. The latter is characterized by the following set of critical exponents (see C 4 for details), $\alpha = 0, \beta = 1/2, \gamma = 1, \delta = 3, \eta = 0, \nu = 1/2$. Interestingly, many physically very different systems show the exact same scaling behavior around continuous phase transitions as the Ising model. If an external field is applied, the character of the transition can change from second- to first-order [157]. We do not consider the model in presence of an external field, and thus, are always concerned with continuous phase transitions in the two-dimensional Ising model.

The q-state vector-Potts model: Here, we introduce the generalization of the Ising model which allows for more than two states per spin. Specifically, the q-state vector Potts model (which is also known as clock model or planar Potts model [157, 161, 162]) is characterized by $n = 2$ and $q \geq 2$. As discussed earlier in this section, for $n = 2$, spins $\mathbf{s}_i$ are two-dimensional objects that can take q different values, i.e., orientations distributed uniformly about the unit circle, at equidistant angles θ_i. Using the angles θ_i instead of two-dimensional unit vectors allows to write the Hamiltonian of the q-state vector Potts model with nearest-neighbor interaction of spins and an externally applied magnetic field as

$$\mathcal{H} = -J\sum_{\langle ij\rangle} \cos\left(\theta_i - \theta_j\right) + \sum_i h_i \cos(\theta_i). \tag{2.31}$$

At this point we want to point out that the q-state vector Potts model should not be confused with the standard Potts model [162]. The latter is a simpler version where coupled spins only interact with each other if they point in the same direction, i.e., when they take the same angle $\theta_i = \theta_j$. For the standard Potts model, the Hamiltonian reads, $\mathcal{H} = -J \sum_{\langle ij \rangle} \delta(s_i, s_j)$, with $\delta(s_i, s_j)$ being the Kronecker delta. Throughout this thesis we only consider the q-state vector Potts model defined in Eq. (2.31), even if we call it Potts model. Clearly, for $q = 2$, the model corresponds to the Ising model, while for $q = 3$ it is equivalent to the just mentioned standard Potts model [162]. Only for $q > 3$, the q-state vector Potts model is not equivalent to other spin models.

Despite its simplicity, the q-state vector Potts model shows diversified critical behavior. On a two-dimensional square-lattice, the number of phase transitions, their order and the corresponding universality class depend on q. While for $q \leq 4$, the model with $h = 0$ exhibits a single continuous (second-order) phase transition from a paramagnetic (PM) to a spin-ordered ferromagnetic phase (FM), the nature of the transition completely changes when $q \geq 5$. In this case, the model exhibits two BKT-like (BKT stands for Berezinskii-Kosterlitz-Thouless) phase transition [57]. Upon lowering the temperature T in the PM phase, the system undergoes an infinite-order phase transition to a quasi long-range ordered (QLRO) BKT phase at the critical temperature T_{c1} [57, 162]. By further lowering T, the system undergoes a second BKT-like transition from the QLRO to a ferromagnetically ordered phase at T_{c2}. Interestingly, while the temperature T_{c1} of the first phase transition from the FM to the QLRO phase is independent of the value of q, the critical temperature of the second transition from the QLRO to the FM phase decreases as the value of q is increased, until in the limit $q \to \infty$, the second transition vanishes. In this case the system, i.e., the XY model, only exhibits a single infinite-order transition from a PM to a QLRO phase at $T_c = 0.8816(5)$ [163, 164]. The lack of a stable ferromagnetic phase for $q \to \infty$ is due to the Mermin-Wagner theorem which states that continuous symmetries (like the continuous spin symmetry in the xy-plane for $q \to \infty$) can not be spontaneously broken at finite temperatures in systems with short-range interactions and $d \leq 2$.

The classical XY model: The classical XY model is the limiting case of the aforementioned q-state vector Potts model with $q \to \infty$. This means that, in contrast to cases where q is finite, the XY model exhibits continuous spin-symmetry, i.e., spins can continuously point in any direction on the unit circle, i.e., $\theta_i \in [0, 2\pi]$. Therefore, the partition function of the model reads

$$Z = \prod_{n=1} \int_{-\pi}^{\pi} \mathrm{d}\theta_n \exp\left[\beta \sum_{\langle ij \rangle} \cos(\theta_i - \theta_j)\right]. \tag{2.32}$$

Different from the solution of discrete spin models, the transfer matrix method is inappropriate for the XY model since for continuous spin symmetry, the transfer matrix dimension would go to infinity. However, at low temperatures, i.e., in the T-regime where one expects neighboring spins to point in rather similar directions, the cosine in Eq. (2.32) is ≈ 1, and can thus be expanded. Thereby, the cosine gets simplified if we neglect all orders higher

than two in the expansion. This simplification of the Hamiltonian is known as spin-wave approximation [157, 162]. It allows us to express the Hamiltonian of the XY model as

$$\mathcal{H} = -\beta \sum_{\langle ij \rangle} \left[1 - \frac{(\theta_i - \theta_j)^2}{2} \right]. \tag{2.33}$$

Taking this equation and making use of the fact that constant parts do cancel when expectation values are calculated, the partition function in spin-wave approximation can be written as

$$Z = \prod_{n=1} \int_{-\pi}^{\pi} \mathrm{d}\theta_n \exp \left[-\frac{\beta}{2} \sum_{\langle ij \rangle} (\theta_i - \theta_j)^2 \right]. \tag{2.34}$$

At low temperatures, i.e., large values of β, the integral boundaries can in good approximation extended to infinity. In this case, the partition function becomes Gaussian [162],

$$Z = \prod_{n=1} \int_{-\infty}^{\infty} \mathrm{d}\theta_n \exp \left[-\frac{\beta}{2} \sum_{\langle ij \rangle} (\theta_i - \theta_j)^2 \right]. \tag{2.35}$$

By using the generating functional together with the two-dimensional lattice Green function,

$$G(\mathbf{r}) = \frac{1}{(2\pi)^2} \int_{-\pi}^{\pi} \mathrm{d}\mathbf{k} \frac{\exp(i\mathbf{kr})}{\sum_{a=1}^{2} 4[1 - \cos(k_a)]}, \tag{2.36}$$

it can be shown [162] that the x-component of the magnetization, m_x, of the XY model depends on the Green function $G(0)$,

$$m_x = \frac{1}{L} \sum_i \cos(\theta_i) = \langle \cos(\theta_i) \rangle = \mathrm{Re} \langle \exp(i\theta_i) \rangle = \mathrm{Re} \left[\exp\left(-\frac{2G(0)}{\beta} \right) \right]. \tag{2.37}$$

Since the integral $G(0)$ diverges, the magnetization vanishes, i.e., $m_x \to 0$. This is in accordance with the Mermin-Wagner theorem. In fact, the magnetization remains zero irrespective of the temperature or the strength of the coupling constant J. In higher spatial dimensions, i.e., $d > 2$, the lattice Green function does not diverge, and thus, a stable ferromagnetic phase emerges at low temperatures T. Therefore, the three-dimensional XY model does exhibit a PM to FM phase transition [71, 162].

Even though there is no net magnetization in the XY model for $d = 1$ and $d = 2$, it can be shown that another type of phase transition is present in the two-dimensional XY model. Despite the fact that $m = 0$ for any value of T, there exists a critical point T_c which divides the system into a high-temperature phase $T > T_c$ where correlations decay exponentially fast and a low-temperature phase $T < T_c$ where correlations show a power-law decay [57, 162]. The transition from power-law to exponential decay corresponds to an infinite-order BKT phase transition. Above T_c, unbound vortices and antivortices freely move in the system. At the critical point T_c, a phase emerges which is characterized by the formation of vortex-antivortex pairs. Within this phase, correlations show a power-law decay [57, 162]. At this point, we do not go deeper into the theoretical foundations of this

type of phase transition. Specifically, we are interested in the behavior of the specific heat c_v and the entropy production rate per spin π in the vicinity of the infinite-order BKT-like phase transition in the XY model under nonequilibrium conditions. We show results for c_v and π in C. 9.

2.3.3 Algorithms to model the dynamics of spin systems

In the following we will discuss details of the most commonly used MCMC algorithms to model the dynamical evolution of spin systems. The algorithms are defined such that in each step of the simulation, a random spin s_i (or a cluster containing multiple spins) is chosen and an attempt to change it's orientation is made. Such a spin (or cluster) flip corresponds to a state transition $\mu \to \nu$ from microstate μ to ν with $\mu, \nu \in \Omega$. The task of the underlying MCMC algorithm is to repeat this procedure and in each step either accept or decline the attempted state transition $\mu \to \nu$. Whether the flip is accepted or declined depends on the rate $w_{\nu\mu}$ of the transition which crucially depends on details of the Hamiltonian, i.e., details of the spin model, and the underlying MCMC algorithm. Each algorithm has it's own strengths and weaknesses. Thus, different algorithms are best suited for different tasks. In the following we discuss the Metropolis and the Glauber algorithm which are the two most prominent local MCMC algorithms used to model the dynamics of discrete spin systems. Additionally, we shortly mention cluster algorithms where in each step a whole cluster of spins is flipped instead of a single spin s_i. Concerning cluster algorithms we shortly mention and explain the single cluster Wolff algorithm [165] and the multi cluster Swendsen-Wang algorithm [166].

The Metropolis algorithm: Even though the Metropolis algorithm was introduced almost 70 years ago in 1953 [167, 168], it is still a standard MCMC used to sample states of stochastic systems exhibintg a discrete state space Ω. This algorithm has proven to be particularly useful to model the dynamics of spin systems. In order to calculate the value of the transition rate $w_{\nu\mu}$ for flipping a spin at site i from s_i to $s_i^{'}$, one first picks a random lattice site i and calculates the energy difference $\Delta E_{\nu\mu} = E_\mu - E_\nu$ between the microstate ν which is occupied after the potential spin flip and the initial state μ the system is occupying before the spin s_i on site i changed it's orientation to $s_i^{'}$. The possible values of $\Delta E_{\nu\mu}$ depend on the local field of the surrounding spins and, if applied, on an external field h which can point in a certain direction. Of course, the external field could also rotate, periodically switch it's orientation or take a random value on each lattice site i. In other words, $\Delta E_{\nu\mu}$ depends on details of the system, e.g., the value and range of the coupling constant J, the number of configurations per spin, q, as well as the lattice geometry and it's dimension d. For a system in contact with a heat bath at temperature T, the transition rate, i.e., the acceptance probability, for a spin flip $\mathbf{s}_i \to \mathbf{s}_i^{'}$ according to the Metropolis algorithm is given by

$$w_{\nu\mu} = \min\left[1, \exp(-\Delta E_{\nu\mu}/k_\mathrm{b}T)\right]. \tag{2.38}$$

Here, k_b is the Boltzmann constant which we always set to unity, $k_\mathrm{b} = 1$. According to the form of this equation, the transition rate is a number between 0 and 1, i.e., $w_{\nu\mu} \in [0, 1]$. Therefore, the transition rate corresponds to an acceptance probability p_a of the attempted spin flip. Equation (2.38) tells us that whenever the energy of the system is reduced by an attempted spin flip, i.e., if $\Delta E_{\nu\mu} \leq 0$, the transition from μ to ν is conduced with probability $p_a = 1$ and the spin flips from s_i to its new configuration $s_i^{'}$. On the contrary, if $\Delta E_{\nu\mu} > 0$, one draws a random number $r \in [0, 1]$, which is uniformly distributed in the given interval, and compares this number with $w_{\nu\mu} = \exp\left(-\Delta E_{\nu\mu}/T\right)$. If $r < \exp\left(-\Delta E_{\nu\mu}/T\right)$, the flip is accepted despite the fact that it leads to an increase of the total energy of the system. In contrast, if $r > \exp\left(-\Delta E_{\nu\mu}/T\right)$, the spin flip attempt is rejected and the system remains in state μ, i.e., spin s_i keeps it's orientation. According to the dependency of $w_{\nu\mu}$ on the energy difference $\Delta E_{\nu\mu}$, the probability to accept an energetically unfavorable configuration decays exponentially with increasing $\Delta E_{\nu\mu}$. The probability p_a for accepting spin flips as function of $\Delta E_{\nu\mu}$ is plotted in Fig. 2.3 for the Metropolis and the Glauber algorithm at different temperatures T. No matter whether the spin flip is accepted or rejected, the procedure of attempting spin flips is repeated many times until the system, depending on the details, eventually reaches, a steady state which may be a state of thermal equilibrium or a NESS.

The Glauber algorithm: In the same manner as for the Metropolis algorithm, the here discussed Glauber dynamics (which is identical to the heat bath dynamics algorithm) corresponds to a MCMC method which, in the case of spin systems, models the dynamical evolution of non-conservative flips of single spins, $s_i \to s_i^{'}$. The difference to the Metropolis algorithm lies in the functional form of the transition rate, i.e., the spin flip acceptance probability p_a. Specifically, according to the Glauber algorithm [169], the transition rate for $\mu \to \nu$ depends on the energy difference $\Delta E_{\nu\mu}$ between state μ and ν in the following way

$$w_{\nu\mu} = \frac{\exp\left(-\Delta E_{\nu\mu}/T\right)}{1 + \exp\left(-\Delta E_{\nu\mu}/T\right)} = \frac{1}{2}\left[1 - s_i \tanh\left(\frac{\Delta E_{\nu\mu}}{T}\right)\right]. \tag{2.39}$$

According to Eq. (2.39), not only state transitions $\mu \to \nu$ which lead to an increase of the system's internal energy, i.e. $\Delta E_{\nu\mu} > 0$, may be rejected, but also state transitions which lead to a reduction of a system's internal energy, i.e., $\Delta E_{\nu\mu} < 0$, are not always accepted. This is in stark contrast to the Metropolis rule for which all spin flips with which lead to $\Delta E_{\nu\mu} \leq 0$ are accepted. To make this explicit, let us compare the Metropolis with the Glauber transition rate for the case $\Delta E_{\nu\mu} = 0$. Following the transition rate of Eq. (2.38), the spin flip is definitely executed, i.e., $w_{\nu\mu} = 1$, whereas according to Eq. (2.39), the transition rate is $w_{\nu\mu} = 0.5$. Figure 2.3 visualizes the difference in the spin flip acceptance ratio $\Delta p_a = \Delta w_{\nu\mu}$ as function of $\Delta E_{\nu\mu}$ between the Metropolis and the Glauber spin flip algorithm for different temperatures T. As can clearly be seen, both algorithms lead to almost identical transition rates for $\Delta E_{\nu\mu} \leq 5$ and $\Delta E_{\nu\mu} \geq 2$ but become significantly different in the interval $5 < \Delta E_{\nu\mu} < 2$. The difference in the spin flip transition rates, $\Delta w_{\nu\mu} = w_{\nu\mu}^{metropolis} - w_{\nu\mu}^{glauber}$ between the Metropolis and the Glauber

algorithm as function of $\Delta E_{\nu\mu}$ is further plotted in Fig. 2.3. There, one clearly sees how Δp_a increases as $\Delta E_{\nu\mu}$ approaches zero coming from negative values. At $\Delta E_{\nu\mu}$ the difference of the acceptance ratio peaks at $\Delta p_a = 0.5$. From there, it quickly decreases and approaches zero for $\Delta E_{\nu\mu} > 2$.

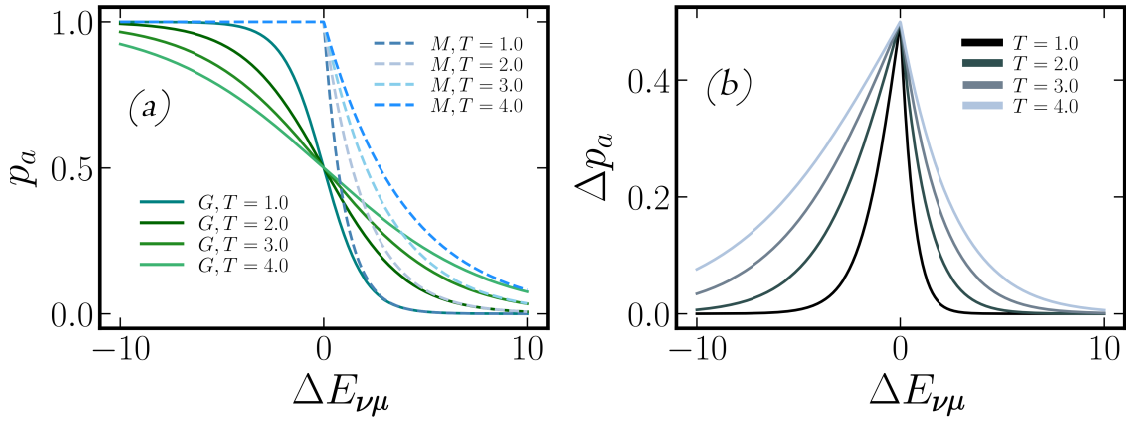

Fig. 2.3: (a) Plot of the spin slip acceptance probability p_a as function of the change of energy $\Delta E_{\nu\mu}$ for four different values of the heat bath temperature T according to the Metropolis and Glauber transition rates as defined in Eq. (2.39) and Eq. (2.38). (b) Shows the difference $\Delta p_a = |p_a^{Glauber} - p_a^{Metropolis}|$ in the spin flip acceptance probability following the Glauber and the Metropolis rule for the same temperatures as used in (a).

It is well established that the Metropolis algorithm is best suited for spin systems with small q, while the Glauber dynamics work better for large q. In this thesis, we solely work with the Glauber algorithm because we mostly work with systems (the q-state vector Potts model and the XY mode) which have $q \geq 4$. However, it is a topic for future research to investigate if the entropy production rate per spin, π, depends on the choice of the algorithm. To this end, it could be interesting to compare π and $\mathrm{d}\pi/\mathrm{d}T$ in the vicinity of the order-disorder phase transition. The main question here is whether the power-law behavior, i.e., the critical exponent ζ of the derivative of the entropy production rate, $\mathrm{d}\pi/\mathrm{d}T$, depends on the choice of the MCMC algorithm.

Cluster algorithm: Simulations of spin models by means of local (single spin-flip) update MCMC algorithms like the Metropolis or Glauber algorithm suffer from critical slowing down near the critical point T_c. Especially for large system sizes L, this issue makes it computationally very challenging to overcome the transient regime. Thus, it can be very time consuming to reach the steady state. In contrast, cluster algorithms do not suffer from critical slowing down. Therefore, they are convenient to model the dynamics of large spin systems in the vicinity of order-disorder phase transitions. In contrast to the (local) single-spin flip Metropolis and Glauber algorithm, cluster algorithms are distinguished from the former by flipping multiple spins, i.e., cluster of spins, in one iteration step. In the following we shortly sketch the Wolff (single cluster) [165]. Furthermore, there is also the Swendsen-Wang multi cluster algorithm [166] which we do not explain here. Similar to the Wolff algorithm, the Swendsen-Wang algorithm does counteract the divergence of auto-correlation times close to the critical point. Accordingly, this algorithm does also

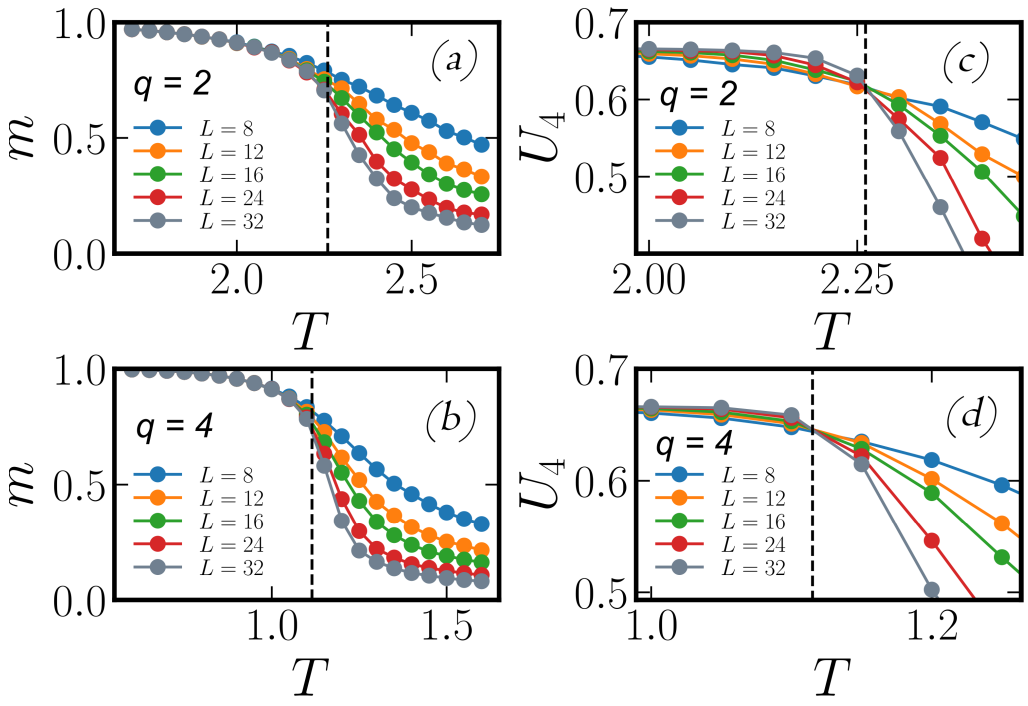

Fig. 2.4: (a) and (b) show the ensemble average absolute magnetization m for the Ising model ($q = 2$) and the 4-state vector Potts model as function of T from $L = 8$ to $L = 32$. (c) and (d) show the fourth-order Binder cumulant U_4 for $q = 2$ (Ising) and $q = 4$. The black lines indicate the corresponding critical temperature T_c.

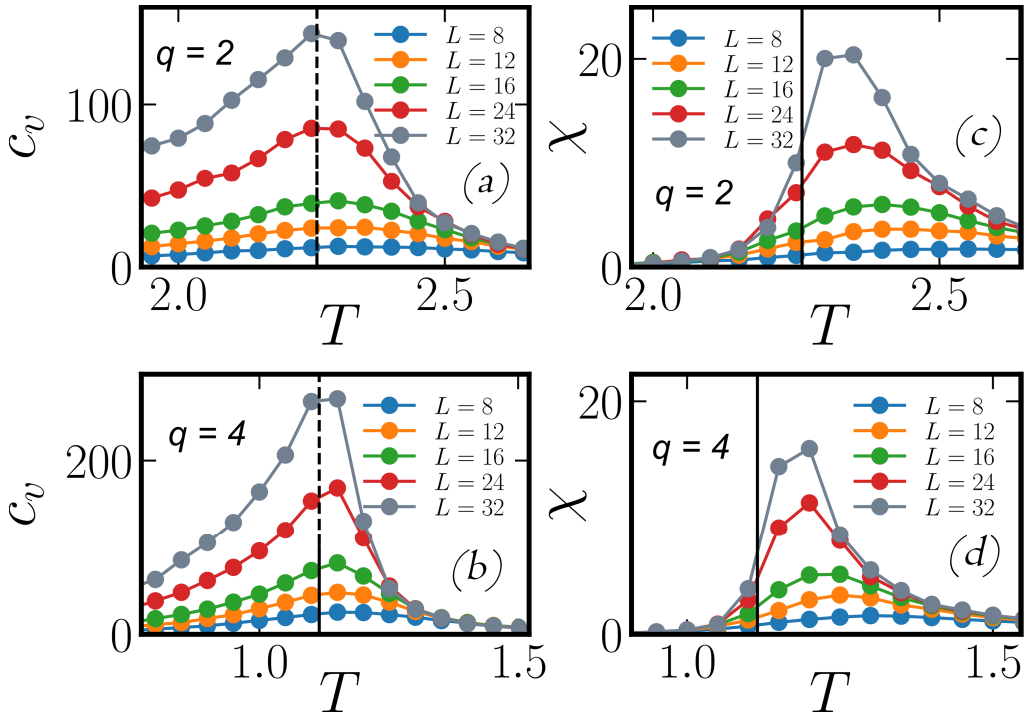

Fig. 2.5: (a) and (b) show the specific heat c_v for the Ising model ($q = 2$) and the 4-state vector Potts model as function of T from $L = 8$ to $L = 32$. (c) and (d) show the magnetic suszeptibility χ for $q = 2$ (Ising) and $q = 4$. The black lines indicate the corresponding critical temperature T_c.

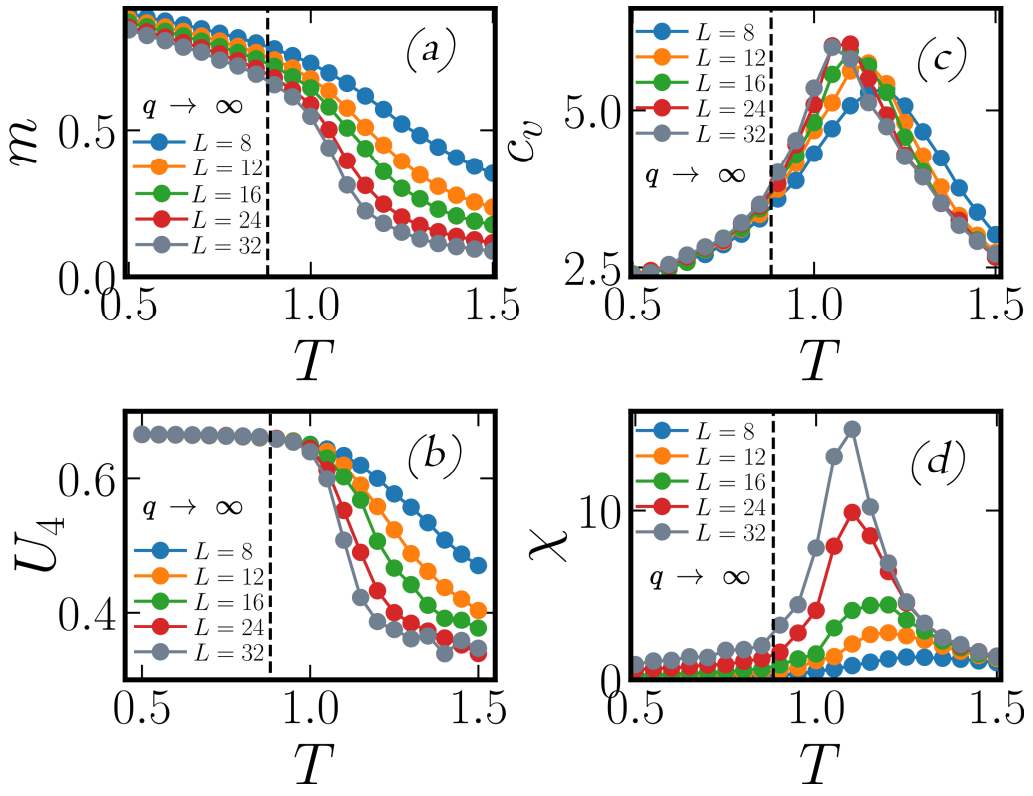

Fig. 2.6: (a) shows the ensemble average absolute magnetization m for the XY model ($q \to \infty$). (b) shows the fourth-order Binder cumulant U_4. In (c) the specific heat is plotted and (d) shows the magnetic susceptibility χ The black lines indicate the corresponding critical temperature T_c of the XY model.

not suffer from critical slowing down near T_c. According to the Wolff algorithm, the construction of a cluster works as follows. One starts by chosing a random spin s_i and iteratively adds neighboring spins $\mathbf{s}_j$ with probability $p = 1 - \exp(1 - 2/T)$ to the cluster if they are in the same spin configuration, i.e., if $s_i = s_j$. The state of the cluster is called a. After this, one calculates the energy inside, E_{in}, and outside, E_{out}, the cluster. Additionally, the number of same, n_s, and different, n_d, links across the cluster boundary are calculated. From this, one can calculate the probability $P(a \to b)$ that each spin inside the cluster flips $s_i \to -s_i$. When the cluster is flipped, it is found in state b. The probability for a cluster flip is given by

$$P(a \to b) = \min \left[\frac{\exp\left(n_d/T\right) \exp\left(-n_s/T\right) (1-p)^{n_d}}{(1-p)^{n_s} \exp\left(-n_d/T\right) \exp\left(n_s/T\right)} \right] \tag{2.40}$$

Regardless of whether the cluster flip attempt is conducted or not, the procedure is repeated by constructing a new cluster, starting again with a randomly chosen spin $\mathbf{s}_i$.

In C. 9 we calculate the entropy production rate per spin, π for the q-state Potts and the XY model using the Glauber algorithm. Concerning this thermodynamically important quantity, it is *a priori* not clear whether the choice of the spin-update algorithm has an effect on the entropy production rate π. Therefore it may be interesting for future investigations

to analyze and compare results for π obtained from simulations with different MCMC algorithms. Since the Glauber and Metropolis acceptance probabilities are different from each other as shown in Fig. 2.3, one might expect a different behavior of π when using the Metropolis instead od the Glauber algorithm. In this sense, it would be interesting to investigate whether the power-law behavior of π which we found for the q-state Potts model by using the Glauber algorithm (see C. 9) gets altered if one uses the Metropolis algorithm or a a non-local cluster update algorithm instead.

Calculating the expectation value and the variance of observables: Concerning simulations by means of MCMC algorithms, the expectation value $\langle \mathcal{O} \rangle$ of some quantity/observable $\mathcal{O}$ (e.g., the mean energy per spin, $\langle E \rangle$ or the ensemble average absolute magnetization $|\langle m \rangle|$ can be estimated as arithmetic mean according to

$$\langle \mathcal{O} \rangle = \sum_{\mu} \mathcal{O}_{\mu} p_{\mu} \approx \overline{\mathcal{O}} = \frac{1}{N} \sum_{k} \mathcal{O}_{k}. \tag{2.41}$$

Here, $\mathcal{O}_{\mu}$ is the value of the quantity $\mathcal{O}$ in microstate μ and p_{μ} is the normalized probability to find the system in state μ. This can be approximated by averaging over the microstates $\mathcal{O}_k$ which are sampled via the underlying MCMC algorithm. The first sum runs over all microstates $\mu \in \Omega$, whereas the second sum runs over all states k which are sampled during a simulation consisting of N sweeps/iterations. Specifically, $\mathcal{O}_k$ is the value of quantity $\mathcal{O}$ in one of the microstates in Ω which the system is occupying in the k-th iteration step of the Markov chain. The variance $\sigma^2_{\mathcal{O}}$ of the quantity $\mathcal{O}$ can be expressed in terms of the individual measurements $\mathcal{O}_k$ of $\mathcal{O}$ during the sampling procedure via the MCMC algorithm,

$$\sigma^2_{\overline{\mathcal{O}}} = \langle |\overline{\mathcal{O}} - \langle \overline{\mathcal{O}} \rangle|^2 \rangle = \langle \overline{\mathcal{O}}^2 \rangle - \langle \overline{\mathcal{O}} \rangle^2. \tag{2.42}$$

Using the explicit expression for $\overline{\mathcal{O}}$ according to Eq. (2.41), the variance of $\overline{\mathcal{O}}$ can be expressed as

$$\sigma^2_{\overline{\mathcal{O}}} = \langle \overline{\mathcal{O}}^2 \rangle - \langle \overline{\mathcal{O}} \rangle^2 = \frac{1}{N^2} \sum_{k} \left(\langle \mathcal{O}_k^2 \rangle - \langle \mathcal{O}_k \rangle^2 \right) + \frac{1}{N^2} \sum_{k \neq m} \left(\langle \mathcal{O}_k \mathcal{O}_m \rangle - \langle \mathcal{O}_k \rangle \langle \mathcal{O}_m \rangle \right) \tag{2.43}$$

Here, we have separated the variance in diagonal and off-diagonal terms. The off-diagonal term encodes the temporal correlations between measurements at different times (i.e., different iteration steps/sweeps) k and m.Thus, it vanishes for data that is completely uncorrelated. For correlated data, the second term in Eq. (2.43) does not vanish. if we make use of the symmetry $k \leftrightarrow m$, we can rewrite the sum in Eq. (2.43) from the original form $\sum_{k \neq m}^{L}$ and end up with a new form corresponding to $2 \sum_{k}^{N} \sum_{m=k+1}^{N}$. By taking this rewritten sum and making use of the time-translation invariance of $\sigma^2_{\overline{\mathcal{O}}}$ in equilibrium, we arrive at

$$\sigma^2_{\overline{\mathcal{O}}} = \frac{1}{N} \left[\sigma^2_{\mathcal{O}} + 2 \sum_{k=1}^{N} \left(\langle \mathcal{O}_1 \mathcal{O}_{1+k} \rangle - \langle \mathcal{O}_1 \rangle \langle \mathcal{O}_{1+k} \rangle \right) \left(1 - \frac{k}{N} \right) \right]. \tag{2.44}$$

This expression shows us how the variance $\sigma^2_{\overline{\mathcal{O}}}$ calculated along a stochastic path of length N is related to the exact value of the equilibrium variance $\sigma^2_{\mathcal{O}}$. By introducing a normalized auto-correlation function

$$A(k) = \frac{\langle \mathcal{O}_1 \mathcal{O}_{1+k} \rangle - \langle \mathcal{O}_1 \rangle \langle \mathcal{O}_{1+k} \rangle}{\sigma^2_{\mathcal{O}}} \lim_{k \to \infty} a \cdot \exp\left(-\frac{k}{\tau_{\mathcal{O}_{\text{exp}}}} \right) \tag{2.45}$$

and the integrated auto correlation time

$$\tau_{\mathcal{O}} = \frac{1}{2} + \sum_{k}^{N} A(k) \left(1 - \frac{k}{N} \right), \tag{2.46}$$

we can express the variance of $\mathcal{O}$ along a stochastic path of length N as

$$\sigma^2_{\overline{\mathcal{O}}} = \frac{2}{N} \sigma^2_{\mathcal{O}} \tau_{\mathcal{O}}. \tag{2.47}$$

This expression directly tells us that one has to make sure that $N \gg \tau_{\mathcal{O}}$, in order to obtain meaningful results for $\sigma^2_{\overline{\mathcal{O}}}$ in numerical simulations. In that case, the autocorrelation function $A(k)$ is already exponentially small before the correction term $(1 - k/N)$ in Eq. (2.46) becomes large enough to be relevant. Therefore, it is important to make sure that the system has spend enough time in the steady state before one starts to measure observables, especially in regions very close to critical points. Moreover, due to the existence of temporal correlations in measurements of $\mathcal{O}$ in MC simulations, the statistical error $\epsilon_{\overline{\mathcal{O}}} = \sqrt{\sigma^2_{\overline{\mathcal{O}}}} = \sqrt{\sigma^2_{\mathcal{O}}/N_{\text{eff}}}$ [with $N_{\text{eff}} = N/(2\tau_{\mathcal{O}})$] of $\overline{\mathcal{O}}$ is enhanced by a factor $\sqrt{2\tau_{\mathcal{O}}}$. Therefore, only every $\sim 2\tau_{\mathcal{O}}$ MC sweeps/iterations, measurements of observables $\mathcal{O}$ are nearly uncorrelated. This makes clear why the length N of a stochastic path along which $\overline{\mathcal{O}}$ is calculated has to be large in MC simulations in order to obtain a meaningful, i.e., uncorrelated, average and variance. Again, this is of particular importance if we sample states close to the critical point. Concerning the numerical calculation the variance, one has to take care not to underestimate it. From he standard estimator for the variance which is given by

$$\hat{\sigma}^2_{\mathcal{O}} = \overline{\mathcal{O}^2} - \overline{\mathcal{O}}^2 = 1/N \sum_{k=1}^{N} \left(\mathcal{O}_k - \overline{\mathcal{O}} \right)^2, \tag{2.48}$$

we find for the expectation value of the variance obtained from averaging over many stochastic paths$\langle \hat{\sigma}^2 \rangle = \langle \overline{\mathcal{O}^2} - \overline{\mathcal{O}}^2 \rangle = \sigma^2_{\mathcal{O}} + \sigma^2_{\overline{\mathcal{O}}}$. This can be rewritten by using Eq. (2.47)

$$\langle \hat{\sigma}^2_{\mathcal{O}} \rangle = \sigma^2_{\mathcal{O}} \left(1 - \frac{2\tau_{\mathcal{O}}}{N} \right) = \sigma^2_{\mathcal{O}} \left(1 - \frac{1}{N_{\text{eff}}} \right). \tag{2.49}$$

This shows that the ensemble average estimator $\langle \hat{\sigma}^2_{\mathcal{O}} \rangle$ underestimates $\sigma^2_{\mathcal{O}}$ by a factor $\sim \sigma^2_{\mathcal{O}}/N_{\text{eff}}$. For infinitely long samples the estimator becomes exact, i.e., $\langle \hat{\sigma}^2_{\mathcal{O}} \rangle = \sigma^2_{\mathcal{O}}$ for $N \to \infty$. When using local spin update MCMCs like the Metropolis or Glauber algorithm, $\tau_{\mathcal{O}}$ strongly depends on the system size L. Therefore, N has to be chosen large enough because otherwise, finite-size effects alter the calculated variance of physical observables. This is of great importance for calculations of the suszeptibility χ and the specific heat c_v.

The latter quantities are defined as the variance of the magnetization m and the energy E per spin. Making sure that results are not affected by finite size effects is of particular importance if we are interested in the scaling behavior of peak values of quantities which are calculated as the variance of some observable $\mathcal{O}$. In Fig. 4.1, Fig. 2.5 and Fig. 2.6, we plot $\chi = L^d/T\left(\langle m^2\rangle - \langle m\rangle^2\right)$ (with m being the magnetization $m = 1/L^d \sum_i s_i$) and $c_v = L^d/T^2\left(\langle E^2\rangle - \langle E\rangle^2\right)$ (with E being the energy per spin) for the 2- and 4-state vector Potts and the XY model. Also in C. 9 we calculate the power-law behavior of c_v in order to determine the universality class of a nonequilibrium Potts model. For all simulation results shown in this thesis we made sure that the data is not affected by measurement errors.

2.4 Nonequilibrium surface growth and simulation details

In this section, we discuss the most established simulation technique that is used to mimic nonequilibrium surface growth via vapor deposition techniques like molecular beam epitaxy. To this end, we explain the surface processes that occur during nonequilibrium growth. A detailed knowledge of these microscopic processes is of particular importance for numerical simulations of surface growth. By means of a reasonable coarse-graining procedure one separates the unimportant from the crucial microscopic processes which determine the morphological evolution of the growing surface. Following this, we will give a detailed explanation of the event-driven KMC algorithm which is the state-of-the-art method to model surface growth on substrates in the micrometer range.

2.4.1 Numerical simulations of nonequilibrium surface growth

Since we assume a discrete lattice in surface growth simulations, one could, in principle, simply solve the corresponding Master equation to obtain the occupation probabilities of all lattice configurations, i.e., microstates $\mu \in \Omega$ of the system. Due to the fact that the height of each lattice site is unlimited, the dimension of the phase space Ω is infinite. Therefore, it is, irrespective of the system size, impossible to numerically set up the transition rate matrix. To overcome this problem, one usually employs event-driven KMC simulations to model nonequilibrium surface growth. A detailed explanation of the algorithm will be given in the next section.

2.4.2 Coarse-graining in surface growth simulations

In order to simulate surface growth by mimicking the experimental vapor deposition techniques discussed earlier in this section, it is in fact sufficient to consider only a handful of the many microscopic processes that take place on the surface during growth. The

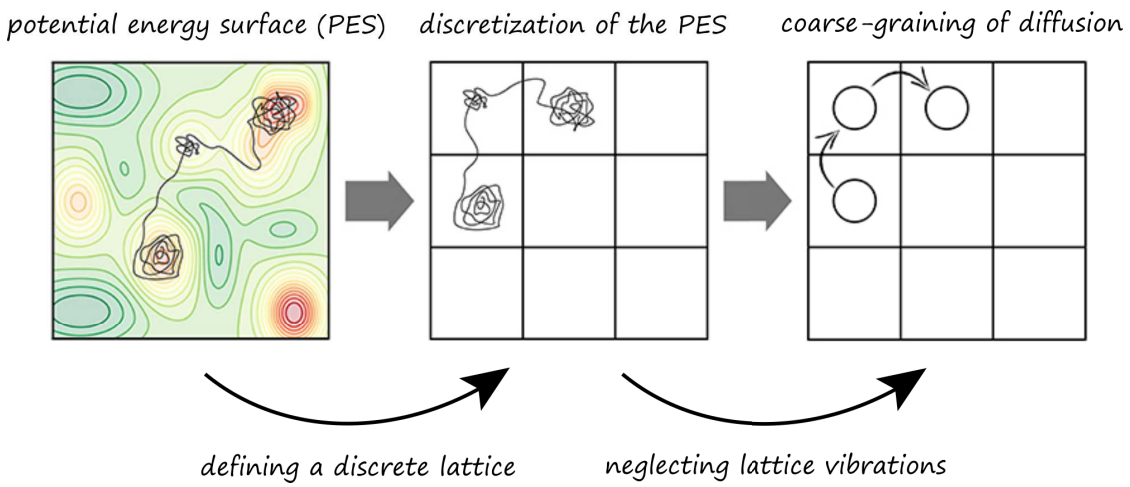

Fig. 2.7: Illustration of the coarse-graining procedure conventionally used to model particle diffusion on the potential energy landscape of a solid surface. First, one replaces the PES with a discrete lattice where each of the equidistant lattice sites represents a local energy minimum of the PES. By neglecting thermal fluctuations of the lattice, we end up with a setup where particles perform activated diffusion processes between neighboring sites of a discrete lattice. The original version of the figure is from [170].

challenge is to make out the ones which are crucial for the morphological evolution. While atoms in a crystal vibrate with frequencies f on the picosecond time scale, i.e., $f \sim 10^{-12}$ 1/s, the time that passes in between two consecutive hopping events of an adatom on a solid substrate which jumps from one energetic minima to a neighboring one can be several orders of magnitude longer. Therefore, it requires simulations up to seconds or minutes in order to reasonably model the growth dynamics of an ever increasing ensemble of particles which diffuse on a solid substrate after deposition and thereby form stable clusters. Since the hopping of adatoms on the solid substrate is obviously important for the morphological evolution of a growing surface, diffusion is definitely one of the key processes that have to be included in particle-based simulations of nonequilibrium surface growth. In contrast, considering the aforementioned atomic lattice vibrations would needlessly increase the computational effort without noticeably affecting the surface structure. Therefore, a full description of atomic vibrations of the solid surface can be neglected in surface growth simulations without hesitation. Usually, they are included as a temperature-dependent constant pre-factor of the Arrhenius-type hopping processes of adatoms as discussed below in this section. The conventional coarse-graining strategy one usually follows in order to simplify the dynamics of hundreds and thousands of individual adatoms which diffuse on a solid surface during growth is illustrated in Fig.2.7. In fact, for surface growth simulations on a strongly coarse-grained, it is sufficient to include the following three processes: I. deposition, i.e., adsorption of particles on the surface, II adatom diffusion and III. desorption, i.e., evaporation of adatoms from the surface back to the gas phase which is above the growing solid. How these processes are modeled in KMC simulations will be explained in the following.

The potential energy surface, fluctuations and the Markov property: After deposition, particles get adsorbed on the potential energy surface (PES), i.e., the potential energy landscape of the growing crystals surface. There, they perform Arrhenius-type activated hopping processes between neighboring local minima of the PES. More precisely, adatoms fluctuate around local minima due to thermal noise and eventually escape it in order to fluctuate in a neighboring minimum. One can assume that the more time an adatom spends in one local energetic minimum of the PES, the more it *forgets* about the path that brought it there. Therefore, it is reasonable to assume that each possible way to escape a minimum becomes completely independent of the history of previously occupied minima. In other words, all state transitions $\mu \to \nu$ of the whole system (due to hopping of individual particles from one minimum to a neighboring one) from state, i.e., lattice configuration, μ to state ν obey the Markov property which is defined in Eq. (2.2).

The lattice approximation of the PES: We assume perfect crystalline surfaces which is a well-established simplification of the PES in simulations of surface growth [9, 170, 171]. Hence, it is reasonable to map the individual minima of the PES onto a suitable periodic arrangement of potential wells. This is exemplary shown in Fig. 2.7 where the minima of the underlying PES are mapped onto a square lattice. Consequently, the diffusion processes of adatoms can be modeled as hopping between neighboring sites of such an perfectly periodic lattice (i.e., particles hop between the coarse-grained translationally invariant minima of the potential wells). In the simplest setup, the rate constants for hopping of an adatom from lattice site $\mathbf{a} = (i, j)$ to a neighboring site **b** depend on the number n of lateral neighbors of the particle on site **a** only. This is due to the fact that we ignore any memory effects as discussed in the previous paragraph. Due to the translational invariance of the coarse-grained PES, adatoms which are located on different lattice sites escape their energetic minima with the same rate constant if they have the to overcome the same activation energy E_A (see Fig. 2.8). The value of E_A only depends on a few details like the number of neighbors a particle has on site **a**. This means that, depending on the lattice geometry, we only have to consider a limited number of distinct rate constants for adatom hopping in a surface growth model. In the following we derive the activation energy-dependent Arrhenius-type expressions of the rate constants for adatom hopping between neighboring potential wells of the PES.

Hopping rate constants from transition state theory: Algorithms to model nonequilibrium surface growth require rate constants for all considered elementary processes as input parameters. Commonly, the rate constants for adatom hopping are obtained by means of Transition State Theory (TST) [172, 173]. In this regard, the transition rates for adatom hopping between neighboring potential wells are expressed through the ratio $T/P_{\mathbf{a}}$ of the transition current T and the probability $P_{\mathbf{a}}$ of finding an adsorbed particle in minimum, i.e., on lattice site, **a** of the PES (note that the potential wells of the PES are periodically arranged on a discrete lattice and **a** corresponds to a discrete lattice position). In the following we shortly sketch how one obtains the transition rate constants

for adatom hopping on a perfectly periodic PES from a potential well located at **a** to a neighboring potential well at **b** across a saddle point s from TST (see Fig. 2.8 for an exemplary illustration of this situation on a one-dimensional substrate). To this end, one first has to simplify the situation. For example, one assumes that the transition current T of paths will only flow from **a** to **b** and not backwards. Furthermore it is assumed that the transition is a classical event, i.e., tunneling between the two potential wells **a** and **b** is forbidden. After applying these simplifications, TST provides simple Arrhenius-like expressions for the hopping rate constants $D_{\mathbf{ab}}$ for hopping between neighboring potential wells **a** and **b** across a saddle point s. The latter equation is also known as Eyring-Polanyi equation [174, 175] which is given by

$$D_{\mathbf{ab}}^{\mathrm{TST}} = \frac{Z_{\mathrm{TS}}^{\mathrm{vib}}}{Z_{\mathbf{a}}^{\mathrm{vib}}} \frac{k_{\mathrm{b}}T}{h} \exp\left(-\frac{E_A}{k_{\mathrm{b}}T}\right) = k_0 \frac{k_{\mathrm{b}}T}{h} \exp\left(-\frac{E_A}{k_{\mathrm{b}}T}\right). \tag{2.50}$$

In this equation, T is the temperature, h represents the Planck constant and $Z_{\mathrm{TS}}^{\mathrm{vib}}$ represents the partition function at the transition state, i.e., at the saddle point s, and $Z_{\mathbf{a}}^{\mathrm{vib}}$ represents the partition function at the initial state **a**. The activation barrier for the hopping process from potential well **a** to **b** is given by $E_A = E_s - E_{\mathbf{a}}$, where E_s is the energy at the saddle point s as illustrated in Fig. 2.8. This shows that the energy barrier for hopping from **a** to **b** does not depend on the potential energy $E_{\mathbf{b}}$ of the final state, i.e., the potential well at lattice position **b**. The value of E_A is directly available from information of the underlying PES. In fact, it can be obtained from first-principles, semilocal DFT calculations [176–180]). For simplicity we ignore entropic corrections to the energy barrier E_A and furthermore, do not consider zero-point vibrational energy corrections which means that we set $k_0 = 1$. Consequently, we have the prefactor $\nu_0 = \frac{k_{\mathrm{b}}T}{h} \sim 10^{-12}$ which is of the order of lattice vibrations in the temperature regime relevant for surface growth, which is $100 \lesssim T \lesssim 1000$ K. After these simplifications the situation we are actually considering for adatom diffusion in surface growth simulations corresponds to the one which is shown on the right hand side of Fig. 2.8. Particle hopping is now simply an Arrhenius-type processes with activation energy-dependent rate $D_{\mathbf{ab}} \sim \exp(-E_A)$.

Composition of the activation energy barrier for surface diffusion: On the typical coarse-graining level used for large-scale growth simulations, the activation energy E_A that has to be overcome in order to perform a hopping process of a particle from lattice site **a** to **b** consists of up to three individual energy contributions

$$E_A = E_D + nE_B + s_{\mathbf{ab}}E_S. \tag{2.51}$$

More precisely, the value of E_A of a particle on **a** depends on the diffusion barrier E_D, which we assume to take the same value on all lattice sites of the crystalline surface, the number n of lateral bonds of strength E_B and an additional step-edge barrier E_S. The value of E_D is of the order of the adsorption energy, i.e., the Van Der Waals energy between a physisorbed adatom and the surface onto which it is deposited. Therefore, the value of

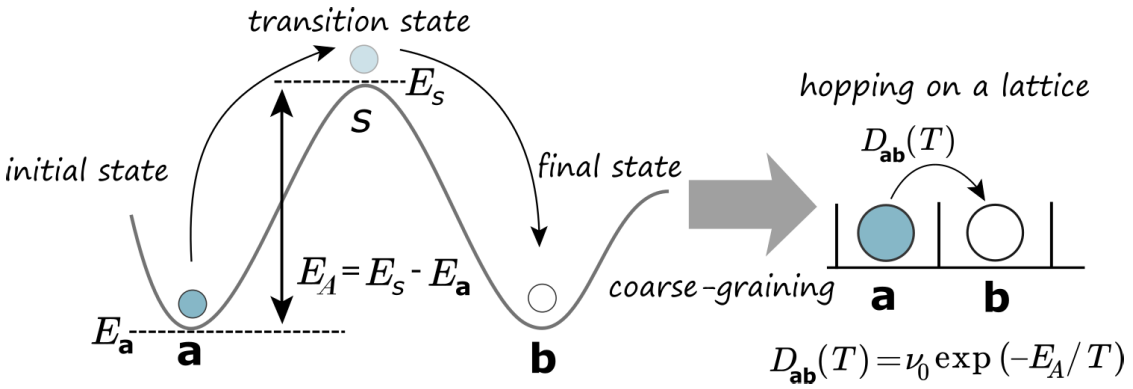

Fig. 2.8: Illustration of a state transition of a particle which is initially located at the minimum of a potential well **a** of the PES. The latter is coarse-grained as periodic array of potential wells whose depth depends on the activation energy E_A. In order to hop to the minimum of a neighboring potential well **b**, the particle at **a** has to cross the transition state s. To this end, it has to overcome the energy barrier $E_A = E_s - E_{\mathbf{a}}$. in KMC simulations this situation is further coarse-grained. Instead of modeling potential wells, one simply uses a discrete lattice and allows the particle to hop from site lattice site **a** to **b** with an activation energy-dependent Arrhenius type hopping rate $D_{\mathbf{ab}}(T)$.

E_D depends on the material details of the substrate and the deposited particles. If during the hopping process $\mathbf{a} \rightarrow \mathbf{b}$ an adatom hops across a step-edge, i.e., if it performs an out-of-plane diffusion process to another layer, it has to overcome a region with a lower number of nearest neighbors where it is weaker bound to it's neighbors. This effect is modeled by an additional energy barrier, E_S, which is referred to as Ehrlich-Schwoebel barrier [181, 182]. If adatom hopping is in-plane, the Ehrlich-Schwoebel barrier is irrelevant, i.e., $s_{\mathbf{ab}} = 0$, whereas it has to be considered for out-of-plane hopping processes, $s_{\mathbf{ab}} = 1$. Due to the Ehrlich-Schwoebel barrier, adatoms located at the boundary of clusters have a higher chance to get reflected than actually hopping down the step-edge. Therefore, they spend more time on top of clusters than they would without the barrier. Consequently, the step-edge barrier promotes the formation of clusters on top of existing clusters, and thus, the Ehrlich-Schwoebel barrier can be responsible for a high surface roughness. Adatom diffusion is modeled as Arrhenius-type processes with hopping rates given by

$$D = \nu_0 \exp\left(-E_A/k_{\mathrm{b}}T\right). \tag{2.52}$$

Here, the attempt-frequence $\nu = k_{\mathrm{b}}T/h$ which is of the order of lattice vibrations is chosen in accordance with simulation studies of surface growth phenomena.

Composition of the activation energy barrier for adatom desorption: Deposited particles can not only diffuse on the surface by performing activated hopping processes. Alternatively, they may also desorb from it again and thereby become part of the gas phase again. The activation energy for desorption from the surface $E_A^{DES} = E_{DES} + nE_B$ is usually higher as compared to the value of E_A for surface diffusion. This is because the physiosorbed particles have to fully overcome the attractive Van der Waals force between adatom and the substrate. This can be modeled by simply assuming the desorption energy

E_{DES} to be larger than the energy barrier for free diffusion, i.e., $E_{DES} > E_D$. In the KMC simulations in C. 5, C. 6 and C. 7 we assume to value of E_{DES} to be so large that desorption can be fully neglected on the time scale of the simulations. Consequently, deposited particles do not desorb from the surface during the simulation. We only consider adatom desorption processes in the context of a thermodynamic analysis of surface growth in C. 8. The Arrhenius-type rates for desorption of adatoms from the surface are given by

$$q = \nu_0 \exp\left(-E_A^{DES}/k_{\mathrm{b}}T\right). \tag{2.53}$$

Here, the prefactor ν_0 is the same as for surface diffusion processes discussed earlier in this paragraph.

The rate for adatom deposition on the surface: In contrast to adatom diffusion and desorption, deposition of particles on the surface is not modeled as an activated process. In order to include particle deposition in our simulations, we simply use a fixed deposition rate F. The value of the latter defines the number of particles deposited per second on the surface per lattice site. This means that the rate F for particle deposition is equal on all lattice sites of the simulation box. The rate F is defined such that it is effectively independent of the depth of the potential wells of the lattice, i.e., it is independent of the underlying PES. In experiments, not all deposited particles do successfully adsorb on the surface. A certain percentage of adsorption attempts fail. We circumvent this by assuming an effective deposition rate F that accounts for failed adsorption events simply by assuming a value for F that is lower compared to deposition rates in experiments where adsorption might fail. Therefore, when particle deposition is chosen, the particle will definitely be deposited on the surface.

2.4.3 The event-driven kinetic Monte-Carlo (KMC) method

From Monte-Carlo to kinetic Monte-Carlo: Within the Monte-Carlo Markov Chain methods we used to model the dynamics of spin systems (discussed in Sec. 2.3 and applied in C. 9), one compares the energy $E_\mu$of the system before with the energy E_ν after the transition from configuration, i.e., (micro)state, μ to ν. Conventional Monte-Carlo algorithms are distinguished from each other by the dependency of the acceptance probability $p_{\mu\nu}$ on the energy difference $\Delta E_{\nu\mu} = E_\mu - E_\nu$ between the initial and final configuration. More precisely, state transitions $\mu \to \nu$ are accepted with probability $p_{\nu\mu} \in [0, 1]$ which is determined by the Boltzmann distribution for the energy difference $\Delta E_{\mu\nu}$ [see Eq. (2.38) for the Metropolis and Eq. (2.39) for the Glauber transition probability]. Accordingly, Monte-Carlo algorithms sample configurations $\mu, \nu \in \Omega$ from the probability state space Ω based on the Boltzmann weight of the states in Ω. To be more precise, the Metropolis and Glauber algorithm perform an importance-weighted sampling of Ω. In this regard, the importance of a state μ is measured via it's relative occupation probability $p_\mu = (1/Z)\exp\left(-E_\mu/T\right)$. The Metropolis and Glauber algorithms contain purely thermodynamic, but no dynamic

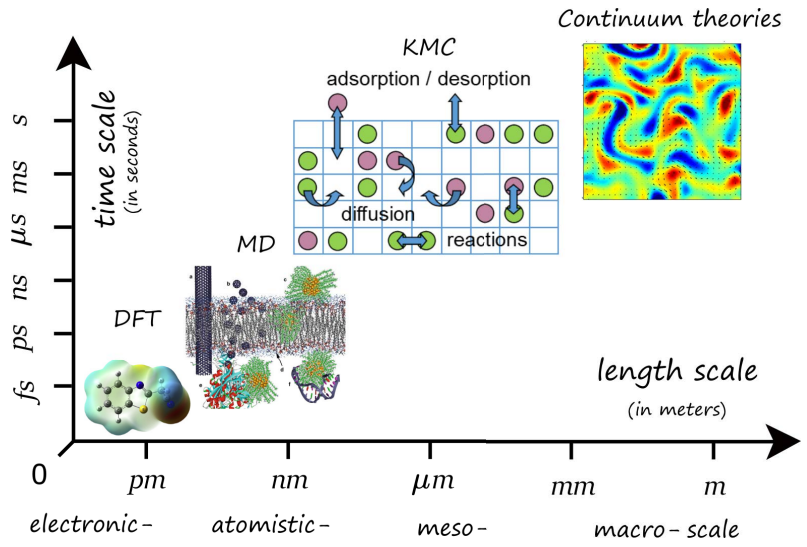

Fig. 2.9: Embedding of different simulation methods and theories according to the time- and length scales of physical processes where they can be applied. To model electronic processes, one usually performs Density functional theory (DFT) calculations, whereas Molecular dynamics (MD) simulations are used to model atomistic processes. The kinetic Monte-Carlo (KMC) method is appropriate to model mesoscale processes like the deposition and diffusion of individual nano- to micrometer-sized particles on surfaces. To model processes on even large length scales, one often neglects microscopic details and follows a continuum approach.Pictures of the simulation methods are taken from [170], [190] and [191]

information of the system. This is due to the fact that their transition probabilities $p_{\nu\mu}$ are determined by $\Delta E_{\nu\mu}$ only, such that kinetic effects are completely neglected. Different from the Metropolis and Glauber algorithm, the dynamical Monte-Carlo method, nowadays simply referred to as kinetic Monte Carlo (KMC) [183–187] method, actually simulates the time-evolution of a pre-defined set of processes, including activated processes which require to overcome an energy barrier E_A in order to be executed. This is of particular importance for systems which include various different processes at multiple time and length scales. Every numerical method is best suited for a certain length and time-scale range. The strength of the KMC method is the simulation of processes on the mesoscale, i.e., events occurring on the length- and time scale of micrometers and microseconds. The embedding of the KMC method in comparison to other approaches is illustrated in Fig. 2.9 The KMC method has proven to be of enormous practical use in the context of surface growth simulations. There exist numerous examples where it has been shown that KMC simulations can correctly model the growth of materials [188, 189].

The event-driven kinetic Monte-Carlo algorithm for surface growth: Figure 2.10 shows an exemplary surface configuration of a system where the process rates of some particles are highlighted. Since we use a lattice approximation to model the underlying PES, we can simply compute the rate constants for any allowed state transition $\mu \to \nu$ via adsorption, desorption or diffusion and save them in a so-called rate catalog (see Fig. 2.10). In each iteration step of the KMC simulation, the current lattice configuration is examined

and all possible processes together with their rate constants are extracted from the rate catalog and a single process is chosen and executed. Specifically, a random lattice site where the chosen process can be executed is picked and the event (adsorption, diffusion or desorption) is performed. Then, the rate catalog is updated and the procedure is repeated many iterations until the simulation time reaches the pre-defined maximum simulation time. In the following, we discuss in detail how the KMC algorithm works. During the KMC simulation, particles can be adsorbed on randomly chosen lattice sites with an (effective) adsorption (or deposition) rate F which is expressed in deposited monolayer (ML) per second (ML/s). If L is the lateral size of the system, then one monolayer corresponds to L^2 particles. Accordingly, a deposition rate of $F = 1$ ML/s corresponds to a simulation setup where, on average, L^2 particles are deposited on the surface per second. The value of F is assumed to be constant throughout the entire simulation. Additionally, we assume the deposition rate to be equal on all lattice sites. The adsorption process of a particle is followed by thermally activated diffusion (or hopping) processes to nearest-neighbor lattice sites. Following the Clarke-Vvedensky bond-counting Ansatz [192], the thermally activated Arrhenius-like hopping rates from site **a** to **b** are given by

$$D(T) = \nu_0 \exp(-E_A/kT), \tag{2.54}$$

with activation energy $E_A = E_D + nE_B + s_{\mathbf{ab}}E_S$. If desorption of particles is allowed in the simulation, we also assume Arrhenius-like rates with activation energy E_A^{DES} (see Sec. 2.4.2 for details). A typical KMC simulation consists of a large number of iterations p. In each iteration step, a particle either performs a hopping process to a neighboring lattice site, a new particle gets adsorbed or one of the particles desorbs from the surface. The simulation starts at $t_0 = 0$. After p iteration steps, the time is updated stochastically according to

$$t_{p+1} = t_p + \tau. \tag{2.55}$$

Here, t_p is the simulation time after p iteration steps and τ corresponds to the time increment that is added to t_p in the $(p+1)$-th iteration step of the simulation. The latter is defined as

$$\tau = -\frac{\ln(X)}{r_{\text{all}}}. \tag{2.56}$$

In this equation, $X \in (0, 1)$ is a random number chosen uniformly from the given interval, and

$$r_{\text{all}} = \sum_{\mathbf{a}}^{L^2} \left[\left(\sum_{\mathbf{b}}^{n_{\max}} D_{\mathbf{ab}} \right) + D_{\mathbf{a}}^d + F \right] \tag{2.57}$$

is the sum of the rates corresponding to all possible state transitions from the current configuration of the system, μ to any configuration ν that can be reached via adsorption, diffusion or desorption of a single particle. Specifically, r_{all} includes the deposition rate F per lattice site (each layer has L^2 sites) and all diffusion rates $D_{\mathbf{ab}}$ and desorption rates $D_{\mathbf{a}}^d$ of particles in the topmost layer of the lattice. The integer $n_{\max}$ corresponds to the maximum number of lateral bonds of a particle. This number depends on the geometry of

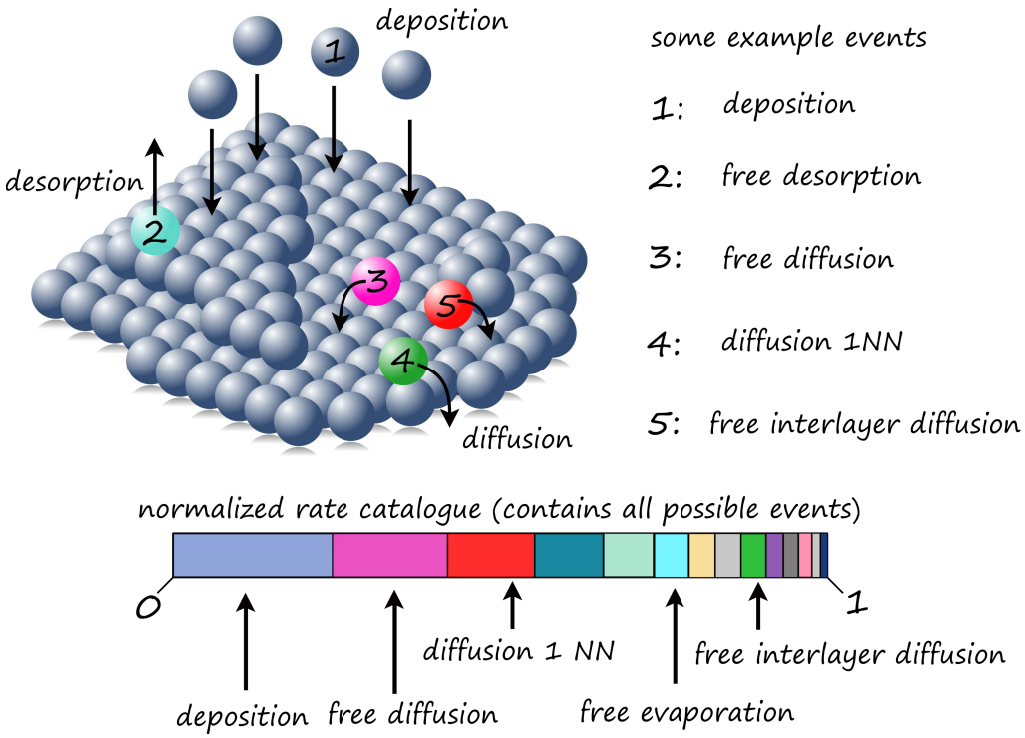

Fig. 2.10: Illustration of a growing two-dimensional surface simulated via the event-driven KMC algorithm. Some events that can occur on the surface are highlighted by different colors. Particles are deposited with constant rate F on the substrate. After deposition, they can diffuse by hopping between neighboring lattice sites **a** and **b** with rates $D(T)_{\mathbf{ab}}$ that depend on the local environment of the particle on site **a**. Instead, particles can also desorb from the surface. The sum of all possible events that can be selected at the current configuration of the system are saved in a normalized rate catalog. The event that takes the largest share has the highest probability to be selected in the next iteration step.

the lattice. For example, a square lattice is characterized by $n_{\max} = 4$, whereas $n_{\max} = 6$ on a hexagonal lattice.

3 Stochastic thermodynamics for discrete Markov chains

After introducing the basic properties of Markov chains, we will in this chapter turn to the thermodynamic properties of discrete Markovian systems with finite probability state space Ω. Specifically, we will utilize a framework from the new, emerging field of *stochastic thermodynamics* [50–52, 193–197], which aims at a generalization of thermodynamic laws to the microscopic scale and to nonequilibrium processes. Before we do this, it is helpful to first recall the fundamental laws of classical, macroscopic thermodynamics [198]. These laws express universally valid empirical facts for a huge class of macroscopic systems, i.e., on length scales where the randomness due to quantum and thermal fluctuations is negligible, like on the length scale of a industrial heat engine. At this scale, the thermodynamic limit applies, i.e., $\Omega \to \infty$. Furthermore, the fundamental laws of classical thermodynamics allow to define various quantities that are relevant and practical for a meaningful interpretation of physical systems. Besides the phenomenological laws of thermodynamics, we will briefly recall the interpretations of the relevant quantities from the viewpoint of statistical mechanics.

3.1 Laws of classical macroscopic thermodynamics

The zeroth law of thermodynamics: *If two systems, A and B, are both in thermal contact with each other, and in a state of thermal equilibrium with a third system C, then there is no net heat flow $\dot{Q}$ between A and C, nor between B and C (i.e., $\dot{Q} = 0$). Moreover, also system A and B are in thermal equilibrium with each other, and consequently, there is also no net heat flow $\dot{Q}$ between system A and system B.*

This law of thermodynamics provides an intuitive foundation for temperature as an empirical parameter in thermodynamic physical systems and establishes thermal equilibrium as an equivalence relationship [199, 200]. Specifically, the zeroth law provides a relation between the temperatures of multiple systems, each of which in a state fo thermal equilibrium with their respective surrounding. More precisely, if two systems which are in contact with thermometers that read the same temperature T are brought in thermal contact, then there is no heat flow between these two systems. As a consequence, temperature is identified as the indicator of thermal equilibrium.

If system A is at temperature T_A, while B is at temperature T_B, and $T_A \neq T_B$ (and A and B are brought in thermal contact), then the joint system is not in a state of thermal equilibrium. There will be a net heat flow between system A and B until a state of thermal equilibrium is reached, i.e., until both systems have the same temperature. Specifically, the net heat flow is such that it flows from the hotter to the colder system until $T_A = T_B$. Note that this only holds if both systems are not externally driven. External driving is able to maintain the temperature difference between A and B and thus, can be responsible for the situation that the joint system does never reach a state of thermal equilibrium (which is only reached if $T_A = T_B$), but will instead always be out of equilibrium and exhibit a net heat flow.

From the viewpoint of statistical mechanics, the temperature of a system is connected to the mean velocity of the involved particles. This connection is, for example, formally seen in the equipartition theorem

$$\frac{mv^2}{2} = \frac{3}{2} k_B T \tag{3.1}$$

for an ideal gas in a three-dimensional box which relates the temperature of the system to the average kinetic energy per particle in the box. For a system in thermal equilibrium, the energy is shared equally among all of its different forms. for example, considering a molecule, then the average kinetic energy per degree of freedom in translational motion should be equal to that in rotational motion.

The first law of thermodynamics: *Energy can not be created or destroyed, but only converted in different forms of energy.*

This fundamental law describes the general validity of the conservation of energy in physical systems and processes. [200, 201] More rigorously, the first law of thermodynamics outlines the general relation between a systems internal energy, U, and work W and heat Q. The law states that there exist only two different forms by which it is possible to transfer energy from or to a physical system in order to change the internal energy U. Mathematically, this can be formulated as follows

$$\mathrm{d}U = Q - W. \tag{3.2}$$

Accordingly, the change ΔU of a sytems internal energy U is equal to the energy transferred from or to the system in form of heat Q dissipated into the heat bath minus the energy that is transferred to or from the system in the form of (chemical or mechanical) work which is supplied by an external system. The precise form of Q and W depends on details of the system. For example, Q could be the heat dissipated due to friction and W may be the work which is performed by changing the position of a piston which regulates the volume that is available for a gas. An alternative formulation the first law of thermodynamics is the statement that perpetual motion machines of the first kind are impossible. In statistical mechanics one considers for any system the statistical distribution across the

ensemble Ω of $\mathcal{N}$ (micro)states. Each state $\mu \in \Omega$ is associated with an energy E_μ and an occupation probability p_μ. The internal energy at a given time corresponds to the the sum of all microstate energies weighted by the respective probability of occurrence, i.e., $U = \sum_\mu E_\mu p_\mu = \langle E_\mu \rangle$.

The second law of thermodynamics: *The total entropy of an isolated system never decreases over time,* $\Delta S \geq 0$.

In the framework of phenomenological, macroscopic thermodynamics, entropy is an extensive (i.e., system size proportional) state function that can be assigned to any system and which can increase or stay constant over time, but has other than that no direct physical interpretation. Nevertheless, it is of fundamental importance as it signals whether a system is in thermal equilibrium, where $\Delta S = 0$, or not ($\Delta S > 0$). Moreover, it is important to calculate the thermodynamic properties, for example, of a cyclic operating heat engine [200, 202].

Let us, as a little example, consider a cyclic operating heat engine. If one supplies amount of heat Q_H coming from a heat bath (reservoir) which is kept at temperature T_H to the heat engine, Q_H can not be fully converted into work W, even if all processes of the cycle are reversible. In that case, an idealized cyclic operating reversible heat engine, i.e., a Carnot heat engine, reaches the exact same initial state with the same internal energy U again after performing one thermodynamic cycle. Specifically, the system is supplied with an amount of heat Q_H from a hot reservoir (heat bath) at T_H which is used to perform work W. According to Carnot's theorem, there exist no heat engine operating between two heat reservoirs (at T_H and T_C with $T_H > T_C$) which is more efficient than a Carnot engine operating between the same reservoirs. The efficiency of such a Carnot engine, which is given by $\eta_c = W/Q_H = 1 - T_C/T_H$, is the theoretical maximum efficiency for heat engines. As a consequence, $Q_C = Q_H - W$ is the minimum amount of heat that can not be used to perform useful work, and therefore, $W = Q_H - Q_C$ is the maximum amount of work that can be performed. In such an idealized system, the amount of dissipated heat Q_d vanishes. The fact that any real processes produce friction and/or sound means that they are not reversible, and consequently, perfect heat engines (e.g., the Carnot heat engine) with $Q_d = 0$ do not exist in the real world. In other words, for any real heat engine, $W = Q_H - Q_C - Q_d$ is the work that can be performed. Therefore, the efficiency of a heat engine which exhibits irreversible processes is always smaller than the Carnot efficiency, $\eta < \eta_c$. One feature of *reversible* cyclic processes is that a state function S, which is called entropy, remains constant after each performed cycle, i.e. $\Delta S = 0$, while for any irreversible processes $\Delta S > 0$. More precisely, entropy represents the inevitable partial loss of an engine's ability to convert heat energy into work. We will discuss entropy and especially entropy production in more detail in the paragraph.

Statistical mechanics directly relates the entropy to the number of accessible microstates μ of a system with probability state space Ω. Specifically, the entropy by Shannon reads

$$S = -\sum_{\mu\in\Omega} p_\mu \ln\left(p_\mu\right). \tag{3.3}$$

For a reversible process, this definition of the entropy turns out to be equivalent to the representation of the change of entropy due to heat transfer in fully reversible classical thermodynamics, $\mathrm{d}S = \delta Q/T$, where Q is the (reversible) transferred heat. This can be proven based on the probability density of (micro)states of the generalized Boltzmann distribution and the identification of the thermodynamic internal energy U as the ensemble average as introduced above. However, this is not the case for irreversible processes which will be analyzed on a microscopic level in the following.

The third law of thermodynamics: *The entropy S of a physical system approaches a constant value as the system's temperature T tends to absolute zero, $T \to 0$.*

As the temperature of a heat bath approaches absolute zero, $T \to 0$, the entropy of a system that is in contact with this heat bath approaches a constant value [200, 203]. From the viewpoint of statistical mechanics, this law directly follows from the following argument. Typically there exist one unique state $\alpha \in \Omega$, i.e., the ground state, with minimum energy E_α (or there exists a group of degenerate ground states with identical energy). At $T \to 0$, the system will solely be found in this state, $p_\alpha = 1$. Consequently follows from equation Eq. (3.3) that the entropy of the system vanishes in this limit.

3.2 Stochastic thermodynamics

So far, we have shortly discussed the fundamental laws of classical thermodynamics which are based on empirical facts of thermodynamic properties of macroscopic systems. While these laws universally apply to various systems and, according to statistical mechanics, even have connections to the microscopic dynamics, they leave two major problems open, which will both be relevant for the systems considered in this thesis. First, these laws do not imply any concrete predictions and statements about systems that are far from thermal equilibrium. For example, the aforementioned heat engine is idealized to be quasistatically driven, i.e., in thermal equilibrium at each instance in time. Such an idealization completely fails when we aim to understand, e.g., growth processes or nonequilibrium spin systems (see C. 9) from a thermodynamic viewpoint. In fact, most systems in nature are not in thermal equilibrium [51, 52, 204].

Moreover, the fundamental laws apply only to systems on the macroscopic scale, where the thermodynamic limit $\Omega \to \infty$ is appropriate, and thus, thermal (and quantum) fluctuations are averaged out. We will directly consider systems on the fluctuating scale in this thesis.

For example, we investigate entropy fluctuations during surface growth and consider these fluctuations in a nonequilibrium Potts and XY model (see C. 9). Recent research aims for a theoretical description of thermodynamic properties of systems on the fluctuating scale and without explicitly relying on equilibrium assumptions. Here, a new theory gains relevance, that is, stochastic thermodynamics [50, 52, 193, 194]. In the following, we will outline the main ideas and introduce various quantities which we will later apply to our systems

We will in the following consider a closed Markovian system, i.e., there is no particle exchange with the environment, in contact with a heat bath at a fixed temperature T. The system can exchange energy with this heat bath, which is assumed to be big enough in order to always be in equilibrium. However, several definitions can be gernealized to situations where the system is in contact with multiple heat baths as it is the case for the nonequilibrium Potts and XY model which are discussed in C. 9.

3.2.1 Defintion of heat, work and internal energy on the microscale

During a transition $\mu \to \nu$ between two microstates μ, ν, the amount of heat, Q, transferred between a system and the connected heat bath, is directly related to the transition rates by

$$Q := T \ln\left(\frac{w_{\nu\mu}}{w_{\mu\nu}}\right). \tag{3.4}$$

Thus, the amount of heat exchanged with the heat bath during a transition $\mu \to \nu$ depends on the question how high the rate of this transition was, as opposed to the respective backward transition. Note that this definition is independent of the question whether the system is in equilibrium, or not.

Next to the exchanged heat, we have to correctly identify work W ((which can be controlled at the macroscopic level) on the microscale. In particular, work on the microscale corresponds to moving an occupied energy level E_μ of the system. For example, this can be realized by applying an external field to a spin system or changing the volume of a box that contains gas particles. Therefore the contribution to changing the energy of a system coming from work can be written as

$$W = \sum_\mu \dot{E}_\mu p_\mu. \tag{3.5}$$

Here, $\dot{E}_\mu$ corresponds to the change of energy of microstate μ. Next to work, there is also chemical work W_c which corresponds to changes in $\dot{p}_\mu$ due to particle exchange with the

environment. The heat flux $\dot{Q}$ due to state transitions $\mu \to \nu$ (which also changes p_μ) together the contribution from W_c can be written as [196, 197]

$$\dot{Q} + W_c = \sum_\mu E_\mu \dot{p}_\mu. \tag{3.6}$$

In this thesis we do not consider particle exchange with the environment, i.e., $W_c = 0$ (we only work with the canonical ensemble). As a consequence, $\dot{Q} = \sum_\mu E_\mu \dot{p}_\mu$. We further assume that no work is applied to the systems considered in this thesis. Specifically, we consider the nonequilibrium Potts and XY model without external field. However, we want to point out that it would be interesting to study thermodynamic properties of these models in presence of systematically varied external fields. For example, the external field can be interpreted as a signal and the system as a sensor that follows this signal [205]. This setup would allow for an informational theoretic interpretation of the model.

As opposed to the definition of the internal energy from statistical mechanics given above (i.e,. $U = \sum_\mu E_\mu p_\mu = \langle E_\mu \rangle$), we now define the internal energy at a given time as the energy of the currently occupied microstate as we are explicitly interested in energy fluctuations. Thus,

$$U = E_\mu \tag{3.7}$$

Clearly, taking the ensemble average, we recover the previous definition from statistical mechanics. Since we assume that no work is applied to the system, the first law of thermodynamics generalized to the level of each individual (random) transition $\mu \to \nu$, simply states

$$E_\nu - E_\mu = Q. \tag{3.8}$$

The heat exchanged between system and bath because of a single transition $\mu \to \nu$ equals the change in internal energy [52]. Specifically, the log-ratio of the forward and backward rate is equal to minus the energy difference $\Delta E_{\nu\mu}$ divided by the temperature T of the heat bath. The energy difference $\Delta E_{\nu\mu}$ between which the system jumps corresponds to minus the heat flowing into or from the heat bath, $\Delta E_{\nu\mu} = -Q$. If $\Delta E_{\nu\mu} > 0$, heat extracted from the bath, while if $\Delta E_{\nu\mu} < 0$, it flows from the system to the bath.

To connect these abstract definitions from stochastic thermodynamics with something well known from statistical mechanics, let us consider as a concrete example the thermal equilibrium case. Statistical mechanics tells us that the thermal equilibrium state of our closed system in contact with single heat bath, is a *canonical ensemble* where the occupation probabilities p_μ for all microstates $\mu \in \Omega$ follow the Boltzmann distribution

$$p_\mu = \exp[-(E_\mu - F)/T] = \frac{1}{Z}\exp(-E_\mu/T). \tag{3.9}$$

Here, F correspond to the Helmholtz free energy from which ones gets the canonical partition function $Z = \exp(-F/T) = \sum_\mu \exp(-E_\mu/T)$. Furthermore, E_μ is the energy

of microstate μ whose precise value depends on details of the interactions among the constituents of the respective physical system. For example, E_μ could be determined by the interaction potential among particles in a box or by interactions between spins which are located on equidistant positions on a lattice, as we will discus in detail in C. 9. Further, we know that DB [see Eq. (2.9)] holds in equilibrium, thus

$$\frac{Q}{T} = \ln\left(\frac{w_{\nu\mu}}{w_{\mu\nu}}\right) = \ln\left(\frac{p_\nu}{p_\mu}\right). \tag{3.10}$$

Now, inserting the Boltzmann distribution, we find

$$\frac{Q}{T} = \ln\left(\frac{w_{\nu\mu}}{w_{\mu\nu}}\right) = \ln\left(\frac{p_\nu}{p_\mu}\right) = \ln\left(\frac{Z}{Z}\exp[-(E_\nu + E_\mu)/T]\right) = \frac{-\Delta E_{\nu\mu}}{T}. \tag{3.11}$$

Thus, the first law on the fluctuating scale, is readily implied in the Boltzmann distributions, showing the consistency of the here employed definitions. On average, the internal energy is conserved in thermal equilibrium, and the heat flow is on average expected to vanish. In the following, we will discuss this in more detail.

3.2.2 Entropy production in discrete Markovian systems

A key quantity that distinguishes systems out of thermal equilibrium from those in equilibrium is the constant net production of entropy. In order to define the *total* production of entropy in discrete Markovian systems with finite probability state space Ω, we need to consider both, the entropy change in the system and the entropy which is exported to the environment.

Let us first recall the time-dependent Shannon entropy from statistical mechanics [206] $S(t) = -\sum_\mu p_\mu(t)\ln(p_\mu(t))$ (see Eq. (3.3)). Corresponding to this definition, one defines in stochastic thermodynamics, the fluctuating Shannon entropy

$$S_{sys}(t) = -\ln[p_\mu(t)] \tag{3.12}$$

which depends on the probability of the currently occupied state. This entropy explicitly depends on the state of the system, i.e., the probability distribution, and we will hence call it system entropy. In the ensemble average, we recover the previous definition [see Eq. (3.3)], $\langle S_{sys}\rangle = S$. From Eq. (3.12) one immediately obtains the change of Shannon entropy during a single transition $\mu \to \nu$

$$\Delta S_{sys} = \ln\left(\frac{p_\mu}{p_\nu}\right). \tag{3.13}$$

The change of system entropy is only one part of the change of the total entropy S_{tot} due to the transition $\mu \to \nu$. The other contribution to the change of the medium entropy due to the amount of heat [see Eq. (3.4)] which is extracted from or given to the heat bath

$$\Delta S_m = -\frac{Q}{T} = \ln\left(\frac{w_{\nu\mu}}{w_{\mu\nu}}\right). \tag{3.14}$$

By combining these two entropy changes, one obtains the total entropy production along the (random) transition $\mu \to \nu$.

$$\Delta S_{tot} = \Delta S_m + \Delta S_{sys} = \ln\left(\frac{w_{\nu\mu}}{w_{\mu\nu}}\right) + \ln\left(\frac{p_\mu}{p_\nu}\right) = \ln\left(\frac{w_{\nu\mu}p_\mu}{w_{\mu\nu}p_\nu}\right). \tag{3.15}$$

Thus, the total entropy production is given by the log-ratio of the transition probability to observe the forward divided by the backward transition.

Thermal equilibrium and nonequilibrium steady states: The definition of the total entropy production [see Eq. (3.15)] directly depends on the transition rates and occupation probabilities. There is a very apparent connection between this definition and the aforementioned concept of detailed balance [see Eq. (2.9)]. Specifically, if DB is fulfilled, $\Delta S_{tot} \equiv 0$ which is readily given by substituting Eq. (2.9) into Eq. (3.15). Then, the system is reversible, or in other words, it is in thermal equilibrium. Note that the entropy contributions may still fluctuate, but around zero average values, $\langle \dot{Q} \rangle = 0$.

Let us now consider a system for which DB is broken for at least one pair of states $\mu, \nu \in \Omega$, i.e., at least one process is irreversible, $p_\mu w_{\nu\mu} \neq p_\nu w_{\mu\nu}$. In that case,

$$J_{\nu\mu} = p_\mu w_{\nu\mu} - p_\nu w_{\mu\nu} \neq 0. \tag{3.16}$$

The system is said to violate DB and is consequently driven out of equilibrium. In this case, the occupation probabilities of states in a canonical ensemble do not necessarily have to follow the Boltzmann distribution anymore. However, under certain conditions, the system may still be found in a (nonequilibrium) stationary state (NESS) with time-independent state vector $\dot{\mathbf{P}} = 0$. In contrast to the equilibrium case of a SS, such a NESS is characterized by non-vanishing probability flows (currents) between certain pairs of states (due to broken DB) which, in total, cancel each other out such that there is no net current in the whole system. The latter is a requirement for a nonequilibrium system in order to maintain a stationary state. To this end, let us shortly review how one can crate such stationary nonequilibrium states in physical systems and discuss some simple examples. NESS can be maintained by constantly driving the system. To give an example of a discrete driven system, let us think of an Ising model in contact with two heat baths at T_1 and T_2. The fixed temperature difference $\Delta T = |T_1 - T_2|$ among the sublattices leads to a constant heat flux $\dot{Q} > 0$ from the hotter to the colder reservoir. The system is constantly driven out of equilibrium. We will discuss this example in C. 9 In the following, we show how

heat Q, entropy S and entropy production $\pi = \dot{S}$ are related to the transition rates $w_{\nu\mu}$ of processes $\mu \to \nu$.

Entropy production in discrete Markov chains: Now we extend the previous definitions for single transitions to entire trajectories. If we consider a stochastic path $\mathbf{X}(N)$ of length N, the change of the medium entropy along this trajectory is given by

$$\Delta S_m = \sum_{i=2}^{N} \ln\left(\frac{w_{\omega_i\omega_{i-1}}}{w_{\omega_{i-1}\omega_i}}\right). \tag{3.17}$$

The change of system entropy along the path $\mathbf{X}(N)$ is given by

$$\Delta S_{sys} = \sum_{i=2}^{N} \ln\left(\frac{p_{\omega_{i-1}}(i-1)}{p_{\omega_i}(i)}\right) = \ln\left(\frac{p_{\omega_1}(1)}{p_{\omega_N}(N)}\right), \tag{3.18}$$

where $p_{\omega_i}(i)$ is the probability to find the system in state ω_i at the i-th step of the trajectory. Thus, in sharp contrast to the medium entropy, the change of system entropy only depends on the initial state ω_1 and the final state ω_N of the trajectory, but not on the intermediate states $\omega_2, \omega_3, ..., \omega_{N-2}, \omega_{N-1}$. One consequence of this observation is that the system entropy change will generally not grow with N, whereas the amount of heat will, in general, increase with the length N of the observed trajectory as long as the trajectory is not taken from an equilibrium system (for which $\Delta S_m = 0$ holds for $N \to \infty$). For example, in a NESS, the mean medium entropy production ΔS_m grows linearly with N. This, in turn, means that the contribution of the system entropy to the total entropy production ΔS_{tot} along very long trajectories vanishes, and consequently, one finds

$$\lim_{N\to\infty} \Delta S_{tot} = \Delta S_m. \tag{3.19}$$

We will exploit this simplification later, when we numerically determine the fluctuations of the total entropy production in a NESS. This will be done in C. 9 for a q-state Potts model in contact with two heat baths and in C. 8 where we investigate entropy production in the context of nonequilibrium surface growth. As shown there, $\Delta S_{tot} \approx \Delta S_m$ is already valid for numerically manageable path lengths N.

The ensemble average entropy production rate in a NESS: Based on the so far introduced changes of entropy along a stochastic path consisting of N state transitions $\omega_{i-1} \to \omega_i$, we will now formally introduce the entropy production rate as a measurable quantity which quantifies the distance from equilibrium in systems maintaining a NESS. As will be shown in C. 9, this quantity (and it's derivative with respect to the control parameter) exhibits characteristic behavior in the vicinity of nonequilibrium phase transitions.

Starting from the definition of the Shannon entropy [see Eq. (3.3)], we can formulate an expression for the time-dependent change of entropy that one the one hand, originates

from the total system internal production of entropy and, on the other hand, by the exchange of entropy with the environment

$$\partial_t S(t) = \dot{S}_{sys}(t) = \Pi(t) - \Phi(t). \tag{3.20}$$

Here, $\Pi(t)$ corresponds to the total system internal production of entropy, whereas $\phi(t)$ is the production of entropy due to the exchange of entropy with the environment (the heat bath). In order to formulate explicit expressions for $\Pi(t)$ and $\phi(t)$, we recall the two constituents of the total change of entropy, ΔS_{sys} and ΔS_m. These two contributions vary discontinuously for a particular stochastic path $\mathbf{X}(N)$. However, their expectation values vary smoothly according to

$$\dot{S}_{sys}(t) := \frac{\mathrm{d}}{\mathrm{d}t}\langle S_{sys}(t)\rangle = \sum_{\mu,\nu} \ln\left(\frac{p_\mu(t)}{p_\nu(t)}\right) p_\mu w_{\nu\mu} \tag{3.21}$$

$$\Phi(t) = \dot{S}_m(t) := \frac{\mathrm{d}}{\mathrm{d}t}\langle S_m(t)\rangle = \sum_{\mu,\nu} \ln\left(\frac{w_{\nu\mu}}{w_{\mu\nu}}\right) p_\mu w_{\nu\mu}, \tag{3.22}$$

where $\langle S_{sys}(t)\rangle$ and $\langle S_m(t)\rangle$ denote the ensemble average of the change of system entropy and medium entropy, respectively. Taken together, the total (ensemble average) change of entropy per time, i.e. $\dot{S}_{sys}(t) + \dot{S}_m(t)$, reads

$$\Pi(t) = \dot{S}_{tot}(t) := \frac{\mathrm{d}}{\mathrm{d}t}\langle S_{tot}(t)\rangle = \sum_{\mu,\nu} \ln\left(\frac{p_\mu w_{\nu\mu}}{p_\nu w_{\mu\nu}}\right) p_\mu w_{\nu\mu}. \tag{3.23}$$

This equation can be rewritten as

$$\Pi(t) = \frac{1}{2}\sum_{\mu,\nu} [p_\mu(t) w_{\nu\mu}(t) - p_\nu(t) w_{\mu\nu}(t)] \ln\left(\frac{p_\mu(t) w_{\nu\mu}(t)}{p_\nu(t) w_{\mu\nu}(t)}\right), \tag{3.24}$$

which corresponds to the formula for the total entropy production rate according to Schnakenberg [207]. This equation obeys the thermodynamically expected properties: $\Pi(t)$ nullifies in thermal equilibrium (whre DB is fulfilled), and is strictly positive otherwise (if DB is broken), in accordance with the second law of thermodynamics. For systems in a NESS, the time-dependencies of the occupation probabilities and the transition rates vanish, and cconsequently, also the time-dependencies of the entropy production rates vanish, i.e. $\dot{S}_{sys}(t) = \dot{S}_{sys}$, $\Pi(t) = \Pi$ and $\Phi(t) = \Phi$. Moreover, in a NESS, the system entropy (i.e., the Shannon entropy) remains constant, $\dot{S}_{sys} = 0$, and therefore, $0 = \Pi - \Phi$. From this, one immediately sees that in this case, the total entropy production rate corresponds the medium entropy production rate, $\Pi = \Phi$. As a consequence, it is sufficient to calculate Φ in order to get the total entropy production rate. As the system is expected to be ergodi in

the steady state, this can be done by calculating the change of medium entropy along an infinitely long trajectory

$$\frac{1}{2}\sum_{\mu,\nu}\left[p_\mu(t)w_{\nu\mu}(t)-p_\nu(t)w_{\mu\nu}(t)\right]\ln\left(\frac{p_\mu(t)w_{\nu\mu}(t)}{p_\nu(t)w_{\mu\nu}(t)}\right)=\lim_{N\to\infty}\frac{1}{N}\sum_{i=2}^{N}\ln\left(\frac{w_{\omega_i-\omega_{i-1}}}{w_{\omega_{i-1}-\omega_i}}\right). \tag{3.25}$$

Alternatively, for a system in a NESS one can compute $\Phi=\Pi$ numerically by averaging over many transitions $\mu\to\nu$ from the current state μ of the Markov chain in the steady state. In spin systems with discrete spin orientations like the vector Potts model with finite q, state transitions $\mu\to\nu$ correspond to the flipping of a randomly chosen spin on the lattice. If we recall the definition of the medium entropy production rate [see Eq. (3.22)], it becomes clear that Φ can be written as an average over all lattice sites of the system

$$\Phi=\Pi=\sum_i\sum_\nu\langle w^i_{\nu\mu}\ln\left(\frac{w^i_{\nu\mu}}{w^i_{\mu\nu}}\right). \tag{3.26}$$

Here, the first sum runs over all lattice sites i of the system and the second sum runs over all final states ν that can be reached by flipping the spin on lattice site i with transition rate $w^i_{\nu\mu}$. We will make use of the fact that $\Pi=\Phi$ for systems in a NESS and calculate the total entropy production rate numerically by either using Eq. (3.26) or by simple tracking the change of medium entropy along stochastic paths of length N. As will be shown in C 9 and C 8, it is often sufficient to take rather small path lengths. Specifically, in C. 8 we compare the exact value of the total entropy production rate according to Eq. (3.23) with the numerically calculated rate for a one-dimensional growing interface. In particular, we find perfect agreement between the exact and the numerical value of Π for various growth conditions (i.e., deposition rate, temperature and binding energy) even for $N\ll 100$. The same is true for the Potts model in contact with two heat baths.

3.3 Fluctuation theorems

Fluctuation theorems (FT) represent one of the few exact relations which are valid for any nonequilibrium system in a NESS [193, 208]. These relations led to fundamental breakthroughs in our understanding of how irreversibility in systems emerges from reversible dynamics. Concerning the entropy, there exists a relation which sets a restriction to the probability distribution of the total entropy change $\Delta S_{tot}(N)$ along a stochastic path $\mathbf{X}(N)$ of length N. Specifically, the FT states that, in any nonequilibrium system, the ratio between the probability $\mathcal{P}(X)\in[0,1]$ that the total entropy increases by $\Delta S_{tot}(N)=X$ along $\mathbf{X}(N)$ is exponentially more likely than the probability $\mathcal{P}(-X)$ to decrease the total entropy by $-\Delta S_{tot}(N)=-X$ [52, 194]

$$\frac{\mathcal{P}[\Delta S_{tot}(N)=X]}{\mathcal{P}[\Delta S_{tot}(N)=-X]}=\exp(X). \tag{3.27}$$

By taking the logarithm, this equation can be rewritten as

$$\ln\left(\frac{\mathcal{P}[\Delta S_{tot}(N)=X]}{\mathcal{P}[\Delta S_{tot}(N)=-X]}\right)=X. \tag{3.28}$$

In other words, the FT expresses that violations of the second law of thermodynamics become exponentially less likely as function of the change of total entropy ΔS_{tot}. This becomes clear if we rewrite Eq. (3.27) as

$$\mathcal{P}[\Delta S_{tot}(N)=-X]=\frac{\mathcal{P}[\Delta S_{tot}(N)=X]}{\exp(X)}. \tag{3.29}$$

From this equation one immediately sees that for $\Delta S_{tot}(N)\to\infty$, the probability to destroy this amount of entropy vanishes, i.e., $\lim_{X\to\infty}\mathcal{P}\left[\Delta S_{tot}(N)=-X\right]\to 0$. It can be mathematically proven that according to the FT, the ensemble average entropy production is always non-negative for any trajectory length N, i.e., $\langle\Delta S_{tot}(N)\rangle\geq 0$ holds in any physical system [51, 52]. This so-called second law inequality is in accordance with the (classical) second law of macroscopic thermodynamics which states that in a physical process, the entropy can never decrease.

In the limit $N\to\infty$, also the change of medium entropy, ΔS_m, fulfills a fluctuation relation

$$\ln\left(\frac{\mathcal{P}[\Delta S_m(N)=X]}{\mathcal{P}[\Delta S_m(N)=-X]}\right)=X. \tag{3.30}$$

This relation directly follows from Eq. (3.27) in the limit of infinitely long observation times, i.e. $N\to\infty$. For individual paths $\mathbf{X}(N)$, the system entropy fluctuations vanish for individual paths such that $\langle\Delta S_{sys}\rangle=0$. However, [Eq. (3.30)] can be approximately valid also for finite N. In particular, the smaller the probability state space Ω of a system, the shorter the trajectories need to be to fulfill almost perfectly the fluctuation theorem for the medium entropy.

4 Critical phenomena and universality of phase transitions and surface growth

This chapter is concerned with phase transitions and universal behavior of systems at criticality. We will introduce the concepts of first-, second- and infinite-order phase transitions. Further, we discuss universal behavior at criticality and introduce the finite-size scaling technique which allows to numerically determine critical exponents. Towards the end of this chapter, we will turn to the critical behavior and universality of surface growth. In this context, we will further discuss the dynamical scaling relation.

4.1 Fundamentals of critical phenomena

When a physical system approaches a critical point where it undergoes a (continuous) transition from one phase A to another phase B, anomalous behavior can occur not only in various dynamic properties, but also in the static ones. This affects the overall physical behavior of systems in the vicinity of phase transitions. Extraordinary physical properties of systems in the vicinity of critical points are comprehensively discussed within the framework of critical phenomena [6, 7, 63, 73, 209]. The latter serves as a general framework to systematically study the physical behavior of systems at criticality where thermodynamic properties become non-analytic. More precisely, a critical point is defined as the critical value q_c of an appropriate control parameter q (e.g., the temperature T, the density ρ or the pressure p) at which a phase A and a further phase B of a pure stable substance become identical. To give an example, let us consider the behavior of water around it's critical point which is at $T_c = 647.096$ K, $\rho_c = 322$ kg/m^3, $p_c = 220,64$ bar. The physical properties of the liquid and the vapor phase of water change dramatically as the critical point is approached. In fact, both phases, i.e., the liquid and vapor phase, become more similar. Under normal conditions, liquid water is nearly incompressible, it has a low thermal expansion coefficient and, at the same time, a high dielectric constant. Near the critical point, these properties change into the exact opposite. There, water becomes suddenly compressible, thermally expandable and is characterized by a low dielectric constant [1, 210, 211]. Such a dramatic change of properties at criticality is not limited to physically complex systems like water. In fact, also the simple stochastic models considered

in this thesis, i.e., the spin and surface growth models studied in C. 5 - C. 8, exhibit noticeable behavior in the vicinity of phase transitions.

Within the framework of critical phenomena it is systematically investigated how the properties of systems change as the system is brought closer to the critical point [6, 7, 63, 209]. In general, this includes the investigation of generic properties such as scaling relations among different quantities. One example is the hyperscaling relation which is discussed further below in this chapter. Furthermore, the power-law divergence of certain system-specific and system-unspecific quantities are investigated within this context. Conventionally, one analyzes the scaling behavior of the correlation length ξ, the specific heat C_v and the magnetic susceptibility χ as the system is brought closer to the critical point q_c where it undergoes a transition from some phase A to another phase B. In many systems, the quantities just mentioned exhibit power-law behavior around q_c. Therefore, they can often be categorized into universality classes according to their corresponding power-law exponents, i.e., critical exponents, which describe the power-law scaling of these quantities in the vicinity of critical points.

The framework of universality classes is well established for equilibrium systems. Concerning phase transitions, nonequilibrium statistical physics is concerned with the question whether the scaling behavior, i.e., the critical exponents, of the aforementioned quantities are altered if a system is driven out of thermal equilibrium [73–75]. In this context, there are two main questions. First, one is interested in how the critical behavior of nonequilibrium systems is different from their equilibrium counterparts. Specifically, this includes analyzing and comparing the critical exponents of systems under equilibrium and nonequilibrium conditions. In this thesis, we address this topic based on the example of a nonequilibrium version of the Potts model and the classical XY model in C. 9. In particular, we find that the specific heat C_v scales with the same critical exponents as C_v in the equilibrium version of the vector Potts model. On the other hand, there is the question whether nonequilibrium systems exhibit characteristic behavior at criticality that generally distinguishes them from equilibrium systems. In this regard, the entropy production rate Π [see Eq. (3.23) in Sec. 3.2] is a promising tool to characterize nonequilibrium phase transitions [109, 112, 205]. The latter quantity is exactly zero for equilibrium systems ($\Pi = 0$) and always positive ($\Pi > 0$) in nonequilibrium systems. It is therefore appealing to investigate whether the entropy production rate exhibits characteristic scaling behavior in the vicinity of critical points. In particular, this concerns the scaling behavior of Π in the vicinity of phase (continuous) transitions. We calculate the entropy production rate in a nonequilibrium vector Potts model in the vicinity of the continuous phase transition in C. 9 and, additionally, round the critical point of the (infinite-order) Berezinskii-Kosterlitz-Thouless phase transition in a nonequilibrium version of the classical XY.

4.2 Classification of phase transitions

Before we come to the discussion of critical exponents and universal behavior at criticality, we first summarize the fundamentals of phase transitions. The critical point q_c of a system is characterized by the vanishing of an appropriate order parameter Ψ. The latter is a measure for some symmetry of a system which allows to distinguish between an ordered phase with broken symmetry and a disordered phase where the respective symmetry is present. The order parameter describes the physical quantity (observable) which is responsible for breaking of the respective symmetry under consideration. More precisely, the order parameter vanishes for $q \geq q_c$, i.e., $\Psi = 0$ in the disordered phase and is greater zero for $q < q_c$, i.e., $\Psi > 0$ in the ordered phase where the symmetry is broken. Therefore, phase transitions are accompanied by the phenomenon of spontaneous symmetry breaking. This is at least the case for first- and second-order phase transitions according to Landau theory of phase transitions[212]. It is well known that the Landau free energy in the vicinity of a critical point is determined by symmetries only. This sort of universality is very useful since it means that the way a thermodynamic system behaves close to q_c does not depend on the microscopic details. In fact, the behavior of a system is sort of universal around the critical point. The idea is to expanded the free energy $F(\Psi, q)$ in form of a power series up to sixth order in the order parameter Ψ

$$F(\Psi, q) \approx f_0(q) + a_0(q - q_c)\Psi^2 + \frac{1}{2}b_0(q)\Psi^4 + \frac{1}{3}c_0(q)\Psi^6, \tag{4.1}$$

where $f_0(q)$ describes dependency of $F(\Psi, q)$ on the order parameter q in the regime $q > q_c$ close to phase transition. The other parameters will become important when we discuss first- and second-order phase transitions in more detail. As the critical point is approached, certain properties of the system change. Depending on how they change, one distinguishes between different types of phase transitions. It is common practice to divide phase transitions into two broad categories, (discontinuous) first-order transitions on the one hand and (continuous) second-order transitions on the other hand. Additionally, there exist infinite-order transition which, in contrast to the two other types, are never associated with spontaneous symmetry breaking [57]. The nonequilibrium Potts model which is investigated in C. 9 exhibits, depending on the number of possible configurations per spin, all three types of phase transitions. We study second and infinite order transitions of this Potts model under nonequilibrium conditions in C. 9.

4.2.1 First-order phase transitions

A phase transition is said to be of first-order if the internal energy of the system changes discontinuously as the appropriate control parameter q approaches the critical value q_c where the system undergoes a transition from some phase A to another phase B [7, 63, 209]. The characteristic feature of such a first-order transition is the release or

absorption (depending on whether the transition is from phase A to phase B or vice versa) of latent heat $Q_L = q\Delta S$. The latter is the amount of exchanged heat that is required to drive the system across the phase transition at constant temperature. At a first-order transition a system remains in phase A until the critical value q_c of the control parameter is reached from above, $q > q_c$. Then, it jumps discontinuously to phase B and thereby dissipates or absorbs Q_L. The Landau theory can be used to study first-order transitions by considering the expansion of the free energy up to sixth-order. By setting $a_0 > 0$, $b_0 < 0$ and $c_0 > 0$ in Eq. (4.1), there will be a first-order phase transition in the system. Since the entropy is given by $S(T) = -\mathrm{d}F(\Psi)/\mathrm{d}q$, the exchanged latent heat can be calculated [212, 213]. One major feature of first-order phase transitions is hysteresis. This implies that the state of a system depends on it's own history. If one drives a system, which is initially in state a and phase A (at $q_a < q_c$), across q_c to a state b in phase B (with $q_b > q_c$), the system will not come back to the very same state a if one decreases q to q_a again. Instead, the system will be found in some state c. Particularly, the area of the thereby formed hysteresis loop is a measure for the amount of energy that has been exchanged (dissipated or absorbed) during the first-order phase transition. This phenomenon can be induced by considering inertia in simple models like the majority vote model [214]. In the case of spin systems the paramagnetic to ferromagnetic phase transition can be of first-order if an magnetic field is applied. The transition can also become first order due to system internal properties.

4.2.2 Second-order phase transitions

In contrast to first-order transitions, there is no latent heat at second-order phase transitions, i.e., $Q_L = 0$ and therefore $\Delta S = 0$. Accordingly, the internal energy of a system around a second-order phase transition changes continuously as function of q. By considering a series of $F(\Psi, q)$ up to fourth order with $b_0 > 0$, one observes a continuous phase transition at q_c where a_0 changes it's sign. The specific heat $C_v = -q\partial^2 F(\Psi, q)/\partial q^2$ diverges at q_c. This means that there is a discontinuity in C_v at q_c which is related to the discontinuity in the second derivative of the free energy $F(\Psi, q)$. This is a characteristic feature for second-order phase transitions. Furthermore, the susceptibility χ diverges and systems which undergo a continuous transition have an infinite correlation length at criticality. Additionally, they show a power law decay of correlations near the critical point q_c. Therefore, one can categorize systems exhibiting second-order phase transitions into different universality classes according to the power-law exponents of the specific heat C_v, the susceptibility χ, the order parameter Ψ and the correlation length ξ in the vicinity of q_c. This is discussed in Sec. 4.3. Important examples for materials undergoing second-order transitions are ferromagnets, superfluids, and superconductors [1, 7, 209].

4.2.3 Infinite-order phase transitions

There also exist phase transitions where the first appearance of a divergence occurs in some higher derivative of the free energy with respect to q. At an infinite-order phase transition, a divergence of the derivatives of the free energy with respect to q does not occur at all. The most prominent type of infinite-order phase transition is the so-called Berezinskii-Kosterlitz-Thouless (BKT) transition which received media attention after Thouless, Kosterlitz and Haldane were awarded with the Nobel Prize for Physics in 2016 [57, 215–217]. The transition is found exclusively in two-dimensional systems. Examples include Josephson junction arrays, thin disordered superconducting granular films and two-dimensional superconductors [218]. The most simple theoretical model of a system exhibiting a BKT transition is the classical XY which is investigated in C. 9. Specifically, there we compare the thermodynamic properties of the equilibrium model with a nonequilibrium version around the BKT transition. Another peculiarity of the BKT transition is the fact that it is not associated with symmetry breaking. In the case of a paramagnetic to ferromagnetic phase transition (which can be first- or second-order), the rotational symmetry of the spin-disordered paramagnetic phase is broken in the long-range ordered ferromagnetic phase where all spins point in a unique direction. In contrast, the BKT transition (in the two-dimensional classical XY model) is between a phase with unpaired vortices and anti-vortices at high temperatures (with exponentially decaying spin-spin correlations) to a quasi long-range ordered phase with bound vortex-antivortex pairs (with power-law decaying spin-spin correlations) below the critical value of q, i.e., the critical temperature T_c. It can be shown that the free energy $F(\Psi, q)$ of the phase with bound vortex-antivortex pairs has a lower free energy, which favors the formation of the BKT phase [57]. The reason why the classical XY model in two dimensions does not have a ferromagnetic phase is due to the Mermin-Wagner theorem [53, 55, 219] which states that continuous symmetries (here the continuous spin symmetry in the XY model) can not be spontaneously broken at finite temperatures T in systems with $d \leq 2$ and short-range interactions. Moreover, it is not known that the specific heat C_v in the vicinity of the transition does not exhibiting any noticeable behavior. In fact, there is only a non-divergent peak above T_c which does not show a power-law increases as function of system size L.

4.3 Universality of phase transitions

4.3.1 Critical exponents and power-law behavior

Critical exponents: Systems can be classified according to the scaling behavior of system-specific quantities as the critical points, q_c is approached. For spin systems, q corresponds to the heat bath temperature T, whereas for surface growth, the control parameter is given by the particle deposition rate F. As mentioned above in this section, physical quantities,

i.e., observables $\mathcal{O}$ often exhibit power-law behavior at criticality. One can classify this behavior by using critical exponents [6, 7, 63]. The latter describe the power-law behavior of certain observables $\mathcal{O}$ around q_c. More precisely, critical exponents describe the behavior of quantities near continuous phase transitions, i.e., second-order phase transitions.

Control parameter and power-law behavior: We want to describe the behavior of a physical observable $\mathcal{O}$ in terms of a power law around q_c. To this end, we use introduce the reduced control parameter

$$\tau = \left| \frac{q - q_c}{q_c} \right| = \left| 1 - \frac{q}{q_c} \right|. \tag{4.2}$$

The parameter τ vanishes at the critical point, i.e., $\tau = 0$ at $q = q_c$, and increases linearly with distance $|q - q_c|$ from the critical point. Proceeding from τ, we now define a critical exponent k according to

$$k := \lim_{\tau \to 0} \frac{\ln|\mathcal{O}(\tau)|}{\ln|\tau|}. \tag{4.3}$$

Here, $\mathcal{O}(\tau)$ corresponds to the functional behavior of $\mathcal{O}$ with respect to τ, i.e., as function of the distance from the critical point. From this generic definition, we immediately arrive at the desired power-law behavior in the vicinity of q_c. In the regime of small values of the reduced control parameter, i.e., for $\tau \to 0$, which is close to q_c, we get

$$\mathcal{O}(\tau) \propto \tau^k, \tag{4.4}$$

which is the asymptotic behavior of the functional form of the observable $\mathcal{O}$. The functional form of different observables $\mathcal{O}(\tau)$ shows different scaling behavior, i.e., they are characterized by other values of the power-law exponent k. The most generic observables for spin systems which show noticeable power-law behavior in the vicinity of q_c include the magnetization (which acts as order parameter in spin systems, i.e., $\Psi = |m|$) $m(\tau) \sim \tau^\beta$, the spin-spin correlation length $\xi(\tau) \sim \tau^{-\nu}$, the magnetic susceptibility $\chi(\tau) \sim \tau^{-\gamma}$, the specific heat $C_v(\tau) \sim \tau^{-\alpha}$ and, if present, the scaling of the magnetization as function of an external field, $m \sim h^{1/\delta}$. The values of the thereby defined set of critical exponents $\alpha, \beta, \gamma, \delta, \nu$ enables a systematic classification of different systems into universality classes. The exponents can be obtained either via analytical calculations or numerically by means of Monte-Carlo simulations. For an analytical determination of the critical exponents, one often performs mean-field type calculations within the framework of the Landau theory [212, 213, 220]. However, mean-field theory neglects the effects of thermal fluctuations. As an extension, the Ginzburg-Landau theory can be used to calculate the corrections to the Landau theory by taking into account the effects of thermal noise [221–224].

Universal behavior and universality classes: In general, a universality class is defined as collection of models sharing a single scale invariant limit under the process of renormalization group flow [225–227]. While all models within a specific universality class may differ dramatically at finite scales, their behavior becomes increasingly similar as the

limit scale of large systems is approached. This means that, irrespective of microscopic details, their critical behavior on the macroscale is significantly similar. In fact, certain properties of systems near critical points are identical for various physically completely different systems. For example, the scaling of the specific heat C_v as function of τ near the liquid-gas transition has the same behavior as C_v at the paramagnetic to ferromagnetic phase transition in magnetic materials and mathematical spin systems. Another example concerns suspensions of active, i.e., self-propelled, particles which undergo a gas-liquid phase separation, known as motility-induced phase separation [148, 149]. Such active suspensions are characterized by the same set of critical exponents as the classical Ising model with Kawasaki spin exchange dynamics at the paramagnetic to ferromagnetic phase transition. In particular, systems sharing the same set $(\alpha, \beta, \gamma, \delta)$ of critical exponents fall in the same universality class, even though they seem to have physically nothing in common. It is generally believed, though not formally proven, that the values of the critical exponents are universal and depend only on some rather general features. Concerning spin systems, these general features include the dimension d and the geometry of the lattice, the range l of spin-spin interaction and the spin dimension n. This implies that changing the interaction strength J in an Ising or Potts model only results in a shift of the critical temperature T_c, but does not affect the scaling behavior of any observable $\mathcal{O}$ around T_c. As shown in numerous analytical, numerical and experimental studies, there truly exist only a handful distinct sets for the critical exponents and many physical systems at criticality are characterized by one of them [7, 63, 73, 74, 209].

Universal behavior at nonequilibrium phase transitions:While critical exponents and universal behavior are well understood for systems in thermodynamic equilibrium, general properties of nonequilibrium systems at criticality are less clear [73–75]. Nonetheless, it has been shown that most of the fundamental concepts valid for equilibrium systems like power-law scaling and universality, also apply under nonequilibrium conditions. However it is *a priori* not clear whether the critical exponents, and thus, the universality class of a system remains unaltered if it is driven out of thermal equilibrium. As shortly mentioned earlier in this chapter, we show in C. 9 for a q-state vector Potts model in a nonequilibrium stationary state that the critical exponents are not affected by driving. In fact, they are identical to the exponents of the equilibrium version of the model. We investigate the behavior of the entropy production rate per spin, π which exhibits characteristic scaling behavior near T_c. Specifically, the derivative of π with respect to T, i.e., $\mathrm{d}\pi/\mathrm{d}T$, diverges at the critical point. This resembles the behavior of the specific heat C_v for $\tau \to 0$ at continuous phase transitions. Furthermore, $\mathrm{d}\pi/\mathrm{d}T$ shows (non-universal) power-law scaling with an exponent whose value depends on the strength of driving, i.e., the distance from equilibrium. It is a topic for future research in this field to investigate the usefulness and universality of the entropy production at criticality.

4.3.2 The finite-size scaling method

Due to the fact that the linear system size L in numerical simulation studies is always finite, i.e., $L < \infty$, the correlation length ξ may become of the order of L but can never exceed the limited size of the simulation box. Therefore, ξ can not diverge in a strictly mathematical sense in computer simulations with finite system size L (where $\xi_{\max} = L$). This means that $\xi \to \infty$ is not possible in numerical simulation studies. This implies for divergences in other quantities $\mathcal{O}$, like the specific heat C_v or the susceptibility χ, that, at criticality, their divergent behavior is also affected by finite system sizes L in simulations. However, the scaling law $\mathcal{O}(\tau) \sim \tau^k$, which we introduced in Sec. 4.3, assumes a true divergence of correlations, i.e., $\xi \to \infty$, at the critical point. Therefore, one has to replace the scaling laws for specific observables $\mathcal{O}$. This is done by proposing a finite-size scaling (FSS) ansatz to compensate for the system size limitation [228, 229]. In the previous paragraph we showed that the divergence of the correlation length (which is connected to the critical exponent ν) close to the critical point scales $\xi \sim \tau^{-\nu}$ for an infinitely large system. We therefore argue that the system with finite L has a pseudocritical point at $q_c(L)$. The shift of the critical point is consistent with the law

$$|q_c - q_c(L)| \sim L^{-1/\nu}, \tag{4.5}$$

where q_c is the exact critical point for the infinitely large system. Accordingly, the power-law scaling of observables $\mathcal{O}$, i.e., the scaling laws, have to be rewritten because the critical exponents are affected by the finite system size. For example, the finite peak $\chi_{\max}(L)$ of the susceptibility (which would diverge in an infinitely large system) at the pseudocritical point $q_c(L)$ scales $\chi_{\max}(L) \sim |q_c - q_c(L)|^{-\gamma} \sim L^{\gamma/\nu}$. By tracking the position $q_c(L)$ of $\chi_{\max}(L)$ for increasing system sizes L and fitting a power-law to the location of the pseudocritical point $q_c(L)$, we can estimate the true critical point, and thus, determine ν according to

$$q_c(L) = q_c - aL^{-1/\nu}, \tag{4.6}$$

where a is a constant. Thus, by performing a finite-size scaling analysis for the scaling of the pseudocritical point of the susceptibility, we directly obtain ν. Further, by tracking the scaling of the peak height which scales $\chi_{\max}(L) \sim |q_c - q_c(L)|^{-\gamma} \sim L^{\gamma/\nu}$, we obtain γ because we already now ν from the scaling of $q_c(L)$. Therefore, we obtain two critical exponents, ν and γ, from the FSS analysis of the susceptibility. This procedure can be repeated for C_v in order to obtain α. However, the FSS has to be very precise because α is usually much smaller than γ for many universality classes.

4.4 Universality in nonequilibrium surface growth

So far, we discussed universal behavior in systems regarding their physical properties in the vicinity of (continuous) phase transitions. The values of the corresponding critical exponents allow us to define universality classes according to the power-law behavior of quantities close to criticality. In the following we investigate the stochastic motion of interfaces, i.e., lines and surfaces and explain what universality means in this context. More specifically, we study the dynamics of driven interfaces which are subjected to white noise. Here, the most important quantity is the interface width $W(L,t)$, i.e., the root mean square value of the height fluctuations as defined in Eq. (6.8). In particular, the width of an interface is a measure of the transverse correlations in the direction of growth [9]. Concerning the surface growth models investigated in this thesis, i.e., the full diffusion KMC model and the DT model with diffusional fluctuations, see C. 9, 5 6 and C. 7, the interface, which separates the growing solid crystal from the overlying gas phase, is flat at the beginning of each simulation run. This means that the height h is set to $h = 0$ at all lattice positions. Thus, the width of the interface, $W(L,0) = 0$, is zero at the beginning of the simulation, $t = 0$. As particle deposition sets in, the interface gets rougher with time. As a consequence, the width of the interface increases. In particular, the incoming flux of particles is both, the driving mechanism for the surface growth process and, at the same time, the source for white noise [9, 13, 230]. The reason for the latter is that we treat deposition such that it is completely uncorrelated in space and time.

For an infinitely large system, i.e., $L \to \infty$, the roughness of the interface diverges, $W(L,t) \to \infty$ if online particle deposition (and/or evaporation events) are considered. This means that the width of the interface would increase $\sim t^{\beta}$ as long as their is an persistent incoming flux of particles. In that case, the interface is said to be delocalized because it continuously deviates from the initial flat structure. However, models studied in the context of surface growth include more processes and rules than just the random deposition (and/or evaporation) of particles. In fact, what is observed in experiments and simulation studies, where the system size L is finite, is a saturation of $W(L,t)$ at a finite, system size-dependent value $W_{sat}(L)$. This means that in systems of finite size L, the interface width gets localized at some point. As a consequence, the roughness depends on the length scale on which one views the system [9]. Specifically, one finds that the larger the system, the higher the surface roughness. The saturation of the roughness is directly related to the correlation length ξ [9, 231]. Similar to what we have discussed in the paragraph above, the correlation length in finite systems can never exceed the system size, i.e., $\xi = L$ is it's maximum value. It is not clear what the microscopic origin of correlations among different lattice sites is. Nevertheless, let us shortly describe, based on the example of random deposition (RD) and ballistic deposition (BD) [232–234], how neighboring sites know of each other, i.e., how they become correlated and how this correlation spreads. At the beginning of the growth process, individual lattice sites do not communicate with

each other, i.e., they are completely uncorrelated. in RD, individual lattice sites do not communicate with each other at any time of the simulation. Therefore, the correlation length is zero. This is the reason why the interface width does not saturate in this model, but keeps growing with $W(L,t) \sim t^{1/2}$. In BD neighboring lattice sites do communicate with each other. The incoming particles stick to the first site which is a nearest-neighbor of the crystal. Thereby, the crystal grows laterally, and, as a consequence, also the height fluctuations will spread laterally in the system. Even though the crystal growth process is local, the information about the height of each site is spread globally through the system due to the specific sticking rules for arriving particles. Specifically, the typical distance over which lattice sites know about each other is the correlation length ξ. As growth proceeds, the correlation length increases and so does the roughness. As soon as ξ becomes of the order of the system size L, the whole interface is correlated. At this point, the interface width can not further increase and it saturates at a system size-dependent value $W_{sat}(L)$. The system size dependency of $W_{sat}(L)$ is due to the fact that ξ is limited by finite system sizes, $\xi \sim L$. In different systems, the sticking rules for arriving particles are different, and therefore, the correlation length grows differently with time, i.e., it scales with a different exponent. In particular, the scaling of the correlation length depends on the microscopic details and transition rules of the respective growth model. Indeed, different models show a different scaling of $W_{sat}(L)$ with system size L and a different scaling of $W(L,t) \sim t^{\beta}$ in the transient regime before the interface width has reached it's maximum value $W_{sat}(L)$. Additionally, the time t_x when the saturation value is reached depends also on the system size. Specifically, it shows a power-law increase as the system size is increased, i.e. $t_x \sim L^z$. This scaling of the interface width suggests that growing interfaces are self-affine fractal structures, i.e., they are statistically indistinguishable from each other under a suitable anisotropic rescaling of space and time. We will come to this point later when we relate discrete growth models to certain continuum equations which describe the evolution of the surface height in the thermodynamic limit, $L \to \infty$.

4.4.1 The dynamical scaling relation for the interface width

To understand what universality in the context of interface growth means, we focus on properties of the surface roughness $W(L,t)$. As particle deposition onto a flat interface sets in, the roughness initially shows a power-law increase with time

$$W(L,t) \sim t^{\beta} \tag{4.7}$$

in the transient regime where the correlation length ξ increases with scaling exponent β. Interestingly, the scaling of $W(L,t)$ can be related to diffusion processes. If we consider the uniformly distributed, uncorrelated random deposition of particles on a surface, the roughness increases as $W(L), t \sim t^{1/2}$, which is exactly the scaling of the root of the mean-squared displacement of a Brownian particle performing an unbiased random walk, $\sqrt{\langle |x(t) - x_0|^2 \rangle} \sim t^{1/2}$. Therefore, the trajectory of a random walk is statistically equivalent

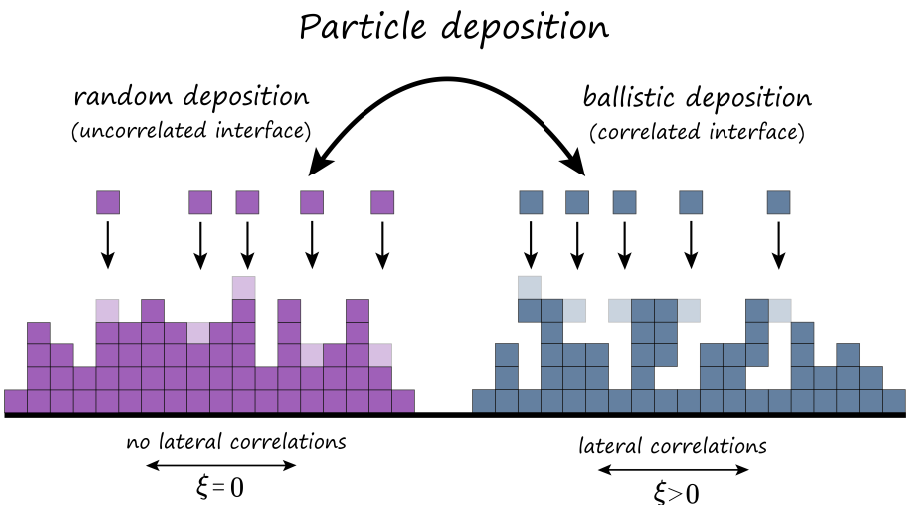

Fig. 4.1: Illustration of random and ballistic deposition of particles on a one-dimensional substrate. During the process of random deposition, particles are deposited on a randomly chosen lattice site i. This results always in an increase $h_i \to h_i + 1$ on that site, irrespective of the configuration on neighboring lattice sites. This is shown by the brighter particles which indicate the final position of deposited particles. Concerning ballistic deposition, the height configurations of neighboring columns of site i affect the deposition on site i. If $h_{i-1} > h_i$ or $h_{i+1} > h_i$, deposited particles stick at the height of neighboring columns. Thereby, lateral correlations spread through the system.

to the long-time height profile if $\beta = 1/2$. If some sort of correlations between lattice sites are introduced, the roughness scales with $\beta \neq 1/2$, i.e., it behaves like the trajectory of a particle exhibiting anomalous diffusion [230]. At a system size-dependent crossover time

$$t_x \sim L^z, \tag{4.8}$$

the system leaves the transient and enters the asymptotic regime where the roughness saturates at $W_{sat}(L)$ because ξ has reached the system size, i.e. $\xi = L$. At this point, ξ can not further increase. The interface is now completely correlated and the system has reached a nonequilibrium steady state which is signaled by the fact that the probability distribution of the roughness is now time-independent. Additionally, the saturation value of the roughness scales with system size according to

$$W_{sat}(L) \sim L^{\alpha}. \tag{4.9}$$

In particular, a system with $\alpha > 1$ is called super rough. We now have a set of three scaling exponents, α, β, z which are related to each other via the scaling law

$$z = \frac{\alpha}{\beta}. \tag{4.10}$$

In particular, this scaling law is valid for any growth process for which the interface width obeys the dynamical scaling relation [9, 232]

$$W(L,t) \sim L^{\alpha} f\left(\frac{t}{L^z}\right), \tag{4.11}$$

where $f(t/L^z)$ is a scaling function [9, 235]. This relation, which is also known as the Family-Vicsek scaling relation, allows to check whether an evolving interface obeys dynamical scaling and, is thus, a self-affine object. If it does obey Eq. (4.11), one gets statistically similar interface profiles under an appropriate rescaling of space and time. Because the roughness depends on t through the function $f(t/L^z)$, we require that $t \to b^z t$ if we rescale space according to $x \to bx$, i.e., $L \to bL$, such that the ratio (t/L^z) remains unchanged under the scaling transformation of space. Due to the rescaling of space, we also get $W_{sat}(L) \to b^\alpha W_{sat}(L)$ for the rescaled interface width. On the other hand, the roughness is linear in h. Therefore, the height must be rescaled as $h \to b^\alpha h$. In summary, the scaling relations for space, time and height are given by

$$x \to bx \tag{4.12a}$$

$$t \to b^z t \tag{4.12b}$$

$$h \to b^\alpha h. \tag{4.12c}$$

If an interface is invariant under this rescaling, it is self-affine and can be characterized by the fixed set (α, β, z) of corresponding scaling exponents. This set of scaling exponents allows to classify the phenomenon of surface growth into different universality classes in the exact same manner as it is done for the systems undergoing continuous phase transitions. If different surface growth systems are characterized by the same set (α, β, z), their interfaces are statistically identical and can not be distinguishes from each other under rescaling with these exponents. Then, these systems are said to belong to the same universality class. To give an example, the above mentioned random deposition model represents a trivial universality class (because there are no correlations in the system) characterized by $(\alpha = \infty, \beta = 1/2, z = \infty)$. Thus, if some system exhibits this set of exponents it is said to belong to the random deposition universality class. In the following we will discuss the most important universality classes and corresponding stochastic differential equations (which describe the surface height evolution in the hydrodynamic limit, $L \to \infty$) in the context of surface growth. Specifically, we will relate lattice models to their continuum counterparts based on the values of the corresponding set (α, β, z) of critical exponents.

4.4.2 Lattice models for surface growth and stochastic equations

While surface growth can be easily investigated by means of numerical simulations of discrete lattice models, continuum models are better suited for an analytical treatment. As discussed above, the set of critical exponents (α, β, z) is independent of the particular system under study. In fact, the values of these exponents depend only on fundamental symmetries of the elementary processes that take place on the surface of the system during growth [9, 236]. In particular, solely in the context of continuum theories we can fully understand the strength of the concept of universality classes which allows us to isolate

Universality class	Stochastic partial differential equation
Random deposition (RD):	$\partial_t h(x,t) = \phi(x,t)$
Edwards-Willkinson (EW):	$\partial_t h(x,t) = \nu\nabla^2 h(x,t) + \phi(x,t)$
Kardar-Parisi-Zhang (KPZ):	$\partial_t h(x,t) = \nu\nabla^2 h(x,t) + \frac{\lambda}{2}\left[\nabla h(x,t)\right]^2 + \phi(x,t)$
Mullins-Herring (MH):	$\partial_t h(x,t) = \nu_4\nabla^4 h(x,t) + \phi(x,t)$
Villain-Lai-Das-Sarma (VLDS):	$\partial_t h(x,t) = \nu_4\nabla^4 h(x,t) + \lambda_4\nabla^2\left[\nabla h(x,t)\right]^2 + \phi(x,t)$

Tab. 4.1: Stochastic partial differential equations of the most important universality classes in the context of nonequilibrium surface growth in one spatial dimension, $d = 1$, i.e., for substrates along the x-direction. In all equations, $\phi(x,t)$ represents nonconservative Gaussian white noise, i.e., $\langle\phi(x,t)\phi(x^{'},t^{'}) = 2D\delta^d(x-x^{'})\delta(t-t^{'})$, where d is the dimension of the lattice.

Universality class	α	β	z
Random deposition (RD):	∞	$1/2$	∞
Edwards-Willkinson (EW):	$1/2$	$1/4$	2
Kardar-Parisi-Zhang (KPZ):	$1/2$	$1/3$	$3/2$
Mullins-Herring (MH):	$3/2$	$3/8$	4
Villain-Lai-Das-Sarma (VLDS):	1	$1/3$	3

Tab. 4.2: Critical exponents of the most important universality classes in the context of surface growth in one spatial dimension, $d = 1$

the irrelevant from the relevant physical processes that truly play a role for shaping the observed surface morphologies in nonequilibrium growth processes.

The most important stochastic PDEs (modeled with a co-moving frame such that the increase of surface height due to the flux F of incoming particles can be neglected) which each represent an individual universality class include: Random deposition (RD), the Edwards-Willkinson (EW) equation [237], (c) the Kardar-Parisi-Zhang (KPZ) equation [238], the Mullins-Herring equation [239, 240] and (e) the Villain-Lai-Das-Sarma equation [236]. For the sake of clarity, we list these equations in table 4.1. All these equations represent a unique universality class and exhibit an individual set of critical exponents. In all the equations listed in table 4.1, $\phi(x,t)$ is non-conservative Gaussian white noise, i.e., $\langle\phi(x,t)\phi(x^{'},t^{'}) = 2D\delta^d(x-x^{'})\delta(t-t^{'})$, where d is the system dimension, i.e., the spatial dimension of the lattice onto which particles are deposited. The equations can be constructed based on symmetry principles. In order to extract the unique set of critical exponents for each of these equations, one can solve them or apply symmetry arguments [9]. The critical exponents of the above mentioned continuum models for one spatial dimension, $d = 1$, are given in table 4.2.

Various real growth processes can be described by these equations. For example, the KPZ equation describes growing turbulence of a liquid crystal [241–243], the height fluctuations of the surface of growing bacteria colonies [244], slow combustion of paper [245] and the interface profile of (coffee) stains that are left by a drying liquid drop

containing ellipsoidal particles [246]. The EW equation describes surface growth with a high mobility of adatoms [247], whereas the VLDS equation represents the continuum limit of low-temperature MBE growth [236].

5 Nonequilibrium surface growth with anisotropic interactions

We use event-driven kinetic Monte-Carlo simulations to investigate the early stage of non-equilibrium surface growth in a generic model with a simple form of anisotropic interactions among the adsorbed particles. Specifically, we deposit isotropically shaped particles on a square lattice where they perform activated hopping processes to neighboring lattice sites. The interaction anisotropy between neighboring particles is characterized by a control parameter η which measures the ratio of interaction energy along the two lattice directions. We systematically study the impact of the interaction energy E_B, the control parameter η and the flux rate F on the shape and the fractal dimension D_f of clusters in the pre-coalescence regime. At finite particle flux, i.e., deposition rate, F we observe the emergence of rod-like and needle-shaped clusters whose aspect ratio R depends on the value of η, E_B and F. In the regime of strong interaction anisotropy, the cluster aspect ratio shows power-law scaling as function of particle flux, $R \sim F^{-\alpha}$. Furthermore, the evolution of the cluster length and width also exhibit power-law scaling with universal growth exponents for all values of F. We identify a critical cluster length L_c that signals a transition from one-dimensional to self-similar two-dimensional cluster growth. The cluster properties depend sensitively on the critical cluster size i^* of the isotropically interacting reference system. Additionally, we compare the KMC results to those of an anisotropic EDEN model and find good agreement regarding cluster properties.

5.1 Anisotropic interactions in surface growth

During the nonequilibrium growth process, particles are adsorbed on an initially empty square lattice with an effective adsorption rate F given in monolayer per minute (ML/min). After adsorption on site **a**, they perform activated Arrhenius-type hopping processes **a** $\rightarrow$ **b** to a randomly chosen nearest-neighbor lattice site **b**. The hopping rates $D_{\mathbf{ab}} \sim \exp(-E_A/T)$ depends on the activation energy barrier E_A which involves the three contributions introduced in Eq. (2.51) in Sec. 2.4.2. In a system with isotropic interactions, the contribution to E_A from the interaction to neighboring particles is simply given by nE_B, where E_B is the energy per bond and n the number of bonds. Here we consider anisotropic nearest-neighbor interactions where not only the number n of in-plane bonds, but also their configuration matters. To this end, we define the interaction anisotropy parameter $\eta \in [0, 1]$ which changes the nearest-neighbor interaction energy of in-plane

bonds along the y-axis, $E_B^y = \eta E_B$, relative to that along the x-axis, $E_B^x = E_B$. Thereby, we model a generic feature of anisotropic interactions. The latter are essentially omnipresent not only for conjugated organic molecules, but also for some atomic systems [248–250]. Specifically, our model breaks the global interaction symmetry. In experiments, this situation could be realized by applying an external field which leads to a favored direction for particle-particle bonds. This is similar to symmetry breaking in an Ising model with an external magnetic field where the direction of the field leads to a favored orientation of spins. One important peculiarity of our system is the fact that the particle shape remains isotropic. This allows us to study the impact of anisotropy in the interactions alone, without accounting for steric effects. Clearly, the latter effects are ubiquitous in a lot of realistic anisotropic systems such as films of organic molecules. However, from the simulation perspective, anisotropic particle shapes lead to additional complications such as blocked pathways for hopping processes, overhangs of adsorbed particles and the difficult question how the out-of-plane diffusion of anisotropically shaped particles should be treated [92, 93, 176, 177, 251]. We consider the present simplified model as a first step to the overall goal to better understand the effect of anisotropic interparticle interactions under non-equilibrium growth conditions.

Possible real systems exhibiting features of our model could be organic oligomers on the $(10\bar{1}0)$ surface of a ZnO semiconductor. The surface generates an electric field that induces dipole moments in the adsorbed molecules along the field direction [178], yielding anisotropic dipolar interactions. Anisotropic dipolar interactions occur between partially fluorinated organic molecule such as di-fluorinated para-sexiphenyl (6P-F2) [252]. By Setting $\eta = -1/8$, one can mimics the interaction of parallel aligned neighboring dipoles in our model. The situation with $\eta < 1$ describes systems where a lattice direction of preferred particle attachment exists as it is the case for the growth of elongated and needle-shaped Zn crystals on isotropic surfaces [250] and the growth of Ag clusters on fcc metal (110) surfaces [248, 249]. In principal, both of these systems can be considered with our model.

5.1.1 The KMC model with anisotropic interactions

An exemplary lattice configuration of our model is shown in Fig. 5.1. The total interaction energy of a particle reads $(n_x + \eta n_y)E_B$, where n_x is the number of lateral neighbors along the x-direction and n_y represents the number of neighbors in y-direction. For $\eta = 1$, the model reduces to the isotropic case where the total interaction energy is given by $(n_x + n_y)E_B = nE_B$. In contrast, $\eta < 1$ represents the situation with anisotropic interactions among the adsorbed particles. Specifically, decreasing η leads to an increase

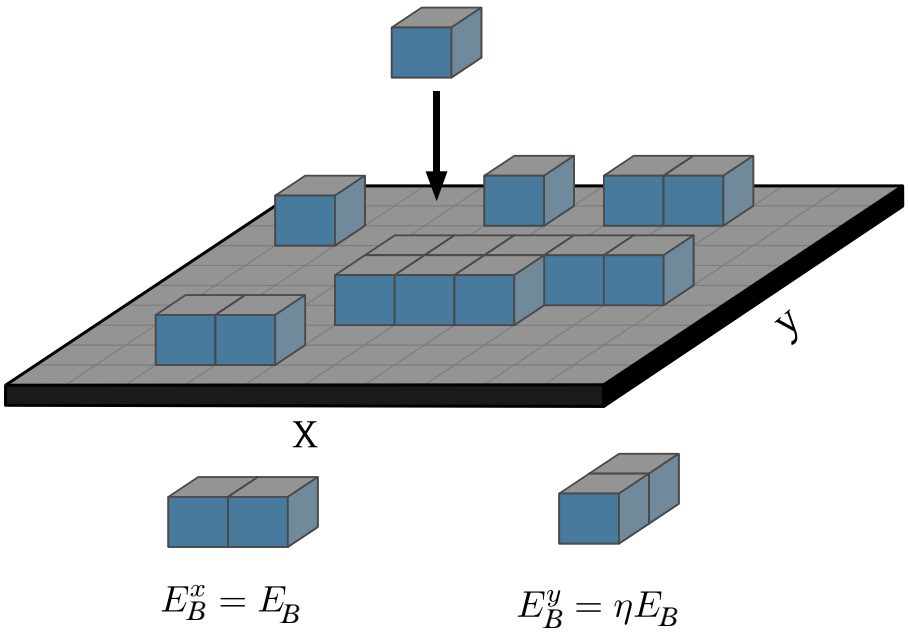

Fig. 5.1: Illustration of our KMC model to study nonequilibrium cluster formation and lateral growth in presence of anisotropic interactions. The in-plane interaction between particles on neighboring lattice sites in x-direction is denoted by $E_B^x = E_B$. The parameter η controls the degree of interaction anisotropy. Interactions are isotropic for $\eta = 1$.For $\eta < 1$, the interaction energy $E_B^y = \eta E_B$ of bonds in y-direction is lowered relative to E_B.

of the interaction anisotropy. The resulting expression for the hopping rate from site **a** to **b** is given according to the Clarke-Vvedensky bond-counting Ansatz [192],

$$D_{\mathbf{ab}} = \nu_0 \exp\left(-\frac{E_A}{k_\mathrm{b}T}\right) = \nu_0 \exp\left(-\frac{E_D + (n_x + \eta n_y)E_B + s_{\mathbf{ab}}E_S}{k_\mathrm{b}T}\right). \tag{5.1}$$

We use the attempt frequency $\nu_0 = 2k_BT/h$, where k_b is the Boltzmann's constant, T the substrate temperature and h the Planck constant. The first term of the activation energy E_A represents the in-plane diffusion barrier E_D. The second one, $(n_x + \eta n_y)E_B$, describes the contribution to E_A that stems from in-plane interparticle bonds and the third term represent the out-of-plane diffusion barrier, i.e., E_S corresponds to the Ehrlich-Schwoebel barrier. The latter leads to a reduced rate for diffusion processes across step-edges (where $s_{\mathbf{ab}} = 1$) by a factor $\alpha = \exp[-E_\mathrm{S}/(k_\mathrm{b}T)]$. The case $s_{\mathbf{ab}} = 0$ corresponds to pure in-plane diffusion of adatoms. The KMC algorithm is explained in Sec. 2.4.3.

For all simulations in this section we use $E_D = 0.5$ eV because this value is a good approximation for various real systems involving organic molecules like C_{60} or atoms like Ag or Pt [171, 253]. We fix the out-of-plane diffusion barrier to $E_S = 0.1$ eV for the same reason. The adsorption rate is varied between $F = 1$ ML/min and $F = 100$ ML/min, while the temperature is kept at $T = 313$ K. The latter value is a commonly used temperature in experimental growth studies with organic molecules [171, 254]. If not stated otherwise, the coverage is fixed to $\theta = 0.05$. We chose such a low coverage to make sure that coalescence of clusters has not yet set in. The simulations are performed

with different values of E_B and η. Thereby, we study the interplay between E_B and η concerning properties of growing clusters in the sub-monolayer growth regime in presence of anisotropic interactions among adsorbed particles.

5.1.2 The Eden model with anisotropic intractions

The KMC algorithm mimics the kinetically driven growth of thin films based on deposition of particles and Arrhenius-type activation energy-dependent hopping processes. One goal here is to compare the KMC results of cluster growth with those from an anisotropic stochastic Eden growth model. The latter is more elementary in the sense that it simulates cluster growth by attachment of particles to existing clusters solely based on attachment probabilities. Thereby one fully neglects the computationally costly hopping processes that usually dominate in KMC simulations, especially under realistic growth conditions [232, 255, 256]. The Eden models thus allows to to investigate to which extend diffusion processes are relevant for the emerging morphology of clusters.

The isotropic Eden model: Within the Eden model, a cluster on the two-dimensional lattice space L^2 is defined as a finite subset $C \in L^2$ of connected, occupied lattice sites. At the boundary of such a cluster, unoccupied sites ∂C that have at least one occupied neighboring site

$$\partial C = \{j \in \mathrm{Z}^2\ C : \exists i \in C \rightarrow \|i - j\| = 1\}, \tag{5.2}$$

represent the full set of growth sites which have a non-zero probability to be occupied in an iteration step of the cluster growth procedure. On a square lattice there exist four different types of nodes $\partial_k C$ where k = 1,2,3,4. Here, k represents the number of occupied neighbor sites. Therefore, the total boundary of a cluster is simply given by $\partial C = \partial_1 C \cup \partial_2 C \cup \partial_3 C \cup \partial_4 C$.

The cluster at the beginning of the simulation, $t_0 = 0$, is a fixed connected set $C_0 \subset Z^2$. In our case, the cluster at t_0 consists of a single occupied site in the middle of the square lattice. Thus, there exist four growth sites in the first iteration step. In each iteration step, $t_n \rightarrow t_{n+1}$, one of the growth sites ∂C is occupied. Thereby, the cluster grows by one lattice site, $C_n \rightarrow C_{n+1}$, and the cluster boundary ∂C changes. Specifically, the probability $p_{\mathbf{a}}$ for particle attachment at boundary site **a** depends on the number $n_{\mathbf{b}}$ of occupied neighbor sites **b**

$$p_i = \sum_{\langle \mathbf{ab} \rangle} n_{\mathbf{b}}. \tag{5.3}$$

Here, $n_{\mathbf{b}} = 1$ if the neighboring site is occupied and $n_{\mathbf{b}} = 0$ if the neighboring site is empty. The sum $\langle \mathbf{ab} \rangle$ is taken over all nearest-neighbors **b** of site **a**. Therefore, only lattice sites **a** with at least one neighboring cluster site have a non-zero probability $p_{\mathbf{a}}$ to be occupied in an iteration step of the cluster growth process.

The anisotropic Eden model: In order to introduce anisotropic interactions to the Eden model, we split the occupation probability $p_{\mathbf{a}}$ for lattice site **a** into two parts corresponding to the x- and y-direction, respectively. We impose an imbalance between these two directions. The anisotropy parameter ξ determines the reduced probability for particles to attach along the y-direction of a cluster [257]

$$p_{\mathbf{a}} = p_{\mathbf{a}}^{x} + p_{\mathbf{a}}^{y} = \sum_{\langle \mathbf{a}\mathbf{b}^{x} \rangle} n_{\mathbf{b}} + \xi \sum_{\langle \mathbf{a}\mathbf{b}^{y} \rangle} n_{\mathbf{b}}. \tag{5.4}$$

Here, $\langle \mathbf{ab}^{\mathrm{x}} \rangle$ denotes neighbors along the x-direction and $\langle \mathbf{ab}^{\mathrm{y}} \rangle$ along the y-direction. Consequently, if $n_{\mathbf{a}} = n_{\mathbf{b}}$ and $\xi < 1$, one gets $p_{\mathbf{a}}^{\mathrm{y}} < p_{\mathbf{a}}^{\mathrm{x}}$. We normalize all probabilities $\tilde{p_{\mathbf{a}}} = p_{\mathbf{a}} / \sum_{\mathbf{b}=1}^{L^2} p_{\mathbf{b}}$ such that $\sum \tilde{p_{\mathbf{a}}} = 1$. All values $\tilde{p_{\mathbf{a}}}$ are saved in a rate catalog. The actual simulation procedure to model the growth of clusters is as follows. In each iteration step, we pick a uniformly distributed random number $r \in [0, 1]$ and choose the site **a** from the rate catalog which is closest to r to be occupied in this iteration step. The attachment anisotropy in the stochastic Eden model mimics the interaction anisotropy in the KMC simulations. Specifically, it results in the formation of elongated clusters for $\xi < 1$ [257]. We use different values for ξ to study the effect of anisotropic interactions on shape clusters in the early stage of thin film growth. The resulting clusters are compared to clusters from the kMC simulations to check whether our minimal model without particle diffusion is able to produce clusters with the same properties.

5.2 Target quantities

Spatial extension of clusters: To study how anisotropic interactions among neighboring particles affect the shape of growing clusters, we calculate the average length L of clusters, i.e., their spatial extension in x-direction, as function of the size S of clusters. The latter is the number of particles a cluster consists of. Further, we calculate the spatial extension in y-direction, i.e. the width W of clusters. From this we get the aspect ratio $R = L/W$ which we calculate for different cluster sizes S as function of the anisotropy parameter $\eta \in [0, 1]$. We average the results over at least 1000 individual clusters for each value of S, E_B and η. Further, we calculate the cluster size distribution $P(S)$ and the cluster length distribution $P(L)$ in order to analyze not only average quantities, but also fluctuations of the cluster shapes.

Fractal dimension of clusters: An additional measure for the cluster morphology is the mass fractal dimension D_f. The latter describes the scaling of the cluster size S (or mass M which would be given by $M = Sm$, where m is the mass of a single particle) with the radius of gyration according to [65, 258–260]

$$S = k_0 (R_g / a)^{D_f}. \tag{5.5}$$

In this equation, the value of the constant pre-factor k_0 (which is of order unity) depends on the cluster shape [258, 259]. Further, R_g is the radius of gyration and a represents the particle radius which we set to $a = 1$. We determine D_f (as function of interaction energy E_B and anisotropy parameter η) via the inertia tensor which, for a cluster formed in the x-y plane and consisting of S particles, is given by [258, 261, 262]

$$\mathbf{T} = \sum_{i=1}^{S} \begin{pmatrix} y_i^2 & -x_i y_i & 0 \\ -x_i y_i & x_i^2 & 0 \\ 0 & 0 & x_i^2 + y_i^2 \end{pmatrix} \tag{5.6}$$

The eigenvalues e_i $(i = 1, 2, 3)$ of $\mathbf{T}$, sorted according to their size $(e_1 \geq e_2 \geq e_3)$, define the square of the principal radii of gyration according to $R_i^2 = e_i/S$. Thus, $R_1 \geq R_2 \geq R_3$. From the quantities R_i, the radius of gyration (given in lattice sites) follows as

$$R_g = \sqrt{\frac{1}{2}(R_1^2 + R_2^2 + R_3^2)}. \tag{5.7}$$

The precise value of the cluster shape-dependent pre-factor k_0 (which accounts for the shape anisotropy of clusters, i.e., their elongation) depends on the ratio of the largest over the smallest squares of principle radii of gyration, that is, $A_{13} = R_1^2/R_3^2$ [258, 263, 264].

Density of clusters: A further important quantity is the density of clusters, $\rho_N = N/L^2$. Here, N is the number of "stable“ clusters on a square lattice consisting of L^2 sites. We calculate the cluster density for different values of the interaction energy E_B and the anisotropy parameter η. Clusters are considered as stable when they rather grow during the simulation by subsequent attachment of particle than dissolve into individual particles again. The latter are called unstable clusters. The distinction between these two types of clusters is typically based on the critical cluster size i^*. The latter defines the largest size of unstable clusters such that clusters of size $S \leq i^*$ dissolve while clusters of size $S > i^*$ grow. In the early stage of nonequilibrium surface growth, the number of stable clusters, and thus, the cluster density ρ_N increases until it saturates at a parameter setting-dependent value ρ_N^c. This maximum value of the cluster density is referred to as the critical cluster density ρ_N^c. According to a rate equation approach [42, 265], ρ_N^c is connected to the critical cluster size i^* via the scaling relation

$$\rho_N^c \sim (D_0(T)/F)^{-\chi}. \tag{5.8}$$

Here, $\chi = i^*/(i^* + 2)$ and $D_0(T) = \nu_0 \exp(-E_D/k_\mathrm{b}T)$ corresponds to the rate for free particle diffusion on a substrate at temperature T and F is the deposition rate. We are particularly interested in the critical cluster size i^* of the systems with isotropic interactions $(\eta = 1)$ for different values of the interaction energy E_B. We take these isotropic systems as *reference* systems since the precise value of i^* in the isotropic systems has a characteristic impact on the cluster shape properties in presence anisotropic interactions, i.e., when $\eta < 1$.

The critical cluster size and reversible versus irreversible cluster growth: The general procedure to determine i^* in the isotropically interacting reference systems is as follows. First, ρ_N^c is calculated for different values of $\Gamma = D_0(T)/F$ by varying the temperature T. We then choose i^* such that the scaling according to E. (5.8) follows the scaling of the critical cluster density ρ_N^c from KMC simulations. When $i^* = 1$ ($\chi = 1/3$), already dimers represent stable clusters which do not decay. In this case, the critical cluster density scales as $\rho_N^c \sim \Gamma^{-1/3}$. In other words, the case $i^* = 1$ corresponds to *irreversible* attachment, where particles become immediately immobilized for the rest of the growth process once they form at least one in-plane bond to a neighboring particle. In contrast to this, when $i^* > 1$, particle attachment is *reversible* in the sense that particles may detach from clusters, further diffuse on the surface until they attach again to the same or some other cluster on the lattice. In this case $\chi < 1/3$, and consequently, ρ_N^c scales differently compared to the situation where $i^* = 1$. A major problem with this procedure is that we need to perform simulations at various different values of Γ to obtain the best fit for the scaling of ρ_N^c that determines i^* when T, or F are varied. However, often we are interested only in whether cluster growth is *reversible* or *irreversible* at a specific value of Γ.

As an estimate to decide whether cluster growth is reversible or not, we calculate the sum of all hopping events at all time steps $t_0, t_1, t_2, .., t_{f-1}, t_f$ [with $t_{n+1} = t_n + \tau$, see Eq. (2.55)] of the KMC simulations. In this time series $t_0 = 0$ corresponds to the empty lattice at the start of a simulation, while t_f corresponds to the simulation time at the end of the simulation when the final coverage of $\theta = 0.05$ has been reached. In each iteration step $t_n \to t_{n+1}$ where a particle performs a hopping event, we distinguish between free particle hopping (i.e., hopping when $n = 0$) with rate $D_{\mathbf{ab}} \sim \exp(-E_D/k_\mathrm{b}T)$ (denoted as r^0) and hopping processes of particles which have at least one in-plane bond ($n > 0$) with rate $D_{\mathbf{ab}} \sim \exp(-(E_D + nE_B)/k_\mathrm{b}T)$ (denoted as $r^{>0}$). We then calculate the sum R_0 of all hopping events r^0 with $n = 0$ and the sum $R_{>0}$ of all hopping events $r^{>0}$ of particles with $n > 0$ during the entire simulation run. Specifically, R_0 and $R_{>0}$ are defined as

$$R_0 = \sum_{t=t_0}^{t_f} r^0(t), \qquad r^0(t) = \begin{cases} 1, & n = 0 \\ 0, & n > 0 \end{cases} \tag{5.9}$$

$$R_{>0} = \sum_{t=t_0}^{t_f} r^{>0}(t), \qquad r^{>0}(t) = \begin{cases} 1, & n > 0 \\ 0, & n = 0. \end{cases} \tag{5.10}$$

Here, n is the number of in-plane bonds of the particle that performed a hopping process at time t_n. From these two sums, we calculate the quantity

$$\omega_1 = \frac{R_{>0}}{R_0}. \tag{5.11}$$

This quantity measures the ratio between the total number of hopping events of free particles and the total number of hopping events of particles with in-plane bonds. If

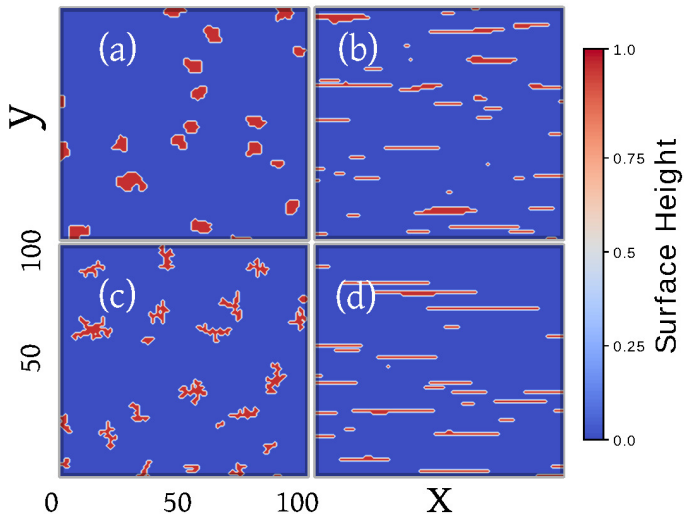

Fig. 5.2: Exemplary surface configurations at coverage $\theta = 0.05$, $T = 313$ K, $F = 1$ ML/min. In (a) and (b) the interaction energy is $E_B = 0.2$ eV. In (a), interactions are isotropic ($\eta = 1$), while in (b) they are strongly anisotropic ($\eta = 0.1$). The configurations in (c) and (d) are obtained from simulations with the same parameters but with higher interaction energy, $E_B = 0.7$ eV.

cluster growth is *irreversible* ($i^* = 1$), no detachment events occur. Thus, $R_{>0} = 0$ and consequently $\omega_1 = 0$. In contrast, non-zero values of ω_1 ($R_{>0} > 0$) indicate the presence of detachment events or, in turn, *reversible* cluster growth ($i^* > 1$). This method does not allow a precise determination of the exact of value of i^*, but it is sufficient to distinguish between the cases $i^* = 1$ and $i^* > 1$. We will use the quantity ω_1 to differentiate between *irreversible* or *reversible* cluster growth conditions in the isotropically interacting reference systems, i.e., the systems where $\eta = 1$.

5.3 Results

In the following, we present KMC simulation results of the nonequilibrium surface growth model with anisotropic interactions. Here, interaction energies ranging from $E_B = 0.1$ eV to $E_B = 3.0$ eV and interaction anisotropies $\eta \in [0, 1]$ are used. We first focus on $E_B = 0.2$ eV and $E_B = 0.7$ eV together with $\eta = 1$ (isotropic interactions) and $\eta = 0.1$ (strongly anisotropic interactions). We chose these two values of E_B because with isotropic interactions, $E_B = 0.7$ eV represents a reference system with $i^* = 1$, whereas at $E_B = 0.2$ eV, the critical cluster size $i^* = 2$ according to the power-law behavior of ρ_N^c. Therefore, with $\eta = 1$, $T = 313$ K and $F = 1$ ML/min, these two values of E_B exemplary represent a setup of the model where cluster growth is *irreversible* and *reversible*.

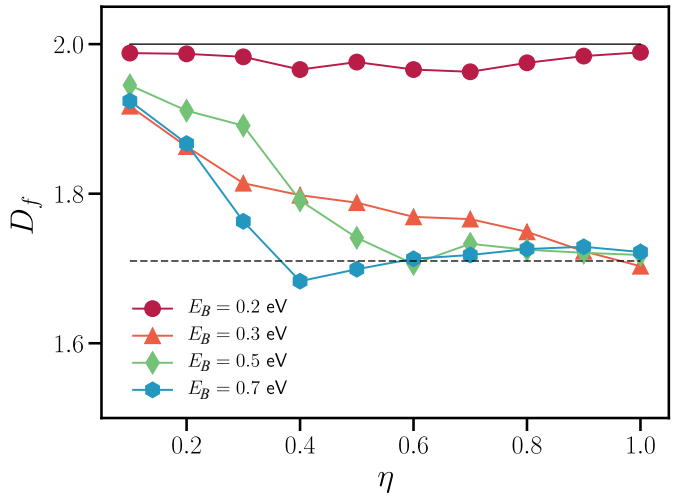

Fig. 5.3: Fractal dimension D_f of clusters for different values of the interaction energy E_B as function of the interaction anisotropy parameter η. The solid line corresponds to the dimension of compact two-dimensional objects, $D_f = 2$, while the dotted line represents the fractal dimension of DLA clusters in two dimensions, $D_f = 1.71$.

5.3.1 Spatial configurations and cluster shapes

Spatial configurations and fractal dimension of clusters: As a starting point, we present surface snapshots in the sub-monolayer growth regime at $\theta = 0.05$ ML for $E_B = 0.2$ [Fig. 5.2 (a) and (b)] and $E_B = 0.7$ [Fig. 5.2 (c) and (d)] eV for isotropic ($\eta = 1$) and strongly anisotropic ($\eta = 0.1$) growth conditions at $T = 313$ K and $F = 1$ ML/min. While at $\eta = 1$ the clusters have compact shapes for $E_B = 0.2$ eV, they are strongly ramified for the much stronger interaction energy $E_B = 0.7$ eV. This can be explained via the corresponding values of i^*. At $E_B = 0.2$ eV, $i^* = 2$ ($\chi = 1/2$). This implies *reversible* particle attachment, i.e., particles with only one lateral bond may detach from clusters in order to attach to cluster boundary sites with a higher coordination number. This leads to compact clusters with $D_f \approx 2$ as shown in Fig. 5.3 where D_f versus η is plotted for different values of E_B. We observe that, at $E_B = 0.2$ eV, D_f is not affected by anisotropic interactions and remains close to $D_f \approx 2$ for all values of η. In contrast, at $E_B = 0.7$ eV, particle attachment is *irreversible*, $i^* = 1$ ($\chi = 1/3$). This leads to ramified cluster shapes and already one lateral bond is enough to suppress detachment. Specifically, we find that, at isotropic growth conditions, the fractal dimension in this case is $D_f \approx 1.7$ (as it is also the case for $E_B = 0.3$ eV and $E_B = 0.5$ eV). The latter value is close to the fractal dimension of clusters grown by diffusion-limited aggregation (DLA), $D_f = 1.71$. [266–270].

We observe that strong interaction anisotropy leads to a visible elongation of clusters in x-direction (i.e., the direction of strong in-plane interaction energy) for both considered values of E_B. Moreover, one clearly sees in Fig. 5.2 that clusters at $E_B = 0.7$ eV are stronger elongated and have a smaller width W compared to clusters at $E_B = 0.2$ eV. This suggests a stronger impact of interaction anisotropy on cluster shapes at higher

E_B. Further, strong interaction anisotropy removes the ramified structure of clusters at $E_B = 0.7$ eV, yielding elongated but compact clusters with smooth boundaries. This is confirmed in Fig. 5.3 where one sees that upon decreasing η from 1, D_f (at $E_B = 0.7$ eV) remains unaffected up to $\eta = 0.4$. However, for $\eta < 0.4$, the fractal dimension steadily increases until it approaches $D_f \approx 2$ for $\eta \to 0$. Further below in this section we give an explanation for the E_B-dependent value of η where D_f starts to increase from $D_f \approx 1.7$. The emergence of elongated clusters reveals an imbalance between attachment and detachment rates of bonds in x- and y-direction, respectively. This is understandable from the fact that, for $\eta < 1$, the hopping rate $D_{\mathbf{ab}}$ [see Eq. (2.51)] of particles with a bond in y-direction only is higher compared to particles with a bond in x-direction because at $\eta < 1$, $\eta E_B = E_B^y < E_B^x$.

In summary, we find that as η is decreased from 1, clusters become elongated for any value of the interaction energy E_B. At sufficiently large interaction energy ($E_B \leq 0.3$ eV), one obtains DLA clusters at isotropic growth conditions. At $E_B \leq 0.2$ eV, $D_f \approx 2$ holds for any value of η. Different from that, at $E_B \geq 0.3$ eV, the fractal dimension reveals a pronounced increase from $D_f \approx 1.7$ (corresponding to the DLA universality class) to $D_f \approx 2$ as $\eta \to 0$.

Distributions of the cluster size and length: There is not only an impact of interaction anisotropy on the distributions of the length L and width W of clusters, but also on their sizes S as shown in Fig. 5.4. For $\eta = 1$ and $E_B = 0.2$ eV, S is equally distributed around the mean value $S \approx 30$. The peak vanishes at $\eta < 0.4$ and $P(S)$ becomes flat for $S \geq 20$. Then, $P(S)$ peaks at $S < 5$. This reflects a mixture of a few large and many very small clusters on the substrate. Thus, the presence of interaction anisotropy leads to a completely different composition of cluster sizes on the lattice compared to the isotropic case. The detachment rate of particles with bonds in y-direction increases as η is decreased. Consequently, less stable clusters are formed on the substrate at $\theta = 0.05$ only a few clusters have reached the critical cluster size to become stable. The situation is different at $E_B = 0.7$ eV where upon decreasing η from $\eta = 1$ to $\eta = 0.4$ does not affect $P(S)$. Only for $\eta < 0.4$, the peak of $P(S)$ shifts from $S \approx 25$ to $S \approx 20$ which reflects only a marginal change in the cluster size distribution. Further, $P(S)$ becomes narrower and clusters of size $S > 40$ vanish. The majority of clusters still has an intermediate size of $S \approx 20$. This value is quite similar to the cluster size at isotropic growth conditions.

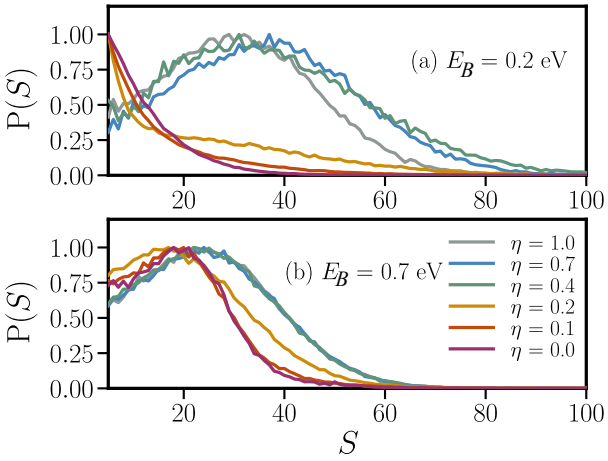

Fig. 5.4: Distribution $P(S)$ of the cluster size S at interaction energy $E_B = 0.2$ eV (a) and $E_B = 0.7$ eV (b) and various values of the anisotropy parameter η ranging from isotropic conditions ($\eta = 1$) to $\eta = 0$ (no interaction energy for bonds along the y-direction). Here and in the following figures, temperature T and adsorption rate F are chosen as in Fig. 5.2.

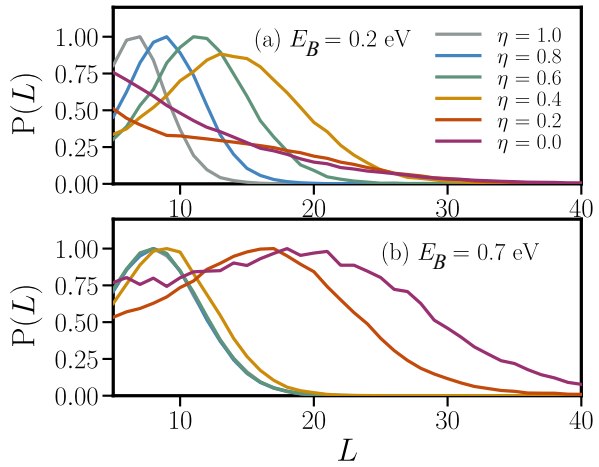

Fig. 5.5: Distribution $P(L)$ of the cluster length L at $E_B = 0.2$ eV (a) and $E_B = 0.7$ eV (b) and various values of the anisotropy parameter η ranging from isotropic to totally anisotropic ($\eta = 0$) interactions.

Additionally, the normalized cluster length distribution $P(L)$ is shown in Fig. 5.5. At $E_B = 0.2$ eV, the peak in $P(L)$ is shifted to larger values of L and is slightly broadening as η is decreased from 1. This reflects the cluster elongation process which continues until $\eta = 0.4$. For $\eta < 0.4$, i.e., stronger interaction anisotropy, we observe a peak at very small L, consistent with the results in Fig. 5.4. At $E_B = 0.7$ eV, the $P(L)$ is not affected as η is decreased from 1 to $\eta = 0.4$. Only if $\eta < 0.4$ the peak in $P(L)$ is shifted towards larger lengths L and $P(L)$ broadens.

Average shapes of clusters: Let us now focus in more detail on the response of average cluster shapes upon different strengths of the interaction anisotropy. To this end we present in Fig. 5.6 average cluster shapes for $S = 40$ at $E_B = 0.2$ [see Fig. 5.6(a)-(c)] and $E_B = 0.7$ eV [see Fig. 5.6(d)-(f)] for three different values of η. As expected, for

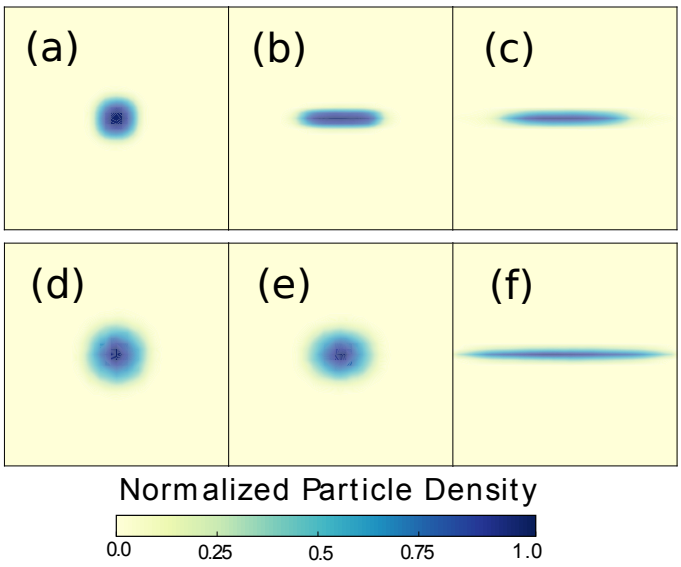

Fig. 5.6: Average shapes of clusters of size $S = 40$ for different values of η and E_B. The two values for E_B considered are $E_B = 0.2$ eV (a)-(c) and $E_B = 0.7$ eV (d)-(f). The parameter η is reduced from isotropic interactions ($\eta = 1$) to 0.7, and 0.1.

$\eta = 1$ the average shape is isotropic at both interaction energies. By decreasing η from 1 at $E_B = 0.2$ eV, the average clusters become immediately elongated along the direction of stronger interaction energy. Thus, already relatively weak interaction anisotropy ($\eta = 0.7$) leads to anisotropic cluster shapes. We conclude that at $E_B = 0.2$ eV there is a gradual cluster shape transformation as function of decreasing η. For strong interaction anisotropy, such as $\eta = 0.1$, we observe strongly elongated clusters whose average shape [see Fig. 5.6(c)] matches quite good with the individual clusters of a random growth simulation as shown in Fig. 5.2(b). At $E_B = 0.7$ eV we encounter a different behavior of the cluster shape transformation. First, decreasing η from 1 to $\eta = 0.4$ has essentially no impact on the initially isotropic shape. Second, at $\eta = 0.1$, the clusters are much stronger elongated compared to the case $E_B = 0.2$ eV. This is in good agreement with the spatial configurations shown in Fig. 2(b) and (d). We conclude that there are two types of the cluster shape transformation, that is, gradual ($E_B = 0.2$ eV) versus sharp ($E_B = 0.7$ eV).

To further illustrate that the type of the cluster shape transformation depends on the interaction energy E_B, we plot the average length L and width W of clusters of size $S = 40$ as function of η in Fig. 5.7. We observe, consistent with anisotropic cluster growth, an immediate splitting of L and W at $E_B = 0.2$ eV which means that L and W grow at different rates. The smooth behavior of the splitting of L and W as function of η at $E_B = 0.2$ eV confirms a gradual cluster shape transformation. In contrast, decreasing η from 1 at $E_B = 0.7$ eV leaves L and W identical up to $\eta = 0.4$. Only for $\eta < 0.4$ we observe a splitting, which, in agreement with the results shown in Fig. 5.2 and Fig. 5.6, is much stronger pronounced compared to $E_B = 0.2$ eV. Therefore the cluster shape transformation is sharp at values of E_B where growth is irreversible at $\eta = 1$.

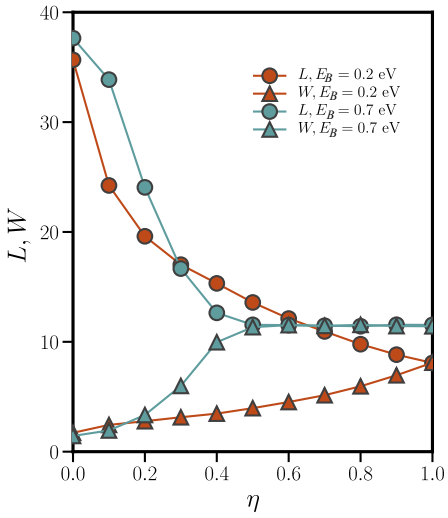

Fig. 5.7: Evolution of the cluster length L and width W at $E_B = 0.2$ eV and $E_B = 0.7$ eV as function of η. The considered clusters are of size $S = 40$. The evolution of L and W as η is decreased from 1 confirms the gradual shape transformation at $E_B = 0.2$ eV and the sharp shape transition at $E_B = 0.7$ eV.

Energy considerations of compact equilibrium clusters: Let us now discuss these results from the perspective of a simple model based on energy minimization. Indeed, for growth conditions close to equilibrium, one would expect that the cluster shapes are simply related to the total energy cost E_{bb} to form a compact cluster. For a compact cluster of size $S = LW$ (with length L and width W), the value of E_{bb} is determined by the total number of cluster boundary sites which corresponds to the energy of all broken bonds

$$E_{bb} = 2WE_B + 2L\eta E_B. \tag{5.12}$$

For a compact cluster of size S, the width is given by $W = S/L$. This allows us to rewrite Eq. (5.12) as

$$E_{bb} = 2E_B(S/L + \eta L), \tag{5.13}$$

From this we find that E_{bb} reaches the minimum value when the cluster length fulfills

$$L(S, \eta) = \sqrt{S/\eta}. \tag{5.14}$$

This equation provides an estimate for the cluster length evolution in presence of anisotropic interactions at growth conditions where particle detachment is possible (i.e., $i^* > 1$) such that clusters can obtain the equilibrium shape. We find that Eq. (5.14) indeed nearly perfectly describes L at small adsorption rates F ($F = 1$ ML/min in Fig. 5.8) and low interaction energies E_B, i.e., under conditions where detachment is possible.

This is shown in Fig. 5.8 where the cluster length L_{40} (of clusters of size $S = 40$) as function of η is plotted for different values of E_B at $F = 1$ ML/min. Consider, as an example, the value $E_B = 0.15$ eV. Here, the rate for breaking lateral bonds (of particles

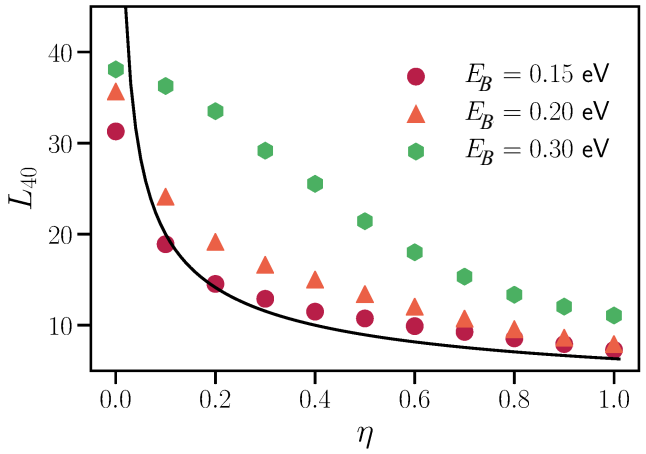

Fig. 5.8: Length L_{40} of clusters of size $S = 40$ as function of the interaction anisotropy parameter η for different interaction energies E_B at $F = 1$ ML/min. The solid black line corresponds to the length $L(S, \eta) = \sqrt{S/\eta}$ for growth close to equilibrium [see Eq. (5.14)].

with one nearest-neighbor) is high enough in both lattice directions such that clusters retain a compact shape. Consequently, L_{40} follows closely to the length predicted by Eq. (5.14) in the range $0.1 \leq \eta \leq 1.0$ (see the black line in Fig. 5.8). In contrast, at $E_B = 0.3$ eV, clusters (at $\eta = 1$) are ramified, $D_f \approx 1.7$ (see Fig. 5.3), which means that they do not exhibit the compact equilibrium shape. As a consequence, we observe large deviations from the equilibrium length predicted by Eq. (5.14). Taken together, these results show that energetic arguments to describe the cluster shapes only hold at growth conditions where particle detachment (i.e., $i^* > 1$) is possible for any value of η.

5.3.2 One-dimensional vs. two-dimensional cluster growth

Evolution of the average cluster length: Let us now focus on the dynamical evolution of cluster shapes during the growth process. Figure 5.9 shows the average cluster length $L(S)$ as function of S for $E_B = 0.2$ eV and $E_B = 0.7$ eV and different values of η. At $E_B = 0.2$ eV and isotropic interactions, $L(S)$ approximately follows the prediction from energy arguments [see Eq. (5.14)], i.e. $L = \sqrt{S}$. In contrast, at $E_B = 0.7$ eV and $\eta = 1$, we observe significant deviations because clusters are ramified and do not exhibit the compact equilibrium shape [see Fig. 5.2(c)]. If $\eta < 1$, we observe an immediate effect on $L(S)$ at $E_B = 0.2$ eV. This is consistent with the results presented above and it confirms a gradual cluster shape transformation. In contrast, at $E_B = 0.7$ eV, $L(S)$ remains unaltered for $\eta \geq 0.4$. This confirms again that at high interaction energy weak interaction anisotropy has far less impact on the cluster shape than at low interaction energies. As η is decreased, one observes a transition to a linear relation $L(S) = S$ (see the dotted line in Fig. 5.9) for small cluster sizes S. The line $L(S) = S$ represents maximally elongated, one-dimensional clusters which grow in the direction of the strong bonds only. This refer to this growth mode as *one-dimensional growth*. At $E_B = 0.7$ eV and $\eta = 0.1$, $L(S)$ growth

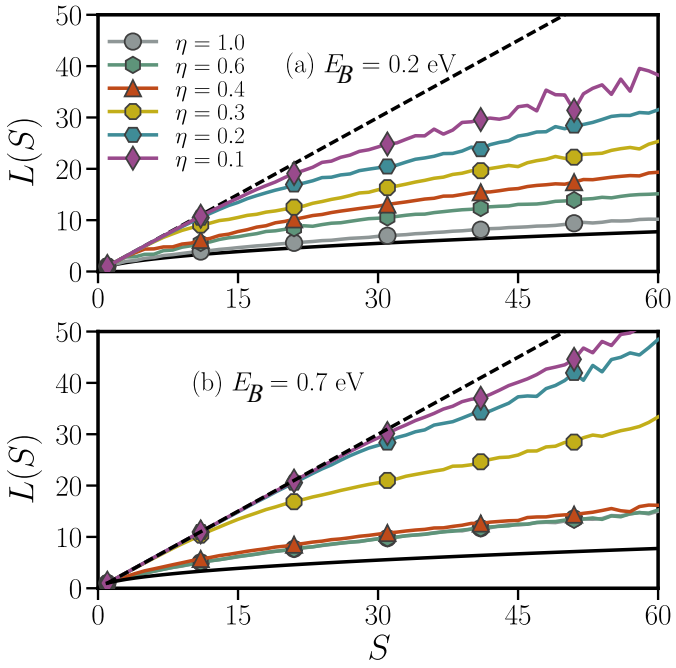

Fig. 5.9: Average cluster length $L(S)$ as function of the cluster size S for interaction energy $E_B = 0.2$ eV (a) and $E_B = 0.7$ eV (b) and different values of η. The solid line represents $L(S) = \sqrt{S}$, while the dotted line corresponds to $L(S) = S$.

is one-dimensional up to $S \approx 30$. In contrast, at $E_B = 0.2$ eV and $\eta = 0.1$, $L(S)$ begins to deviate from $L(S) = S$ already at $S \approx 10$. Therefore, one-dimensional cluster growth is more robust at high interaction energy.

We conclude that in presence of strong anisotropic interactions, the initial stage of cluster growth appears to be one-dimensional. This growth mode breaks down at a specific cluster length L_c (or size) which depends on E_B and η. Specifically, L_c is defined as the length where $|L(S) - S| \geq 1$ sets in as cluster growth proceeds. The value of L_c increases with increasing E_B, resulting in stronger elongated clusters at high interaction energy

The breakdown of the one-dimensional cluster growth mode: In Fig. 5.10, $L_c(\eta)$ as function of η is plotted for different values of E_B. Irrespective of E_B, $L_c(\eta)$ increases as η is decreased from 1 and converges to a finite value in the limit $\eta \to 0$. Specifically, in the range $E_B \geq 0.3$ eV, L_c converges to similar values $L_c(0) = L_c^0 \approx 35$. In contrast, at $E_B < 0.3$ eV, L_c^0 depends on E_B, e.g. $L_c^0 \approx 25$ at $E_B = 0.2$ eV and $L_c^0 \approx 18$ at $E_B = 0.15$ eV. Further, we observe that, at $E_B \leq 0.3$ eV, the increase of L_c as function of η is smooth and sets in already at weak interaction anisotropy. In contrast, at $E_B > 0.3$ eV, L_c remains essentially unaffected by weak interaction anisotropy. Figure 5.10 also shows $L_c(\eta)$ resulting from energy considerations (see Eq. (5.14)). We observe that this function yields a reliable estimate for small values of E_B (consistent with the discussion of L_{40} in Fig. 5.8).

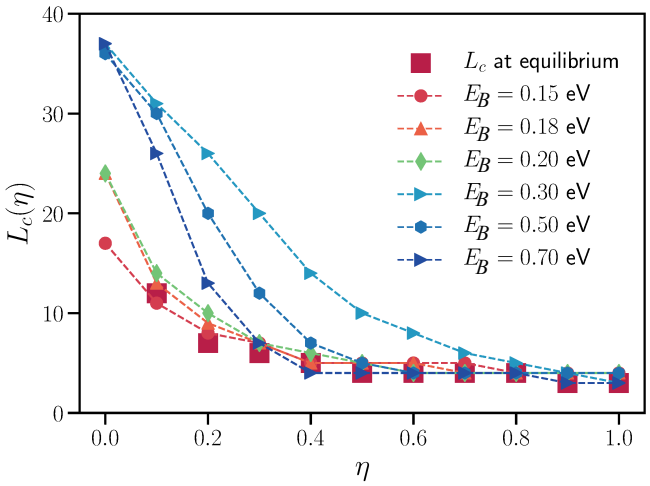

Fig. 5.10: Critical length $L_c(\eta)$ for various values of E_B as function of η. For comparison, we have included the corresponding critical length from equilibrium energy considerations [see Eq. (5.14)].

Transition to two-dimensional self-similar cluster growth: To better characterize the growth mode that follows the one-dimensional cluster growth, we calculate the average aspect ratio $R(S) = L(S)/W(S)$, where $W(S)$ is the cluster width. An aspect ratio R that remains constant as function of S implies self-similar cluster growth. This means that $L(S)$ and $W(S)$ increase at constant rates. Fig. 5.11 (a) shows $R(S)$ for $\eta \leq 0.4$ and different values of E_B. After a linear increase, corresponding to one-dimensional cluster growth, the aspect ratio $R(S)$ reaches a plateau and remains constant as S further increases. We call this saturation value R^{sat}. A saturation value $R^{sat} = 1$ would correspond to isotropic self-similar growth without preferred growth direction, i.e., $L(S) = W(S)$. For $R^{sat} > 1$, clusters are elongated, i.e., $L(S) > W(S)$, but growth is still self-similar. Such a plateau exists for all considered combinations of E_B and η. Only the actual value of R^{sat} and the cluster size S, where the plateau is reached, depends on the values of E_B and η. In addition, R^{sat} is plotted for various values of E_B as function of η in Fig. 5.11(b). For $E_B \geq 0.3$ eV, R^{sat} converges to similar values as $\eta \to 0$. The onset of anisotropic self-similar growth is shifted to smaller values of η as E_B is increased. Furthermore, we observe that for $E_B < 0.3$ eV, R^{sat} is lower compared to the value of R^{sat} we found for $E_B \geq 0.3$ eV.

5.3.3 The role of the critical cluster size i^*

A major observation in presence of anisotropic interactions is the existence of two types of cluster shape transformation as discussed above. It turns out that this can be explained by properties of the isotropic reference systems ($\eta = 1$). To this end, we take a closer look at the critical cluster size i^* at $\eta = 1$ as function of E_B. For this purpose, the critical cluster density ρ_N^c is plotted as function of E_B at $\eta = 1$ in Fig. 5.12. We recall that $\rho_N^c \sim (D_0(T)/F)^{-\chi}$ [with $\chi = i^*/(i^* + 2)$]. As can be seen in Fig. 5.12, ρ_N^c increases as

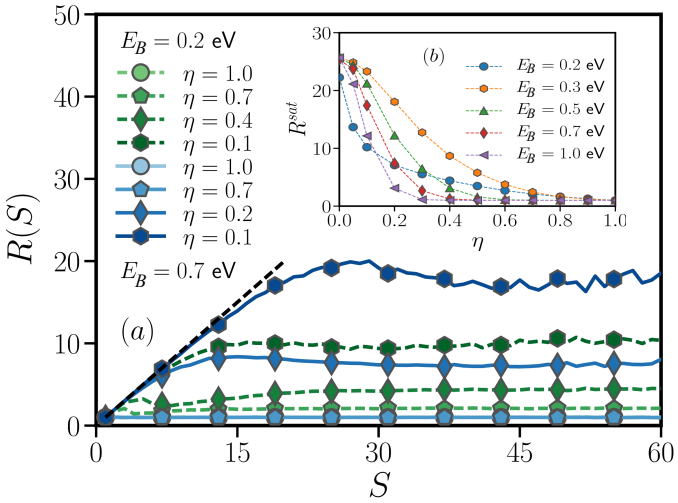

Fig. 5.11: (a) Evolution of the average aspect ratio $R(S) = L(S)/W(S)$ as function of cluster size S at $E_B = 0.2$ eV (greens) and $E_B = 0.7$ eV (blues) at different values of η. The black dotted line corresponds to $R(S) = S$. (b) Saturation value $R^{sat}(\eta)$ for various interaction energies E_B

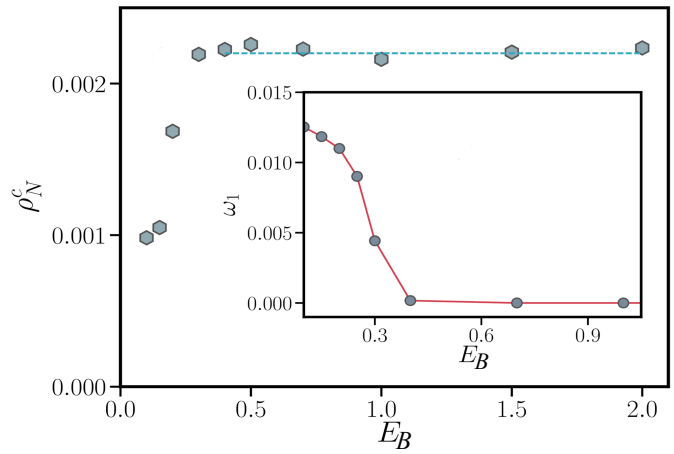

Fig. 5.12: Critical cluster density ρ_N^c for different values of E_B in the (isotropic, i.e., $\eta = 1$) reference system. The inset shows the detachment ratio ω_1 as function of E_B.

E_B is increased from $E_B = 0.1$ eV to $E_B = 0.3$ eV, but saturates for $E_B > 0.3$ eV. Since we do not change the temperature T and adsorption rate F, it follows from the known scaling of ρ_N^c [271–274] that i^* has to be identical for $E_B > 0.3$ eV. Therefore, the critical cluster size $i^* = 1$ in this regim where bonds are *irreversible*.

This is confirmed by the analysis of $\omega_1(E_B)$ [see Eq. (5.11)] at $\eta = 1$ (see the inset of Fig. 5.12). We find, $\omega_1 = 0$ for $E_B > 0.3$ eV, which means absence of particle detachment (i.e., bonds are *irreversible*). In other words, already dimers form stable clusters and $i^* = 1$. As E_B is decreased, ω_1 becomes nonzero, which means that bonds become *reversible* (i.e., particles can break bonds and detach from clusters). Consequently, one enters the regime where $i^* > 1$. We conclude that, coming from high interaction energies, there is a transition from *irreversible* to *reversible* bonds at $E_B \approx 0.3$ eV. This observation allows to explain

the type and the onset of the cluster shape transformation in presence of anisotropic interactions. In particular, we can distinguish between three different scenarios.

• $E_B > 0.3$ *eV and* $\eta = 1$*:* In this case, bonds are *irreversible* in both lattice directions. As a consequence, cluster growth is isotropic for any $E_B > 0.3$ eV (see inset of Fig. 5.11 at $\eta = 1$ where $R^{sat} = 1$ at $\eta = 1$ is shown).

• $E_B > 0.3$ *eV and* $\eta < 1$*:* In this situation, bonds in x-direction are *irreversible*. As long as $E_B^y = \eta E_B > 0.3$, also bonds in y-direction are *irreversible*. Therefore, cluster growth is isotropic even for $\eta < 1$ (as long as $E_B^y > 0.3$ eV). However, as soon as $E_B^y = \eta E_B < 0.3$, bonds in y-direction become *reversible* while bonds in x-direction remain *irreversible*. As a consequence, anisotropic cluster growth sets. For example, at $E_B = 0.5$ eV, we find the onset of the transformation at $\eta = 0.6$, which corresponds to $E_B^y = 0.3$ eV. The same holds at $E_B = 1.0$ eV, where we find the onset at $\eta = 0.3$, which again corresponds to $E_B^y = 0.3$ eV. This explains, depending on E_B, the sharp cluster shape transformation and the precise value η where it sets in.

• $E_B < 0.3$ *eV and* $\eta \leq 1$*:* Here, bonds in both, x- and y-direction are *reversible*. At $\eta = 1$, isotropic, compact clusters grow because there is no imbalance between the bond strengths, i.e., $E_B^x = E_B^y$. In contrast to the scenario above, clusters become elongated for any $\eta < 1$ because growth is *reversible* for any η. Even though bonds in x-direction are *reversible*, the detachment rate for bonds in y-direction is higher at $\eta < 1$. Therefore, clusters growth is anisotropic with growth preferred in x-direction. The cluster shape transformation is gradual because we are always in the regime where bonds are *reversible*. Moreover, we can also explain why both, L_c and R^{sat} converge to similar values for $E_B \geq 0.3$ as $\eta \to 0$ (see Fig. 5.10 and Fig. 5.11). In this case, $E_B^y = 0$. Therefore, all setups with $\eta = 0$ are identical in the sense that bonds in x-direction are *irreversible* while bonds in y-direction are not present at all. The hopping rate for particles with lateral neighbors in y-direction only is the same as for free particles, $D_{\mathbf{ab}} \sim \exp(-E_D/k_\mathrm{b}T)$. At $\eta = 0$ their is no contribution to the activation energy barrier E_A from bonds y-direction. Consequently, $L_c(0)$ and $R^{sat}(0)$ are essentially identical for $E_B \geq 0.3$ eV.

5.3.4 The impact of the adsorption rate F on cluster properties

So far, we have focused on the interplay between the interaction energy E_B and the interaction anisotropy η at fixed deposition rate, $F = 1$ ML/min. Usually, the values of E_B and η are fixed in experimental studies. The parameter which can be precisely varied in experiments (next to the temperature T) is the adsorption rate F. This parameter has indeed a profound impact since it determines not only the cluster shape and density, $\rho_N \sim 1/F$, but also the thin film morphology in the multilayer growth regime as it is

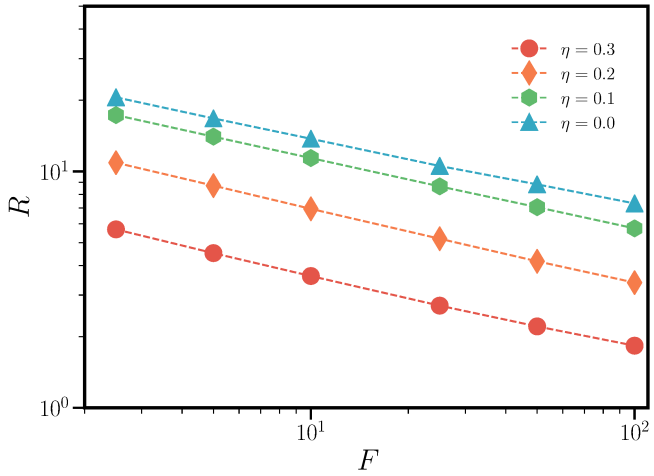

Fig. 5.13: Double logarithmic plot of the average aspect ratio $\langle R \rangle$ at $\theta = 0.1$ and $E_B = 0.5$ eV as function of adsorption rate F in the regime of strong interaction anisotropy.

well known for atomic systems [275–279]. Motivated by this, we study the impact of the adsorption rate F in presence of anisotropic interactions between adsorbed particles.

First, we consider the scaling of the average aspect ratio $\langle R \rangle$ as function of F in the regime of strong interaction anisotropy, $\eta \leq 0.3$ at $\theta = 0.1$. Second, we focus on the evolution of the average cluster length $\langle L \rangle$ and width $\langle W \rangle$ as function of θ in the pre-coalescence regime.

We observe that $\langle R \rangle$ exhibits power-law scaling, $\langle R \rangle \sim F^{-\alpha}$, with $\alpha \approx 0.3$. This is shown in Fig. 5.13 where $\langle R \rangle$ is plotted as function of F at $E_B = 0.5$ eV and $\eta \leq 0.3$ eV. Interestingly, the scaling exponent $\alpha \approx 0.3$ is constant for $\eta \leq 0.3$ at all analyzed interaction energies from $E_B = 0.2$ eV to $E_B = 0.7$ eV.

The evolution of $\langle L \rangle$ as function of θ at $E_B = 0.5$ eV and $\eta = 0.3$ for different values of F is plotted in Fig. 5.14(a). We observe power-law scaling of $\langle L \rangle$ with exponent g_L. The latter exponents is nearly constant for all considered values of the adsorption rate F. We further found that the power-law scaling holds for any value of the interaction energy in the range from $E_B = 0.2$ eV to $E_B = 0.7$ eV. Figure 5.14(b) reveals that g_L increases from $g_L = 0.5$ to $g_L \approx 0.75$ as η is decreased from $\eta = 0.6$ to $\eta = 0$. However, g_L remains constant for different adsorption rates F. Different from the behavior of g_L, the power-law exponent g_W which describes the cluster width evolution decreases for decreasing η. Again, g_W is nearl constant for all values of F as shown in Fig. 5.14(c). Moreover, we find that, as long as cluster growth is isotropic, the scaling exponents are given by $g_L \approx g_W \approx 0.5$. These values are consistent with those observed during domain growth in the random-field Ising model with isotropic interactions (RFIM-DI) [280] and the Axial Next-Nearest-Neighbor Ising Model (ANNNI) [281]. When anisotropic interactions are introduced in the RFIM-DI and the ANNNI, the scaling exponents become different along the x- and y-direction,

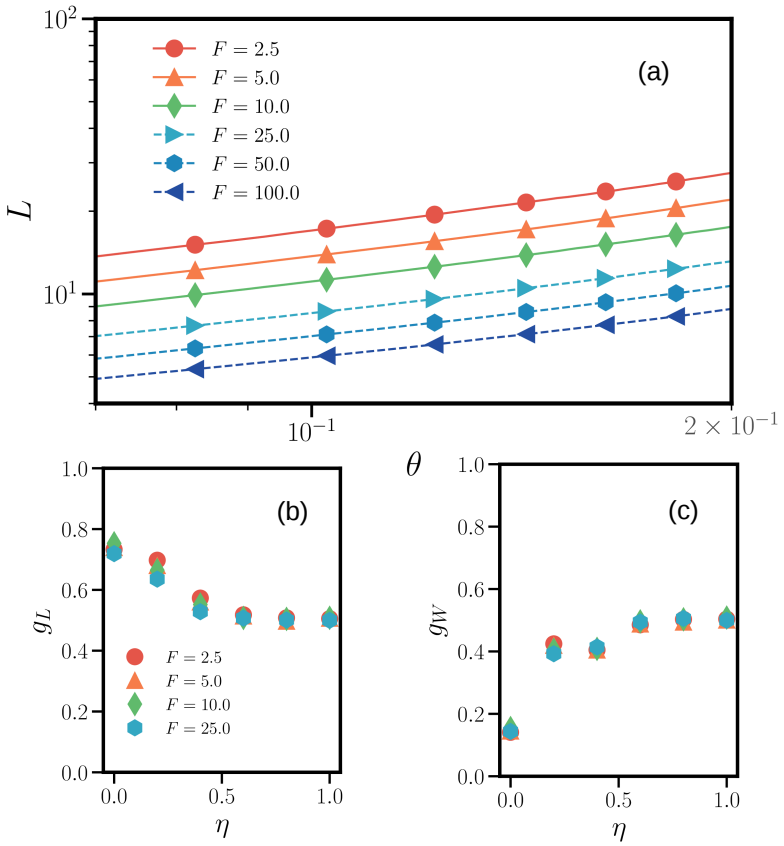

Fig. 5.14: (a) Double logarithmic plot of the average cluster length $\langle L \rangle$ as function of θ for various adsorption rates F at $E_B = 0.5$ eV and $\eta = 1$. (b) Cluster length scaling exponent g_l and (c) cluster width scaling exponent g_w as function of η.

respectively. In our model we also find different exponents for the two lattice directions when cluster growth becomes anisotropic. This indicates an interesting similarity between our nonequilibrium growth model and Ising type models.

5.3.5 Comparison with the anisotropic stochastic Eden growth model

We have simulated anisotropic cluster growth by means of an event-driven KMC algorithm where various microscopic procsses like adsorption, nucleation, attachment, detachment and diffusion processes of individual particles on the substrate are fully included. Now, we consider the much simpler anisotropic Eden model for cluster growth, where anisotropy of lateral bonds is taken into account by an imbalance of attachment probabilities as described by Eq. (5.4). One main difference to the KMC model is that diffusion processes are absent. In the Eden model, cluster growth is determined by the attachment probabilities of boundary sites only. Our key question here is whether this minimal growth model contains sufficient information to reproduce the clusters obtained via the KMC algorithm at anisotropic growth conditions.

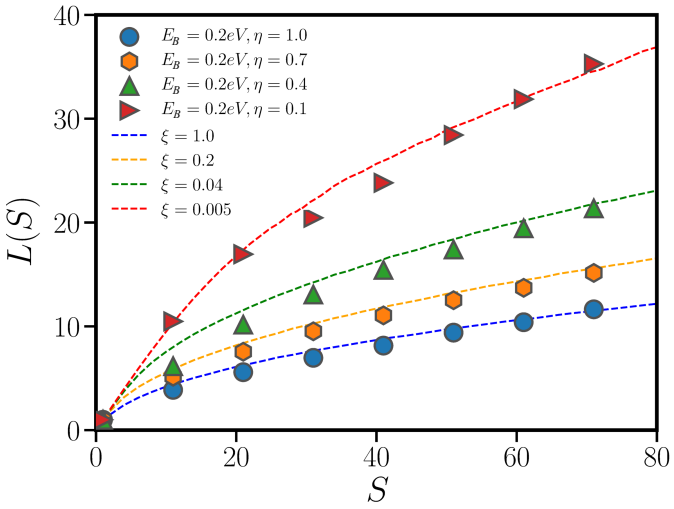

Fig. 5.15: Comparison of the cluster length evolution between clusters obtained from kinetic Monte-Carlo simulations (at $E_B = 0.2$ eV and different values of η) with clusters obtained from the stochastic Eden model at different ratios ξ of the attachment probability in x- and y-direction, respectively.

To this end, we plot in Fig. 5.15 the cluster length $L(S)$ obtained from KMC simulations at $E_B = 0.2$ eV together results from the Eden model. Moreover (as confirmed by Fig. 5.8), the cluster shape at $E_B = 0.2$ eV is close to the equilibrium shape for any η, and the Eden model with anisotropic interactions is supposed to describe equilibrium clusters. The good agreement between KMC and the Eden model for the isotropic case, i.e., at $\eta = \xi = 1$, is expected since there is no imbalance between attachment and detachment rates in both lattice directions. Interestingly, the cluster length evolution in both models also match perfectly in presence of anisotropic interactions. The anisotropy parameter ξ [see Eq. (5.4)] has been used as fitting parameter to reproduce the KMC results. The Eden model does not only correctly describe the cluster length evolution $L(S)$, but also gives the correct critical lengths L_c and aspect ratio R^{sat} in the self-similar growth regime as shown in Fig. 5.16(a) and Fig. 5.16(b). However, the anisotropic Eden model can not reproduce clusters at interaction energies E_B where cluster shapes deviate from the equilibrium shape (see L_{40} at $E_B = 0.3$ eV in Fig. 5.8).

The good agreement between clusters obtained from the KMC and the Eden model shows that isotropic diffusion of free particles is not critical for the cluster formation process in presence of anisotropic interactions. This however, is only the case for growth conditions close to thermal equilibrium. Only then one operates in the regime where detachment of particles from clusters is possible, i.e., $i^* > 1$. However, we expect that a more detailed analysis of the attachment and detachment rates will generally (also for the case $i^* = 1$) help to better understand the resulting cluster shapes under nonequilibrium growth conditions in presence of anisotropic interactions. This could be done by means of a rate equation approach of the nucleation kinetics.

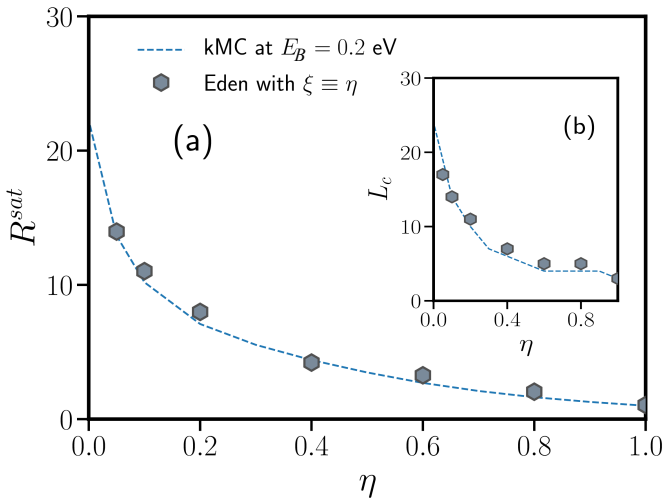

Fig. 5.16: Saturation value of the aspect ratio R^{sat} and (b) the critical length L_c of clusters obtained from kinetic Monte-Carlo simulations and the Eden model. The in-plane interaction energy in kMC simulations is $E_B = 0.2$ eV. The anisotropy parameter $\eta \in [0, 1]$ and ξ is modified such that it fits the kMC results.

5.4 Conclusion and outlook

We have studied the effect of anisotropic interactions on cluster growth in the submonolayer growth regime by means of KMC simulations. As expected, anisotropic interactions lead to elongated, rod-like and needle-shaped compact clusters with fractal dimension $D_f \approx 2$. It turns out that energetic arguments to describe cluster shapes can only be applied at low adsorption rates and low interaction energies. Furthermore, from cluster size distributions we find that clusters become smaller as the anisotropy is increased. This effect is stronger for low interaction energies.

A detailed analysis of cluster shapes as function of the strength of anisotropy reveals two different types of cluster shape transformation. For low interaction energies, the transformation from isotropic to elongated clusters is gradual, whereas it is sharp at high interaction energies. For strong interaction anisotropy, growing clusters are initially one-dimensional, i.e., particles attach only along the direction of strong bonds. This growth mode breaks down at a critical cluster length. From analyzing the aspect ratio we identify the subsequent self-similar growth mode.

We observe that the critical cluster density and the detachment ratio in the isotropic reference system are helpful to explain the properties of the cluster shape transformation in presence of anisotropic interactions. Furthermore, considering the isotropic reference systems also explains the value of the anisotropy parameter at which the cluster shape transformation sets in.

Furthermore, we investigated the impact of the adsorption rate on cluster shape properties. It turns out that the average aspect ratio as function of the adsorption rate displays power law scaling in the regime of strong interaction anisotropy. In particular, the corresponding scaling exponent does not depend on the value of the anisotropy parameter. Also, the evolution of the average cluster length and width as function of coverage exhibit power-law scaling. The corresponding scaling exponents depend only weakly on the adsorption rate.

Additionally, we have employed an anisotropic version of the Eden model for cluster growth. In this context, we used the anisotropy parameter as a fitting parameter. The latter controls the attachment probabilities of particles on cluster boundary sites. As we have shown, the Eden model can reproduce some main features of cluster growth in our KMC model. In particular, we find good agreement between both models regarding the cluster length evolution, the critical length and the saturation value of the aspect ratio where growth becomes self-similar. The good agreement between the KMC simulations and the Eden model suggest that attachment (rather than diffusion) is the dominant mechanism that determines cluster shapes. Therefore it may be interesting to further investigate attachment and detachment rates to better understand cluster shape transformations in presence of anisotropic interactions .

The KMC model can be extended in several directions. For example, appropriately setting the values of the anisotropy parameter, our model could be used to study the experimentally relevant growth of elongated Zn clusters on isotropic surfaces [250]. Further, one could study the effect of dipole-dipole interactions in systems that have already been studied experimentally [178, 252]. Additionally, it would be interesting to investigate the surface structure in the multilayer growth regime.

6 Nonequilibrium surface growth with limited particle mobility

In this chapter we discuss a variety of simulation methods that can be used to model nonequilibrium surface growth. We will focus on limited mobility models and introduce a variant that exhibits a variable diffusion length. The model can realistically mimic low-temperature surface growth by means of molecular beam epitaxy. This is confirmed by comparing results obtained from our model with conventional kinetic Monte-Carlo simulations on one- and two-dimensional substrates for various growth conditions.

6.1 Approaches to model nonequilibrium surface growth

There are various conceptually different simulation strategies to model the morphologies observed in nonequilibrium surface growth experiments by means of vapor deposition methods. Popular approaches include the level-set method [282, 283], geometry-based approaches [284], molecular dynamics simulations [285–289] and numerical solutions of stochastic equations governing the evolution of the surface height [290–293]. One further, very popular simulation strategy is to employ lattice models which are based on activation energy-dependent hopping rates for all particles in the topmost layer. These models are often referred to as ”full diffusion” or Arrhenius-type models (see C. 2.4) [8, 90–93, 95, 96, 107, 253, 294–296]. The KMC method is useful to simulate full diffusion models in order to better understand the evolution of the surface morphology in molecular beam epitaxy (MBE) experiments on the microscale. In parallel, simplified approaches such as limited mobility (LM) models have been studied in order to make out the essential microscopic processes which determine the morphologies observed in growth experiments [96, 236, 297–301]. In these models, particles perform a single diffusion step directly after deposition. We introduce an extended LM model to better understand the impact of adatom diffusion on the surface morphology. Our model is an extended version of the stochastic Das Sarma-Tamborena (DT) [97, 98, 236] model which differs from the latter via a variable diffusion length. We find that LM models can reproduce results from KMC simulations only if fluctuations are added to the diffusion length of adatoms. We propose to add fluctuations by choosing the diffusion length for each adsorbed particle from a Gaussian distribution. The variance of the distribution serves as a fitting parameter which

allows to control the strength of fluctuations. We show that the diffusional fluctuations have a huge impact not only on cluster properties during submonolayer growth, but also on the surface profile in the multilayer growth regime. The analysis of morphologies on one- and two-dimensional substrates during sub- and multilayer growth shows that the LM model can produce structures that are indistinguishable from those obtained through KMC simulations.

6.2 Motivation to use limited mobility models

Even though the KMC method can nowadays handle growth simulations on large lattices at high values of the growth parameter

$$R = D_0(T)/F, \tag{6.1}$$

they still require a significant amount of computation time to reach the multilayer growth regime. This is mainly due to the computational effort required to simulate the trajectories of freely diffusing particles, without making much progress in the actual time evolution of the system. To speed up the simulations, multiscale approaches, where the fastest dynamical process involved (i.e., free lateral diffusion) is described in an averaged mean-field manner or by an appropriate diffusion equation, have been introduced and investigated in detail [302–306].

As an alternative to these approaches, one can coarse-grain the diffusion processes in surface growth simulations on discrete lattices by imposing a limited mobility for deposited particles. There exist many lattice-based growth models which pick up on this idea and many variants of these so-called LM models have been intensively investigated in the past [98, 236, 247, 297, 299, 307, 308]. Due to their simplicity, they are especially suitable to investigate the high coverage regime in growth simulations. Specifically, one can investigate scaling properties, study kinetic surface roughening and morphological properties as well as details like crossover and long-lived transient effects in nonequilibrium surface growth [297, 299, 308, 309]. In LM models, the process rates used in KMC simulations are replaced by a certain set of stochastic rules for particle movements. The latter depend on the local spatial environment of lattice position where particles are adsorbed. Importantly, the deposited particles only perform one single movement that depends on the specific rules of the underlying LM model. Well-known examples of LM models with surface diffusion include the Family (F) model [310], the Wolf-Villain (WV) model [247, 307] and the model of Das Sarma and Tamborenea (DT) [97, 98].

We introduce an extended version of the just mentioned DT model since the latter is particularly suitable to describe *low* temperature MBE growth where particle detachment from clusters can essentially be neglected. In the original version of the DT model [97],

deposited particles only explore their immediate environment. Specifically, they are only allowed to hop to a lattice site adjacent to the site where they have been deposited. This means that particles have a diffusion length of $l = 1$ (in units of the lattice constant which we set to unity). However, under realistic conditions for surface growth by means of vapor deposition techniques, the average diffusion length l is usually larger, i.e., $l > 1$. Concerning LM models, this situation has been investigated in different variants [308, 311–313]. Studying the case $l > 1$ generally requires various fitting parameters in the LM model to match the results of corresponding KMC simulations [312, 313] or real growth experiments. We employ a LM model with fitting parameters which are based on physical quantities only. Therefore, we have to find a prescription of how to determine l to reproduce results of KMC simulations at a given value of the growth parameter R [see Eq. (6.1)]. More specifically, we seek a mapping procedure between full diffusion KMC simulations and our limited mobility model such that surface structures from the LM model are indistinguishable to those obtained from full diffusion KMC simulations (and therefore also identical to *low* temperature MBE growth) at any value of R. If this is possible, it would mean that we can significantly reduce the computational effort to simulate surface growth. We then can use the LM model for simulations at growth conditions and system sizes that are typically hard to achieve via full diffusion KMC simulations, especially when one has to average over many realizations. It would allow us to study the asymptotic regime where we expect to observe scaling behavior of the growing surface. In particular, one could extract the corresponding critical exponents describing the scaling of the surface roughness [232, 310] without being limited by finite-size effects or computational manipulations like the noise reduction technique (NRT) [297, 299, 301, 314, 315]. Our second main goal is to investigate how the strength of fluctuations in l alters the resulting surface morphologies, as compared to conventional LM models where the diffusion length of all particles is fixed to a constant value. These conventional LM models fail to reproduce KMC results at all stages of surface growth. However, as will be shown in the following, a fluctuating diffusion length solves this problem and allows to correctly mimic full diffusion KMC simulations from the sub- to the multilayer growth regime.

6.3 A limited mobility model with distributed diffusion length

In the following we introduce our LM model which is a variant of the model by Das Sarma and Tamborenea (DT model) [97, 98]. In the latter, the diffusion length is restricted to one, i.e., $l = 1$. In contrast, we consider the case $l \geq 1$ [308, 312, 313] and, additionally, consider l as a fluctuating quantity. Specifically, the values of l are chosen from a Gaussian distribution where the variance σ^2 controls the strength of diffusional fluctuations.

To clarify our approach, we first summarize the algorithm of the original DT model in one dimension. In each iteration step, a particle gets adsorbed at a randomly chosen lattice site $i \in [1, L]$. It sticks there permanently if it has at least one in-plane bond, i.e., if $n \geq 1$. Otherwise, if $n = 0$, the particle is allowed to hop either to the left site, $j = i - 1$, or to the right site, $j = i + 1$, if one of these sites provides at least one bond. If both sites provide at least one bond, either $j = i + 1$ or $j = i - 1$ is chosen randomly and the particle hops to this site and sticks there for the rest of the simulation. If none of the neighboring sites provides lateral bonds, i.e., $n = 0$, the particle will remain at the initial adsorption site i. In-plane bonds for a particle at site i are present if $h_i + 1 \leq h_j$ $(j = i \pm 1)$. If the site provides exactly one in-plane bond, i.e., if $n = 1$, it is called kink site, while a site that provides two such bonds, i.e., $n = 2$, is called a valley site. Since already one in-plane bond is enough to suppress particle diffusion, the DT model represents a minimal model for nonequilibrium surface growth at *low* T.

We extend the DT model by allowing adsorbed particles to diffuse not only to adjacent sites, but also to sites which are farther away from the deposition site i. In other words, we consider the case $l \geq 1$. In general, nonequilibrium surface growth is dominated by stochastic processes involving fluctuations not only in the deposition, but also in the diffusive motion of the particles. By setting a *constant* diffusion length l in LM models, this fundamental aspect is totally neglected. Our strategy to add fluctuations to the diffusion processes is as follows. Instead of assuming a fixed diffusion length l for all particles, we choose l individually for each particle from a Gaussian distribution

$$P(l \mid l_n, \sigma^2) = \frac{1}{\sqrt{2\pi\sigma^2}} \exp\left[-\frac{(l - l_n)^2}{2\sigma^2}\right]. \tag{6.2}$$

Here, l_n is the mean value of the diffusion length (which we determine via KMC simulations) and the variance σ^2 represents the control parameter. The latter allows to vary the strength of diffusional fluctuations of deposited particles. Our LM in one dimension is illustrated in Fig. 6.1. Our model can be simply generalized to two dimensions. In that case, care has to be taken since there may exist multiple appropriate final sites at the same distance from the adsorption site and one has to define rules which of the possible final sites is chosen.

We perform simulations of our model on one- and quadratic two-dimensional substrates $(d = 1, 2)$ with discrete, equidistant positions $i, j = 1, 2, ..., L$. The corresponding local surface heights in one-dimension are given by the integers h_i and by h_{ij} in two dimensions (i.e., $h_i = 0$ corresponds to an empty site). We apply periodic boundary conditions and the solid-on-solid condition. The latter forbids vacancies and overhanging particles. As a consequence, the spatially averaged surface height of a one-dimensional lattice at time t is given by

$$\langle h(t) \rangle = \frac{1}{L} \sum_{i=1}^{L} h_i(t) = Ft. \tag{6.3}$$

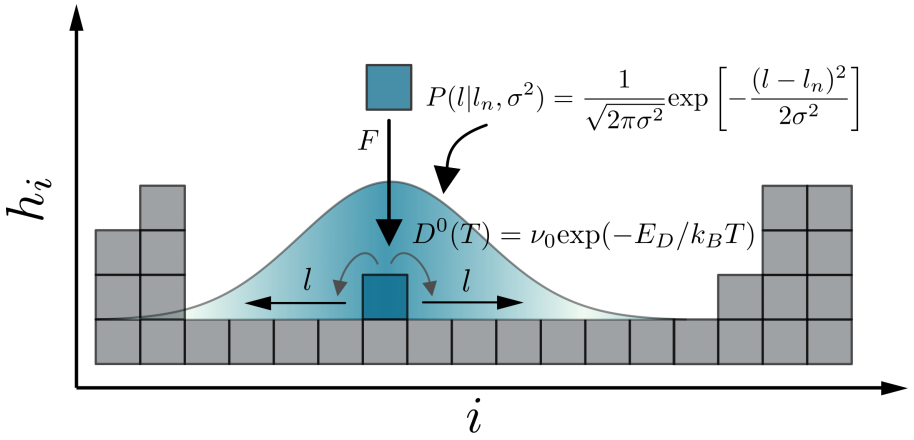

Fig. 6.1: Illustration of particle deposition and surface relaxation in the system (in one dimension) that is used to simulate low temperature MBE growth. The quantities F and $D^0(T)$ refer to the KMC simulation, while the Gaussian distribution $P(l|l_n,\sigma^2)$ for the diffusion length l is characteristic for the LM model with diffusional fluctuations whose strength is controlled via the variance σ^2.

Here, the expression Ft corresponds to the number of deposited particles. Generalization to the two-dimensional case is straightforward. The product Ft is henceforth referred to as coverage $\theta = Ft$. Therefore, time-dependent quantities can also be expressed as function of θ. Throughout this work, we characterize growth conditions via the free diffusion to adsorption ratio R of full diffusion KMC simulations as defined in Eq. (6.1). To relate our LM model with the full diffusion model, we seek a set (l,σ^2) such that surface morphologies generated by the LM model are indistinguishable from KMC results at growth conditions characterized by R. Specifically, to connect both models we have to identify a suitable set (l,σ^2) for any value of R.

6.4 Connecting the full diffusion KMC with the LM model

Details of the KMC simulations: In the following we compare results of our LM model with results from full diffusion KMC simulations. To this end, we shortly summarize details of the KMC setup (see Sec. 2.4.3). For all simulations, we use $E_D = 0.5$ eV and fix the binding energy to $E_B = 1.0$ eV to make sure that detachment of particles from clusters is not possible. Therefore, we always simulate in the regime of irreversible growth. The temperature is fixed to $T = 273$ K. For simplicity, we do not consider an additional Ehrlich-Schwoebel barrier for inter-layer diffusion processes across step-edges, i.e. $E_S = 0$ eV [181, 182, 316]. In principal, such a barrier could be included in our LM model. This may be a topic for future investigations in this direction. In order to realize different growth conditions expressed via the growth parameter R, we use the deposition rate F as a variable.

It is well established that surface morphologies observed in vapor deposition experiments, and thus, also in KMC simulations, depend on the growth parameter R [see Eq. (6.1)]. We aim to directly connect full diffusion KMC simulations with our LM model. To compare the resulting morphologies in the submonolayer regime, we calculate the total number of clusters on the lattice, $N(\theta)$, and the cluster size distribution, $P(S)$, at various values of the growth parameters R. In the multilayer regime, we compare layer coverages θ_k [with k being the layer index, see Eq. (6.14)], compute the global interface width $W(L,\theta)$ and perform a scaling analysis. Moreover, we consider the height-height autocorrelation function $\Gamma(r,\theta)$ [where $r = |i-j|$, see Eq. (6.18)] to extract a correlation length ξ_0 that allows to characterize mounded surface profiles. If all these measured quantities match in both models for all values of the growth parameter R, we conclude that our LM model correctly mimics the emerging surface structures from full diffusion KMC simulations.

First, we have to find a consistent relation between the growth parameter R in the KMC model and the diffusion length l and the variance σ^2 in the LM model such that the morphologies generated by both models are indistinguishable. Second, we investigate the general effect of the variance σ^2 in our LM model on the morphological evolution of the surface in the sub- and multilayer growth regime

Diffusion properties - Nucleation length and the geometrical cluster distance: We calculate via full diffusion KMC simulations the mean-squared displacement (MSD) of adsorbed particles as function of time $\tilde{t}$ they spend on the lattice. The MSD is defined as

$$MSD(\tilde{t}) = \langle (i(\tilde{t}) - i(0))^2 \rangle. \tag{6.4}$$

Here, $i(\tilde{t}) \in [1, L]$ represents the discrete position of the particle on the lattice at time $\tilde{t}$, and $i(0)$ is the site where the particle has been initially adsorbed at $\tilde{t} = 0$. Further, $\langle ... \rangle$ is an average over many realizations. Depending on the growth conditions, $MSD(\tilde{t})$ saturates at a characteristic time $\tilde{t}_S$ and corresponding value $MSD_S = MSD(\tilde{t}_S)$. Saturation of the MSD reflects the immobilization of particles induced by the formation of bonds. In each simulation run, only the first deposited particle is tracked because this particle is expected to travel the maximum distance at the given value of the growth parameter R. We average $MSD(\tilde{t})$ over at least (10^5) realizations for each considered value of R.

Based on the saturation value MSD_S, we define the *nucleation length* of adsorbed particles according to

$$l_n(R) = \sqrt{MSD_S(R)}. \tag{6.5}$$

An additional (and experimentally accessible) measure for the length a particle travels until getting immobilized, is the *geometrical cluster distance*. For a d-dimensional lattice, this quantity is given by

$$d_g(R) = \left(\frac{L^d}{N_{max}(R)} \right)^{1/d}. \tag{6.6}$$

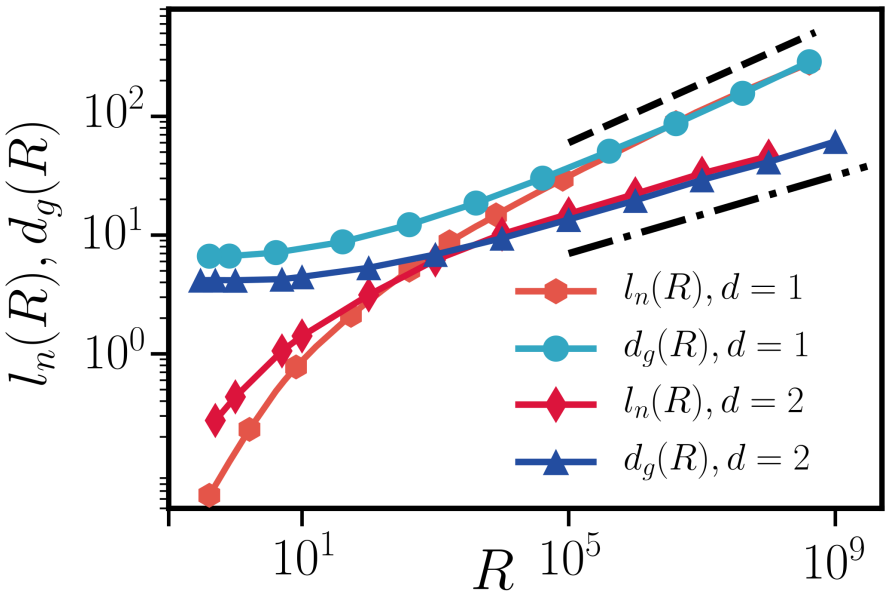

Fig. 6.2: KMC results for the nucleation length l_n [see Eq. (6.5)] of particles adsorbed at the very early stage of submonolayer growth, and the geometrical distance d_g [see Eq. (6.6)] between clusters, as function of R. The dashed black line describes the dependency $\sim R^{\gamma}$, with $\gamma = 1/4$ ($d = 1$), while the dash-dotted line follows $\sim R^{1/6}$ ($d = 2$).

Here, $N_{max}(R)$ is the maximum number of clusters in the first layer during submonolayer growth and L is the linear size of the lattice. For a one-dimensional lattice with irreversible cluster growth, $N_{max} \sim R^{-1/4}$ [317, 318], whereas $N_{max} \sim R^{-1/3}$ for irreversible growth in two dimensions [319].

We now check whether l_n and d_g might serve as appropriate choice for the diffusion length l in our LM model. To this end, we plot l_n along with d_g as function of R (in the experimentally relevant regime) in Fig. 6.2. For values $R < 10^3$, adsorption dominates and particles only marginally diffuse. In this regime, we observe an increase of l_n with R, while d_g remains nearly constant. As soon as we enter the regime $R \geq 10^3$, particle diffusion becomes the dominant process and we identify the characteristic scaling $l_n \approx d_g \sim R^{1/4}$, because $d_g \sim 1/N_{max}$ and $N_{max} \sim R^{-1/4}$ when $d = 1$. For $d = 2$ we find $d_g \sim R^{1/6}$, since $d_g \sim (1/N_{max})^{1/2}$ and $N_{max} \sim R^{-1/3}$. The intriguing result is that l_n follows the *same* scaling and takes (approximately) the same values as d_g for $R \geq 10^3$. This means that it is sufficient to calculate N_{max} (which can be experimentally determined from AFM or STM snapshots) in order to determine the diffusion length l_n together with the geometrical cluster distance d_g.

Based on these findings, we henceforth take the nucleation length l_n (or, equivalently, d_g for $R \geq 10^3$) as an estimate for the diffusion length l in the LM model. In the following, we analyze corresponding numerical results in detail where we particularly focus on the effect of diffusional fluctuations which we control via σ^2.

R	l	N_{max} KMC	N_{max} LM, $\sigma^2 = 0$	ϵ in %
1.5×10^2	3	403.85	403.21	0.16
4.0×10^2	5	333.72	332.56	0.35
1.3×10^3	8	272.54	252.55	7.33
4.0×10^3	12	220.08	186.29	15.35
4.0×10^4	23	134.84	105.36	21.86
8.0×10^4	30	116.76	86.99	25.50
4.0×10^5	46	80.69	59.61	26.13
4.0×10^6	85	32.55	21.61	33.61

Tab. 6.1: Maximum number of clusters N_{max} and the relative error ϵ (in %) in N_{max} during submonolayer growth in the LM model without fluctuations in l comparison to KMC simulations at various values of the growth parameter R (in $d = 1$).

6.5 Results in one spatial dimension

The submonolayer growth regime: Let us now investigate whether the LM model with mean diffusion length $l = l_n(R)$ and variance σ^2 can indeed reproduce morphologies in the submonolayer regime ($\theta < 1$) that are equivalent to those obtained from full diffusion KMC simulations at arbitrary values of R. Here we focus on the one-dimensional case. To compare the two models quantitatively, we calculate the number of clusters in the first layer, $N(\theta)$, as well as the corresponding distribution $P(S)$ of clusters of size S. Since detachment of particles from cluster boundary sites is neglected, already dimers represent stable clusters. We thus distinguish between clusters N (of size $2 \leq S \leq L$) and monomers n.

Number of clusters in the first layer: The evolution of $N(\theta)$ for various values of the growth parameter R is shown in Fig. 6.3. We focus on clusters in the first layer and monitor them up to a final coverage of $\theta = 2.5$. We find good agreement between the KMC (solid lines) and the LM model with constant l, i.e., with $\sigma^2 = 0$ (dashed lines) at the lowest value of R considered, $R = 4 \times 10^2$ (corresponding to $l = 5$ in the LM model). In particular, the location and value of the maximum cluster density, N_{max}, are matching perfectly. However, for larger values of R, we find pronounced deviations. Particularly striking are the discrepancies in N_{max} and the emergence of a plateau in $N(\theta)$ within the LM model in comparison to KMC simulations at $R \geq 10^3$. Therefore, at growth conditions where diffusion dominates, the LM model with constant diffusion length for all particles fails to correctly reproduce the KMC results. To quantify the mismatch between the KMC model and the LM model in absence of diffusional fluctuations, i.e., at $\sigma^2 = 0$, we show in table 6.1 the values of N_{max} and the relative error ϵ for various growth conditions expressed via R and the corresponding values of l.

Furthermore, Fig. 6.3 also shows that deviations in $N(\theta)$ between the two models become much smaller when fluctuations in l are added, i.e., $\sigma^2 > 0$. This is done by choosing

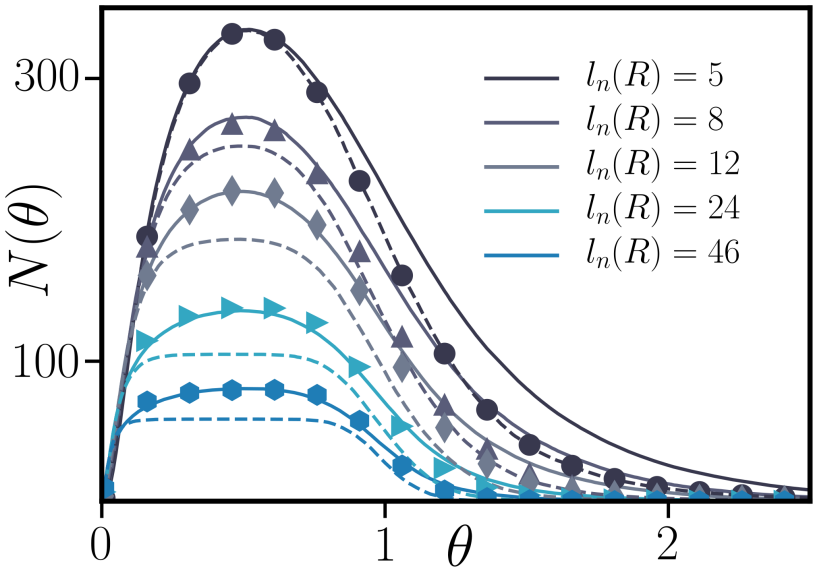

Fig. 6.3: Comparison of $N(\theta)$ in the KMC model for various values of R (solid lines) with the LM model where $l = l_n(R)$ is used. The dashed lines represent results of the LM model with $\sigma^2 = 0$, while the dots correspond to $N(\theta)$ with optimal values of σ^2.

the value of σ^2 appropriately for a given value of l (symbols in Fig. 6.3 represent the LM model with th optimal values of σ^2). To this end, we consider the difference between the maximum number of clusters

$$\Delta N_{max} = N_{max}^{KMC}(R) - N_{max}^{LM}(l, \sigma^2) \tag{6.7}$$

in the KMC and the LM model, respectively. Results for ΔN_{max} as function of σ^2 for various growth conditions are shown in Fig. 6.4. One observes that ΔN_{max} is positive for small values of σ^2, reflecting that the LM model with negligible diffusional fluctuations underestimates the values of N_{max} from KMC simulations. As the strength of fluctuations is increased, ΔN_{max} decreases until it crosses the black dashed line corresponding to $\Delta N_{max} = 0$. The value of σ^2 for which $\Delta N_{max} = 0$ is referred to as optimal σ^2. The inset of Fig. 6.4 shows the optimal value of σ^2 as function of l. These optimal values are used in Fig. 6.3 to match the KMC results. Upon increasing σ^2 above the optimal value, ΔN_{max} takes negative values. This means that the number of clusters in the LM model overshoots N_{max} from KMC simulations. Taken together, Fig. 6.4 illustrates the importance of diffusional fluctuations in the LM model. However, it also tells that their strength has to be chosen carefully.

It is established that for $d = 1$, the asymptotic scaling of N_{max} as function of θ follows $N \sim \theta^{1/4}$ [306, 320]. The results in Fig. 6.5 reveal that the LM model obeys this scaling only with optimal σ^2. Additionally, we observe unexpectedly good agreement with KMC results concerning the number of monomers on the lattixe n as function of θ, provided that the optimal σ^2 is taken. Even though the values of n obtained from KMC and LM do

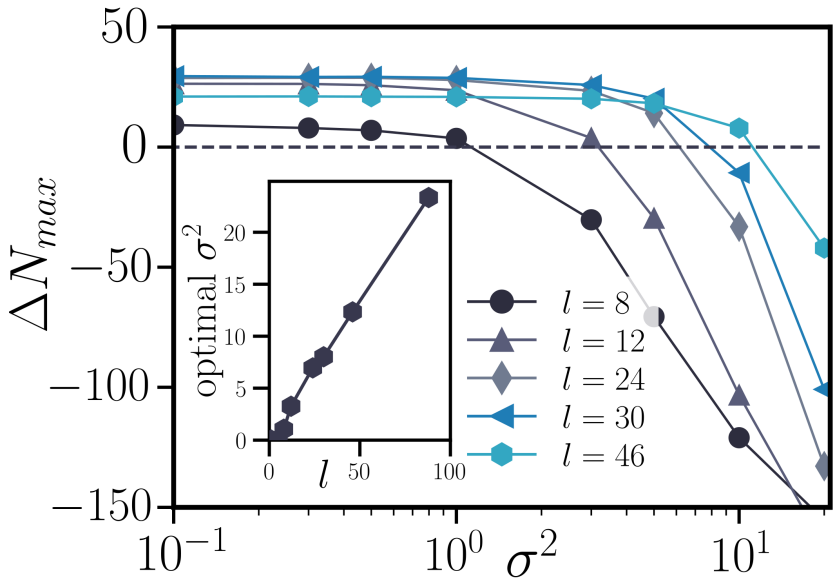

Fig. 6.4: The quantity ΔN_{max} [see Eq. (12)] as function of the variance σ^2 in the LM model for various values of the mean diffusion length $l_n(R) = l$. The black dashed line indicates $\Delta N_{max} = 0$. The inset shows the optimal values of σ^2 as function of l fulfilling $\Delta N_{max} = 0$.

not perfectly match, the scaling $n \sim \theta^{-r}$, with $r \approx 0.64$ is quite similar [306]. Please note that mean-field considerations predicts $r = 0.5$ [320] and the difference in r (between simulations and mean-field theory) is because our value for R in Fig. 6.5 is chosen too small to resemble the mean-field resuld. However, $r \approx 0.64$ was also found in [306]. This is rather surprising since we do not explicitly model the particle diffusion and thus can *a priori* not expect such a resemblance. In contrast, the LM model with fixed diffusion length, i.e., $\sigma^2 = 0$, gives a wrong scaling for both, the number of clusters N and the number of monomers n.

Cluster size distributions in the first layer: Let us now consider the cluster size distribution $P(S)$ in the LM model for two representative values of the mean diffusion length, $l = 12$ and $l = 24$ (see Fig. 6). Here, we aim to explore the effect of fluctuations in l on $P(S)$ in the submonolayer regime on a qualitative level (see [317, 321] for a detailed scaling analysis of cluster size distributions). For both values of l, we observe a shift of the maximum of $P(S)$ towards smaller cluster sizes as the value of σ^2 is increased. Additionally, there emerges a left shoulder that indeed resembles the correct form of $P(S)$ for small cluster sizes S in the pre-coalescence regime [13, 322]. At $\sigma^2 = 0$, the shoulder is absent for $l = 24$, and too small for $l = 12$. Using the earlier obtained optimal values for σ^2 (see Fig. 6.4), we find good agreement between $P(S)$ obtained from the LM and the KMC model, respectively. As σ^2 is increased above the optimal σ^2, the maximum of $P(S)$ is shifted to even smaller values of S until the left shoulder vanishes. Then, $P(S)$ becomes a monotonically decreasing function of S. The dependency of $P(S)$ on σ^2 shows that diffusional fluctuations are essential to retain the correct form of $P(S)$ in systems that model nonequilibrium surface growth with limited particle mobility.

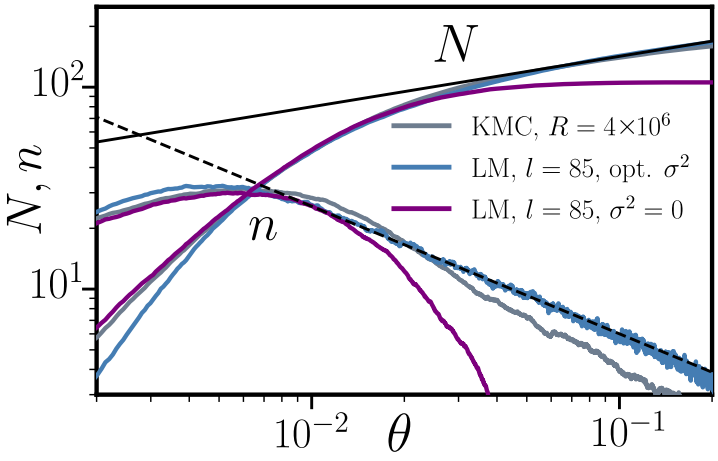

Fig. 6.5: Number of clusters N and monomers n as function of coverage θ on a lattice of size $L = 16384$ for the KMC model and the LM model with corresponding diffusion length and different values of the variance σ^2. The solid black line follows $\sim \theta^{1/4}$, while the dashed black line scales according to $\sim \theta^{-r}$, with $r \approx 0.64$ [306, 320].

Finally, we shortly summarize our reasoning for the observed discrepancies in $N(\theta)$ and $P(S)$ between the KMC and the LM model without fluctuations in l for $R > 4 \times 10^2$ ($l > 5$) and thereby justify our LM model with diffusional fluctations. Nonequilibrium surface growth is dominated by stochastic processes that involve fluctuations not only in the deposition, but also in the diffusive motion of the adsorbed particles. By setting a *constant* diffusion length l in the LM model, this fundamental aspect of stochastic systems is fully neglected. As a consequence, we obtain less clusters which are, moreover, too regular in size as opposed to the clusters from KMC simulations, where the stochastic nature of diffusion is naturally included (see Fig. 6.3, 6.5, 6.6). While diffusional fluctuations seem to be negligible at $R \leq 4 \times 10^2$ ($l \leq 5$), they become significant for growth conditions where diffusion dominates, $R > 10^3$ ($l > 5$). Therefore, to realistically model nonequilibrium surface growth in LM models at large values of R, one has to consider diffusional fluctuations. The way we have chosen to include them is to pick the diffusion length for each deposited particle from a Gaussian distribution $P(l|l_n, \sigma^2)$ where the variance σ^2 controls the strength of fluctuations around the mean diffusion length l.

The multilayer growth regime: It is crucial to check whether our LM model can also correctly describe the multilayer growth regime. Here, the main quantity of interest concerning the surface morphology is the global interface width [9, 238, 310, 323, 324], which is defined as the root of the integrated mean square fluctuations of the local surface height at coverage θ. In continuous form, the global interface width in one dimension reads

$$W(L, \theta) = \sqrt{\frac{1}{L} \int_0^L (h(x, \theta) - \langle h(\theta) \rangle)^2 \, dx}. \tag{6.8}$$

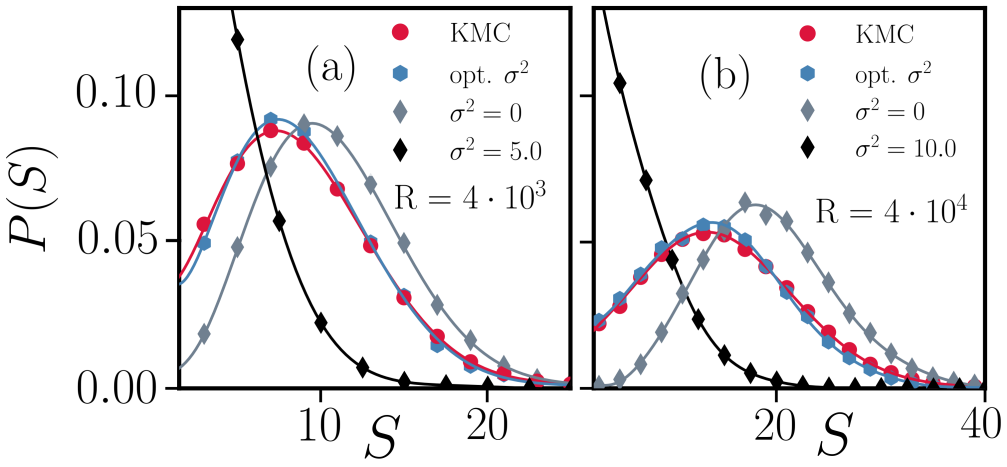

Fig. 6.6: Comparison of the cluster size distribution $P(S)$ during submonolayer growth at $\theta = 0.5$ for (a) $l = 12$, (b) $l = 24$ and various values of the variance σ^2 that controls the strength of diffusional fluctuations.

Here, $h(x, \theta)$ is the local surface height at position x (or i in discrete form) and coverage θ, L is the size of the substrate, and

$$\langle h(\theta) \rangle = \frac{1}{L} \int_0^L h(x, \theta)\, dx \tag{6.9}$$

represents the average surface height of the growing film. Thus, $W(L, \theta)$ is a measure of the surface roughness. Further, studying $W(L, \theta)$ allows to explore whether the dynamics of the growing surface exhibits universal scaling behavior and can thus be assigned to one of the established universality classes in nonequilibrium surface growth [9, 97, 98, 236, 238, 242, 322, 325–327]. More precisely, investigating $W(L, \theta)$ helps to identify whether the local surface height evolves (in the hydrodynamic limit) according to the functional form

$$\partial_\theta h(x, \theta) = \mathcal{F}[\nabla^n h(x, \theta)], \tag{6.10}$$

where $\mathcal{F}$ is a characteristic functional involving gradient terms. Thus, examining $W(L, \theta)$ can contribute to a deeper understanding of the interface dynamics during nonequilibrium surface growth and may thus help to establish improved control strategies for epitaxially fabricated devices.

In general, the global interface width is expected to follow the Family-Vicsek scaling relation [9, 232, 310]

$$W(L, \theta) \sim \theta^\beta f\left(\frac{L}{\theta^{1/z}}\right), \tag{6.11}$$

where β and z are the growth and dynamic exponent, respectively. Further, $f(u)$ is a scaling function that obeys

$$f(u) \sim \begin{cases} u^\alpha & u \ll 1 \\ \text{const.} & u \gg 1, \end{cases} \tag{6.12}$$

which involves the global roughness exponent $\alpha = \beta z$ that depends on the two independent exponents β and z. The set of these three critical exponents (α, β, z) determines the universality class of the growth process under study as explained in detail in C. 4

The growth exponent β can be extracted from the short-time behavior of the interface width which is known [9, 232] to scale as $W(L,\theta) \sim \theta^{\beta}$ for coverages $\theta < \theta^*$ [with θ^* being the crossover coverage at which $W(L,\theta)$ reaches a saturation value $W_{sat}(L)$]. To obtain the exponents α and z, it is necessary to reach the asymptotic regime, $\theta \geq \theta^*$. Since the crossover coverage θ^* scales with system size L according to [9, 232]

$$\theta^* \sim L^z, \tag{6.13}$$

it is very difficult to determine α and z for large L in simulations. This is due to the required computation time to reach $W_{\text{sat}}(L)$, especially when $\alpha > 1$ and $z > 2$ [299, 301, 308].

Evolution of layer coverages: In order to compare both models the initial stage of multilayer growth, we compute the coverage evolution in the first ten layers. In the following, layer coverages are denoted by θ_k, with k being the layer index. Layer coverages are defined as

$$\theta_k = \frac{1}{L}\sum_{i=1}^{L} \Theta(|h_i - k|), \tag{6.14}$$

with the Heaviside step function $\Theta(X)$ that obeys $\Theta(X) = 0$ for $X < 0$ and $\Theta(X) = 1$ for $X \geq 0$. We note that θ_k is different from the quantity θ, since the latter describes the *total* coverage.

Results for θ_k (for $k = 1$ to $k = 10$) are shown in Fig. 6.7 for two different values of R and corresponding distributions $P(l \mid l_n, \sigma^2)$. For both considered growth conditions we find perfect agreement between the layer coverage evolution in both models. To show that this agreement holds at any value of R, we plot in Fig. 6.7(c) the evolution of $\theta_{10}(\theta)$ for various values of R and corresponding $P(l \mid l_n, \sigma^2)$. Again, we find nearly perfect agreement between the corresponding results from both models. Thus, we conclude that the LM model with optimal σ^2 yields a very good description of the KMC model during the early stage of multilayer growth.

Roughness and scaling in the multilayer growth regime: Let us now study the regime of many deposited layers of particles (up to $\theta = 10^6$) by investigating the global interface width $W(L,\theta)$ [see Eq. (6.8)]. The evolution of $W(L,\theta)$ for different system sizes L and four exemplary values of R and corresponding distributions $P(l \mid l_n, \sigma^2)$ is shown in Fig. 6.8. Results for $W(L,\theta)$ from KMC simulations are given by symbols, whereas results from the LM model are represented by solid lines.

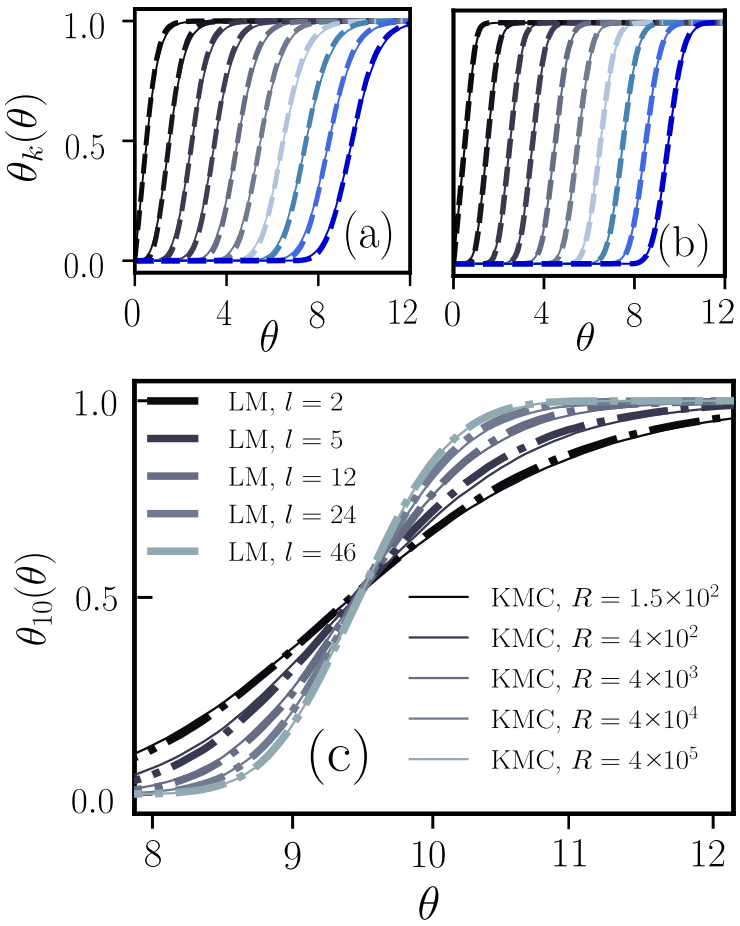

Fig. 6.7: (a) Evolution of the coverage in the first ten layers in the KMC model at $R = 10^2$ and $l = 5$ ($\sigma^2 = 0.1$) in the LM model. (b) The same at $R = 4 \times 10^4$ in the KMC model and $l = 24$ ($\sigma^2 = 7.0$) in the LM model. (c) Coverage evolution of the tenth layer at various growth conditions in both models. Solid lines represent KMC simulations, dotted lines are results from the LM model (with optimal variance σ^2).

According to the Family-Vicsek scaling relation [9, 232], $W(L, \theta)$ initially shows power-law scaling, $W(L, \theta) \sim \theta^{\beta}$. From the KMC data we identify $\beta \approx 1/3$ for all considered values of R. The reason why β does not depend on R is because it does not affect the symmetry properties of the system [326, 328, 329]. The growth exponent $\beta \approx 1/3$ also correctly describes the roughening in the LM model. Interestingly, not only the scaling exponent $\beta \approx 1/3$ is the same in both models, but also the actual values of $W(L, \theta)$ for all considered growth conditions and system sizes L [see Fig. 6.9(c)].

After the crossover from the transient to the asymptotic growth regimeregime at θ^*, the interface width saturates. Independent of the value of R and $P(l \mid l_n, \sigma^2)$, the saturation coverage scales $\theta^* \sim L^3$. Again, the scaling exponents are very similar in both models for all considered growth conditions [See Fig. 6.9(d)]. Additionally, we observe that the saturation values scale $W_{sat}(L) \sim L^1$ [See Fig. 6.9(b)]. Thus, the roughness exponent $\alpha \approx 1$ is the same in both models for all considered growth conditions.

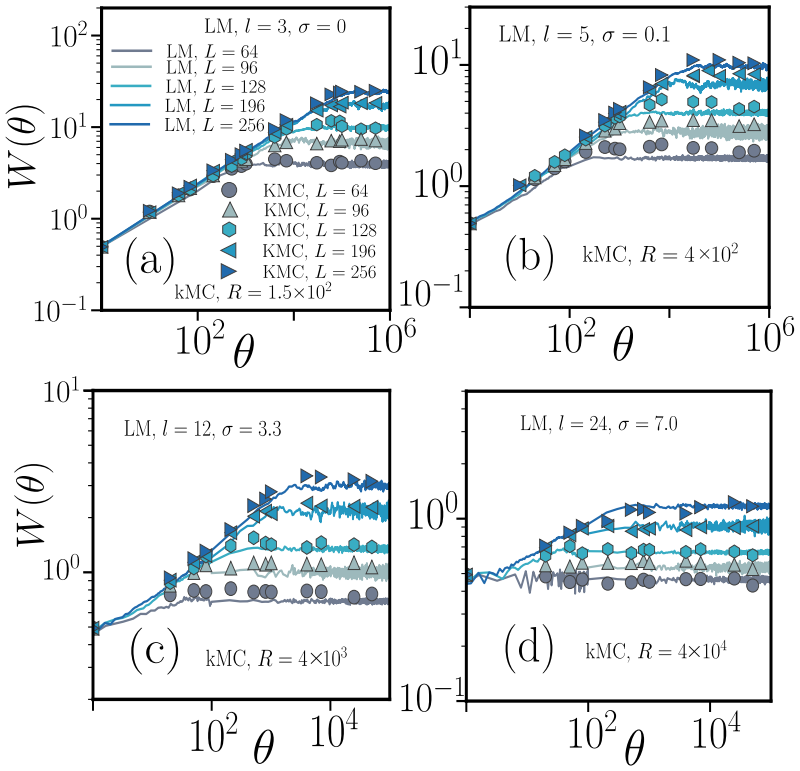

Fig. 6.8: Global interface width $W(L, \theta)$ as function of coverage θ for four different values of R in the KMC model (symbols) and corresponding diffusion length l in the LM model (solid lines) with optimal values for σ^2 for system sizes from $L = 64$ to $L = 256$.

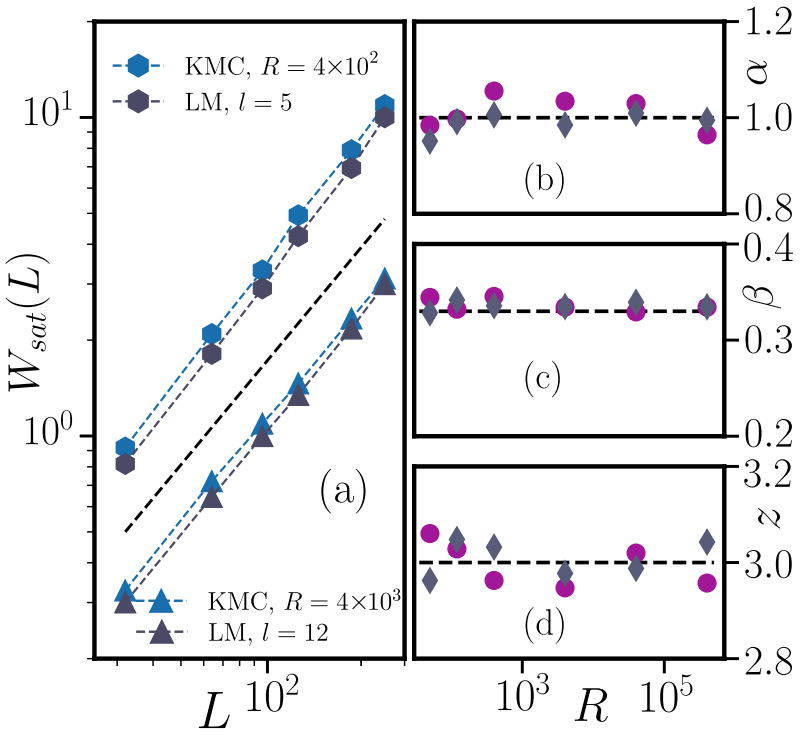

Fig. 6.9: (a) Scaling of the saturation roughness W_{sat} as function of system size L for two values of R in the KMC model and the corresponding values of l and σ^2 in the LM model (dotted black line $\sim L^1$). (b) Roughness exponent α, (c) growth exponent β and (d) dynamic exponent z for various growth conditions in both models. The lines in (b)-(d) represent the values of α, β, z according to the VLDS universality class in one dimension.

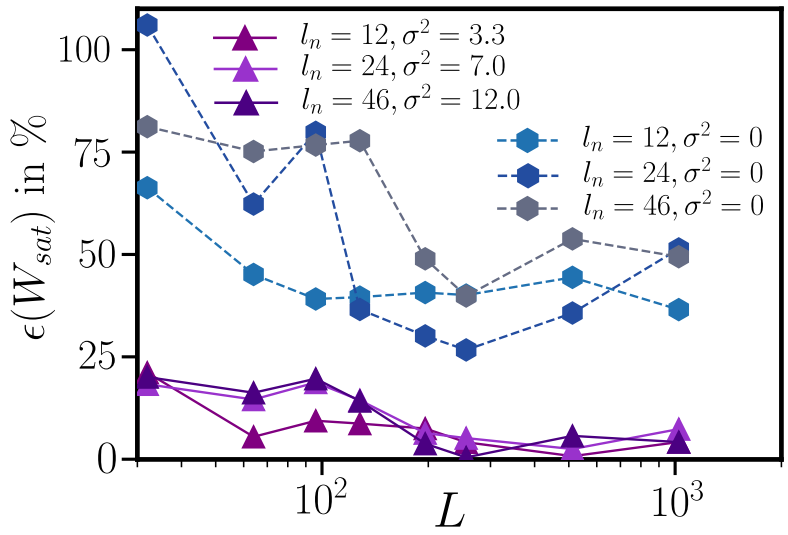

Fig. 6.10: Relative error $\epsilon(W_{sat})$ of the saturation roughness $W_{sat}(L)$ in the LM model compared to KMC simulations. Results for $\epsilon(W_{sat})$ without fluctuations in the diffusion length l (i.e., $\sigma^2 = 0$) are given by hexagons, while $\epsilon(W_{sat})$ with optimal σ^2 are represented by triangles.

We identify the following critical exponents in our simulations: $\alpha \approx 1$, $\beta \approx 1/3$, $z \approx 3$. As known from simulations and analytical calculations of the DT model (with $l = 1$), this set of critical exponents corresponds to the Villain-Lai-Das Sarma (VLDS) universality class in one dimension [98, 236, 330]. The corresponding evolution equation for the surface height in the hydrodynamic limit is given by

$$\partial_t h(x,t) = -\nu_4 \partial_x^4 h(x,t) + \lambda_4 [\partial_x^2 h(x,t)]^2 + \phi. \tag{6.15}$$

Here, $h(x,t)$ is the surface height at position x at time t, ν_4 and λ_4 are constants, and ϕ is a Gaussian white noise, representing the randomness of the particle deposition process. Thus, Eq. (6.15) is a stochastic, nonlinear partial differential equation. Note that for $\lambda_4 = 0$ the equation reduces to the linear Mullins-Herring (MH) equation (characterized by the following critical exponents, in one dimension: $\alpha = 3/2$, $\beta = 3/8$, $z = 4$) [239, 240]. The non-linear equation, $\lambda_4 \neq 0$, is known to have the same symmetry as several discrete lattice models (including the DT model) [97, 98] which are frequently used to model surface growth. Thus, these discrete lattice models have the same set of critical exponents as the nonlinear equation Eq. (6.15). As a consequence, Eq. (6.15) describes the dynamical evolution of the surface height in the continuum limit.

To demonstrate the importance of diffusional fluctuations in the multilayer regime, we show in Fig. 6.10 the relative error $\epsilon(W_{sat}) = |W_{sat}(L)^{LM} - W_{sat}(L)^{KMC}|/W_{sat}(L)^{KMC} \times 100$ of $W_{sat}(L)$ for the LM model with $\sigma^2 = 0$ and the version with optimal σ^2. We find that, as L is increased, $\epsilon(W_{sat})$ diminishes with optimal σ^2, while $\epsilon(W_{sat}) \geq 40\%$ in absence of diffusional fluctuations, i.e., when $\sigma^2 = 0$.

Interface profiles and the effect of diffusional fluctuations: As known from experiments [331–333] and KMC simulations [9, 13, 334, 335], the surface of a growing thin film becomes smoother as the value of R is increased. We systematically study this smoothing of the surface and the thus resulting decrease of the surface roughness in the LM model by plotting W_{sat} versus l for different system sizes L in Fig. 6.11(a). We find that $W_{sat}(L,l)$ obeys a power-law, $W_{sat}(L,l) \sim l^{-\phi}$, with scaling exponent $\phi \approx 3/2$. The value of the latter exponent is independent of L. In KMC simulations, the saturation roughness decreases according to $W_{sat}(L,R) \sim R^{-\delta}$, with $\delta \approx 1/2$ [see Fig. 6.11(b)]. To confirm the correctness of the scaling exponents ϕ and δ, we define a rescaled saturation roughness for both models. The rescaled saturation roughness for the LM model reads

$$W_{sat}^{RE} = W_{sat}(L,l)/(L^{\alpha} l^{-\phi}). \tag{6.16}$$

For the full diffusion KMC model the rescaled saturation roughness is given by

$$W_{sat}^{RE} = W_{sat}(L,R)/(L^{\alpha} R^{-\delta}). \tag{6.17}$$

Results for W_{sat}^{RE} are shown in Fig. 6.11(c). We find that W_{sat}^{RE} as function of l in the LM model is indeed a constant. The same holds for KMC simulations where W_{sat}^{RE} is plotted as function of $l_n(R)$.

Growth instabilities can induce the formation of mound-like patterns. It is well accepted that the original DT model displays the formation quasiregular mounds [299, 300, 308, 309, 336–338]. To investigate how diffusional fluctuations alter this characteristic feature, we show exemplary interface profiles for two diffusion lengths l and different values of σ^2 in Fig. 6.12(a) - (f) [please note that $h(x) = h_i - h_{min}$, where h_{min} is the minimum height in the depicted profiles]. We observe that as σ^2 is increased from zero, the characteristic mound size decreases, while the number of mounds increases. Further, individual mounds appear to be sharper and steeper. As a consequence, the overall interface looks rougher and does indeed yield a higher value of the interface width.

To analyze in detail how the value of σ^2 modifies the interface height profile, we calculate a characteristic length ξ_0 that contains information regarding the characteristic mound size [313, 338]. This quantity is defined as the first zero of the height-height correlation function

$$\Gamma(r,\theta) = \frac{\langle \tilde{h}_i(\theta)\tilde{h}_{i+r}(\theta)\rangle}{\langle \tilde{h}_i(\theta)^2\rangle}, \tag{6.18}$$

with $\tilde{h}_i(\theta) = h_i(\theta) - \langle h(\theta)\rangle$. Calculating $\Gamma(r)/\Gamma(0)$ reveals that with increasing σ^2, $\Gamma(r)/\Gamma(0)$ decays faster to zero as function of the distance $r = |i-(i+r)|$ from reference site i. Accordingly, the value of ξ_0 decreases [see Fig. 6.12(g) and (h) where $\Gamma(r)/\Gamma(0)$ crosses zero at smaller values of r when σ^2 is increased]. This goes along with a decrease of the characteristic mound size.

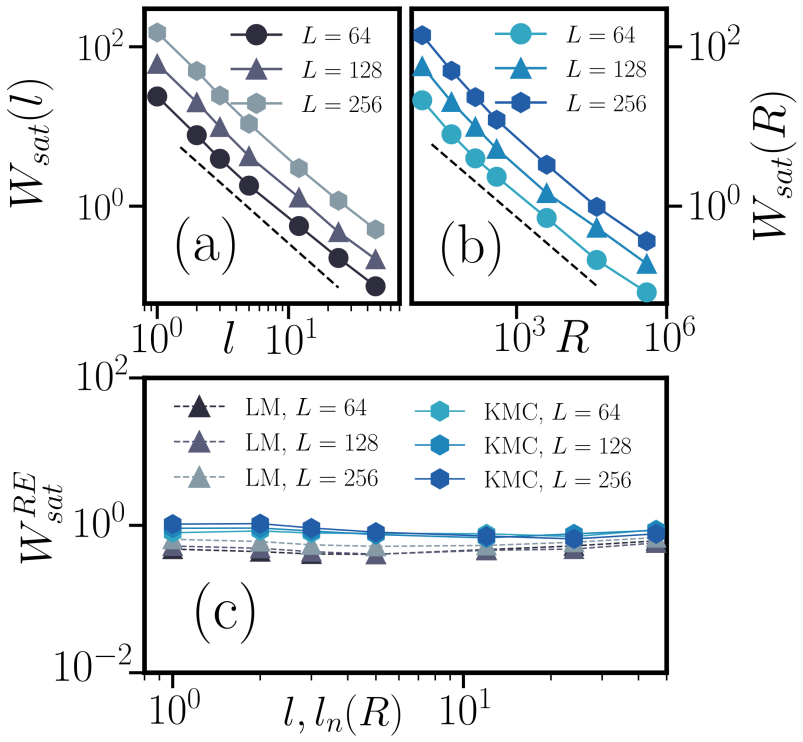

Fig. 6.11: (a) Scaling of the saturation roughness $W_{sat}(l)$ in the LM model as function of the average diffusion length l with optimal values for σ^2 for different system sizes L. The black dotted line follows $\sim l^{-3/2}$. (b) Scaling of $W_{sat}(R)$ as function of the growth parameter R. The black dotted line follows $\sim R^{-1/2}$. (c) Rescaled saturation roughness W^{RE}_{sat} in the LM model and corresponding KMC simulations.

To demonstrate the equality of the morphologies generated by both models, we compare $\Gamma(r)/\Gamma(0)$ obtained from the KMC and the LM model at $\theta = 10^4$ in Fig. 6.13. For both considered growth conditions [$l = 5$ and $l = 12$, Fig. 6.13(c) additionally shows ξ_0 for $l = 20$], we observe good agreement between KMC and the LM model when the optimal values of σ^2 are used.

6.6 Results in two spatial dimensions

So far we investigated the LM model in one dimension. From an application-oriented point of view it is clear that the case of two spatial dimensions is more relevant. Here, we show by exemplary calculations that the mapping strategies developed for the one-dimensional case can simply be transferred to other spatial dimensions. To relate the values of R in KMC simulations to the parameters l and σ^2 in the LM model for $d = 2$, one can straightforwardly follow the one-dimensional case. However, the decision for the final attachment site has to be carefully considered, since in two dimensions more than two lattice sites at the same distance from the adsorption site can provide at least one lateral bond. As a first step, we decided to select the cluster boundary site for attachment that

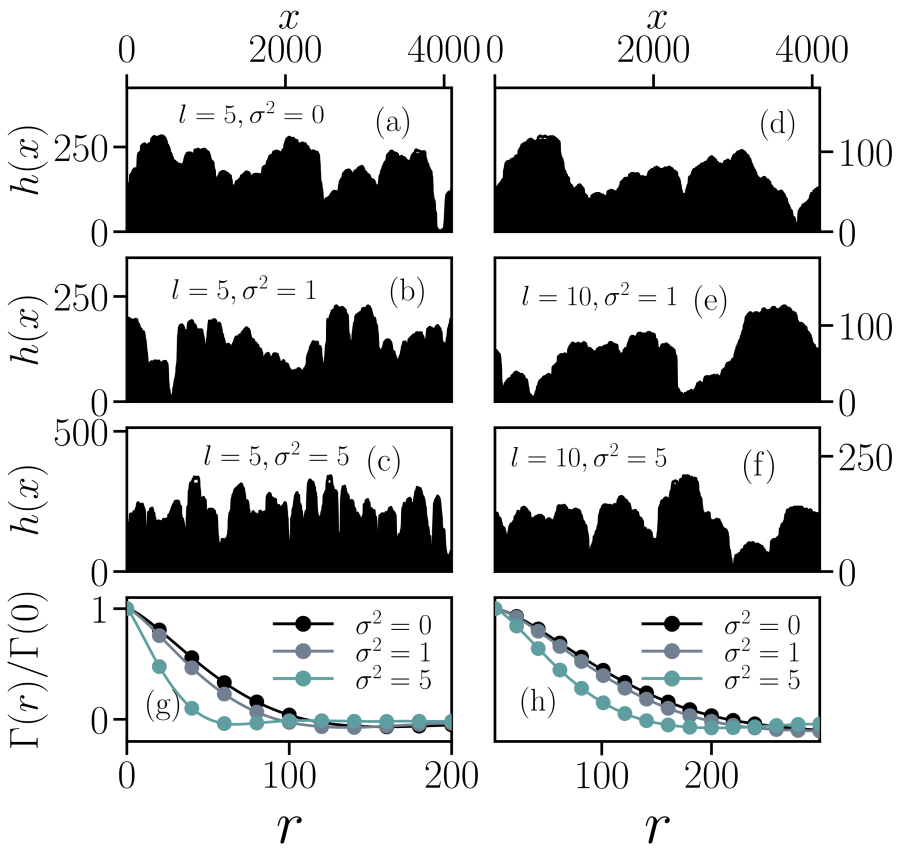

Fig. 6.12: (a) - (f) Height profiles in the LM model at $\theta = 10^6$ for two representative values of l and different values of the variance σ^2 at coverage $\theta = 10^6$ in systems of size $L = 4096$. (g) Height-height correlation function $\Gamma(r)/\Gamma(0)$ for the depicted system settings with $l = 5$ and different values of σ^2 at $\theta = 10^4$. (h) The same as in (g) for $l = 10$.

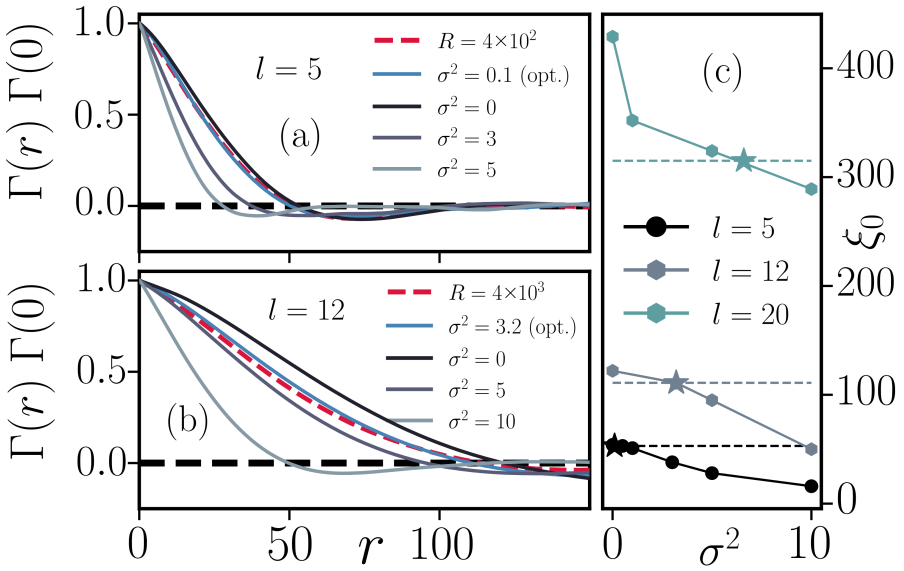

Fig. 6.13: (a) Height-height correlation function $\Gamma(r)/\Gamma(0)$ for KMC simulations at $R = 4 \times 10^2$ together with results of the LM model at $l = 5$ and various values of the variance σ^2. (b) The same as in (a) for $R = 4 \times 10^3$ and $l = 12$. (c) Correlation length ξ_0 for different combinations of l and σ^2 (lines with symbols) together with corresponding values of ξ_0 from KMC simulations (dashed lines). Stars in (c) represent the optimal values of σ^2.

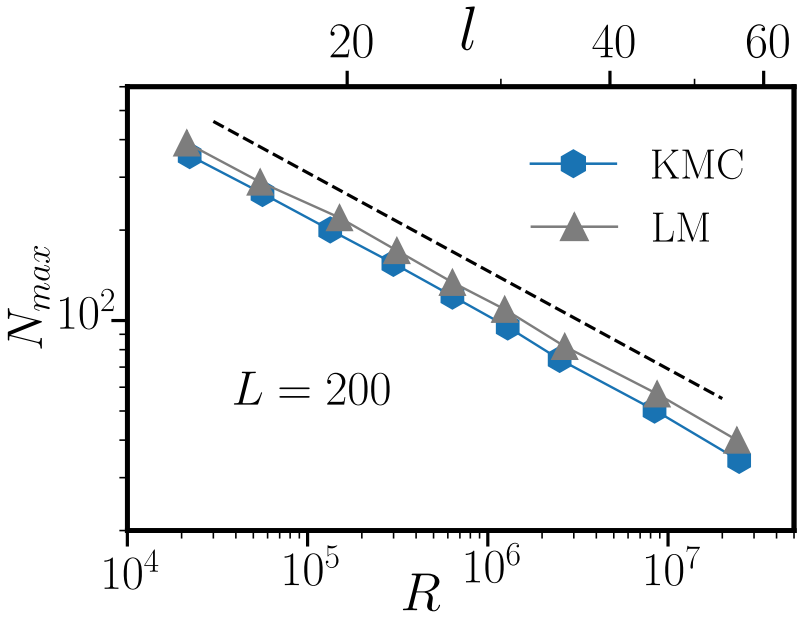

Fig. 6.14: N_{max} in the submonolayer growth regime on two dimensional substrates of lateral size $L = 200$ for various growth conditions in the KMC and the LM model, respectively. The black dotted line follows $\sim R^{-1/3}$.

is closest to the initial adsorption site. In case that their exist multiple sites at the same distance, we randomly choose one of them. However, we want to emphasize that different variants for choosing the final site are possible. This is of great importance for growth conditions where edge-diffusion and bond breaking is possible.

The submonolayer growth regime: To demonstrate that our approach also works on two-dimensional lattices, we show in Fig. 6.14 N_{max} in the submonolayer growth regime as function of R and corresponding $P(l|l_n, \sigma^2)$ (with optimal σ^2). The results for N_{max} reflect a good agreement between both models for all considered growth conditions. In particular, N_{max} decays identically in both models as the values of R and l (together with the optimal σ^2) are increased.

By analyzing $P(S)$, we observe, analogous to the one-dimensional scenario (see Fig. 6.6), a shift of the peak of $P(S)$ towards smaller values of S as the strength of diffusional fluctuations is increased (see Fig. 6.15). Again, this results in the emergence of a left shoulder in $P(S)$ as observed earlier for $d = 1$. If the variance σ^2 takes too large values, the distributions $P(S)$ become monotonically decreasing functions of S. This behavior is clearly unphysical. For $l = 10$, this is seen already at $\sigma^2 = 5$, while for $l = 30$ it only occurs for $\sigma^2 > 10$. Therefore, also for $d = 2$, the value of σ^2 has to be chosen carefully.

The multilayer growth regime: To compare both models on two-dimensional lattices in the multilayer regime, we show exemplary lattice structures in Fig. 6.16 for two values of R and corresponding optimal distributions $P(l|l_n, \sigma^2)$. While the lattice structures at $R = 4 \times 10^2$ look indistinguishable [see Fig. 6.16(a) and (b)], we find visible deviations at

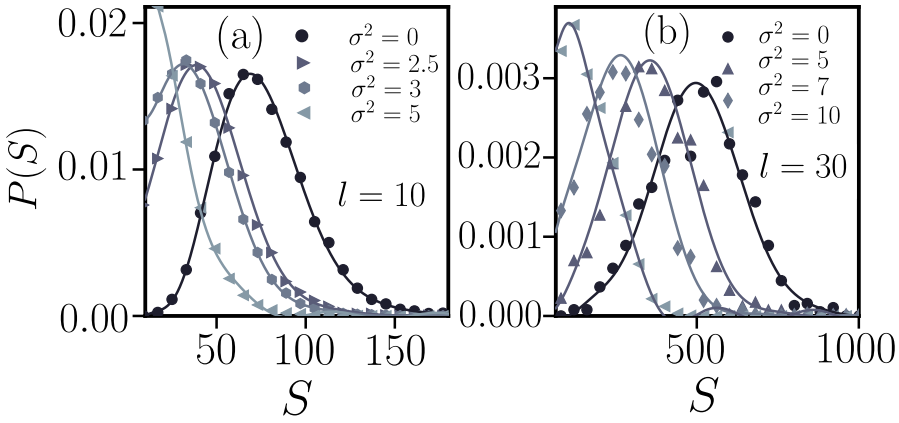

Fig. 6.15: Cluster size distribution $P(S)$ during submonolayer growth at $\theta = 0.3$ on two dimensional substrates of lateral size $L = 200$ for two values of l and various strengths of diffusional fluctuations controlled via σ^2 in the LM model.

$R = 2 \times 10^4$ [see Fig. 6.16(d) and (e)]. These discrepancies may be resolved by using a different variant for choosing the final attachment site as discussed earlier in this section. Despite the spatial deviations, the functions $\Gamma(r)/\Gamma(0)$ for $R = 4 \times 10^2$ and $R = 2 \times 10^4$] reveal a good agreement between both models concerning height-height correlations and the correlation length ξ_0. Both of these quantities are very sensitive to changes in l and σ^2, as shown in Fig. 6.12 and Fig. 6.13 for the one-dimensional case.

6.7 Conclusions and Outlook

In this work, we have introduced an extended limited mobility (LM) model for nonequilibrium surface growth, which is capable of predicting *low* temperature MBE growth for arbitrary values of the growth parameter R. Compared to earlier versions of the LM model, particularly the DT model, our extension concerns the diffusion length l which we treat as a variable parameter whose value for each deposited particle is chosen from a Gaussian distribution.

To relate our LM model to another standard model for surface growth, namely KMC, we proposed to set the mean value of l equal to the nucleation length l_n resulting from short KMC simulations for the particle displacements. We tested this ansatz by comparing LM and KMC results for the cluster evolution during sub- and multilayer growth. While the LM model with fixed l works well at small values of the growth parameter R, this is not the case at larger R. As a next step, we therefore included fluctuations to the diffusion length of particles in the LM model in order to model diffusional fluctuations. Specifically, we employed a Gaussian distribution where the mean diffusion length l is given by the nucleation length extracted from KMC, whereas the variance σ^2 is fitted to match the maximum number of clusters N_{max} in KMC simulations during growth in the submonolayer regime. For each considered value of l we have identified the variance σ^2

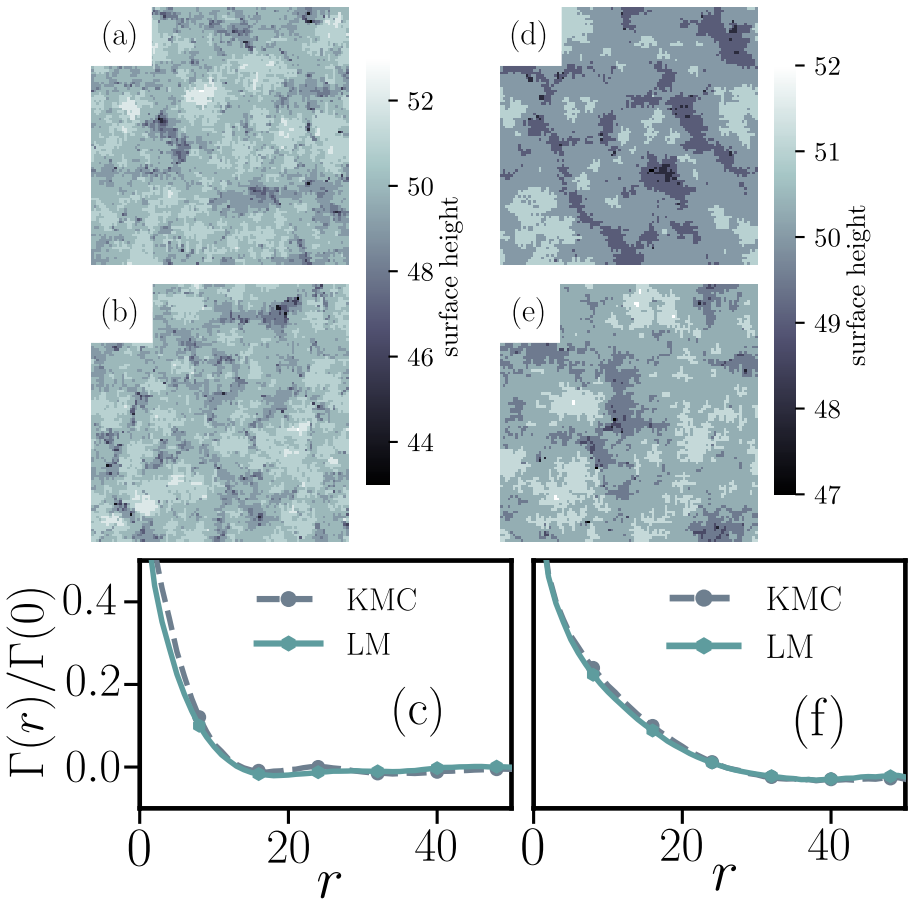

Fig. 6.16: (a) Exemplary lattice structures (of size 100×100 from lattice with $L = 200$) from KMC simulations with $R = 4 \times 10^2$ (a) and $R = 2 \times 10^4$ (d) at $\theta = 50$ along with results obtained from the LM model with $l = 4$ and $\sigma^2 = 1.1$ (b) $l = 11$ and $\sigma^2 = 2.8$ (e) at the same coverage, $\theta = 50$. (c) and (f) depict $\Gamma(r)/\Gamma(0)$ for both considered growth conditions in the KMC and the LM model, respectively.

that leads to $N_{max}^{KMC} - N_{max}^{LM} \approx 0$. Using these *optimal* values of σ^2 also lead to nearly identical cluster size distributions $P(S)$.

Turning towards multilayer growth, we compared layer coverages for different growth conditions and found excellent agreement between both models. Moreover, we analyzed in detail the global interface width for different system sizes up to coverages deep in the regime of saturated surface roughness. Not only is transient regime of the global interface width identical in both models, but also the crossover coverage where saturation is reached. Additionally, we showed that by using our LM model with variable diffusion length, also the values of the saturation roughness match in both models for all considered system sizes and growth conditions. A scaling analysis revealed that the LM model belongs to the VLDS universality class for arbitrary diffusion lengths. We also observed that the variance σ^2 can strongly alter the interface height profile in the high coverage regime. As the value of σ^2 is increased, we observed less and, at the same time, steeper mounds. Moreover, we found good agreement concerning height-height correlations in both models using the optimal values of σ^2 in both, one- and two-dimensional systems.

The present model can be extended in various directions. First of all, it is possible to modify the model such that it also mimics MBE growth at *high* temperatures where detachment of particles is present. This may be achieved by using a mixture of the transition rules of the DT and the Wolf-Villain model [247, 307] with a variable, distributed diffusion length. Concerning the two-dimensional scenario, it would be very interesting to investigate how different variants for the rules regarding the final attachment site of deposited particles affects the cluster shape properties and the overall growth behavior. This is especially important when moving towards higher temperatures or lower binding energies, where clusters are usually compact rather than ramified.

Second, the effect of an additional energy barrier for interlayer diffusion processes across step-edges, usually referred to as Ehrlich-Schwoebel barrier, can be included to account for growth instabilities. Normally, in presence of such a barrier, KMC simulations are slowed down due to the sampling of diffusion trajectories of free particles on top of clusters that are reflected at the cluster edge due to the additional energy-barrier for crossing step-edges. A physically reasonable treatment of an Ehrlich-Schwoebel barrier in our LM model would lead to a further computational speedup compared to KMC simulations.

Finally, we want to point out that, especially concerning growth conditions where the critical cluster size takes large values, there exist alternative numerical techniques beyond the lattice-based models with limited particle mobility that can be further advanced to realistically model this specific growth regime. Examples include level-set [283] and geometry-based [284] models.

7 Applying machine learning to nonequilibrium surface growth

In recent years, machine learning (ML) has become an important part in the discovery of novel materials [100, 101, 103, 106, 339, 340]. In future investigations, ML approaches may also facilitate the industrial fabrication, i.e., the nonequilibrium growth process, of high quality crystals and thin films. In the following, we demonstrate that a convolutional neural network (CNN), which is trained on labeled data, can unravel the microscopic details of single particle diffusion processes during thin film growth. Diffusion processes of particles on the surface play an important in thin film growth role since they heavily affect the morphology, and thus, also the quality of crystalline materials fabricated by means of vapor deposition techniques [9, 13, 23]. In this chapter, we perform KMC simulations of sub-monolayer surface growth to generate a training and validation data set for a CNN. We show that the CNN, which was trained under supervised learning, can predict the lateral binding energy E_B and the diffusion barrier E_D, and thus, the single particle process rates from a single snapshot of the surface morphology with an accuracy. Additionally, we further demonstrate that the CNN can also correctly predict the underlying values of E_D and E_B from images with noise and lower than atomic scale resolution. We show that the prediction performance of network is not much affected by noise. The latter is inevitable in experimental atomic force microscopy (AFM) or scanning tunneling microscopy (STM) images of thin film surfaces. This paves the way to apply the on noisy numerical data trained CNN to experimental data in order to unravel the microscopic energy barriers of materials under experimental conditions from snapshots of the surface configurations.

7.1 Fundamentals of convolutional neural networks

Over the last decade, ML based approaches have been applied in various disciplines including finance, biology, chemistry, materials science, mathematics and physics and may support fundamental research in these fields [100, 101, 103, 105, 106, 341–344]. Focusing on physics, various ML techniques have been successfully applied in materials science, many-body quantum matter, statistical physics, particle physics, cosmology and quantum computing [341, 345–351]. For example, CNNs have proven to identify different phases of matter and, moreover, have shown to detect phase transitions in different classical and quantum condensed-matter systems. Especially deep learning methods have an enormous potential for applications in various disciplines [352, 353]. Recently, deep

learning had been combined with statistical mechanics to develop Boltzmann Generators that are trained on a given energy function and capable to generate unbiased *one-shot* equilibrium samples of representative condensed matter systems and proteins [354]. These are just a few of the many examples that show the great potential of ML applications in the field of physics.

In the following we will give a short introduction to the basics of CNNs. We will discuss the general structure of a CNN and explain how input data is processed through the network. Moreover, we shortly sketch the learning process of a CNN by which it improves it's prediction performance. Details of the functioning of neural networks are well explained in the book by Bishop [355] and the recently published book by Goodfellow [356]. Moreover, recent review articles summarize the current standing of ML applications in physics [341, 357].

The convolution operation: CNNs represent a specialized class of neural networks. In particular, they are suitable for processing input data that exhibits a known, discrete, grid-like topology. Therefore, they are especially appropriate to process input data in the form of pixel images. Of fundamental importance for the functioning of a CNN is the convolution operation. In general, the convolution of some real-valued functions $I(t)$ and $K(t)$ is defined as the integral of the product of these two functions where one, say $K(t)$, is reversed and shifted, $K(\tau - t)$. Then, the convolution of $I(t)$ and $K(\tau - t)$ can be written as

$$(I * K)(t) = \int_{t=-\infty}^{t=\infty} I(t)K(\tau - t)dt. \tag{7.1}$$

If we only allow integer values for the index t, we can define the discrete convolution of the functions $I(t)$ and $K(t)$,

$$(I * K)(t) = \sum_{t=-\infty}^{t=\infty} I(t)K(\tau - t). \tag{7.2}$$

Since we want to feed our CNN with two-dimensional input data, we have to add another argument. A discrete convolutions in two dimensions with arguments t and k (where κ is used to denote shifts in k) are given by

$$(I * K)(t, k) = \sum_{t=-\infty}^{t=\infty} \sum_{k=-\infty}^{k=\infty} I(t, k)K(\tau - t, \kappa - k). \tag{7.3}$$

In particular, the first argument, i.e., the function $I(t, k)$, can be interpreted as the input, whereas the second function $K(\tau - t, \kappa - k)$ represents the filter kernel that slides across the convolutional layer and thereby performs the integration, i.e., the sum in Eq. 7.3. Often the output of such a convolution is referred to as feature map. Processing of data through a CNN occurs via discrete convolutions between the input data and the filter kernel. This is exemplary shown in Fig. 7.1, where we illustrate for a random cutout of a two-dimensional convolutional layer the convolution with a 2×2 filter kernel that is used

to process the input data further to an activation function (in general, a sigmoid function or a rectifying linear unit) whose output corresponds to the activity of the neurons in the next convolutional layer. In fact, a discrete convolution simply corresponds to a matrix multiplication. We explicitly show the convolution of the input with the filter kernel for the first three operations in the first and second line of the random input data in Fig. 7.1. The brightness of the neurons labeled from A to T corresponds to their activity $a \in [0, 1]$, where $a = 0$ corresponds to black and $a = 1$ to white.

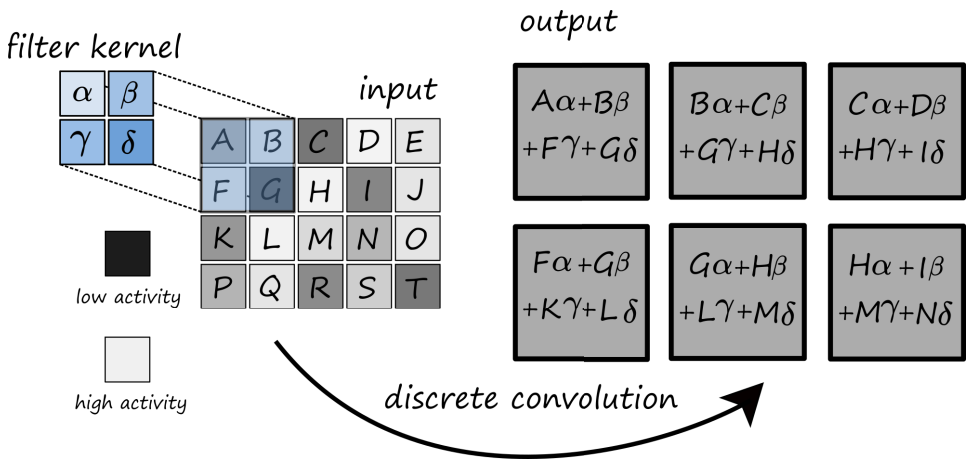

Fig. 7.1: Illustration of a two-dimensional convolution operation on the example of a 5×5 pixel input data and a 2×2 pixel filter kernel. A discrete convolution is performed for each position of the filter kernel in order to generate the output which is partly shown for 6 convolutions., i.e., positions of the filter kernel. matrix

Basic architecture and data processing in a CNN: In general, the structure of a convolutional layer consists of three distinct parts, i.e., there are three steps that have to be executed in order to transfer the data from one convolutional layer to the next convolutional layer. In the first step, one performs several convolutions of the input with the filter kernel in parallel to produce a set of linear activations as illustrated in Fig. 7.1. More precisely, at each position of the filter kernel, a convolution is performed. This means that each pixel value of the convolution layer is multiplied with the value at the respective position in the filter matrix. One simply calculates the sum of all multiplications between the layer and the filter kernel. These dot products between the weights of the filter kernel and the inputs are integrated across channels as the filter slides across the convolutional layer. In the second stage, each of these linear activations which we just obtained from the convolution is used as input for a nonlinear activation function. In early studies, the sigmoid function

$$\sigma(a) = \frac{1}{1 + \exp(-a)} \tag{7.4}$$

was often used for this task, but it has been widely replaced by the rectified linear activation (ReLU) which is defined as

$$R(a) = \max(0, a). \tag{7.5}$$

Specifically, the ReLU activation function tackles the problem of vanishing gradients that may occur when the sigmoid function is used [352, 355, 356]. This step of the data

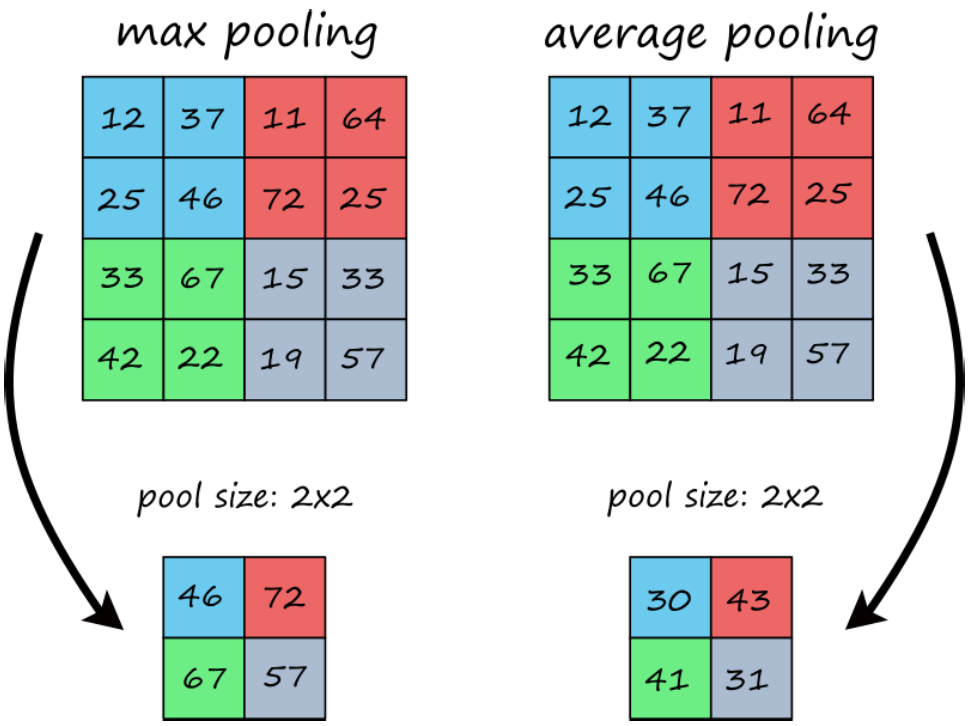

Fig. 7.2: Comparison the max pooling with the average pooling operation based on a two-dimensional convolutional layer of size 4×4 with random entries. The pooling operation in both cases is such that the size of the layer is reduced to 2×2 pixels. The different colors indicate the neurons which are grouped for the pooling operation. By using max pooling, the largest entry is used for the down-scaled layer, whereas for average pooling, the average value, i.e., activity, of the involved neurons is taken.

processing, where the output of the convolution is used as input for the activation function is often called detector step. In the last step, one often applies a pooling operation as exemplary illustrated in Fig. 7.2 where the processes of max pooling and average pooling are shown for an example with random data. Specifically, the process of pooling can, to some extend, help to make the output approximately invariant to small translations of the input data. It may thereby improve the statistical efficiency of the network [352, 356]. In this context invariant means that most of the pooled output values do not change upon small translations of the input. Moreover, the size of the input images often has to be reduced to a single-valued number. To this end, pooling is used to reduce the size of the convolutional layer in a CNN, i.e., the number of neurons in the next layer. Pooling thereby compresses the information content to a smaller scale [352, 356]. However, pooling can be an aggressive step that may heavily affect the transferred information. The trend in recent fundamental studies of neural networks is to decrease the filter size or to completely abandon the pooling process [352, 355, 356]. Within the CNN we use to predict the energy barriers involved in surface growth in Sec. 7.2, we use the max pooling operation. After the input data has been processed through a certain number of convolution and pooling layer, it will further be transferred to a few dense, i.e., fully connected, layer before the final output is calculated. These fully connected layer are identical to simple multilayer perceptron (MLP) networks which are used to learn for the respective classification or

regression task [358]. In contrast, the preceding convolutional layer extract the relevant features for the MLP. This means that the data from the last convolutional layer has to be flattened as it is transferred to the first fully connected layer. To this end, one simply reshapes the two-dimensional convolutional layer and transforms it into a one-dimensional layer, i.e., transforms the matrix into a vector. From this, the processing of the data to the final output is identical to the functioning of a standard MLP network [358]. In short, a standard CNN consists of three different types of layer. There is an alternating set of convolutional and pooling layer which are followed by some fully connected layer. Each of these three different layer types performs a different task on the data and is characterized by different layer-specific parameters that are optimized during the training process.

Basic learning mechanism of a CNN: Similar to the learning of weights in conventional MLPs, learning within the part of a neural network where we have convolutional layer is such that the network learns the most optimal filter kernels for recognizing specific objects and pattern it identifies in the input data [352, 355, 356]. To this end, the CNN learns multiple filters in each layer of the network. More precisely, each filter kernel learns to identify a specific pattern, or feature of the input data. That's why the collections of many parallel filters are called stacks of the respective feature or activation maps [352, 355, 356]. Deep neural networks are usually trained by using the stochastic gradient descent optimization algorithm [359]. In this context, the learning rate is an important hyper-parameter that controls how much the weights of the model are changed in each training step in response to the estimation error. The learning rate has to be chosen carefully because too small values may result in a time consuming training process. Moreover, the network could get stuck without further improving it's performance [355, 356]. In case the learning rate is chosen too large, the network may learn a sub-optimal set of weights too quickly and the total training process might furthermore be completely unstable. The learning rate is one of the most important hyper-parameter when it comes to the configuration of neural networks. The predictions of the network in supervised learning are connected with a loss function that plays an important part in the training process. In most cases, one uses a cross-entropy loss function. Since all weights of all the filter kernel contribute to the activity of neurons in all the following layer, any change of the networks weights will affect the output. Thus, all these changes contribute to the final loss. In our case, where the CNN learns to predict the values of the diffusion energy E_D and the binding energy E_B, the network simply attempts to change the weights such that the difference between the predictions of E_D and E_B are as close as possible to the true, labeled values of E_D and E_B that were used in the corresponding KMC simulation from which the shown surface configuration snapshot originates.

7.2 Unraveling the energetics of nonequilibrium surface growth via machine learning

In the following, details of the KMC simulation setup that was used to generate the training and validation data set are discussed. We explain how the surface snapshots are modified in order to make them comparable to real AFM or STM surface snapshots. Then, we shortly discuss the structure of the CNN that wa used for training and validation. At the end, we present results of the networks performance on predicting the diffusion energy E_D and the binding energy $_B$ from noise-free and noisy surface snapshots obtained from KMC simulations.

7.2.1 Simulation details and data set generation

In the following, we discuss details of the training data and validation data sets and explain specific details of the CNN that we use to determine the values of the diffusion energy E_D and the binding energy E_B from snapshots of sub-monolayer surface growth on a square lattice at fixed temperature T and a constant particle deposition rate F. We explain in detail how we visually modify the surface snapshots generated by KMC simulations in order to make them comparable to the appearance of real experimental atomic force microscopy images of sub-monolayer thin film morphologies generated by vapor deposition techniques.

Generation of the training and validation data set: The surface configurations we use for training and validation of the CNN are obtained from event-driven KMC simulations according to the algorithm which is explained in detail in Sec. 2.4.3. Within the KMC simulations, nucleation and the subsequent cluster growth occur via the two stochastic processes of adatom deposition and surface diffusion. To this end, coarse-grained particles, i.e., we fully neglect internal rotational and vibrational degrees of freedom, are deposited with an effective rate $F = 0.166(7)$ ML/s on randomly chosen sites $\mathbf{a} = (m, n)$ of a discrete square lattice of lateral length L, where $m, n \in [1, L]$. We apply periodic boundary conditions and the solid-on-solid condition which forbids vacancies and overhanging particles. The surface coverage θ corresponds to the number of deposited particles divided by L^2. In our KMC simulations, growth proceeds at a constant speed via $\theta = ft$, with t being the simulation time. After deposition on the substrate, which is kept at a fixed temperature of $T = 313$ K, adatoms explore the potential energy surface of the substrate via stochastic Arrhenius-type hopping processes $\mathbf{a} \rightarrow \mathbf{b}$. The local energetic environment of a particle at site $\mathbf{a}$ determines the activation energy E_A it has to overcome in order to perform a diffusion processes to a neighboring lattice site $\mathbf{b}$ with corresponding diffusion rate $D_{\mathbf{ab}}(T) = [(2k_\mathrm{b}T)/h] \exp[-E_A/(k_\mathrm{b}T)]$ as explained in detail in Sec. 2.4.2. In accordance with KMC simulations performed in C. 5, C. 6 and C. 8, the activation energy consists of

up to three individual energy barriers, $E_A = E_D + nE_B + S_{\mathbf{ab}}E_S$ (see Sec. 2.4.2). The three barriers E_D, E_B and E_B in interplay with the effective deposition rate F and the substrate temperature T, eventually determine the resulting surface morphology of the growing thin film. In all simulations which are used for training and validation of the CNN, the value of the Ehrlich-Schwoebel interlayer diffusion barrier is fixed to $E_S = 0.1$ eV. We chose this value because it is in the typical range of the interlayer diffusion barrier of many materials [171, 188]. Furthermore, the value is chosen such that at $\theta = 0.15$, i.e., the coverage of the surface snapshots for training and validation, stable clusters in the second layer are not present. In fact, the exact value of E_S is not critical for the morphology, because we investigate the low coverage sub-monolayer regime, $\theta = 0.15$. At this point we want to note that the CNN used to determine the values of E_D and E_B could in principal also be used to determine the value of E_S. To this end, one should fix E_D and E_B and train the network on data where the value of E_S is varied in a certain parameter range. In contrast to E_S, the values of the diffusion and the binding energy are varied. Specifically, $E_D \in [0.4, 0.4125, \ldots, 0.5375, 0.55]$ and $E_B \in [0.1, 0.10625, \ldots, 0.39375, 0.4]$. As a consequence, there are 13 individual values for E_D and 49 for E_B such that there are $13 \times 49 = 637$ combinations for E_D and E_B in the training and validation data set. The distribution of diffusion rates $D_{\mathbf{ab}}(T)$ at substrate temperature $T = 313$ K for particles with up to $n = 4$ bonds of strength E_B is plotted in Fig. 7.3.

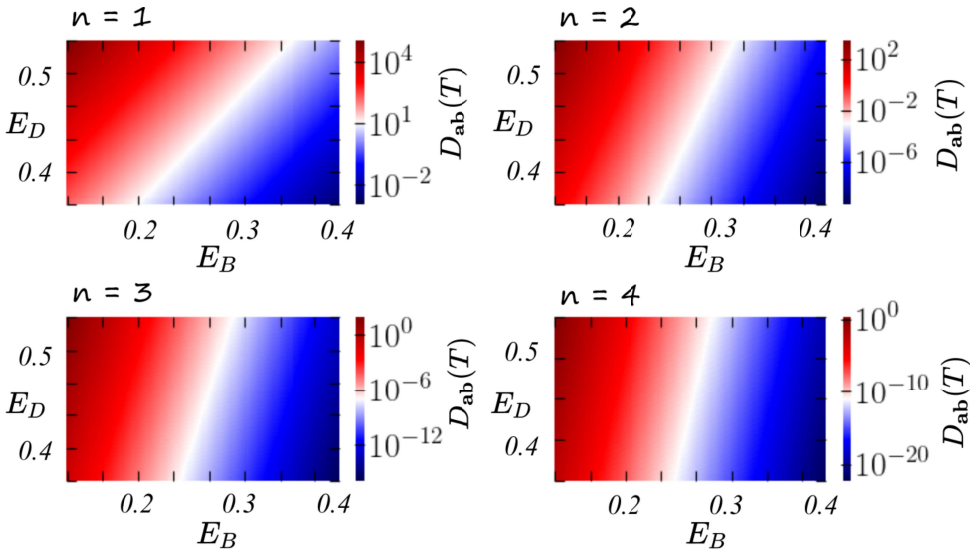

Fig. 7.3: Heatmaps for the diffusion rates $D_{\mathbf{ab}}(T)$ as function of the diffusion energy E_D and the binding energy E_B for particle with different numbers n of lateral bonds at substrate temperature $T = 313$ K. The attempt frequency of diffusion processes $D_{\mathbf{ab}}(T)$ is given by $(2k_{\mathrm{b}}T)/h$.

As can be seen there, the rate for particle diffusion ranges from $D_{\mathbf{ab}}(T) \sim 10^{-22}$ up to $D_{\mathbf{ab}}(T) \sim 10^5$, and thus, spans across around ~ 25 orders of magnitude. Exemplary lattice configurations for some combinations of E_D and E_B at $E_S = 0.1$ eV, $T = 313$ K and $F = 0.0166(7)$ monolayer/s at coverage $\theta = 0.15$ are shown in Fig. 7.4. The size of the snapshots is 100×200 lattice sites which roughly corresponds to an image size

of 50×100 nm for typical lattice constants in thin film growth experiments. The shown surface configurations reveal a wide range of island (cluster) sizes, island densities and island shapes. One can clearly see that for the smallest values of E_D and E_B, one gets very few, almost quadratic islands, whereas for the highest values of E_D and E_B, there are many small, rather dendritic clusters on the substrate. For increasing values of E_D, molecular diffusion is hindered and adatoms are less likely to diffuse the average distance to reach an existing nucleus. It is more likely that they form new clusters with freshly deposited particles. As a consequence, more islands nucleate on the substrate compared to lower values of E_D where the average traveled distance per particle is usually larger. Similarly, an increase in E_B leads to an increased number of nucleation events, and thus, results in a higher island density compared to simulation runs with lower values of the binding energy E_B. Different combinations of E_D and E_B then result in varying island shapes ranging from compact rounded to rectangular and dendritic islands with fractal dimensions from $D_f \approx 1.71$ (diffusion-limited aggregation cluster) to $D_f = 2.0$ (compact cluster). However, if we compare snapshots with rather similar energy barriers, differences in the surface morphology are not visible to the eye. However, as will be shown in the following, CNNs detect the nonetheless existing differences in the cluster morphologies of configurations simulated with very similar values for E_D and E_B and are able to determine the values of the energy barriers with high precision.

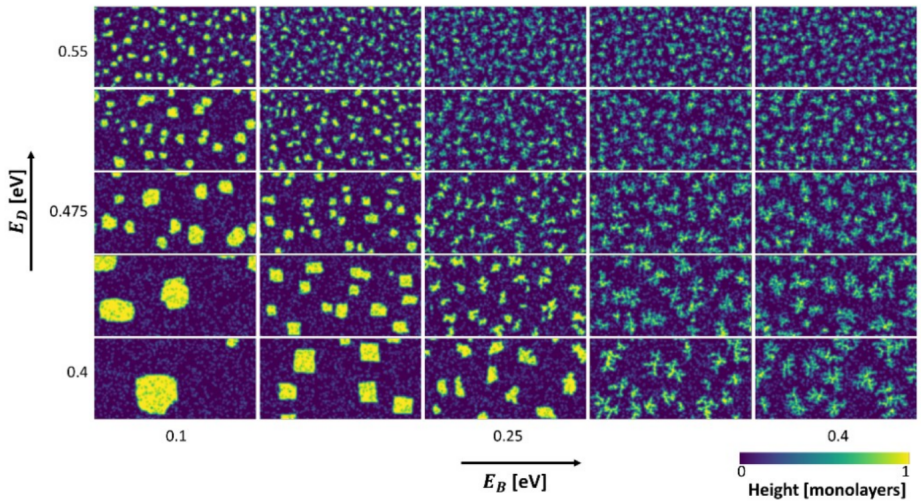

Fig. 7.4: Surface morphologies obtained from KMC simulations of submonolayer growth for different values of E_D and E_B at fixed adatom deposition rate $F = 0.0167$ monolayer/s, temperature $T = 313$, and coverage $\theta = 0.15$, result in a wide range of island sizes, island densities and compact or dendritic island shapes. The images shown have added noise and smoothing, i.e., lowered resolution, to mimic surface images obtained from scanning probe microscopy experiments. The scale corresponds to 100×200 lattice sites, that is roughly 50×100 nm for typical lattice constants in growth experiments.

Adding noise and Gaussian blur to surface snapshots: In order to mimic the noise that is omnipresent in real AFM and STM snapshots, we alter the surface configurations by adding various amounts of random noise and applying Gaussian smoothing. In particular, we use salt and pepper noise together with Gaussian blur. The salt and pepper noise

flips a certain percentage of pixels. Thereby, it generates noise by randomly adding and removing adatoms to the system when empty or filled lattice sites are flipped. Moreover, it creates holes within islands. Through the generation of a random number of adatoms in every image, we reduce correlations in the adatom density of snapshots which are generated by randomly shifting or rotating a snapshot from the same KMC run. Depending on the specific experimental technique used to generate surface snapshots, other noise variants such as background noise, or line-scan artefacts as found in scanning probe microscopy images may be added to the training data set to make the snapshots as realistic as possible. Since we do not focus on mimicking the peculiarities of specific experimental techniques, we did not add such specific noise terms. However, we want to point out that this, in principle, is no problem. After adding noise to the KMC results, a Gaussian smoothing filter was applied to simulate a limited, sub-atomic resolution that some experimental techniques may have. The Gaussian smoothing was implemented in Python using multidimensional image processing (scipy.ndimage) with the $gaussian_filter$ function. This function performs a convolution of the image with a Gaussian kernel whose standard deviation is varied between 0 and 20 pixels, corresponding to blurring of 0 to 20 lattice constants. We use Gaussian smoothing with different standard deviations of the Gaussian filter kernel. For example, the images shown in Fig. 7.4 contain 5% salt and pepper noise and smoothing with a two-dimensional Gaussian with one pixel (i.e., one lattice constant) standard deviation, i.e. $\sigma^2 = 1$.

Details of the data sets: We carried out multiple realizations (on average we performed ~ 10 realizations) for each of the 637 E_D-E_B-pairs and let the simulations run on square lattices of lateral length $L = 200$ sites until a coverage of $\theta = 0.15$ is reached. This means that the unaltered, raw surface images obtained from KMC simulations consist o40000 pixels and contain 6000 particles. In total, we performed ~ 6000 individual KMC runs at identical growth conditions, i.e., the same temperature $T = 313$ K and the same deposition rate $F = 0.0166(7)$ monolayer/s (which corresponds to $F = 1$ monolayer per minute). We made sure that the data sets for training and validation are strictly separated from each other, irrespective of the data augmentation that is applied in the form of rotations and random lateral shifts of the snapshots. We use 5 to 6 individual realizations of each E_D-E_B combination for the training process. In order to increase the size of the data sets, we rotate each picked configuration by a random multiple of $90°$. Further, we shift the whole configuration either in the x- or the y-direction by a random number of lattice sites. This not only increases the size of the data sets, but also leads to a higher variability of the training and validation sets. Salt and pepper noise empties and fills a fixed percentage of lattice sites. However, which sites are flipped from empty to filled and vice versa is completely random in each configuration. This further increases the variability of our data sets. For grayscale images, the pixel value is a single number that represents it's brightness. We use the byte image pixel format where the number on each lattice site of the surface configuration is an integer in the range of values from 0 to 255. Typically zero represents a black and 255 a white pixel. Therefore, empty lattice sites are represented in white,

whereas particles in the topmost layer of the respective surface image are given in black. The color of all lattice sites with a height in between 0 and the maximum height is given by a height-dependent shade of gray. For simplicity, we rescale the grayscale axis between 0 and 1 such that 0 corresponds to black and 1 represents white pixels.

7.2.2 Details of the convolutional neural network

Architecture and details of the CNN: In order to predict the diffusion energy E_D and the binding energy E_B from static atomic-scale snapshots of sub-monolayer surface configurations, we use a well-established CNN architecture that has proven to perform well for image recognition and classification tasks [360]. The structure of the sequential CNN from the first convolutional layer that takes the two-dimensional data as input, i.e., the sub-monolayer surface configurations, up to the single-valued output, i.e., the predicted diffusion energy E_D and binding energy E_B, is illustrated in Fig. 7.5. We use a standard two-dimensional deep CNN which is a smaller version of the standard VGG16 CNN [360] (from the Visual Geometry Group at Oxford University) which we implemented in TensorFlow [361]. Our neural network consists of a sequence of 13 convolutional layer which are followed by three fully connected layers of decreasing size from 2048, to 1024 and 32 up to the final output that is the guess for the diffusion energy E_D and the binding energy E_B.

In Fig. 7.5 (a) we show a exemplary conventional fitting procedure that can be applied in order to extract energy barriers from surface growth experiments and compare the workflow with our proposed method which involves ML techniques. Our proposed method can determine the atomistic energy parameters E_D (diffusion barrier) and E_B (binding energy) from a single image of a thin film in the sub-monolayer growth regime. We use a deep learning CNN architecture which is illustrated in In Fig. 7.5 (b). The architecture of the CNN is similar to the VGG16 network [360]. Convolutional layers $Conv1_1$ to $Conv5_3$ use a 3x3 pixel filter kernel and the number of filters increases from 16 to 128 in deeper layers.

The filter kernel is fixed to a very small receptive field of size of 3×3 pixel in all layers of the network from the first layer $Conv\_1$ up to the deepest convolutional layer $Conv\_5$. The size of the first convolutional layer $Conv1\_1$ that takes the surface configurations is of size 200×200 and contains 16 filters of size 3×3. Layer $Conv1\_2$ has the same size and uses an identical number of filter. Following the two first convolutional layer, we use max pooling in order to minimize over-fitting and to reduce the dimensionality, i.e., the number of parameters. This process reduces the computational cost. The size of the following two convolutional layer $Conv2\_1$ and $Conv2\_2$ is 100×100. We use the same filter kernel size and increase the number of filters to 32. Again, after the input data has been processed through these two layer, we again use max pooling and transfer the data to convolutional

layer $Conv3\_1$ which is of size 50×50. Here, and also in $Conv3\_2$ and $Conv3\_3$, the number of filters is set to 64. Again, max pooling is applied as the data is transfered to $Conv4\_1$, $Conv4\_2$ and $Conv4\_3$ which are all of size 50×50. All of them exhibit 128 filters. The same is true for layer $Conv5\_1$, $Conv5\_2$ and $Conv5\_3$. After them, we again apply max pooling and we flatten the data which is transfered to a fully connected layer of lateral size 2048. Our CNN determines the values of E_D and E_B with a higher precision compared to other conventional neural network architectures we tested. These include a VGG19 CNN [360] and an AlexNet inspired CNN [362]). In particular, comparing our CNN with the AlexNet inspired network (which is not as deep as our VGG16-type CNN) showed larger prediction errors in E_D and E_B.

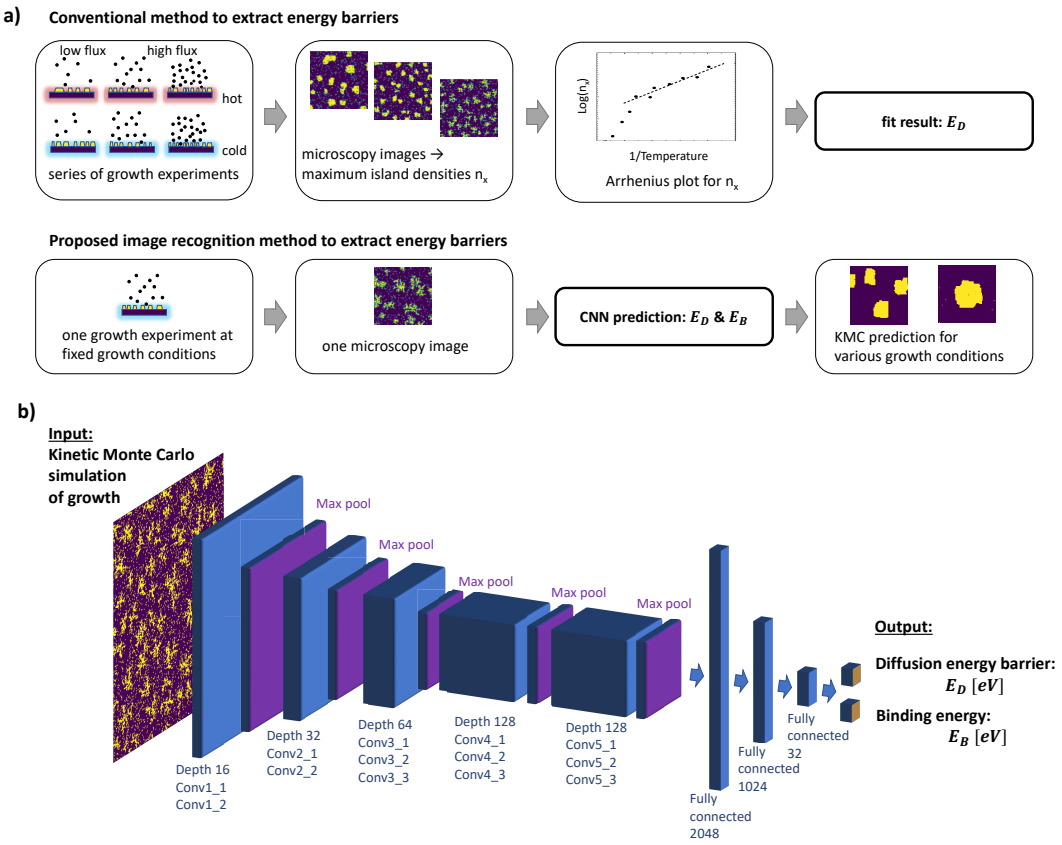

Fig. 7.5: (a) Comparison of a conventional fitting procedure to extract energy barriers from surface growth experiments (top) with our proposed method of applying a ML techniques in order to predict energy barriers (bottom). (b) Image recognition can determine the atomistic energy parameters E_D (diffusion barrier) and E_B (binding energy) from a single image of a thin film in the submonolayer growth regime. We use a deep learning CNN architecture very similar to the VGG16 network [360]. Convolutional layers $Conv1\_1$ to $Conv5\_3$ use a 3×3 pixel filter kernel and the number of filters increases from 16 to 128 in deeper layers.

7.2.3 The two-step training process

First training step using noise free input data: The CNN is trained in two stages using only surface configurations from the KMC training data set. We leave the validation data

set for performance checks of our network. In the first stage, we trained the CNN for a total number of 500 epochs (where we use ~ 55000 augmented images per epoch) on noise-free, full-resolution data. This means that each of the input surface images contains 40000 pixel. Each batch was augmented via rotations of all snapshots by a random multiple of $90°$ and lateral shifts of by a random number of pixels in the x- and y direction. Due to the applied periodic boundary conditions in the KMC simulations, such random shifts of the configurations result in surface snapshots which are not altered by any border effects. The with noise-free trained CNN achieved a mean absolute percentage errors of 0.8% in E_D and 4.0% in E_B without showing any signs of overfitting. Using the investigate toolkit for interpretable machine learning [363], we found that the rim of islands is important for predictions but sometimes also individual pixels representing unbound, freely diffusing adatoms had a significant role. As individual adatoms are very difficult to observe in experiments at higher temperatures (due to their high mobility), predictions based on properties of the adatom densities are undesirable. Consequently, we introduced (salt and pepper) noise terms that stochastically added and removed adatoms in the surface images we used in a second training step.

Second training step using noisy and blurred input data: We performed a second training step with noisy and blurred images. The salt and pepper noise was added in order to reduce correlation effects due to free adatoms on the substrate which may affect the prediction performance of the CNN. Further, we mimicked experimental conditions by adding salt and pepper noise together with Gaussian blur to the surface snapshots to investigate whether the CNN is, in principle, still able to make predictions for images with noise and limited lateral resolution. The latter modifications resemble the quality of experimental STM or AFM snapshots of surface configurations. The percentage of pixels affected by salt and pepper noise and the standard deviation σ^2 of the Gaussian blur were randomly set in each image augmentation procedure. The training with noisy and blurred input data was continued for another 500 epochs resulting in a validation performance of 1% error in predictions of the diffusion barrier E_D and an error of 4.5% in the predictions for the binding energy E_B. As one would expect, the CNN that is trained on a wide range of clean and noisy images performs slightly worse on clean snapshots only compared to the CNN that was trained on clean data only. While the CNN used here is trained to accept a wide range of noise levels and resolution settings, for a given experiment even higher CNN performance may be achieved by training with synthetic data for the specific noise and resolution of the experiment. In the context of this work, our training procedure however enables direct comparisons of the performance of one CNN with different noise and resolution settings.

7.2.4 Energy barrier prediction performance

Prediction performance on noise-free data: After the two-step training process, we tested the prediction performance of the CNN with a separated validation data set that contains surface snapshots from ~ 1800 individual KMC simulations. These simulations were performed at the same growth conditions that we used to generate the training data set, i.e., $T = 313$ K and $F = 0.0166(6)$ monolayer/s. We made sure that the individual KMC realizations of the validation set were not part of the training data set. The validation process to test the performance of the CNN is as follows. For each presented surface snapshot with labeled *true* values for E_D and E_B that were used in the corresponding KMC simulation, the trained CNN makes a prediction for the values of these two energy barriers. Specifically, for each shown surface image, the network gives a prediction for both energy barriers simultaneously.

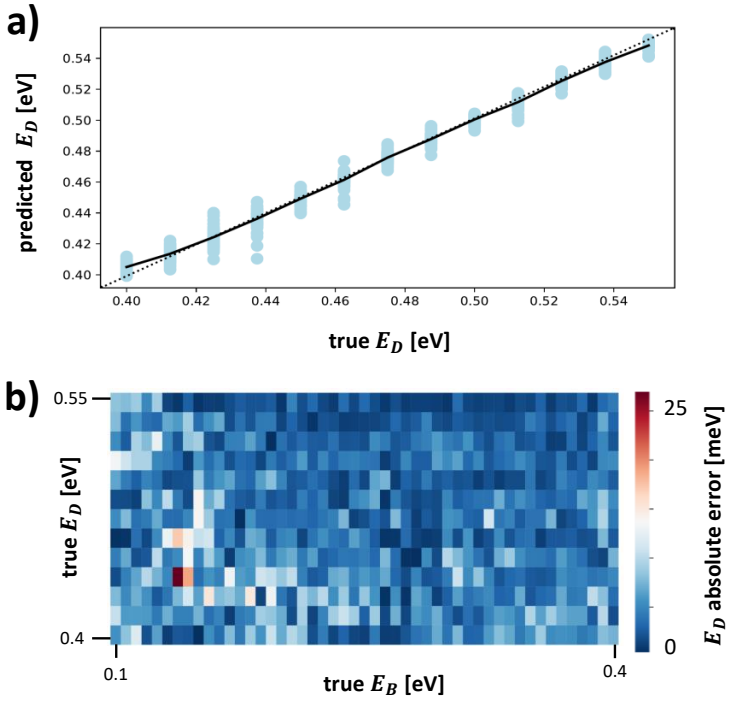

Fig. 7.6: (a) The CNN determination of the diffusion barrier E_D. The estimates of the CNN follow closely the true E_D values (predictions: blue dots, mean value: black line, true values: diagonal dashed line). (b) Heatmap of the absolute prediction error of E_D which is low across the whole parameter range with a mean deviation of 4.5 meV.

Predictions of the network based on surface snapshots for the diffusion energy E_D together with the true values of the corresponding KMC simulations are shown in Fig. 7.6. As can clearly be seen, the individual predictions for the diffusion barrier E_D (blue dots) as function of the true barrier E_D show good agreement over the whole parameter range from $E_D = 0.4$ to $E_D = 0.55$ eV. For none of the E_D values used in KMC simulations we find noticeable deviations between the predictions by the CNN and the true value. Most of the predicted values for E_D are very close to the true E_D values. If the CNN makes

prediction errors, the deviations for predictions of E_D from the true E_D values are nearly uniformly distributed. In fact, the CNN slightly underestimates and, in equal measure, overestimates the true E_D values without showing any systematic error in one of the two directions.

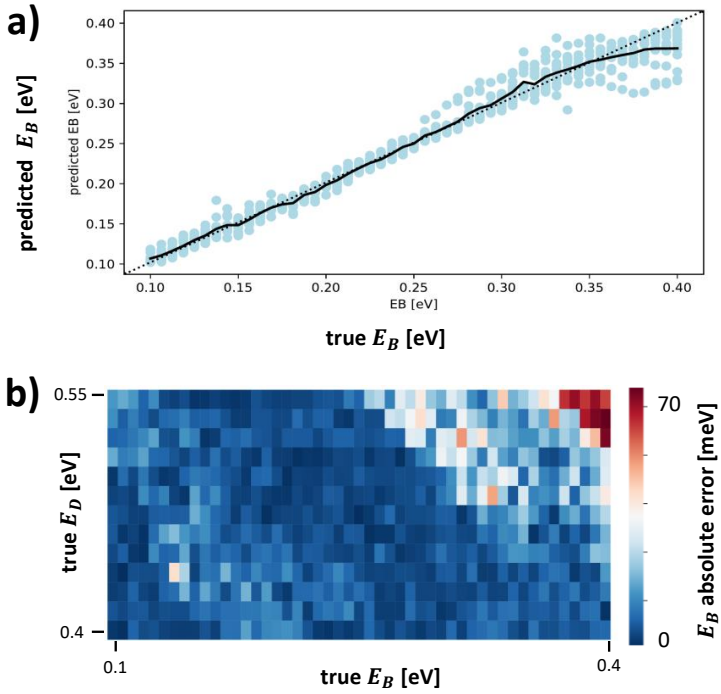

Fig. 7.7: (a) The CNN determination of the binding energy E_B. The estimates of the CNN follow closely the true E_B values (predictions: blue dots, mean value: black line, true values: diagonal dashed line). (b) Heatmap of the absolute prediction error of E_B which is 9.1 meV across the whole parameter range. As can clearly be seen, the E_B predictions have larger errors for large true E_B and E_D values where fractal islands become very small and nearly indistinguishable.

Specifically, the average predictions of the diffusion barrier E_D (see the solid black line) in Fig. 7.6 (a) are very close to the true values of E_D which are shown by the dashed black line. To better understand the deviations of E_D predictions over the whole E_D-E_B parameter space, we show in Fig. 7.6 (b) the absolute error of E_D predictions in meV as function of true E_D and true E_B values. We find that the error of E_D predictions is fairly low across the whole parameter space with a mean prediction error of 4.5 meV. Similarly, also the CNN predictions for E_B works well as can be seen in Fig. 7.7 (a). One clearly sees that the CNN predictions of E_B do not exhibit a s systematic error. The blue dots which represent the predictions of E_B are evenly distributed above and below the true bindings energies of the corresponding KMC simulations. The mean prediction value of E_B (see the solid black line) follows closely the true binding energies E_B (see the dashed black line). With 9.1 meV, the average prediction error E_B is quite low and actually even lower across most parts of the whole parameter range as can be seen in Fig. 7.7 (b). However, some deviations occur for large values of E_D and E_B as can be seen in the upper right corner in Fig. 7.7 (b). In this parameter region, the CNN does not correctly predict

the corresponding E_B values but tends to predict a median value for the binding energy. This is also indicated by a flattening of the average E_B prediction in Fig. 7.7 (a) where we see that the slope of the solid black line decreases for $E_B \geq 0.35$ eV. This may be a consequence of a low variation in island densities and island shapes in this parameter range where it is harder for the CNN to distinguish dendritic and compact island shapes from each other for very small islands. Another reason for the constantly high prediction error for KMC simulations with large E_D and E_B values could be that at the chosen growth conditions, we simply encounter the situation that cluster growth is fully irreversible. This means that particles can not detach from islands again, i.e., one lateral bond of strength E_B is sufficient to fully suppress diffusion. In this case, the fractal dimension of islands is given by $D_f \approx 1.71$, which is the result for island growth by diffusion limited aggregation [268, 270]. If additionally the island density n_x saturates, then there are no visible differences between different surface snapshots from KMC simulations where $E_D \geq 0.5$ and $E_B \geq 0.35$. In summary, the prediction of the diffusion barrier E_D and the binding energy E_B works very well over almost the entire E_D-E_B parameter space. Only for the largest values of E_D and E_B at the chosen growth conditions with $T = 313$ K and $F = 0.0166(7)$ monolayer/s, the surface configurations become indistinguishable from each other and the CNN fails to correctly predict the diffusion and binding energy. In a next step, we investigate the prediction performance of the CNN when imperfect, i.e., noisy and blurred data is used for validation.

Prediction performance on noisy and blurred data: We also studied the prediction accuracy of the CNN with imperfect data where salt and pepper noise together with Gaussian smoothing was applied to the surface snapshots in order to mimic random noise and a limited resolution such that they look more similar to experimental surface images. The goal of this investigation is find out whether the determination of microscopic energy parameters from images may, in principle, be applicable also to imperfect experimental STM or AFM images of thin films in the sub-monolayer growth regime. We expect the CNN to perform worse on noisy data as compared to noise-free data. Therefore, the prediction accuracy of the network on noise-free data serves as reference for the tests on noisy and blurred snapshots. To this end, we use the coefficient of determination R^2 [364] which is defined as 100% for perfectly accurate predictions, i.e., predictions with the same accuracy as on noise-free data and 0% when the prediction accuracy corresponds to the null hypothesis. The null hypothesis corresponds to estimating the mid-range values of the parameter space of the investigated diffusion and binding energies. This means that the latter corresponds to estimating the diffusion barriers as $E_D = 0.475$ eV and the binding energy as $E_B = 0.25$ eV. The R^2 measure of the accuracy is better suited than the absolute error, because, depending on the strength of noise and blur, the CNN tends to make wrong predictions close to the null hypothesis. Therefore, by plotting R^2 as function of the noise level, we can clearly determine the critical noise and blur strength where the prediction accuracy of the CNN breaks down. For all investigated strengths of noise an blur, the values for R^2 have been calculated for data across the full range of E_D and

E_B values in order to render the performance over the whole parameter space. In Fig. 7.8, we plot the coefficient of determination R^2 for both, E_D and E_B as function of noise strength given in $\%$ of randomly flipped spins. The image series above the graph serves as exemplary illustrations how increasing noise strength impacts an individual example images of the surface configuration. The results show a surprisingly high tolerance of the CNN performance to the noise strength. Even for 60% of the pixels replaced by noise, the CNN still exhibits an R^2 value above 90% for E_D and E_B. For $> 60\%$ of random pixel flips, the values of R^2 for E_D and E_B quickly drop to zero with the same slope.

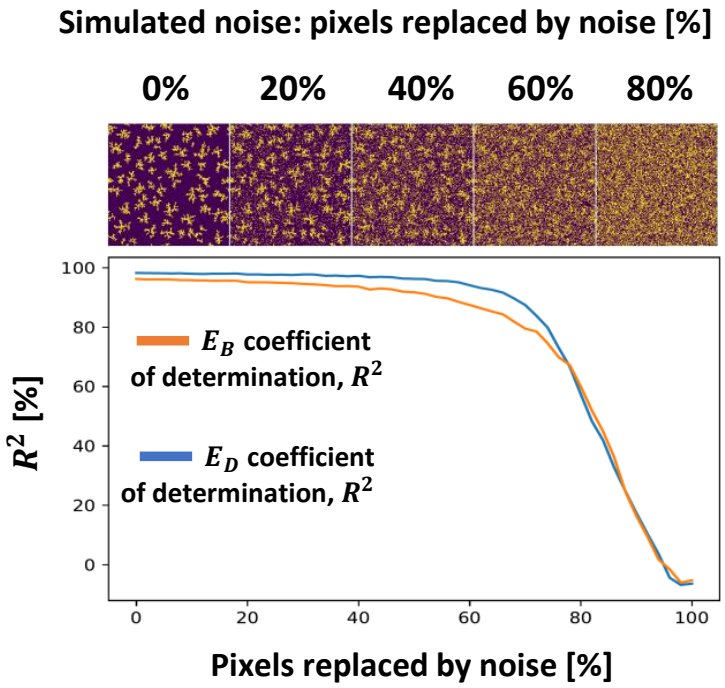

Fig. 7.8: Dependency of the prediction quality of E_D and E_B on images with salt and pepper noise based on the coefficient of determination R^2. The coefficient exhibits a surprising tolerance to random salt and pepper noise, as up to 60% of the pixels can be replaced with random values before predictions of the underlying energy barriers get significantly worse. The image series above the graphs serves to illustrate how an increasing level of noise impacts a single example image consisting of 200×200 pixels.

Concerning the reduction of the image resolution, we observe similar behavior of the corresponding coefficient of determination R^2 for E_D and E_B. As can be seen in Fig. 7.9, images with lower than atomic resolution still can be used for meaningful predictions of the microscopic energy parameters E_D and E_B (The image series above the graph illustrates how decreasing the image resolution impact an exemplary surface configuration). The image resolution has been degraded by smoothing through convolution via a 2-dimensional Gaussian. One clearly sees that if the standard deviation σ^2 of the corresponding Gaussian is chosen to be three pixels, which roughly corresponds to an image resolution of three lattice constants, the R^2 value for E_D and E_B is above 90%. This means that for image resolutions in the range of experimental AFM or STM snapshots, the prediction accuracy of the CNN is not much affected as compared to the accuracy for perfect, noise-free data. For

$\sigma^2 > 3$, the prediction accuracy for E_B quickly drops and approaches the null hypothesis for $\sigma^2 \geq 10$. In contrast, R^2 for E_D remains above 90% for $\sigma^2 \leq 5$. As the standard deviation of the corresponding Gaussian is further increased, also R^2 of E_D approaches the null hypothesis which corresponds to a random guess of the CNN.

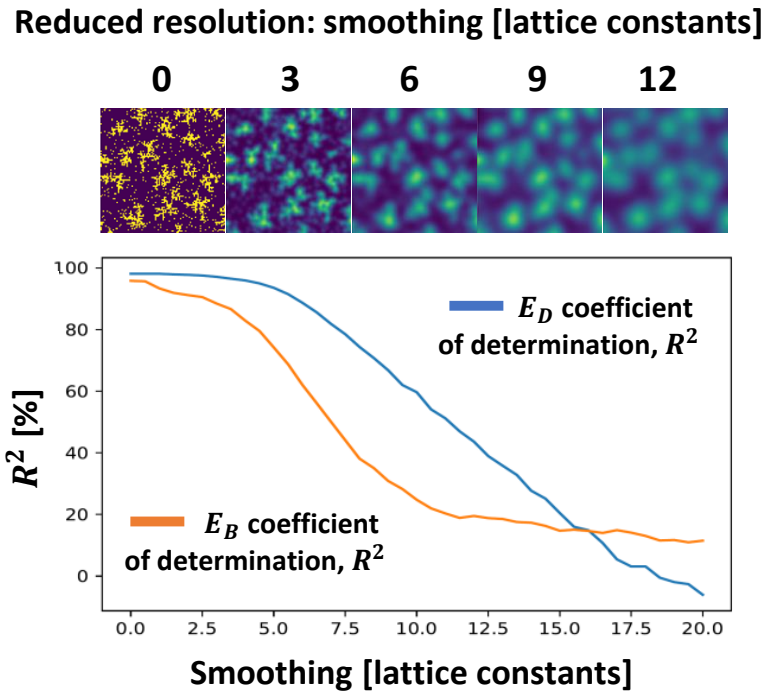

Fig. 7.9: Dependency of the prediction quality of E_D and E_B on images with with degraded resolution based on the coefficient of determination R^2. The coefficient reveals that a downgrading the resolution by merging of $3-5$ pixels (or lattice constants) still yields an acceptable prediction quality. The image series above the graphs serves to illustrate how decreasing the image resolution impacts a single example image consisting of 100×100 lattice sites.

For both, noise and blur, the predictions of E_D are less sensitive to image degradation than the prediction of E_B. The reason for this may be because E_B predictions depend more strongly on fine detail of island shapes. The latter get easily shadowed by noise blurred with degraded image resolution. We note that the same CNN was used for all predictions with or without noise and with degraded or perfect resolution. In principle, we expect that a CNN which is trained for specific noise levels or a fixed image resolution can outperform the more general CNN that we used here. Indeed, for applying a CNN to experimental data, the KMC training images should be modified such that they resemble as closely as possible the experimental resolution and noise types present in the STM or AFM images for which we want to use the CNN to determine the underlying values of the microscopic energy barriers E_D and E_B.

7.3 Future machine learning-based investigations

The results presented in this chapter demonstrate how artificial intelligence methods can help to unravel microscopic details of nonequilibrium surface processes. Our ML-based approach of using a single image to extract the energy barriers involved in its formation is quintessentially different from well-established procedures which require information from several iteratively repeated laboratory experiment series at different growth conditions, e.g. different temperatures T and adatom deposition rates F. The physical information that is gained from such measurement series allows to calculate mesoscopic parameters, such as the island density n_x, from which the value of E_D can be determined under certain conditions using scaling relations based on classical nucleation theory [9, 13]. However, there is no easy way to determine from the experiment both, the diffusion barrier E_D and the binding energy E_B that cause the observed morphologies. Alternatively, the experimentally obtained value of n_x can be used to start an elaborate fitting procedure employing KMC simulations to find the energy barriers that lead to island densities matching the experiment. The present approach significantly facilitates the problem: It only requires a single image of the surface morphology at fixed growth conditions (defined by surface temperature T, deposition rate F and coverage θ) in combination with an appropriately trained CNN to determine both, the values of E_D and E_B. We have demonstrated that this analysis works very well in terms of prediction of energy barriers, even in presence of strong noise and highly reduced resolution of the images. Therefore, we are confident that a single STM or AFM image obtained in a real growth experiment would be sufficient to estimate the values of E_D and E_B, provided that the CNN was trained by appropriate KMC simulations.

Our method requires many KMC simulation runs, as simulations with different energy barriers must be performed over a range of values typical for the class of materials under study. Preliminary investigations with a training data set containing only 10% of the images used here indicate that the CNN is, to some extent, capable of interpolating in between E_D and E_B values of KMC simulations. Thus, a sparser sampling of the E_D - E_B space seems sufficient, which could substantially reduce KMC simulation time as compared to the present analysis. This potential reduction of computational effort is a topic of further studies.

Once the values of E_D and E_B of a material are calibrated at the growth conditions at hand via the KMC-trained CNN, one can once again employ KMC simulations to predict the surface morphology at a different deposition rate F, temperature T or sub-monolayer coverage θ (as compared to the training growth conditions). Of course, such an investigation foots on the implicit assumption that the obtained energy barriers are transferable between, e.g., different temperatures or deposition rates. Given that the energy barriers in KMC are essentially effective, i.e., coarse-grained, quantities, the assumption

of transferability can indeed be an issue as in any coarse-grained theoretical approach. Whether the energy barriers can be transferred should therefore either be tested by comparison of KMC results and experiments at different growth conditions or the suitability of a KMC model for the material class under study must be previously established. Even though the precise E_D and E_B values may depend on the type of KMC algorithm and the choice of attempt frequencies, the above procedure of training and predicting with a certain KMC model will be self-consistent. Taken together, predicting the deposition rate and temperature dependency of growth enables data-driven materials research as costly experimental growth parameter searches can be guided through faster KMC simulations. This becomes even more important as the dimensionality of the growth parameter space is extended beyond substrate temperature and adatom deposition rate.

We would like to mention that our method can be extended to different lattice symmetries, e.g., hexagonal, triangular or rectangular substrates, and, in principle, also to other particle shapes, e.g., elongated organic molecules. In the latter case, the underlying KMC algorithm clearly has to include additional processes (and thus, energy barriers) related to internal and orientational degrees of freedom. While the intentionally simple model used in this work may be sufficiently precise for a self-consistent description and prediction of energy barriers in many atomic systems, we are aware that even in these seemingly simple cases, additional microscopic processes such as diffusion along step-edges, particle exchange or the presence of grain boundaries can impact the resulting surface morphology. The presence of these processes may be identified in Molecular Dynamics simulations or studies based on Density Functional Theory. For example, additional surface processes have been included in KMC simulations of atomic systems such as Pt on Pt(111) [188] or C_{60} on C_{60} [171, 365] to refine the morphology predictions for these systems. For future research, it would be very interesting to investigate whether a CNN can precisely predict the energy barriers and rates of simulation setups that include more surface processes and energy parameters.

We also want to point out that the approach presented here can be extended to predict the Ehrlich-Schwoebel barrier. Indeed, we have performed first tests by training a CNN with images at higher coverages θ, where second layer nucleation has already set in. The results show that, after determining E_D and E_B at a sub-monolayer coverage of $\theta = 0.15$, the value of the interlayer diffusion barrier E_{ES} can be predicted from a second image of the surface at a coverage of $\theta = 0.5$ with high accuracy that is comparable to the results for E_D and E_B. Future work may investigate whether all three parameters can be predicted at the same time from a single image in a coverage regime where stable islands in the second layer are present. In conclusion, ML techniques such as CNNs represent a significant untapped potential for advanced data analysis in surface science and material engineering. This holds, in particular, for complex non-equilibrium processes such as nucleation and crystal growth where various microscopic processes with different activation energies strongly influence the resulting morphologies. Here, a nearly instantaneous method

to extract the underlying kinetics and energetics of a growth process seems especially valuable. Encapsulating the knowledge about a wide range of energy parameters and possible surface morphologies in a CNN enables a novel and direct analysis of microscope images that circumvents the need for iteratively fitting KMC simulations to data at different growth conditions. Therefore, in light of the demonstrated tolerance of the CNN to noise and lower resolution images, we expect the here presented approach to be very applicable to experiments and to speed up the optimization of growth conditions for defect-free materials. This is particularly needed at the moment, as ML algorithms also suggest an ever-increasing number of candidate materials that have to be grown and tested. Finally, we want to note that the method of using image recognition to predict nanoscale processes from microscopic morphology can potentially be extended beyond growth studies to research fields such as catalysis at surfaces.

8 Stochastic Thermodynamics for discrete systems I: Nonequilibrium surface growth

In this chapter we study the entropy production rate of a free and a bound one-dimensional (restricted) solid on solid (RSOS) and unrestricted interface growth model consisting of L lattice sites. We have introduced the relevant concepts of the theoretical formalism of stochastic thermodynamics in C. 3. Here, we investigate how the presence of surface diffusion processes and the value of the maximum height difference, i.e., the height restriction, between neighboring lattice sites affects the entropy production rate. The model which we introduce in the following includes particle deposition at a constant rate and Arrhenius-type desorption and surface diffusion processes. First, we study the entropy production in the state of a free interface where the crystal can also dissolve. Second, we study the entropy production rate in presence of a hard wall which forbids evaporation.

8.1 Surface growth including deposition, diffusion and desorption processes

Importance of desorption processes in surface growth simulations: Evaporation events are often neglected in particle-based surface growth simulations. For practical reasons, one often assumes an effective adsorption (deposition) rate $F = f_{ads} - q_{eff}$ [171, 188, 366, 367], where q_{eff} is the effective rate of particle desorption, i.e., the rate of evaporation events where particles detach from the surface. This may drastically reduce the computational demand of growth simulations without affecting the emerging surface morphologies [171, 188, 367]. While ignoring evaporation events may be unproblematic for studies focusing on morphological properties, it causes a problem for a thermodynamic investigation of surface growth. According to the definition of the entropy production rate by Schnakenberg [207], the backwards rate of any possible state transition $\mu \to \nu$ with rate $w_{\nu\mu}$ has to be to be positive, i.e., when $w_{\nu\mu>0}$, then $w_{\mu\nu} > 0$ must hold. This means that particle adsorption processes have to be reversible, i.e., desorption of particles from the surface must be considered. The reason for this is that otherwise, the change of medium entropy for a state transition $\mu \to \nu$, i.e., $\Delta S_m = \ln\left(w_{\nu\mu}/w_{\mu\nu}\right)$, could not be calculated if $w_{\mu\nu} = 0$. Let us consider a concrete example in the context of surface growth simulations. If the forward process corresponds to particle deposition, $w_{\nu\mu} = F$,

then $w_{\mu\nu} = q > 0$ must hold. Here, F is the rate for adsorption of a particle and q the rate for desorption of the same particle. If $q = 0$, we could not calculate ΔS_m for a deposition event.

In the following, we introduce a surface growth model including evaporation of particles. Further, we explain the dynamics of the model in presence of a hard-wall at zero height. Then, we exactly calculate the entropy production rate in small systems in presence of a height restriction and compare the results to numerical calculations of π. Further, we investigate the impact of surface diffusion on the thermodynamic properties of the free and the bound system.

Surface growth with adsorption, desorption and diffusion: The model with periodic boundary conditions is defined on a one-dimensional line segnet of length L. The height on each lattice site $i \in [1, L]$ is denoted by h_i. In absence of a hard wall, the heights can take positive as well as negative values, i.e. $h_i > 0$, $h_i < 0$ and $h_i = 0$ is allowed. At the beginning of each simulation run, the height is set to zero on all lattice sites i, i.e., $h = 1/L \sum_i h_i = 0$. Particles are deposited with constant deposition (flux) rate F which takes the same value on all lattice sites. In particular, F acts as control parameter of the system. Desorption of particles from the surface is modeled as activated process with Arrhenius-type rates according to Eq. (2.53),

$$q_n = C_0 \exp\left[-(E_{DES} + nE_B)\right]. \tag{8.1}$$

Here, C_0 is a variable attempt frequency which acts as an additional control parameter next to F. As in conventional growth simulations, $E_A = E_{DES} + nE_B$, where E_{DES} is the desorption energy barrier, E_B the in-plane bond energy and n the number of in-plane bonds a particle has to break in order to evaporate. We arrive at this form by setting the Boltzmann constant and the temperature to unity, i.e., $k_\mathrm{b} = 1$ and $T = 1$. Further, we set $E_{DES} = 0$ and $E_B = 1$. Therefore, if $C_0 = 1$, we get $q_0 = 1$ for the desorption rate of free particles which do not have lateral nearest-neighbors and thus, no in-plane bonds. The desorption rate for particles with one bond is then given by $q_1 = \exp(-1) = 0.36787(9)$ and the rate for desorption of particles with two in-plane bonds reads $q_2 = \exp(-2) = 0.13533(5)$. Similar, diffusion rates are given by

$$D_n = d_0 \exp\left[-(E_D + nE_B)\right]. \tag{8.2}$$

In this equation, the attempt frequency for particle diffusion is given by d_0 and $E_D = 0$ corresponds to the diffusion barrier which, analog to E_{DES}, we neglect. Therefore, for $C_0 = d_0 = 1$, the diffusion rates are identical to the desorption rates. We set $E_D = E_{DES} = 0$ because then, we can control the ratio of diffusion over desorption via the ratio d_0/C_0. Further, this setup allows us to separately investigate the effect of a varying the adsorption rate via changing F and varying the desorption rate simply by tuning the ratio F/C_0.

The model without surface diffusion, i.e., with $d_0 = 0$, is known to belong to the KPZ universality class [373]. Therefore, investigating the entropy production rate in this model means that one analyzes thermodynamic properties of a growth model that is part of the non-linear KPZ universality class [238] (see Sec. 4.4.2). As surface diffusion is introduced by setting $d_0 > 0$, symmetry properties of the model change and the system is then part of the EW universality class (see Sec. 4.4.2) for linear surface growth [9, 247]. Therefore, by investigating π in the model with $d_0 > 0$, one analyzes thermodynamic properties of a growth model belonging to universality class different from KPZ. No the question arises whether the belonging universality class has an impact on the thermodynamic properties. To some extent we touch this topic by comparing the entropy production rate in the model with $d_0 = 0$ to the setup with $d_0 > 0$.

Height restriction and effective surface tension: An analytical treatment of the entropy production rate in the model is possible if we impose a height restriction between neighboring sites h_i and h_{i+1}, i.e.,

$$|h_i - h_{i+1}| \leq H. \tag{8.3}$$

Here, H is the maximum height difference which is allowed between neighboring lattice sites. Due to a finite height restriction $H < \infty$, the state space Ω of the model is finite which makes an exact treatment of the model possible. In general, lattice models obeying Eq. (8.3) are called restricted solid on solid (RSOS) models. Various RSOS surface growth models have been studied in the literature [314, 369–372]. Surprisingly, they do not distort the physics of their unrestricted counterparts where no height restriction is applied, i.e., when $H = \infty$. In fact, the height restriction introduces an effective surface tension [9, 314, 370, 373]. Concerning the continuum KPZ equation, the height restriction affects the value of the pre-factor λ in the term $\sim \lambda[\nabla h(x,t)]^2$.

We calculate the entropy production rate per spin, π, exactly in the system with $H = 1$ and small values of L and perform numerical simulations for different values of H and L in order to investigate the impact of a height restriction on the entropy production rate of the model. In presence of the strongest height restriction $H = 1$, it is convenient to describe the interface configuration in terms of charges,

$$s_i := h_{i+1} - h_i \in [-1, 0, 1]. \tag{8.4}$$

Here, $s_i = 1$ corresponds to a positive charge, $s_i = -1$ to a negative charge and $s_i = 0$ to a neutral charge. The mapping and all state transitions of the model with $H = 1$ and $L = 3$ onto charges s_i is shown in Fig. 8.1. Generally, the phase space dimension scales $\sim (2H + 1)^L$. However, since the sum of all charges in each configuration has to sum up to zero, $\sum_i s_i = 0$, the actual phase space dimension is much smaller. In fact, for $L = 3$ and $H = 1$, only 7 individual charge configurations are allowed. In particular, the charge representation cancels out the height-dependency of individual lattice configurations. This

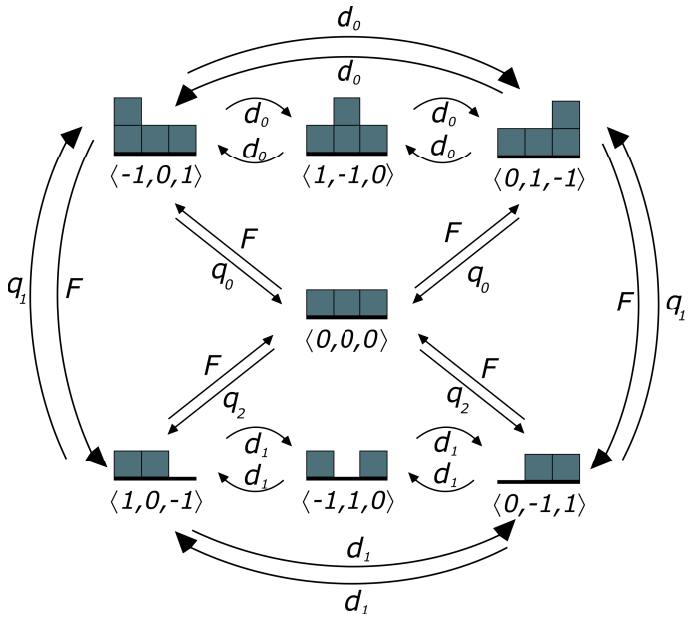

Fig. 8.1: Visualization of all 7 lattice configurations and all possible transitions between states via deposition with constant rate F, evaporation with rates q_n and diffusion with rates d_n in the system with $L = 3$ and $H = 1$. The Arrhenius-type evaporation and diffusion rates depend on the number n of bonds that have to be broken in order to evaporate or diffuse.

enables to calculate the occupation probabilities of each state in the charge representation via an exact diagonalization of the transition rate matrix $\underline{\mathbf{W}}$.

The entropy production rate in surface growth: In order to calculate the entropy production rate in the surface growth model in a NESS numerically, one can simply use calculate the ensemble average according to Eq. (3.26) or calculate the change of medium entropy along individual stochastic paths by following Eq. (3.17). Analytically, the most direct way to calculate π is to diagonalize the transition rate matrix $\underline{\mathbf{W}}$. This gives us the probability state vector $\mathbf{P}$ which contains the occupation probabilities p_μ, p_ν of all states $\mu, \nu \in \Omega$. From this we get the exact result for π by using Eq. (3.23). The problem is that the dimension of Ω scales $\sim (2H+1)^L$. Consequently, an exact treatment is limited to small system sizes L and small values of H.

Entropy production in charge representation without surface diffusion: In the model with $H = 1$ and $L = 3$, there are only 7 possible surface configurations which, in the charge representation (s_1, s_1, s_2), are given by $(0,0,0)$, $(-1,0,1)$, $(1,-1,0)$, $(0,1,-1)$, $(1,0,-1)$, $(-1,1,0)$ and $(0,-1,1)$ as shown in Fig. 8.1. The occupation probability of a state (lattice configuration) is denoted as $p_{s_1 s_2 s_3}$ All possible transitions $\mu \to \nu$ between configurations due to deposition and desorption of a single particle are illustrated in Fig. 8.1. Since we only have 7 states and do know all transition rates $w_{\nu\mu}$ between these states, we can

directly use Eq. (3.22) to calculate the medium entropy production rate which, in a NESS, equals the total entropy production rate,

$$\Pi = \left(3F\ln\frac{F}{q_0} + 3q_2\ln\frac{q_2}{F}\right)p_{000} + \left(q_0\ln\frac{q_0}{F} + 2F\frac{F}{q_1}\right)(p_{-101} + p_{1-10} + p_{01-1}) + \left(F\ln\frac{F}{q_2} + 2q_1\ln\frac{q_1}{F}\right)(p_{10-1} + p_{-1110} + p_{0-11})\,. \tag{8.5}$$

The occupation probabilities $p_{s_1 s_2 s_3}$ can be obtained from the transition rate matrix $\underline{\mathbf{W}}$ which, in this particular case, is a 7×7 matrix containg all transition rates between the states. The transition rate matrix for the system with $L = 3$ and $H = 1$ is given by

$$\underline{\mathbf{W}} = \begin{pmatrix} \phi_2 & F & F & F & q_0 & q_0 & q_0 \\ q_0 & \phi_0 & D_0 & D_0 & 0 & F & F \\ q_0 & D_0 & \phi_1 & D_0 & F & 0 & F \\ q_0 & D_0 & D_0 & \phi_0 & F & F & 0 \\ F & 0 & q_1 & q_1 & \phi_1 & D_1 & D_1 \\ F & q_1 & 0 & q_1 & D_1 & \phi_1 & D_1 \\ F & q_1 & q_1 & 0 & D_1 & D_1 & \phi_1 \end{pmatrix}, \tag{8.6}$$

with $\phi_2 = -3F - 3q_2$, $\phi_0 = -q_0 - 2F - 2D_0$, and $\phi_1 = -2q_1 - F - 2D_1$. Interestingly, the phase space can be further reduced by grouping translational invariant states. For example, $(-1, 0, 1)$, $(1, -1, 0)$ and $(0, 1, -1)$ are only lateral shifts of the same configuration. This is also true for $(1, 0, -1)$, $(-1, 1, 0)$ and $(0, -1, 1)$. Therefore, the dimension of the state space for $L = 3$ and $H = 1$ can be reduced to $\dim(\Omega) = 3$. For $L = 4$ and $H = 1$, there are 19 lattice configurations. By make use of the translational invariance of states, it is possible to reduce the number of configurations to 6 unique charge representations. Especially when it comes to diagonalizing $\underline{\mathbf{W}}$, one can go to larger system sizes L if one makes use of the translational invariance of lattice configurations. In the following sections, we show exact results for the entropy production rate as function of F for some values of the evaporation constant C_0 and the diffusion constant d_0 and compare them with numerical results from Monte-Carlo simulations according to Eq. (3.17).

8.1.1 Entropy production without surface diffusion

Unbound interface growth: We first consider the entropy production rate in the unbound model where the heights of the initially flat interface, i.e. $h_i = 0$ at $t = 0$ for all lattice sites i, can also become negative, $h_i < 0$. The interface growth velocity is given by $v = h/t$, where h is the average heigt $h = 1/Lsum_i h_i$ and t the time. If an unbound interface grows, it's height increases with time and consequently, the velocity is positive, $v > 0$. If the interface declines, the velocity is negative, $v < 0$, and if the keeps it's height, i.e., if it fluctuates around $h = 0$ (which is the case when deposition and evaporation events balance out), then the velocity vanishes, $v = 0$.

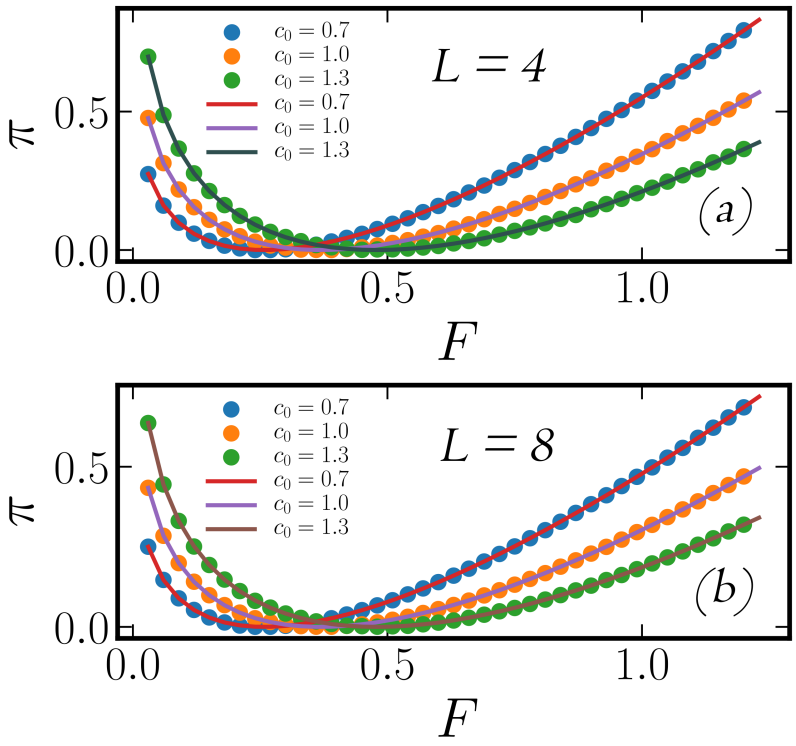

Fig. 8.2: (a) Entropy production rate π per lattice site (for free surface growth without a hard wall at $h = 0$) as function of deposition rate F for system size $L = 4$, height restriction $H = 1$ and three values of the desorption constant c_0. Symbols show results from Monte-Carlo simulations and solid lines represent exact results according to Eq. 3.23 with the same parameters. (b) shows the same for $L = 8$.

Exact and numerical results for the entropy production rate per lattice site $\pi = \Pi/L$ for two system sizes and three different values of the evaporation constant C_0 for an unbound interface without diffusion, $d_0 = 0$, and $H = 1$ are shown in Fig. 8.2. Numerical data from MC simulations is given by symbols and exact results are represented by solid lines. We find perfect agreement between the numerical and exact results for both considered system sizes and all three values of C_0. For small values of F, the entropy production rate π is a decreasing function of F. At a value F_0 which increases with increasing C_0, the entropy production rate vanishes, $\pi = 0$. This means that the system is in thermal equilibrium. In this case, deposition and evaporation events cancel out. For $F > F_0$, the entropy production rate, π, persistently increases for all values of C_0.

To interpret these three regimes of π (π decreasing for $F < F_0$, $\pi = 0$ at F_0 and increasing π for $F > F_0$), let us consider Fig. 8.3 where π is plotted together with the interface velocity v for $C_0 = 0.7$ and $C_0 = 1.3$. We clearly see that in the regime $F < F_0$ (where π is decreasing as function of F), the interface velocity is negative, $v < 0$. Consequently, the crystal is dissolving, i.e., it's height decreases with time. This means that more particles evaporate than particles are deposited. As F approaches F_0 from below, the velocity decreases and approaches $v = 0$. In the paragraph above, we defined F_0 as the deposition rate where $\pi = 0$. We observe that the velocity is zero at exactly this value F_0 for both

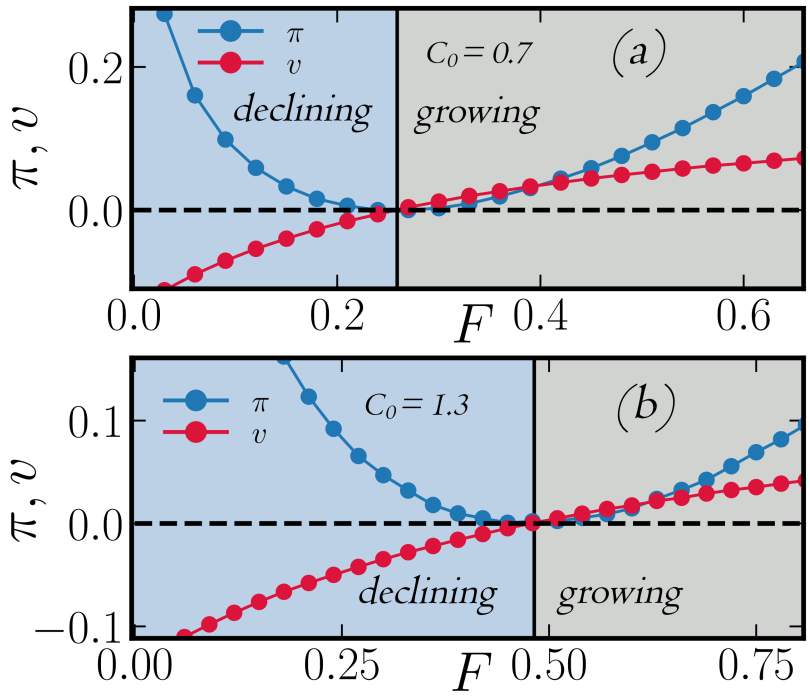

Fig. 8.3: (a) Entropy production rate π per lattice site (for free surface growth without a hard wall at $h = 0$) and the interface velocity v as function of deposition rate F for system size $L = 3$, height restriction $H = 1$ and $C_0 = 0.7$. The blue region shows the region where the interface is declining, i.e., it's height decreases, whereas gray marks the region where the interface grows, i.e., it's height increases. The solid black line is located at the equilibrium point F_0 where $\pi = v = 0$ holds. (b) shows the same for $C_0 = 1.3$.

shown values of C_0 (we checked that this holds for any value of C_0). This means that the interface is in thermal equilibrium exactly at the point where it is not moving, i.e., where it is fluctuating around $h = 0$, and thus, not moving. Therefore, at F_0, we have a fluctuating interface which is in thermal equilibrium, whereas for $F \neq F_0$, the fluctuating interface is in a nonequilibrium state. As we enter the regime $F > F_0$, the velocity of the interface is positive. This means that the interface is growing, i.e., more particles are deposited than particles do evaporate. As the interface grows, π increases with increasing F. We can conclude that the interface is producing entropy whenever it is growing or declining. Only exactly at F_0 it's velocity vanishes and the interface is in a state of thermal equilibrium at which $\pi = v = 0$ holds.

In order to investigate how the entropy production rate is affected by finite-size effects, we plot π (with $C_0 = 0.7$, $C_0 = 1.0$ and $C_0 = 1.3$) obtained from numerical simulations for system sizes ranging from $L = 3$ to $L = 32$ in Fig. 8.4. We see that the smallest system sizes overestimate the entropy production rate. However, already for $L = 8$, the calculated entropy production rate π is close to the value for $L = 32$. This means that we do not need to consider very large systems in order to obtain meaningful, i.e., converged results for π.

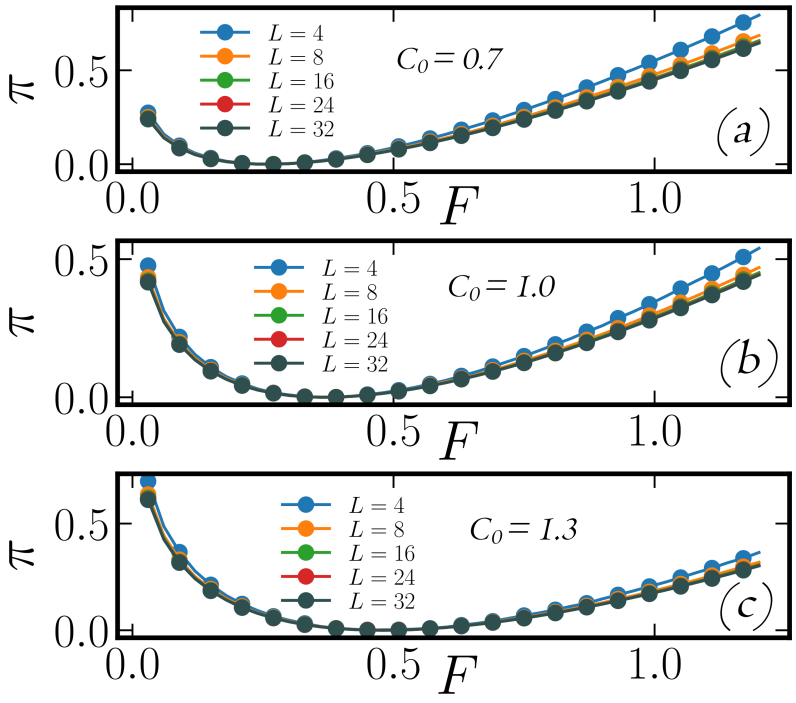

Fig. 8.4: (a) Entropy production rate π per lattice site as function of deposition rate F with height restriction $H = 1$ and $C_0 = 0.7$ for system sizes ranging from $L = 4$ to $L = 32$. (b) and (c) show the same for $C_0 = 1.0$ and $C_0 = 1.3$.

Finite-size effects seem to only play a minor role when it comes to calculating the entropy production rate in discrete one-dimensional surface growth models.

So far we considered unbound interface growth without diffusion only with the strongest height restriction $H = 1$. For $H > 1$, the phase space dimension drastically increases and goes to infinity for the unrestricted model $H \to \infty$. In order to investigate how the height restriction affects the entropy production rate as compared to the unrestricted case, $H = \infty$, we show results for π as function of F for different values of H in Fig. 8.5. There, we see that the entropy production of restricted interfaces is always lower as compared to π of the unrestricted version. The difference between the system with $H = 1$ and the unrestricted one is quite large. Interestingly, already with $H = 3$, the function $\pi(F)$ follows quite closely the entropy production rate in the unrestricted model for both shown values of C_0.

Interface growth in presence of a hard wall: The growth conditions change dramatically if we introduce a hard wall at $h = 0$. Such a boundary represents an inert substrate which can not dissolve during the growth process. The wall forbids evaporation on lattice sites if $h_i = 0$. Therefore, the interface velocity can not become negative, i.e., $v \geq 0$. At growth conditions where, without the wall, the crystal would have a negative velocity $v < 0$, the interface is bound to the hard wall, i.e., the substrate, and $v = 0$. Particles are deposited

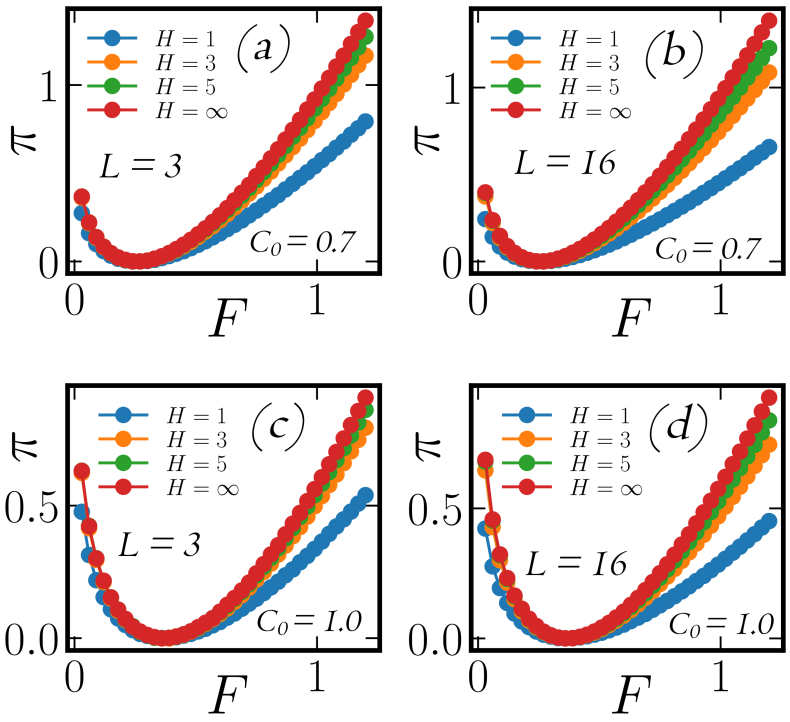

Fig. 8.5: (a) Entropy production rate π per lattice site as function of deposition rate F for system size $L = 3$ with $C_0 = 0.7$ and different values of the height restriction from $H = 1$ to $H = \infty$ (corresponding to unrestricted growth). (b) shows the same for $L = 16$. (c) and (d) show the same as (a) and (b) but with $C_0 = 1.0$.

on the substrate but they evaporate again before they can form stable clusters. At a critical value F_c, deposition dominates over evaporation and the interface begins to grow when $F > F_c$ exactly as in the case without a hard wall. Then, the interface is unbound and the hard wall becomes irrelevant for the growth process.

Previous studies have indicated that an interface in the bound phase can produce more entropy than the model with the same parameter setting without a hard wall [374]. However, the rates for evaporation that were used are not appropriate to describe surface growth by means of vapor deposition techniques. Specifically, the rates used in [374] are not activation energy-dependent process rates. In contrast, we here use activation energy-dependent Arrhenius-type rates for evaporation (and diffusion) and find that the entropy production of the system is always exactly zero, $\pi = 0$, in the bound phase, irrespective of the parameter settings. This means that the system in the bound phase is in thermal equilibrium as can be seen in Fig. 8.6. In the bound phase, both, the velocity and the entropy production rate vanish, $\pi = v = 0$. For $F > F_c$ (F_c is indicated by the solid black line which separates the blue and grey region which correspond to the bound and growing phase) we observe that $v > 0$ and $\pi > 0$. This again shows that the interface velocity is coupled to the entropy production rate, i.e., $\pi = 0 \Leftrightarrow v = 0$ and $\pi > 0 \Leftrightarrow v \neq 0$.

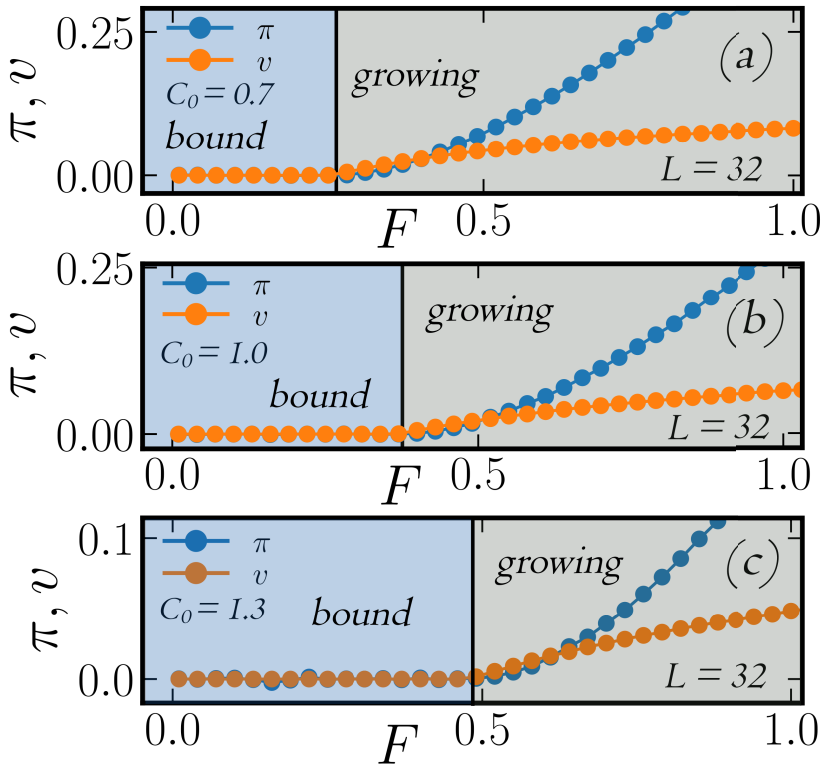

Fig. 8.6: (a) Entropy production rate π per lattice site and interface velocity v as function of deposition rate F in presence of a hard wall at $h = 0$ which mimics a solid substrate. The system size is $L = 32$, the height restriction is $H = 1$ and the desorption constant is set to $C_0 = 0.7$. The region where the interface is bound to the substrate is shown in blue, whereas the region where the interface grows is given in gray. The critical value F_c where the interface detaches from the hard wall is given by the solid black line. (b) and (c) show the same for $C_0 = 1.0$ and $C_0 = 1.3$.

8.1.2 Entropy production with surface diffusion

Unbound interface growth : In order to study the impact of surface diffusion (which changes the universality class of the system from KPZ to EW [9]) on the entropy production rate of the interface, we show results for π as function of F for different values of the diffusion constant d_0 at $C_0 = 0.7$, $C_0 = 1.0$ and $C_0 = 1.3$ in Fig. 8.7. As can be seen, the behavior of π is qualitatively the same if surface diffusion is present. In fact, surface diffusion only has an quantitative effect on π. The interesting point here is that also in presence of surface diffusion, there exist a unique point F_0 where the system is in thermal equilibrium, $\pi = 0$. It seems like only the value of F_0, where $\pi = 0$, is shifted towards larger values as d_0 is increased from zero, i.e., as surface diffusion is switched on. We also checked that the velocity of the interface vanishes at the equilibrium point, i.e., $v = 0$ at F_0 for all values of d_0.

Interface growth in presence of a hard wall: For the model without surface diffusion, i.e., with $d_0 = 0$, we found that the system in the bound phase is always in thermal equilibrium, $\pi = 0$. In this paragraph we aim to find out whether surface diffusion may

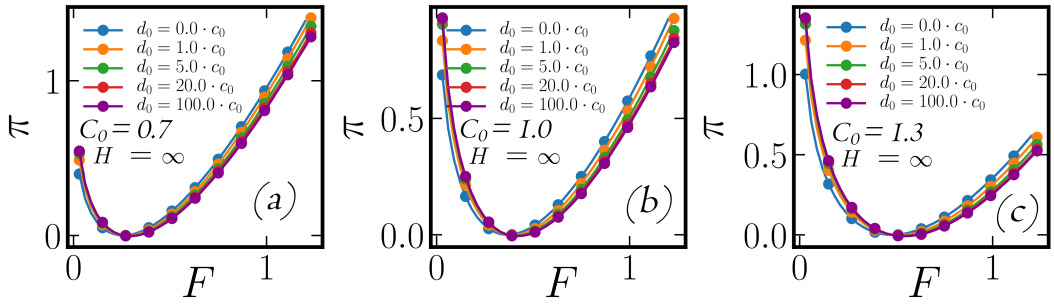

Fig. 8.7: (a) Entropy production rate π per lattice site (for free surface growth without a hard wall at $h = 0$) in presence of surface diffusion of particles as function of deposition rate F for system size $L = 16$, without height restriction, $H = \infty$, and $C_0 = 0.7$. The value of the diffusion constant ranges from $d_0 = 0.0C_0$ (no diffusion) up to $d_0 = 100.0c_o$. (b) and (c) shows the same for $C_0 = 1.0$ and $C_0 = 1.3$.

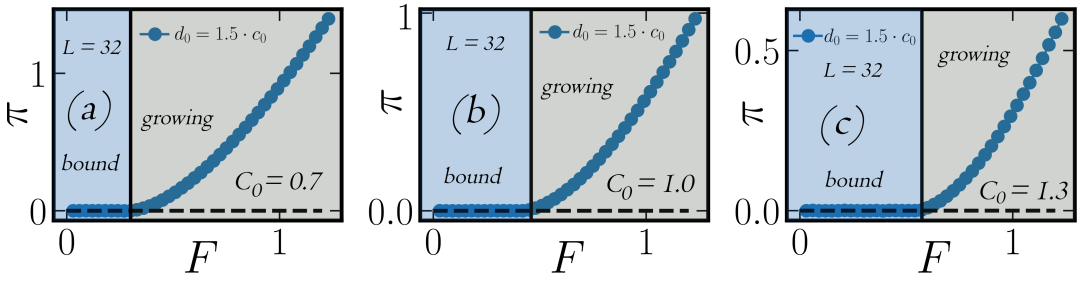

Fig. 8.8: (a) Entropy production rate π per lattice site with surface diffusion of particles as function of deposition rate F in presence of a hard wall at $h = 0$. The system size is $L = 32$, the height restriction $H = \infty$ and the desorption constant is set to $C_0 = 0.7$. The diffusion constant is given by $d_0 = 1.5C_0$. (b) and (c) show the same for $C_0 = 1.0$ and $C_0 = 1.3$.

drive the system out of equilibrium in the bound phase. To this end, we plot results for the entropy production rate π as function of F in presence of surface diffusion in Fig. 8.8. We see that also in presence of surface diffusion, i.e., when $d_0 > 0$, the interface remains in a state of thermal equilibrium in the bound phase. Therefore, Arrhenius-type surface diffusion processes of adatoms do not drive the system in a nonequilibrium state in the bound phase. Therefore, it seems like the condition $\pi = 0 \Leftrightarrow v = 0$ generally holds when diffusion and evaporation are treated as activated Arrhenius-type processes, irrespective of the parameter settings.

8.2 Conclusion and outlook

We have investigated the entropy production rate of a one-dimensional interface growth model which includes particle deposition and Arrhenius-type surface diffusion and evaporation processes for individual particles. We found that π always vanishes when the velocity of the interface is zero, i.e., when the system is in equilibrium where the interface fluctuates around zero height. This is true for the free, as well as for the bound interface.

Whenever $v \neq 0$, the interface produces entropy. In presence of surface diffusion, we only observe quantitatively changes of π.

Concerning further investigations in this direction, it would be interesting to analyze the entropy production rate in the two-dimensional version of the model. The latter is a more realistic representation of growth by vapor deposition techniques. Moreover, it would be interesting to study the model with two species of particles (denotes as A and B) which are characterized by different binding energies. For example, one could investigate the cases $E_B^{AA} = E_B^{BB} \neq E_B^{AB}$ or $E_B^{AA} \neq E_B^{BB} \neq E_B^{AB}$. It is *a priori* not clear whether this setup is a nonequilibrium system in the bound phase. If this is the case, the system would undergo a nonequilibrium phase transition from a bound to a growing phase at F_c. Investigating the behavior of π in the vicinity of nonequilibrium phase transitions is a timely topic [109, 111, 112] to which we contributed by investigating the power-law behavior of π in a nonequilibrium Potts model in C. 9.

9 Stochastic Thermodynamics for discrete systems II: Nonequilibrium spin systems

In this chapter we show results of a thermodynamic investigation of the nonequilibrium q-state vector Potts model (see Sec. 2.3.2). In particular, we analyze the model in the vicinity of the order–disorder phase transition which is either second- or infinite order, depending on q, the number of possible configurations per spin. We calculate the critical properties of the model and investigate the total entropy production rate Π.

9.1 The nonequilibrium q-state vector Potts model

The Hamiltonian of the q-state vector Potts model (also known as the q-state clock model) with nearest-neighbor spin interactions on a discrete lattice] is defined in Eq. (2.31). For the investigation of the nonequilibrium (two-temperature) q-state vector Potts model we use nearest-neighbor interactions and set $J = 1$, i.e., we ferromagnetically couple interacting spins s_i, s_j, and we do not apply an external magnetic field, $h = 0$. If all spins s_i of the system are exposed to a single heat bath at temperature T, the system (that is initially prepared in a configuration with random spin orientations) eventually reaches a state of thermal equilibrium and thus, does not produce any form of entropy, $\Pi = \Phi = 0$ (see Sec. 3.2.2 for a definition of entropy production). In contrast to this setup, we drive the Potts model into a nonequilibrium steady state by coupling the spins s_i to two different heat baths T_k ($k = 1, 2$) which are kept at temperatures T_1 and T_2. With this setup, the system is out of equilibrium whenever $T_1 \neq T_2$, i.e., when there is a temperature gradient $\Delta T = |T_1 - T_2|$ among the sublattices. Then, there is a constant heat flux $\dot{Q}$ from the hotter to the colder heat reservoir that goes along with a constant rate of entropy production, $\Pi > 0$ (see Sec. 3.2.2). Our setup splits the system into two sublattices, $\mathcal{L}_1$ and $\mathcal{L}_2$, each containing all spins connected to the bath at T_1 or T_2, respectively. As a consequence, all nearest-neighbors of a spin s_i are coupled to the respective other heat bath, yielding a checkerboard configuration as illustrated in Fig. 9.1. Interestingly, with this setup, the system reaches a NESS where $\Pi = \Phi > 0$ holds. In the following, we fix T_2, but vary T_1 and calculate all observables as function of the mean temperature

$$T = (T_1 + T_2)/2. \tag{9.1}$$

We consider square lattices in two dimensions with a total number of L^2 spins, where L the lateral extension of the system which we refer to as the “system size". In order to study the dynamical evolution of the system in presence of thermal noise, we perform Monte-Carlo simulations with single spin-flip Glauber dynamics (see 2.39). The difference to the conventional Potts model with only one coupled heat bath, is that the rate $w^i_{\nu\mu}(k)$ for a transition of a randomly chosen spin s_i from state μ (before the spin flip) to ν (after the spin flip) depends on the temperature T_k of the heat bath the considered spin is coupled to. As a consequence, the transition rates between neighboring spins s_i, s_j (which are coupled to different heat baths) are different, even in the case that the energy change $\Delta E_{\nu\mu}$ due to the flipping of either s_i or s_j is the same. Regarding the number of configurations per spin, we limit ourselves to $q = 4$, i.e., the Ashkin-Teller model and $q \to \infty$, i.e., the XY model.

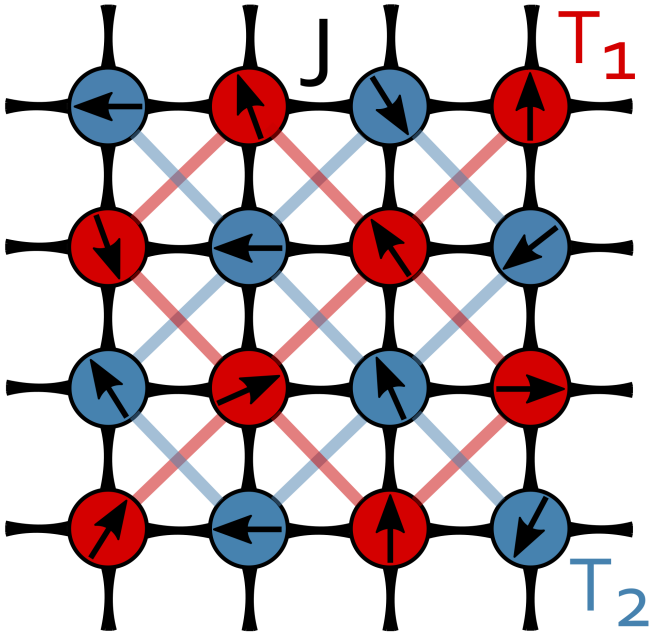

Fig. 9.1: Illustration of a 4×4 cutout of the q-state vector Potts model on a two-dimensional square lattice with periodic boundary conditions. The spins are coupled to heat baths at two different temperatures T_1 and T_2, here indicated by the colors red and blue, respectively, with a checkerboard arrangement. Black lines represent the nearest-neighbor interactions of strength $J = 1$, while red and blue lines highlight the two sublattices $\mathcal{L}_1$ and $\mathcal{L}_2$ formed by the coupling to heat two baths which are kept different temperatures, i.e., $T_1 \neq T_2$. As a consequence, there is a temperature gradient $\Delta T = |T_1 - T_2|$ among the two sublattices $\mathcal{L}_1$ and $\mathcal{L}_2$ which results in a heat flux $\dot{Q}$ from the hotter to the colder heat bath.

The two-temperature Ashkin Teller model ($q = 4$): For, $q = 4$ the model shows a second-order phase transition from a PM to a FM phase similar to the Ising model, yet with different characteristics, i.e., different critical exponents [162]. The question is whether the exponents of the model with $q = 4$ get altered or remain unchanged when a temperature difference ($T_1 \neq T_2$) among the two sublattices is introduced, i.e., when the system is driven out of equilibrium. Furthermore, it is of interest to study the behavior of the total entropy production rate Π in the vicinity of the PM to FM phase transition to see

whether Π shows noticeable behavior, i.e., power-law scaling, around the critical point. If this is the case, the next step would be to investigate if this scaling is universal or not.

The two-temperature XY model ($q \to \infty$): In contrast, in the two-dimensional XY model, there exists no long-range ordered FM phase at finite temperatures as stated by the Mermin-Wagner theorem [53–55, 219]. Instead, the sytem undergoes an infinite-order BKT transition from a PM to a BKT phase as the temperature is reduced below T_c. In contrast to the model with $q = 4$, the specific heat C_v in the XY model does not peak in the vicinity of the critical temperature $T_c = T_{BKT} \approx 0.892880(6)$ [57, 163]. As a consequence, there is no peak value in C_v around T_c that shows a logarithmic divergence as function of system size L. A characteristic, but nonuniversal feature of the two-dimensional XY model is the presence of a pronounced, asymmetric peak of C_v above the critical point, i.e. at $T \approx 1.1 > T_c$, which is found in both, numerical simulations as well as analytical calculations [57, 162]. The occurrence of this maximum above T_c is usually attributed to a rapid increase of entropy due to the unbinding of vortex-antivortex pairs. It is somewhat extraordinary that this peak in C_v is well separated from the asymptotic critical region of the phase transition where the unbinding of cortex-antivortex pairs happens. In particular, the maximum occurs in a temperature region where the correlation length is still very large [57, 162]. It is therefore of particular interest to study the behavior of the entropy production around the critical point T_{BKT} as well as around the temperature where C_v peaks, which is at $T \approx 1.15 T_{BKT}$.

Entropy production in the nonequilibrium q-state vector Potts model: As discussed in C 2, a key quantity that distinguishes systems out of thermal equilibrium from those in equilibrium is the constant net production of entropy (3.20). For the vector Potts model in thermal equilibrium, the detailed balance (DB) condition, $w_{\nu\mu}(k)p_\mu = w_{\mu\nu}(k)p_\nu$, holds for all μ and ν. Specifically, $w_{\nu\mu}(k)$ refers to the transition rate due to the flipping of a spin which is in contact with a heatbath which is kept at T_k ($k = 1, 2$). When DB is violated, there are non-vanishing local probability flows between certain microstates, i.e., $w_{\nu\mu}p_\mu - w_{\mu\nu}p_\nu \neq 0$. As a consequence, the system constantly produces entropy $\Pi(t) > 0$ (3.23), which is the case whenever $\Delta T > 0$. Since we only consider the system after it has reached a NESS, $\Pi = \Phi$ holds. Then, we can use (3.22) to calculate the total entropy production rate. In particular, (3.22) can be computed numerically by averaging over many transitions $\mu \to \nu$ from the current state μ, i.e., the current spin configuration of the lattice. In spin systems with discrete spin orientations like the vector Potts model with finite q, state transitions $\mu \to \nu$ correspond to the flipping of a randomly chosen spin s_i on lattice site i. Thus, the sum in (3.22) can be written as an average over all lattice sites as shown in (3.26). Specifically, $w_{\nu\mu}(k)^i$ corresponds to the Glauber-type flipping rate of the spin σ_i on lattice site i (which is connected to the heat bath at T_k). The steady exchange of entropy with the environment results from the net heat flux $\dot{Q}$ from the hotter to the colder sublattice. We here employ the sign convention $\dot{Q} > 0$ for the heat flow from hot to cold.

Due to energy conservation (and because no external fields, forces or further gradients act on the system), all of the three relevant heat flows transport the same amount of energy per timestep: the flow from the hotter heat bath T_1 (here we assume for a moment $T_1 > T_2$) to the corresponding sublattice $\mathcal{L}_1$, the flow from $\mathcal{L}_1$ to $\mathcal{L}_2$, and the heat flow from $\mathcal{L}_2$ to the cold bath at T_2 (or everything reversed, if $T_2 > T_1$). This amounts to an overall entropy flow to the environment of

$$\Phi = |(\dot{Q}/T_2) - (\dot{Q}/T_1)| = \dot{Q}\,|T_2 - T_1|/(T_1 T_2). \tag{9.2}$$

A problem with (3.26) is that it can not be used to calculate Π in systems with continuous degrees of freedom, as it is the case for the vector Potts model with $q \to \infty$, i.e., the XY model. As an alternative, we can calculate the entropy production rate by following individual stochastic trajectories consisting of consecutively executed state transitions $\omega_{n-1} \to \omega_n$ between microstates as the system dynamically evolves via the reorientation of single spins $s_i \to s_i^{'}$ [50, 52]. To this end, we use (3.17) to calculate the change of medium entropy along a stochastic path $\mathbf{X}(N)$ consisting of N steps, each connected with a transition rate, $w_{\omega_n \omega_{n-1}}(k)^i$ for the forward process and a rate $w_{\omega_{n-1}\omega_n}(k)^i$ or the corresponding backward process $s_i^{'} \to s_i$. Note that each individual state that is part of the trajectory simply corresponds to one of the microstates of the system, $\omega_n \in \Omega$, i.e., to one of the possible spin configurations on the two-dimensional $L \times L$ lattice. Specifically, the total number of distinct spin configurations on the lattice, i.e., the dimension of the probability state space, is given by $\dim(\Omega) = q^{L^2}$. Since we are considering the system in a NESS, the total change of entropy along an individual stochastic path consisting of N transitions is given by (3.17). In the limit of infinitely long trajectories, $N \to \infty$, (3.17) divided by the length N of the trajectory becomes identical to the ensemble averaged medium entropy production rate Φ due to the ergodicity of the system. In a steady state this is further identical to the total entropy production rate Π. Due to the fact that for $q \geq 3$ the state space grows faster than an exponential, one might think that extremely long trajectories are required to get a meaningful result for the entropy prouction rate. However, as will be shown in the results section, already for, $N = 1$, one gets convincing results, even in the limit $q \to \infty$. However, one needs good statistics, i.e., many trajectories, for a precise measurement of Π and Φ. Therefore, the length of the trajectories is irrelevant if we just want to calculate the entropy production rate. Therefore, it is advisable to take many short trajectories in order to minimize the computational effort to calculate Π.

In addition, we also use (3.17) to obtain distributions $P[\Delta\phi(N = 100)]$ for the 4-state model as well as the version with $q \to \infty$. Such distributions of the change of the medium entropy along paths of length $N = 100$ are plotted und discussed in the results section.

Measurement details and parameter settings: In the present study, simulations of the vector Potts model with nearest-neighbor interactions are performed on square lattices with lateral extension ranging from $L = 16$ to $L = 96$. This means that we consider

$L^2 = 256$ up to $L^2 = 9216$ spins per simulation. Before calculating any physical quantity, we first let the system in each individual simulation run evolve for 5×10^4 Monte Carlo steps (MCS) [where one MCS consists of L^2 spin flip attempts with spin-flip rates $w^i_{\mu\nu}$ according to Eq. (3)] to assure that the system has reached a steady state. We then let each system further evolve up to a maximum of 10^6 MCS and use (depending on the system size L) between 100 and 1000 realizations for each parameter setting (i.e., combination of T_1 and T_2) in order to guarantee the convergence of average quantities.

In order to quantify the phase behavior of the system, we calculate the magnetic order parameter

$$m = \frac{1}{L^2}\sqrt{\left(\sum_i \cos\theta_i\right)^2 + \left(\sum_i \sin\theta_i\right)^2}. \tag{9.3}$$

The value of $m \in [0, 1]$ is a measure for the spin ordering in the system. For perfect order, $m = 1$, while in a completely disordered system, $m = 0$. We also define the magnetic order parameters for the two sublattices $\mathcal{L}_1$ and $\mathcal{L}_2$

$$m_k = \frac{1}{2L^2}\sqrt{\left(\sum_{i\in\mathcal{L}_k} \cos\theta_i\right)^2 + \left(\sum_{i\in\mathcal{L}_k} \sin\theta_i\right)^2}, \tag{9.4}$$

where the index $k = 1, 2$ denotes the respective sublattice.

To precisely determine the value of the critical temperature T_c where the phase transition (from the PM to FM or from PM to the BKT phase) sets in, we compute the fourth-order Binder cumulant [228] of the magnetic order parameter m

$$U_4 = 1 - \frac{\langle m^4\rangle}{3\langle m^2\rangle^2}, \tag{9.5}$$

which is universal at criticality. The critical value T_c of the control parameter is given by the intersection point of U_4 for different lateral sizes L of the system. The Binder cumulant for a specific sublattice $\mathcal{L}_k$ is accordingly given by

$$U_4^k = 1 - \frac{\langle m_k^4\rangle}{3\langle m_k^2\rangle^2}. \tag{9.6}$$

In addition, we calculate the specific heat per lattice site which is given by

$$C_v = \frac{1}{T^2}\left[\langle E^2\rangle - \langle E\rangle^2\right], \tag{9.7}$$

what can also be expresses as $\mathrm{d}\langle E\rangle/\mathrm{d}T$. Here, $\langle E\rangle$ corresponds to the average energy per spin due to the interaction with it's nearest neighbors. Specifically, the average energy for a spin s_i is given $\langle E\rangle = \langle -J\sum_{\langle ij\rangle} s_j\rangle$. The specific heat is known to exhibit power-law scaling (with an universal scaling exponent α, at least in the equilibrium version of the model for which $\Delta T = 0$) as the critical temperature T_c is approached from the PM

disordered phase. Additionally, C_v peaks at T_c where its maximum shows power-law scaling as function of L which is often universal [63, 73, 75, 375].

The average EP rate per spin, $\pi = \Pi/L^2$, is calculated according to (3.26) for the 4-state vector Potts model, while (3.17) is used in the case of the XY model ($q \to \infty$) where the spin orientation is continuous. However, π can also be obtained from (3.17) for the 4-state model. In both cases, we check whether the change of π, with respect to the control parameter T, $\mathbf{d}\pi/\mathbf{d}T$, shows universal features (similar to the specific heat C_v) regarding its scaling behavior as function of system size L around the critical point T_c of the phase transition.

Distributions $P(\phi)$ of the change of entropy $\phi = \Delta\phi(N)$ for trajectories of length $N = 100$ are obtained via (3.17) for $q = 4$ and $q \to \infty$. To be exact, we calculate ϕ for the whole lattice and the individual sublattices $\mathcal{L}_1$ and $\mathcal{L}_2$, respectively. This is done by defining trajectories that only account for the change of medium entropy induced by state transitions due to a reorientation of spins which are connected to the respective heat bath T_k (k = 1,2), i.e., spins which are part of either sublattice $\mathcal{L}_1$ or $\mathcal{L}_2$. The distributions $P(\phi)$ are obtained from at least 10^7 individual trajectories from simulations in the steady state.

9.2 Results

In the following, we present a numerical investigation of the nonequilibrium q-state vector Potts model with discrete ($q = 4$) and continuous ($q \to \infty$) spin symmetry. In both cases, we find that the nonequilibrium model exhibits the same type of phase transition as in the equilibrium case. We therefore focus for $q = 4$ on the transition from the spin-disordered PM to the (long-range) spin-ordered FM phase (second-order phase transition), whereas for $q \to \infty$ we analyze the BKT-like transition from the disordered PM to the quasi long-range ordered BKT phase (infinite-order phase transition). In both cases the transitions are continuous in the order parameter. To characterize the critical behavior, we study the specific heat, C_v, and the total entropy production rate per spin, π, and compare the results in the vicinity of the respective critical point T_c for both kinds of nonequilibrium phase transition with their equilibrium counterparts.

9.2.1 Nonequilibrium phase transition in the discrete q-state vector Potts model with $q = 4$

Before we numerically investigate the phase transition of our nonequilibrium spin model by means of MC simualtions with Glauber dynamics, let us briefly review some important properties of the equilibrium version of the 4-state vector Potts model. It is well known [162, 163, 376–378] that the equilibrium model exhibits a second-order phase transition

at $T_c^{eq} = 1.13$. This value corresponds to half the exactly known critical temperature of the classical Ising model ($T_c^{eq} = 2.26$) which is characterized by $q = 2$, and thus, exhibits up-down symmetry. Moreover, the critical exponents of the equilibrium 4-state version are different from the equilibrium Ising model [162].

Behavior of the ensemble-averaged magnetization: To begin with the analysis of the nonequilibrium model, we consider the behavior of the ensemble-averaged magnetization m (9.3), which serves as a global order parameter. Figure 9.2 displays m as function of the mean temperature T for four different (fixed) values of T_2 and various system sizes ranging from $L = 16$ to $L = 96$. The most prominent observation is that while decreasing the mean temperature from high values, the order parameter increases and eventually approaches its maximum value, $m = 1$ (reflecting perfect spin order). This implies the existence of a stable FM phase at low bath temperatures, although the system is clearly out of equilibrium, i.e, $\Delta T > 0$.

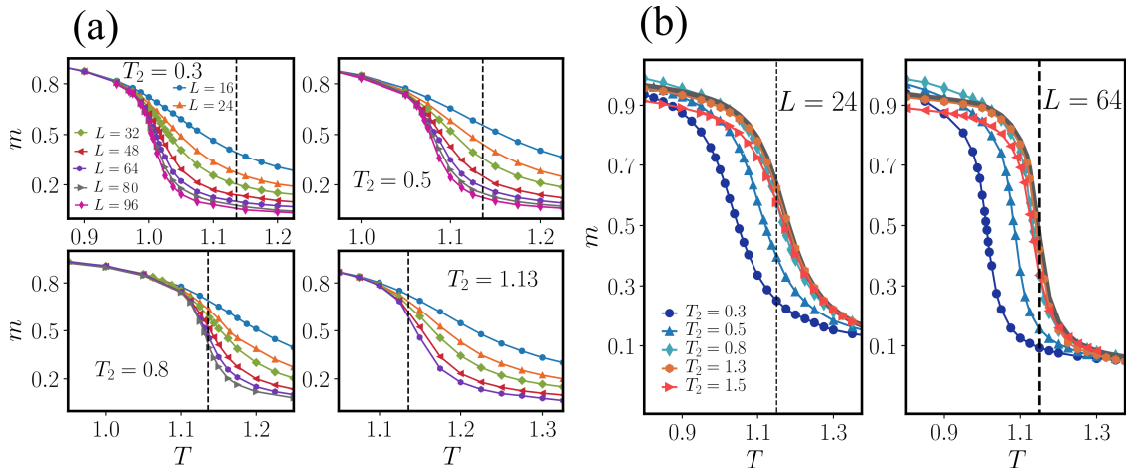

Fig. 9.2: (a) The ensemble-averaged magnetization m vs. mean temperature $T = (T_1 + T_2)/2$ in the q-state vector Potts model with $q = 4$, for system sizes ranging from $L = 16$ to $L = 96$ (different colors and symbols indicate different system sizes) and fixed value for the temperature T_2 in each panel. Accordingly, the mean temperature T is changed by varying the temperature of the first heat bath T_1. (b) The magnetization m in the model with $q = 4$ as function of T for $L = 24$ and $L = 64$ and different fixed values of T_2 ranging from $T_2 = 0.3$ to $T_2 = 1.5$. The solid gray lines correspond to the mean magnetization m in the equilibrium model where $T = T_1 = T_2$, i.e., $\Delta T = 0$. The dashed vertical lines in both panels indicate the critical temperature $T_c^{eq} = 1.13$ of the equilibrium model.

Figure 9.2(a) indicates that the nonequilibrium phase transition occurs at a temperature T_c which is comparable to the one of the equilibirum model, $T_c^{eq} = 1.13$. However, a closer inspection reveals that the precise value of T_c depends on the fixed temperature T_2 in such a way that T_c becomes smaller as T_2 is shifted away from the critical value T_c^{eq} of the equilibrium model. This conspicuousness is further confirmed by Fig. 9.2(b), where (for $L = 24$ and $L = 64$) m is plotted as function of T for different fixed values of T_2. Remarkably, the shift of the temperature region (compared to the equilibrium model) where m as function of T increases to large values (indicating the emergence of spin order in the system) is found to be equally large for both system sizes L. This, in turn,

signals that the temperature shift of the curves is not a finite size effect (which would vanish for $L \to \infty$), but an actual property of this nonequilibrium q-state vector Potts model. A further interesting observation from Fig. 9.2(b) is that the nonequilibrium q-state vector Potts model studied here displays an ordered phase, even if one of the heat bath's temperatures is higher than the critical temperature T_c^{eq} of the corresponding equilibrium model. Even for $T_2 = 1.3$ and $T_2 = 1.5$ the mean magnetization signals the existence of an ordered phase. However, the critical mean temperature T_c is always below the equilibrium value, as we will show in the following.

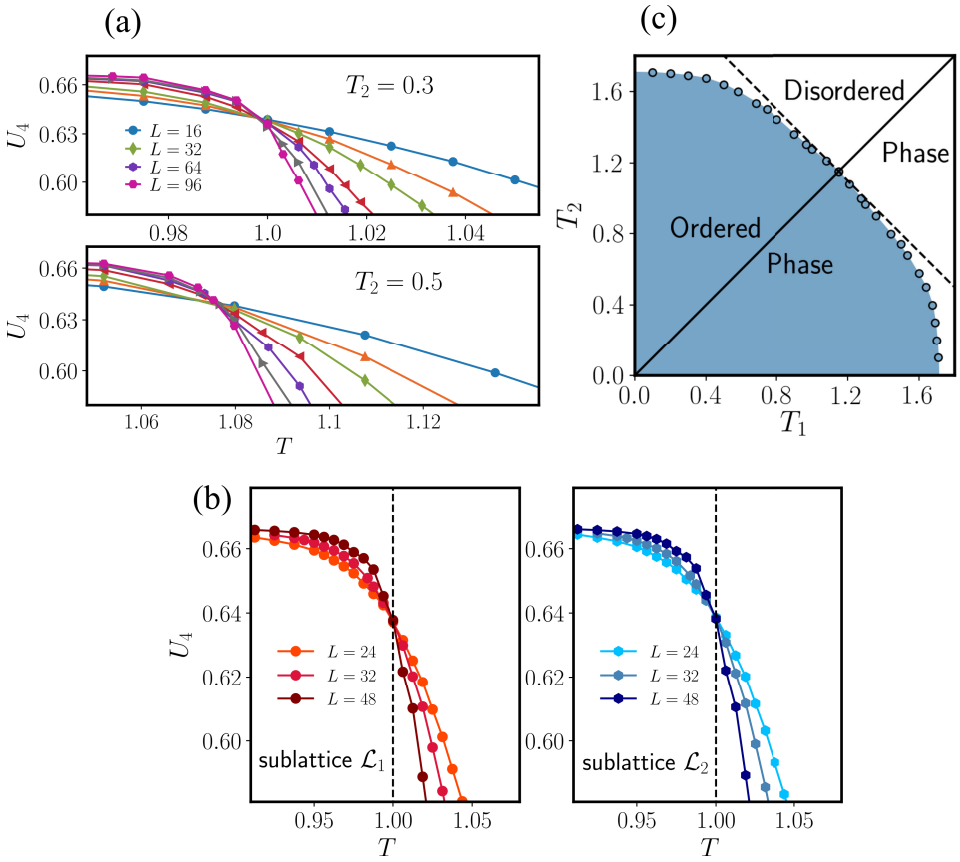

Fig. 9.3: (a) Binder cumulant U_4 in the q-state vector Potts model with $q = 4$ and system sizes ranging from $L = 16$ to $L = 96$. The intersection point of different lines (i.e., different system sizes L) marks the value of the critical temperature T_c. Specifically, at $T_2 = 0.3$ we find $T_c = 0.997(4)$, while at $T_2 = 0.5$ the lines intersect at $T_c = 1.075(8)$. (b) Binder cumulant of the two sublattices $\mathcal{L}_1$ and $\mathcal{L}_2$ with $q = 4$ for $T_2 = 0.3$ and T_1 ranging from $T_1 = 1.5$ to $T_1 = 1.9$ (i.e., T ranges from 0.9 to 1.1) for $L = 24$ to $L = 48$. The vertical dashed black lines mark the critical value T_c where the Binder cumulant intersects. As can be seen, the transition occurs in both sublattices,$\mathcal{L}_1$, $\mathcal{L}_2$, at the same mean temperature T_c which means that there is one critical mean temperature T_c at which the system as a whole undergoes the order-disorder phase transition. (c) Phase diagram of the nonequilibrium q-state vector Potts model with $q = 4$ showing the boundary (circles) between the FM ordered (indicated by the blue shaded region) and the PM disordered phase (white region) as function of T_1 and T_2. The critical temperatures have been obtained from the crossing of the Binder cumulant for different system sizes L at the respective combinations of T_1 and T_2. The solid black line represents the equilibrium case ($T_1 = T_2$) for which $T_c^{eq} = 1.13$. The dashed line marks the region for which $T = (T_1 + T_2)/2 = T_c^{eq}$ holds.

Determination of the critical temperature and the nonequilibrium phase diagram: To precisely analyze the dependency of T_c on T_2 and T_1, we compute the Binder cumulant U_4 as function of T for different values of L [see (9.5) and (9.6)]. Figure 9.3(a) shows the crossing of the respective Binder cumulant lines for two exemplary temperatures T_2, clearly confirming the aforementioned shift of T_c towards smaller values compared to the equilibrium critical temperature T_c^{eq}.

Since the spins s_i on the square lattice are coupled to two different heat baths which are kept at T_1 and T_2, one might expect differences in the phase behavior of the two sublattices $\mathcal{L}_1$ and $\mathcal{L}_2$. However, as one can see in Fig. 9.3(b), the Binder cumulants for different values of L intersect at the same temperature T_c in both sublattices. This shows that the transition from the paramagnetic to the ferromagnetic phase occurs collectively in the entire system at the same critical temperature T_c.

For an overview of the critical temperatures in the plane spanned by T_1 and T_2, we now take a look at the nonequilibrium phase diagram plotted in Fig. 9.3(c). The diagonal (black solid) line where $T_1 = T_2$ corresponds to the equilibrium model. For the nonequilibrium system ($T_1 \neq T_2$), T_c depends on T_1 and T_2 approximately linearly in the vicinity of equilibrium ($T_1 \approx T_2$) but the dependency becomes strongly nonlinear when $T_1 \gg T_2$ or $T_2 \gg T_1$ (i.e., when ΔT becomes large). This is clearly seen when one compares the actual phase boundary with the dashed curve corresponding to the line along which $T = T_c^{eq}$ holds, i.e., $T_2 = 2T_c^{eq} - T_1$. One can further see that when $T_1 = T_2$ (i.e., in the equilibrium model), the phase transition occurs at the highest mean temperature T_c^{eq}. As soon as there is a temperature difference $\Delta T > 0$ between the two sublattices, the nonequilibrium phase transitions occur at a lower critical temperature, which deviates from T_c^{eq} the more as the difference $\Delta T = |T_1 - T_2|$ between T_1 and T_2 increases. Moreover, there exists a new type of critical temperature $T_c^* = 1.700(2)$ with the following property: If one sublattice has a temperature higher than T_c^*, global order is destroyed, irrespective of the temperature of the other sublattice. As consequence, there is no phase transition in the model whenever one of the sublattices is kept at a temperature $T_k > T_c^*$.

Physically, one may understand the phase behavior in the following manner. When heating the system up in the presence of a temperature difference ΔT between the sublattices, disorder is favored already at lower system-averaged temperatures T, showing that a smaller amount of thermal noise destroys the long-range order. Consistent with our physical intuition, a breaking of the translational symmetry (by the temperature difference between the sublattices) reduces the stability of long-range order. Note that this is in sharp contrast to the situation where an homogeneous external magnetic field acts on the system (breaking the up-down symmetry) which increases the stability of long-range ordering.

9.2.2 Critical behavior of specific heat

After the determination of T_c and its dependency on the temperatures of the two heat baths, we now turn to the investigation of the thermodynamic properties of our nonequilibrium spin model in the vicinity of the nonequilibrium order-disorder phase transition. To this end, we first calculate the specific heat C_v [see Eq. (9.7)] as function of the mean temperature T for different values of L and T_2. This quantity is commonly considered in order to characterize second-order phase transitions. As can be seen in Fig. 9.4(a), C_v peaks at a temperature very close to the values of T_c that we have previously determined via the Binder cumulant (recall Fig. 9.3).

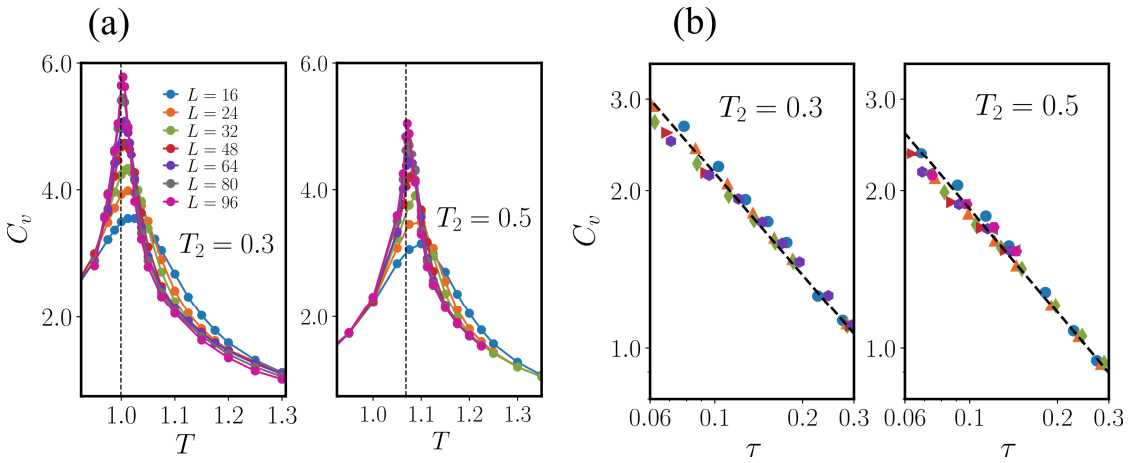

Fig. 9.4: (a) The specific heat C_v vs. T for $T_2 = 0.3$ and $T_2 = 0.5$ and system sizes ranging from $L = 16$ up to $L = 96$. The dashed lines indicate the value of T_c obtained from the crossing of the Binder cumulant U_4. (b) Power-law scaling of the specific heat C_v vs. the reduced temperature $\tau = |1 - T/T_c|$ in the disordered (paramagnetic) phase for fixed T_2 and system sizes ranging from $L = 16$ up to $L = 96$ indicated by different colors and symbols. For both values of T_2 the dashed black line follows $\sim 2/3$.

For both depicted values of T_2, the precise location of the peak depends on L in such a way that as the system size is increased, the temperature where the peak is located decreases and approaches T_c. We suspect that the peak is exactly at T_c in the limit $L \to \infty$, as it is well-known for the equilibrium version of this model. In thermal equilibrium, the specific heat of the model is further known to show universal (power-law) scaling behavior with respect to the reduced temperature τ, i.e.,

$$C_\nu \sim |1 - T/T_c|^{-\alpha} = \tau^{-\alpha}, \tag{9.8}$$

with $\alpha = 2/3$ in the disordered phase [162]. Interestingly, we find that the nonequilibrium model also displays a power-law divergence of C_v. Moreover, the critical exponent α is the same as in equilibrium, irrespective of the value of the temperature gradient $\Delta T = |T_2 - T_1|$ among the two heat baths (as long as $T_1 \leq T_c^*$ and $T_2 \leq T_c^*$). This is exemplarily illustrated for $T_2 = 0.3$ and $T_2 = 0.5$ in Fig. 9.4(b), where C_v is plotted for different system sizes (from $L = 16$ to $L = 96$) as function of the reduced temperature $\tau = |1 - T/T_c|$ together with straight (black dashed) lines (with slope $-2/3$). We checked the scaling behavior for

various additional values of $T_2 \leq T_c^*$ and found that all of them show a power-law scaling with $\alpha = 2/3$, demonstrating the robustness of the critical exponent under nonequilibrium conditions. To analyze the critical behavior based on our numerical data in detail, we employ the finite-size scaling technique. To this end, we consider the positions of the peaks of C_ν, which give an approximation for the critical temperature as function of the system size L. For the equilibrium 4-state vector Potts model on a square lattice, this quantity scales as $\sim L^{-\nu}$, with the corresponding critical exponent $\nu = 2/3$ [379]. Also for the nonequilibrium model we obtain $\nu = 2/3$ for all values of T_2, consistent with the well-known scaling law $\nu d = 2 - \alpha$ [380] (where $d = 2$ is the spatial dimension of the lattice). This consistency check confirms the correctness of our numerically determined critical exponents for the nonequilibrium 4-state vector Potts model.

9.2.3 Critical behavior of total entropy production

Let us now consider the behavior of the total entropy production which is a direct measure for irreversibility of our model in the sense that it quantifies the distance from equilibrium. To start with, we find that the total EPR per spin is always positive, $\pi > 0$, whenever $T_1 \neq T_2$. Moreover, π is a convex function of the mean temperature T with a minimum at the equilibrium point $T = T_1 = T_2$, where $\pi = 0$ [consistent with Eq. (3.23)]. This can be seen in Fig. 9.5(a), which depicts π vs. T for an exemplary system setting with $T_2 = 1.5$ and $L = 32$ around the equilibrium mean temperature $T = T_1 = T_2 = 1.5$.

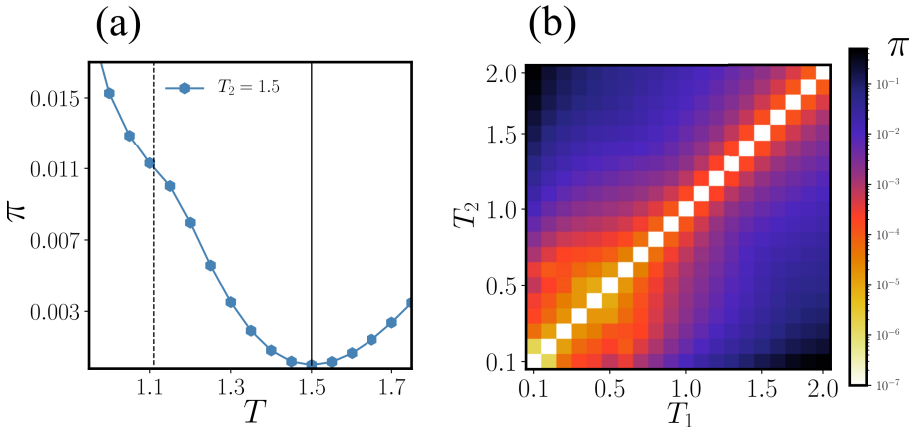

Fig. 9.5: (a) The total entropy production rate per spin, π, as function of the mean temperature T for fixed $T_2 = 1.5$ and system size $L = 32$ in the q-state vector Potts model with $q = 4$. The solid black line corresponds to the equilibrium point where $T_1 = T_2$, i.e., where $\Delta T = 0$, and the dashed black line marks the critical temperature T_c of the continuous nonequilibrium transition from the paramagnetic to ferromagnetic phase. (b) Heatmap of the total entropy prouction rate per spin, π on a lattice of size $L = 32$ for temperatures of the two sublattices ranging from $T_1 = T_2 = 0.1$ up to $T_1 = T_2 = 2.0$.

Depending on whether T_2 is higher or lower than T_c^{eq}, the phase transition of the nonequilibrium model lies below or above that minimum (where $\pi = 0$) (which is always located at $T = T_1 = T_2$, i.e., at the equilibrium point where $\Delta T = 0$). In other words, if $T_2 > T_c$, which is the situation considered in Fig. 9.5(a), the nonequilibrium phase transition occurs

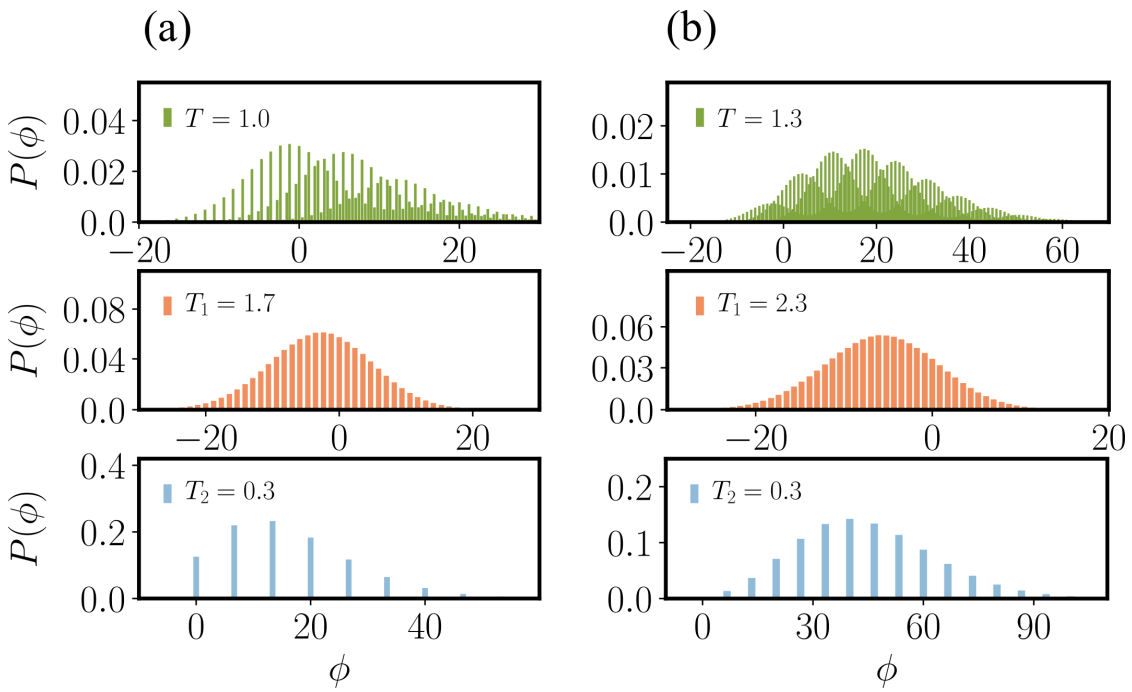

Fig. 9.6: Distribution $P(\phi)$ of the stochastic medium entropy $\phi = \Delta\phi(N)$ that is produced in the system along individual stochastic trajectories of length $N = 100$ in the 4-state vector Potts model. The panels of (a) show $P(\phi)$ in the vicinity of the phase transition [which is at $T = T_c = 0.997(4)$] for a system with $L = 64$, at $T_1 = 1.7$ and $T_2 = 0.3$ (here $\Delta T = 1.4$). The top panel shows the distribution of the whole system. The middle panel shows the distribution of the medium entropy production of the spins which belong to the sublattice $\mathcal{L}_1$, whereas the panel at the bottom shows the distribution $P(\phi)$ for $\mathcal{L}_2$. (b) Depicts the corresponding distributions in the PM disordered phase, at $T = 1.3 > T_c$, specifically at $T_1 = 2.3$ and $T_2 = 0.3$ (here $\Delta T = 2.0$).

at the left hand side of the minimum, whereas if $T_2 < T_c$, the transition occurs at the right hand side of it. Interestingly, we observe that π as function of T shows a bump around the value of the critical temperature $T_c = 1.11$ [see Fig. 9.3(c)]. In that sense, the function $\pi(T)$ itself already signals the occurence of the phase transition. How exactly π indicates the phase transition will be investigated further below in this section.

The dependency of entropy production rate per spin on the temperatures of the two heat baths is plotted in Fig. 9.5(b), which shows π for different combinations of T_1 and T_2 ranging from 0.1 up to 2.0. As expected, $\pi = 0$ whenever $T_1 = T_2$ [i.e., no temperature gradient ΔT is present and detailed balance is fulfilled, see Eq. (3.23)]. In contrast to this, there is always a positive rate of entropy production ($\pi > 0$) when $T_1 \neq T_2$, consistent with the special case considered in Fig. 9.5(a). As the gradient ΔT increases, the entropy production rate increases roughly $\pi \sim \Delta T^2$, no matter whether the system is in the disordered PM or the ordered FM phase.

To resolve the change of medium entropy along individual stochastic trajectories, $\phi = \Delta S_m(N = 100)$, we analyzed distributions of the medium entropy production $P(\phi)$. Figure 9.6 displays numerical results for $P(\phi)$ at the critical temperature T_c [Fig. 9.6(a)]

and above T_c [Fig. 9.6(b)], for trajectories of length $N = 100$ [recall Eq. (3.17) for the calculation of the medium entropy production along a stochastic path of length N]. We consider both, the distribution of the entire system as a whole (top panels), and the separate distributions obtained by restricting our observation to one of the two sublattices, $\mathcal{L}_1$ or $\mathcal{L}_2$, only (middle and bottom panels, respectively). For example, the middle panels show the histograms of all detected values of the medium entropy change ϕ from spins that belong to the sublattice $\mathcal{L}_1$. Overall, the main characteristics seem to be quite similar for the system at and above the phase transition [compare (a) and (b)]. Let us now take a closer look at the different distributions. Remarkably, in both cases, $P(\phi)$ for the whole lattice exhibits a multi-peaked structure [see top panels in Fig. 9.6]. When inspecting the corresponding sublattice distributions of ϕ, we notice that the multi-peak structure of the whole system appears to arise as a combination of both sublattices. This is reasonable, as the stochastic trajectories of the whole system expectantly include both, many contributions from the hotter sublattice (where spin flips $s_i \to s_i^{'}$ happen more frequently because the transition rate $w_{\nu\mu}$ for a spin flip with the same $\Delta E_{\nu\mu}$ is higher in the subsystem which is in contact with the hotter heat bath), and some seldom contributions from the colder sublattice in which spin flips $s_i \to s_i^{'}$ are more seldom. In fact, the multi-peaked structure looks like a convolution of the distributions from the belonging sublattices $\mathcal{L}_1, \mathcal{L}_2$. Further, we notice that $P(\phi)$ of the individual sublattices have smooth single-peaked shapes. Furthermore, all distributions are discrete, reflecting that the number of possible transitions (and thus, the possible ϕ values) is finite, because of the discreteness of the underlying spin dynamics. For the colder sublattice, $\mathcal{L}_2$, the medium entropy production, ϕ, only takes a particularly small number of values. This is due to the fact that at low bath temperatures, the sublattice only explores a small part of the phase space, and hence, the number of distinct state transitions is small. As a consequence, changes of the medium entropy along stochastic paths of length $N = 100$ are limited to a rather small number of possible values ϕ. In contrast to this, for the hotter sublattice, $\mathcal{L}_1$, we notice that the maxima and mean values of $P(\phi)$ lie at $\phi < 0$ [in both cases, (a) and (b)]. This alone would violate the second-law of thermodynamics since it implies a negative mean entropy production rate. However, in its usual form, $\Phi = \Pi \geq 0$, the second law only applies to the entire system which consists of the two sublattices $\mathcal{L}_1$ and $\mathcal{L}_2$ joined together. In fact, the negative mean value simply reflects the situation that heat flows from the hotter to the colder heat bath. Overall, the entropy is increased over time in the whole system, i.e., $\pi \geq 0$ for all values of ΔT.

Next, we study the system size dependency of the total entropy production rate per spin, π, around the critical point T_c of the phase transition. To this end, we consider a system where T_2 is fixed to a value below T_c^{eq} [see the left panel of Fig. 9.7(a)], and another one where $T_2 > T_c^{eq}$ [see the right panel of Fig. 9.7(a) which is essentially an enlarged version of Fig. 9.5(a) for different L close to T_c]. Both parts of Fig. 9.7(a) indicate that π is *identical* for all system sizes for T values far away from T_c, i.e., all lines collapse on a single curves when $T \ll T_c$ or $T \gg T_c$. In contrast, the lines begin to split up in the vicinity of T_c. This means that, around the phase transition π suddenly becomes dependent on

the system size L. This resembles the behavior of the specific heat [recall Fig. 9.4]. One can further observe the emergence of a shoulder around T_c which gets more pronounced while increasing L. It is, however, noteworthy that we do not observe the formation of a saddlepoint or even non-monotonous behavior for all considered system sizes, i.e., until the value $L = 96$.

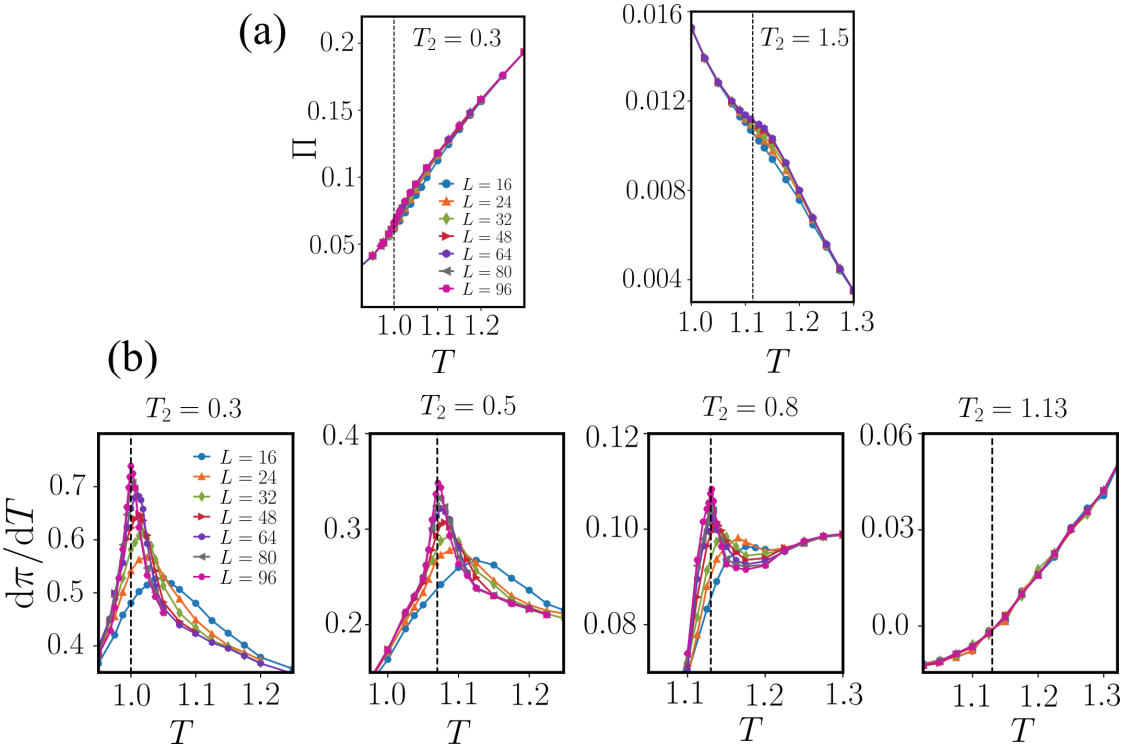

Fig. 9.7: (a) The entropy production rate per spin, π, as function of the mean temperature T for fixed T_2 and system sizes ranging from $L = 16$ to $L = 96$. In the left panel, the temperature of sublattice $\mathcal{L}_2$ is fixed to $T_2 = 0.3$ which is below the critical temperature T_c^{eq} of the equilibrium model, while in the right panel, the temperature of $\mathcal{L}_2$ is $T_2 = 1.5$, which is above T_c^{eq} [see also Fig. 9.5(a)]. The black dashed lines mark the critical temperature T_c. (b) Derivative $\mathrm{d}\pi/\mathrm{d}T$ of the entropy production rate per spin as function of the mean temperature T for different fixed values of T_2 ranging from $T_2 = 0.3$ up to $T_2 = 1.13 = T_c^{eq}$ and system sizes ranging from $L = 16$ to $L = 96$. The black dashed lines mark the critical temperature T_c.

In order to study the behavior around the critical point, we inspect the derivative of the entropy production rate per spin, $\mathrm{d}\pi/\mathrm{d}T$, for various values of T_2 as shown in Fig. 9.7(b). Interestingly, $\mathrm{d}\pi/\mathrm{d}T$ peaks around the mean temperature of the phase transition. An exception is the case $T_2 = T_c^{eq}$ where the total entropy production naturally vanishes because at this point, the system is in thermal equilibrium, i.e., $\Delta T = 0$. Thus, detailed balance is fulfilled and consequently, $\mathrm{d}\pi/\mathrm{d}T = 0$ for all system sizes L. This is the reason why the derivative of π with respect to T does not peak and split up at T_c. In fact, $\mathrm{d}\pi/\mathrm{d}T$ is identical for all system sizes L. Interestingly, the temperature where the peak of $\mathrm{d}\pi/\mathrm{d}T$ is located decreases as does the peak of the specific heat. This further resembles the behavior of C_v in the vicinity of the critical point. Moreover, one observes a dependency of the maximum of $\mathrm{d}\pi/\mathrm{d}T$ on the value of T_2 which (for fixed L) decreases as T_2 approaches T_c^{eq}.

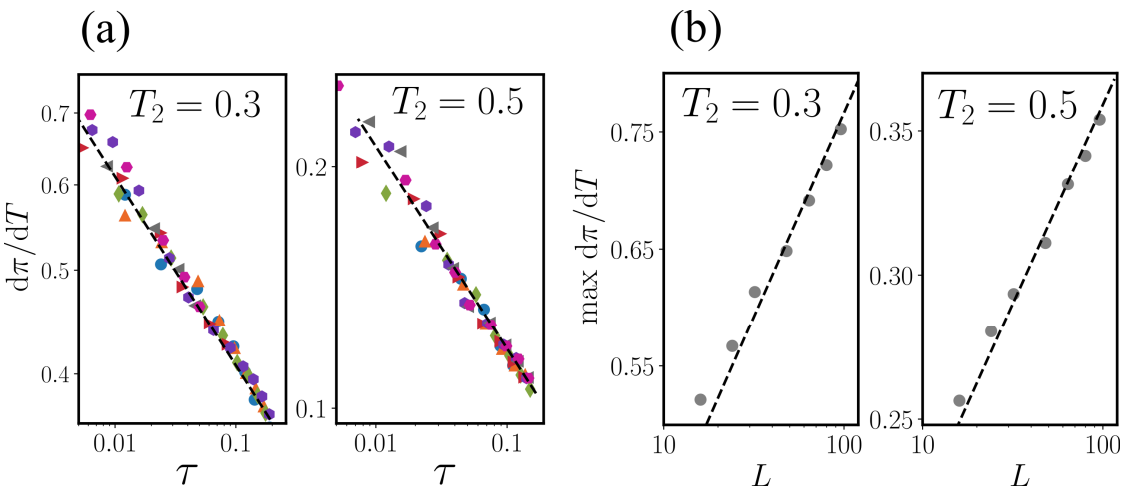

Fig. 9.8: (a) Power-law scaling of the derivative of the entropy production rate as function of the reduced temperature $\tau = |1 - T/T_c|$ for two values of T_2 ($T_2 = 0.3$ and $T_2 = 0.2$) and system sizes ranging from $L = 16$ to $L = 96$. The black dashed line in the left panel follows $\sim -0.175(11)$, while in the right panel it follows $\sim -0.145(15)$. (b) Maximum of the derivative of the entropy production rate as function of system size L. The left panel shows the scaling of $\mathrm{d}\pi/\mathrm{d}T_{max}$ at $T_2 = 0.3$ for system sizes from $L = 16$ up to $L = 96$. The black dashed lines scales ~ 0.245. In the right panel the same is plotted for $T_2 = 0.5$ and the black dashed line follows ~ 0.205.

To analyze the nonequilibrium phase transitions in more detail, we perform a finite-size scaling analysis of π, similar to our investigation of the specific heat (see Fig. 9.4). We aim to stress that the application of a finite-size scaling analysis to the entropy production at a nonequilibrium transition is, to our knowledge, novel. In fact, there are no studies so far where the attempt is made to assign a critical exponent to the entropy production by investigating it's scaling behavior around T_c. To this end, we first study the scaling behavior of $\mathrm{d}\pi/\mathrm{d}T$ in the disordered phase as function of the reduced temperature τ. Second, we consider the peak height of $\mathrm{d}\pi/\mathrm{d}T$ as function of the system size L. As can be seen in Fig. 9.8(a), $\mathrm{d}\pi/\mathrm{d}T$ shows power-law behavior $\sim \tau^{\zeta}$ with an exponent ζ, whose precise value depends on the distance from equilibrium at the phase transition (i.e., on the value of $\Delta T = |T_2 - T_1|$). Specifically, we detect power-law behavior of $\mathrm{d}\pi/\mathrm{d}T$ for all considered values of T_2 with a decreasing value for ζ as T_2 approaches T_c^{eq}, where it nullifies. For $T_2 = 0.3$ [see the left panel in Fig. 9.8(a)] the exponent reads $\zeta = 0.175(11)$, while for $T_2 = 0.5$ [see the right panel in Fig. 9.8(a)] $\zeta = 0.145(15)$ (see the dashed black lines). While the power-law behavior resembles that of the specific heat, there is a marked difference in the sense that the exponent ζ is not constant (such as the exponent α of C_v), but depends on ΔT. This means that ζ is not universal but depends on the distance from equilibrium. In addition, we analyze the scaling behavior of the maximum of $\mathrm{d}\pi/\mathrm{d}T$ as the system size L is increased and show results for $T_2 = 0.3$ and $T_2 = 0.5$ in Fig. 9.8(b). According to the finite-size scaling theory for equilibrium systems [228], all divergent quantities scale as $\sim L^{\mathrm{a}/\nu}$, where a is the critical exponent of the power-law decay of that very quantity. Thus, we test whether the maximum of $\mathrm{d}\pi/\mathrm{d}T$ scales as $\sim L^{\zeta/\nu}$, with $\nu = 2/3$. From our numerical data, we find $\mathrm{d}\pi/\mathrm{d}T_{max} \sim L^{0.245}$ for $T_2 = 0.3$

and $\mathrm{d}\pi/\mathrm{d}T_{max} \sim L^{0.205}$ for $T_2 = 0.5$ which is indeed in good agreement with $\zeta = 0.175(11)$ ($T_2 = 0.3$) and $\zeta = 0.145(15)$ ($T_2 = 0.5$) as obtained in Fig. 9.8(a). The fulfillment of the finite-size scaling relation shows indeed that the derivative of the entropy production rate behaves as a diverging quantity as the critical point T_c of the nonequilibrium phase transition is approached. It further demonstrates that the finite-size scaling theory is applicable to the entropy production rate, despite the dependency of the critical exponent ζ on the temperature gradient ΔT between the two sublattices $\mathcal{L}_1$ and $\mathcal{L}_2$.

9.2.4 BKT-like phase transition in the continuous q-state vector Potts model with $q \to \infty$

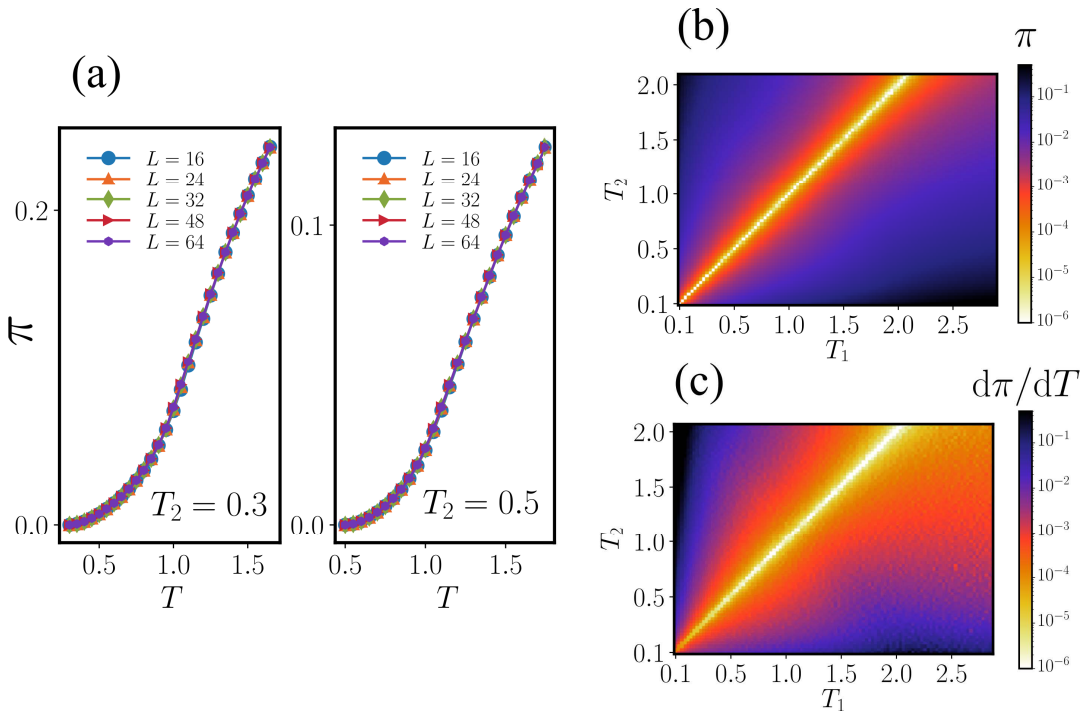

Fig. 9.9: (a) Entropy production rate per spin π of the nonequilibrium q-state vector Potts model with $q \to \infty$ (XY model) as function of the mean temperature T for system sizes ranging from $L = 16$ to $L = 64$ with $T_2 = 0.3$ and $T_2 = 0.5$. (b) Heatmap of π in the XY model on a lattice of size $L = 32$ for temperatures of the two sublattices ranging from $T_1 = T_2 = 0.1$ up to $T_1 = 2.0$ and $T_2 = 2.5$. (c) Derivative of the entropy production rate per spin, $\mathrm{d}\pi/\mathrm{d}T$ in the XY model on a lattice of size $L = 32$.

Now we turn to the investigation of the nonequilibrium q-state vector Potts model with $q \to \infty$ (also known as the XY model), where the spins can freely rotate in the $x - y$ plane, i.e., all spin orientations $s_i \in [0, 2\pi]$ are allowed. As a consequence of the continuous spin symmetry and the two-dimensional character of the system, there exists no long-range ordered phase at finite temperatures as stated by the Mermin-Wagner theorem [53–55, 219]. Instead, a quasi-long range ordered phase, the BKT phase, occurs at low bath temperatures $T < T_c$. While the infinite-order transition between the disordered paramagnetic and the quasi long-range ordered BKT phase is quite well understood in the equilbrium model [57, 162], nonequilibrium BKT phase transitions are in general less

understood. In particular, the question of how the entropy production rate behaves at this transition has, to the best of our knowledge, not been considered in earlier literature. In the previous discussion of the case $q = 4$, we have seen that the derivative of the total entropy production rate per spin shows critical behavior which partially resembles the behavior of the specific heat. Let us now see if this analogy carries over to the infinite-order BKT transition, which has very different overall characteristics and, in particular, is not accompanied with a divergence of C_v at the critical temperature which is given by $T_c^{eq} = 0.892880(6)$ in the equilibrium XY model [57, 163, 164, 381–383]. In Fig. 9.9(a), we show results for π at $T_2 = 0.3$ and $T_2 = 0.5$ for system sizes ranging from $L = 16$ up to $L = 64$. As indicated there, the π does not split with respect to L in the vicinity of the phase transition. Instead, π is apparently size-independent in the whole depicted temperature range which includes the BKT transition. From this we conclude that there is no system size dependency of π at all. In order to visualize the entropy production rate for different combinations of T_1 and T_2, we plot π in the $T_1 - T_2$ plane in Fig. 9.9(b) together with the derivative of π with respect to temperature, $\mathrm{d}\pi/\mathrm{d}T$ in Fig. 9.9(c) for system size $L = 32$.

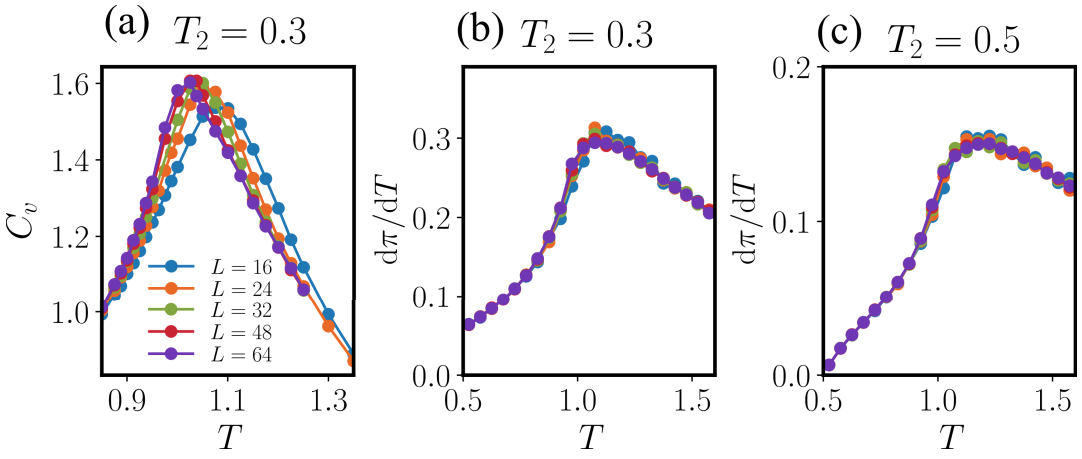

Fig. 9.10: (a) Specific heat C_v of the nonequilibrium vector Potts model with $q \to \infty$ (XY model) as function of the mean temperature T for $T_2 = 0.5$ and system sizes ranging from $L = 16$ to $L = 64$. (b) shows the derivative, $\mathrm{d}\pi/\mathrm{d}T$, of the EP rate as function T for the same system sizes and $T_2 = 0.3$, while $T_2 = 0.5$ in (c).

Additionally, the specific heat C_v for $T_2 = 0.5$ and $\mathrm{d}\pi/\mathrm{d}T$ for $T_2 = 0.3$ and $T_2 = 0.5$ are plotted in Fig. 9.10. In contrast to the PM to FM transition of the 4-state vector Potts model, C_v in the nonequilibrium XY model does not show any feature like a divergence at criticality. In particular, it only shows a peak around $T = 1.1$, as does the equilibrium XY model [162, 163], which is above T_c. Specifically, the value of T where the peak in C_v is observed in our nonequilibrium model is identical to the equilibrium value. Interestingly, also the derivative of the entropy production rate with respect to the mean temperature, $\mathrm{d}\pi/\mathrm{d}T$, does not peak in the vicinity of the critical point. Similar to the specific heat, $\mathrm{d}\pi/\mathrm{d}T$ also shows the peak around $T = 1.1$ which does not depend on L, i.e., the maximum of $\mathrm{d}\pi/\mathrm{d}T$ does not diverge, but remains constant for all considered system sizes L. However, we observe that the maximum of $\mathrm{d}\pi/\mathrm{d}T$ depends on the temperature difference ΔT between

the two sublattices $\mathcal{L}_1$ and $\mathcal{L}_2$ in the vicinity of the peak as confirmed by comparing Fig. 9.10(b) with Fig. 9.10(c), where one observes that the maximum value of $\mathrm{d}\pi/\mathrm{d}T$ at $T_2 = 0.3$ is at around $(\mathrm{d}\pi/\mathrm{d}T)_{max} \approx 0.30$ which is larger compared to $T_2 = 0.5$ where it is at around $(\mathrm{d}\pi/\mathrm{d}T)_{max} \approx 0.15$.

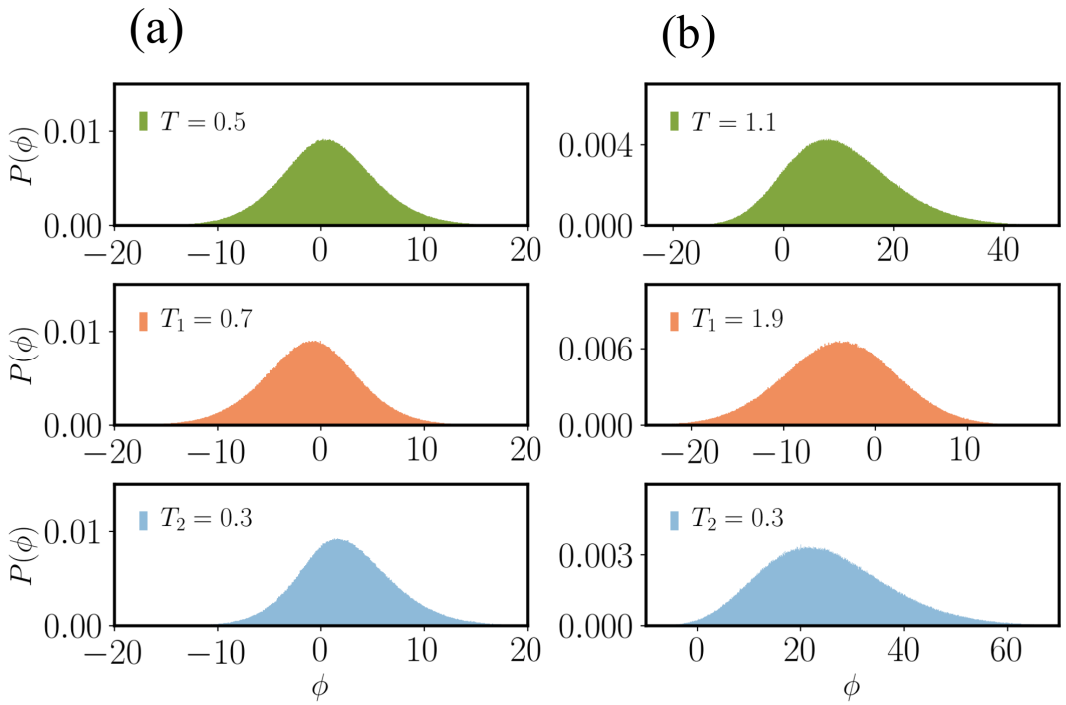

Fig. 9.11: Distribution $P(\phi)$ of the medium entropy $\phi = \Delta S_m(N)$ that is produced in the system along stochastic trajectories of length $N = 100$ in the XY model (where $q \to \infty$). The top panel in (a) shows $P(\phi)$ below the critical point in the BKT phase (i.e., in the quasi long-range ordered BKT phase) for a system with $L = 64$ at $T_1 = 0.7$ and $T_2 = 0.3$. The middle panel in (a) shows $P(\phi)$ for $\mathcal{L}_1$ and the one at the bottom of (a) for $\mathcal{L}_2$. (b) shows the same in the PM disordered phase with for $T_1 = 1.9$ and $T_2 = 0.3$.

Just as for the q-state vector Potts model with $q = 4$, we investigate the distribution $P(\phi)$ of entropy $\phi = \Delta S_m(N)$ that is produced along stochastic trajectories of length $N = 100$. To this end, we plot $P(\phi)$ for a system of size $L = 64$ in the quasi long-range ordered BKT phase at $T = 0.5$ with $T_1 = 0.7$ and $T_2 = 0.3$ (i.e., $\Delta T = 0.4$) in the top panel of Fig. 9.11(a). The distribution for the whole system seems to be symmetric around the peak position of $P(\phi)$ which is located in the positive range, $\phi > 0$ in accordance with the second law of thermodynamics. In contrast, $P(\phi)$ for subsystem $\mathcal{L}_1$ peaks in the negative range, and $P(\phi)$ for subsystem $\mathcal{L}_2$ peaks at a positive value of ϕ. This difference in the peak positions just reflects the expected entropy flow from the hot to the cold reservoir exactly like in the case of the model with discrete spin symmetry. Additionally, one observes different skew directions for $P(\phi)$ in the two subsystems. $P(\phi)$ for subsystem $\mathcal{L}_1$ is slightly right-skewed, while $P(\phi)$ in $\mathcal{L}_2$ is a left-skewed distribution. This effect becomes more pronounced for the system in the disordered PM phase [see Fig. 9.11(b)] where one clearly observes that $P(\phi)$ is skewed in both sublattices $\mathcal{L}_1$ and $\mathcal{L}_2$. Since the distribution for $\mathcal{L}_2$ is stronger skewed, the distribution for the whole system is also left-skewed. However, the effect there is weaker because the contribution of $\mathcal{L}_1$.

9.3 Conclusions and Outlook

In summary, we have analyzed the behavior of various critical quantities and that of the total entropy production rate per spin around the critical point in a nonequilibrium q-state vector Potts model with discrete spin symmetry (i.e., with $q = 4$) as well as with continuous spin symmetry (i.e., with $q \to \infty$). The nonequilibrium character results from coupling the spins to two heat baths at different temperatures, T_1 and T_2. Based on this generic nonequilibrium model, we address several questions: Does the type of phase transition, i.e., it's order, and the corresponding critical exponents change by driving the system away from equilibrium? Does the entropy production exhibit universal behavior in the vicinity of a continuous phase transition? To be more precisely, is is possible to assign the entropy production a critical exponent which is constant, irrespective of the strength of the driving, i.e., the temperature difference ΔT among the two heat bath temperatures? What exactly happens to the entropy production rate in the vicinity of an a infinite-order phase transition? Does it show noticeable behavior which could allow to classify nonequilibrium systems which undergo an infinite-order phase transition?

To answer these questions, we have first investigated the model with $q = 4$ in the vicinity of the second–order PM to FM phase transition. We found that the critical temperature T_c of the transition decreases as the temperature difference ΔT between the two heat baths T_1 and T_2 increases. Moreover, the behavior of the specific heat C_v resembles that of the equilibrium model, i.e., it shows power-law divergence with a critical exponent that is independent of the temperature difference ΔT. Interestingly, the derivative of the entropy production rate with respect to the mean temperature behaves, to some extent, similar. It also shows power-law divergence. However, the value of the scaling exponents does explicitly depend on the ΔT and is thus non-universal. Concerning the model with $q \to \infty$, the specific heat as well as the derivative of the entropy production rate do not show any noticeable behavior around the infinite–order transition from the PM to the quasi long-range ordered BKT phase. Instead, both quantites have a finite peak at a temperature above the critical temperature, i.e., in the PM disordered phase. As the temperature difference between the heat baths is increased, the maximum value of the derivative of the entropy production rate becomes more pronounced. In total, our results provide evidence that the derivative of the entropy production rate behaves like a critical quantity, but, as we report here, is non-universal regarding it's power-law scaling behavior.

Finally, we aim at pointing out possible perspectives for future work in this direction, starting with some questions directly following from the results presented here. For the sake of generality one should study and compare the behavior of the specific heat with the entropy production rate in other lattice dimensions d and for different lattice topologies. In this sense, the cases $d = 1$ and $d = 3$ are especially interesting. While equilibrium spin systems in one spatial dimension do not show a phase transition, their

nonequilibrium versions might undergo a order-disorder transition. It would be interesting to study and compare the power-law behavior of the entropy production with the specific heat for the two temperature q-state vector Potts model also in one and three spatial dimensions. According to the Mermin-Wagner theorem the XY model with $d = 2$ does not exhibit a stable ferromagnetic phase. In contrast, the version with $d = 3$ exhibits spontaneous magnetization and shows a PM to FM transition. It would be interesting to study the critical behavior of the entropy production in this model which exhibits continuous symmetry. Further, although the BKT phase transition is not accompanied by a divergence of thermodynamic quantities, in equilibrium, it still obeys characteristic scaling dimensions [73, 74]. A more detailed analysis of this transition in the nonequilbrium model, and, specifically, with respect to the derivative of the entropy production rate, represents an interesting objective for future research in this direction. From a theoretical point of view, it would moreover be worth to think about the connection between entropy production and specific heat, which seem to behave analogously around criticality, on a fundamental level.

Furthermore, an interesting novel perspective on the nonequilibrium model considered here is the reinterpretation as a model with non-reciprocal coupling between interacing isothermal spins. To be more specific, a vector-Potts model where interacting spins are coupled among each other with two distinct coupling constants ($J_1 = J/T_1$ and $J_2 = J/T_2$) and uniform temperature follows the exact same equations of motions as our model (with two temperatures and identical coupling constants J). This provides a connection to spin models on directed graphs [153, 384–388], and to the topic of non-reciprocal interactions, which is currently a focus in nonequilibrium statistical mechanics [389–391]. It would be interesting to compare the thermodynamic properties of spin systems subjected to different driving mechanisms, e.g., non-reciprocal couplings, temperature gradients, external fields and colored noise.

10 Concluding remarks and future directions

In this thesis we have performed particle-based computer simulations to study the collective behavior of two prototypical discrete systems. Due to their simplicity, these systems are particular suitable to study physical behavior under nonequilibrium conditions on a fundamental level. First, we have investigated a growth model that mimics the self-assembly of crystalline structures under nonequilibrium growth conditions. Second, we have studied nonequilibrium phase transitions by means of a driven q-state vector Potts model.

First, we have investigated the impact of anisotropic interactions on nonequilibrium surface growth in a model which assumes a spherical shape of deposited particles. The strength of anisotropic interactions is regulated by a control parameter that measures the ratio of interaction energy along the two lattice directions of a square substrate. Our results reveal that anisotropic interactions can lead to compact, non-spherical, elongated cluster shapes under growth conditions where clusters would be dendritic for isotropic interactions. We have shown this explicitly by calculating the aspect ratio and the fractal cluster dimension. The cluster size distributions reveal that clusters become on average smaller as the interaction anisotropy is increased. Moreover, as the interaction anisotropy gets stronger, there exist two types of cluster shape transformation. On the one hand, the transformation from isotropic to elongated clusters is gradual at low interaction energies. On the other hand, it is sharp at high values of the interaction energy. For strong interaction anisotropy, clusters grow initially one-dimensionally until this growth mode breaks down at a critical length. Further, we have investigated the effect of the adsorption rate. We found that the average cluster aspect ratio as function of adsorption rate displays power-law scaling in the regime of strong interaction anisotropy. This is also true for the evolution of the average cluster length and width. We have also employed an anisotropic Eden model with a fitting parameter that controls the attachment probabilities along the two lattice directions. This model, which completely neglects diffusion of particles on the substrate, reproduces the main features of the cluster growth observed in the kinetic Monte-Carlo simulations.

A natural extension of our studies so far would be the investigation of our model in the multilayer growth regime. In this sense, it would be interesting to study the scaling behavior of the surface roughness in order to find out whether the model exhibits universal behavior. Conjugated organic molecules which are used for the industrial fabrication

of thin film devices often exhibit dipole moments. Using our model, one could study the impact of long-range dipole-dipole interactions between deposited particles on the emerging surface morphologies. Further, it is possible to investigate the effect of dipolar interactions between particles and the substrate on the growth behavior.

Second, we have introduced a limited mobility model with variable diffusion length. The model is tempted to model low-temperature surface growth by means of molecular beam epitaxy. In particular, the diffusion length of each deposited particle is chosen from a Gaussian distribution. The mean value of the distribution corresponds to the average nucleation length obtained from “material-dependent full diffusion" kinetic Monte-Carlo simulations which include diffusion rates for all particles in the topmost layer at any time step of the simulation. The variance of the distribution allows to control the strength of fluctuations in the diffusion length. Our model is capable to correctly mimic low-temperature surface growth through kinetic Monte-Carlo simulations for arbitrary values of the growth parameter. The latter corresponds to the free diffusion to deposition ratio. For all growth parameters in the "full diffusion" model, we found a corresponding variance of the distribution in the limited mobility model such that the resulting morphologies obtained from both models are nearly indistinguishable from each other. In particular, the cluster size distributions in the submonolayer growth regime match very well. Turning towards multilayer growth, we compared layer coverages for different growth conditions and found excellent agreement between both models. Moreover, we analyzed in detail the global interface width and found perfect agreement between both models in the transient regime where the roughness increases. Furthermore, also the crossover coverage where saturation of the roughness is reached matches perfectly. Additionally, we showed that also the values of the saturation roughness in both models match perfectly for all considered system sizes and values of the growth parameter. A scaling analysis revealed that our model belongs to the Villain-Lai-Das Sarma universality class. We also found good agreement of the height-height correlations in both models. First results on two-dimensional substrates reveal a good agreement between "full diffusion" kinetic Monte-Carlo simulations and our model in the submonolayer and the multilayer growth regime.

There are various possible extensions of our limited mobility model. For example, one could modify the model such that it also reproduces surface growth at high temperatures where detachment of particles is present. One way to realize this is to use the transition rules of the Wolf-Villain model [247] with a variable, distributed diffusion length. For growth on two-dimensional substrates, it would be interesting to study the effect of different variants for the attachment rules on the cluster shapes and the surface roughness. In order to account for growth instabilities, one could include an Ehrlich-Schwoebel barrier for interlayer diffusion processes. Kinetic Monte-Carlo simulations are usually slowed down in presence of such a barrier because particles that freely diffuse on top of clusters are reflected at the cluster edge. A physically reasonable treatment of an interlayer diffusion

barrier in our model would lead to a further computational speedup compared to "full diffusion" growth simulations.

Third, we investigated the applicability of machine learning techniques in the field of nonequilibrium surface growth. The goal of our study was to unravel the microscopic energetic details that govern the morphological evolution of thin films grown by vapor deposition techniques. Our machine learning-based approach is quintessentially different from well-established procedures which normally require information from several iteratively repeated laboratory experiment series at different growth conditions, e.g. different temperatures and adatom deposition rates. In order to circumvent such a laborious procedure, we have used a VGG16-type convolutional neural network with the aim to determine the energy barriers of the underlying diffusion and binding events from images of corresponding surface configurations. To this end, we have trained the neural network via supervised learning with snapshots of surface configurations obtained from kinetic Monte-Carlo simulations in the submonolayer growth regime. In particular, the training process involved around 80000 images from simulation runs with more than 600 different combinations of the binding and diffusion energy barriers. We used clean and noisy images for the training process. The latter were manipulated by adding salt and pepper noise and applying a Gaussian smoothing filter to mimic a lower than atomic resolution. This has been done to make the snapshots more comparable to images of surface configurations obtained from atomic force microscopy or scanning tunneling microscopy. It turned out that the prediction performance of the convolutional neural network is very good across the whole space of diffusion and binding energies for both, clean and noisy data.

The main goal of future investigations in this direction is the determination of the diffusion and binding energy from experimental data. In this regard, we ask the question whether a on numerical data trained convolutional neural network can determine the underlying energy barriers from atomic force microscopy or scanning tunneling microscopy images of surface configurations. This could be tested by using surface snapshots of microscopically well understood systems for which the energy barriers have been precisely determined in various elaborate experimental studies. Examples include the homoepitaxial growth of platinum on platinum(111) [188] and the growth of the fullerence C_{60} on C_{60} [171, 365].

In the last part of this thesis we have investigated thermodynamic properties of a simple model for surface growth including a constant deposition rate and Arrhenius-type rates for diffusion and desorption of particles. We have focused on the entropy production rate as function of the deposition rate and found that it is always positive for conditions where the crystal either grows or shrinks. Only when deposition and evaporation events balance out, i.e., when the height of the crystal remains constant, the entropy production rate vanishes even though there is a constant flux of incoming particles. Moreover, we found that in presence of a hard wall, i.e., a inert substrate at zero height, the system in the

bound phase is always in a state of thermal equilibrium. As the deposition rate is increased above a critical value, the crystal begins to grow. It turned out that the entropy production rate does not exhibit noticeable behavior at the transition from the bound to the growing phase.

We have also studied the critical behavior of a nonequilibrium q-state vector Potts model and here again paid special attention to the entropy production rate. The model is driven out of thermal equilibrium because the spins are coupled to two heat baths which are kept at different temperatures T_1 and T_2. Using this generic setup, we investigated the type of phase transition and the critical exponents. For $q = 4$, i.e., discrete spin symmetry, the model exhibits a single second-order phase transition. We found that the critical temperature decreases as the temperature difference between the two heat baths increases. Moreover, the behavior of the specific heat resembles that of the equilibrium model, i.e., it shows power-law divergence. The corresponding critical exponent is independent of the temperature difference. The derivative of the entropy production rate with respect to temperature behaves, to some extent, similar. It also shows power-law divergence, but the value of the scaling exponent depends on the temperature difference of the heat baths and is thus non-universal. Concerning the model with continuous spin symmetry, i.e., for $q \to \infty$, the specific heat as well as the derivative of the entropy production rate do not show noticeable behavior around the infinite-order transition. Instead, both quantities have a finite peak at a temperature above the critical temperature. As the temperature difference between the heat baths increases, the maximum value of the derivative of the entropy production rate becomes more pronounced. In total, our results provide evidence that the derivative of the entropy production behaves like a critical quantity, but, as we report here, is non-universal.

Finally, we aim at pointing out perspectives for future work in this direction. For the sake of generality one should study and compare the behavior of the specific heat with the entropy production rate in other dimensions and for different lattice topologies. Further, a more detailed analysis of infinite-order phase transitions under nonequilibrium conditions represents an interesting objective for future research. It would moreover be worth to think about the fundamental connection between entropy production and specific heat, which seem to behave analogously around criticality. Furthermore, another interesting perspective is the reinterpretation of the here considered Potts model as a system non-reciprocal coupling between interacting isothermal spins. To be more specific, a vector-Potts model where neighboring spins are coupled with two distinct coupling constants $J_1 = J/T_1$ and $J_2 = J/T_2$ and uniform temperature follows the exact same equations of motions as our model. This provides a connection to spin models on directed graphs [385, 386], and to the topic of non-reciprocal interactions, which is currently a focus in nonequilibrium statistical mechanics [389–391].

Bibliography

[1] Hansen, J.-P. & McDonald, I. R. *Theory of simple liquids* (Elsevier, 1990).

[2] Chaikin, P. M., Lubensky, T. C. & Witten, T. A. *Principles of condensed matter physics*, vol. 10 (Cambridge university press Cambridge, 1995).

[3] Bloch, I., Dalibard, J. & Zwerger, W. Many-body physics with ultracold gases. *Rev. Mod. Phys.* **80**, 885–964 (2008). URL https://link.aps.org/doi/10.1103/RevModPhys.80.885.

[4] Blundell, S. Magnetism in condensed matter (2003).

[5] *Ferromagnetism*, chap. 6, 259–331 (John Wiley & Sons, Ltd, 2001). URL https://onlinelibrary.wiley.com/doi/abs/10.1002/9780470546581.ch6.

[6] Hohenberg, P. C. & Halperin, B. I. Theory of dynamic critical phenomena. *Reviews of Modern Physics* **49**, 435 (1977).

[7] Ho, K.-y. Phase transition and critical phenomena (2007).

[8] Weeks, J. D. & Gilmer, G. H. *Dynamics of Crystal Growth*, 157–228 (John Wiley & Sons, Ltd, 1979). URL https://onlinelibrary.wiley.com/doi/abs/10.1002/9780470142592.ch4.

[9] Barabási, A.-L. & Stanley, H. E. *Fractal Concepts in Surface Growth* (Cambridge University Press, 1995).

[10] Zhang, Z. & Lagally, M. G. Atomistic Processes in the Early Stages of Thin-Film Growth. *Science* **276**, 377 LP – 383 (1997). URL http://science.sciencemag.org/content/276/5311/377.abstract.

[11] Pimpinelli, A. & Villain, J. *Physics of Crystal Growth* (1999).

[12] Venables, J. A. *Introduction to Surface and Thin Film Processes* (Cambridge University Press, 2000). URL https://www.cambridge.org/core/product/identifier/9780511755651/type/book.

[13] Michely, Thomas, Krug, J. Islands, Mounds and Atoms - Patterns and Processes in Crystal Growth Far From Equilibrium. *Thin Solid Films* (2002).

[14] Kagan, C. R. & Andry, P. *Thin-film transistors* (CRC Press, 2003).

[15] Chopra, K. L., Paulson, P. D. & Dutta, V. Thin-film solar cells: an overview. *Progress in Photovoltaics: Research and applications* **12**, 69–92 (2004).

[16] Barnham, K. & Vvedensky, D. *Low-dimensional semiconductor structures: Fundamentals and device applications* (Cambridge university press, 2008).

[17] Street, R. A. Thin-film transistors. *Advanced Materials* **21**, 2007–2022 (2009).

[18] Fortunato, E., Barquinha, P. & Martins, R. Oxide semiconductor thin-film transistors: a review of recent advances. *Advanced materials* **24**, 2945–2986 (2012).

[19] Frey, H. & Khan, H. R. *Handbook of thin film technology* (Springer, 2015).

[20] Pierson, H. O. *Handbook of chemical vapor deposition: principles, technology and applications* (William Andrew, 1999).

[21] Mahan, J. E. Physical vapor deposition of thin films (2000).

[22] Park, J.-H. & Sudarshan, T. S. *Chemical vapor deposition*, vol. 2 (ASM international, 2001).

[23] Helmersson, U., Lattemann, M., Bohlmark, J., Ehiasarian, A. P. & Gudmundsson, J. T. Ionized physical vapor deposition (IPVD): A review of technology and applications. *Thin solid films* **513**, 1–24 (2006).

[24] Mattox, D. M. *Handbook of physical vapor deposition (PVD) processing* (William Andrew, 2010).

[25] Chrisey, D. B., Hubler, G. K. & Others. Pulsed laser deposition of thin films (1994).

[26] Lowndes, D. H., Geohegan, D. B., Puretzky, A. A., Norton, D. P. & Rouleau, C. M. Synthesis of Novel Thin-Film Materials by Pulsed Laser Deposition. *Science* **273**, 898 LP – 903 (1996). URL `http://science.sciencemag.org/content/273/5277/898.abstract`.

[27] Eason, R. *Pulsed laser deposition of thin films: applications-led growth of functional materials* (John Wiley & Sons, 2007).

[28] Cho, A. Y. & Arthur, J. R. Molecular beam epitaxy. *Progress in solid state chemistry* **10**, 157–191 (1975).

[29] Herman, M. A. & Sitter, H. *Molecular beam epitaxy: fundamentals and current status*, vol. 7 (Springer Science & Business Media, 2012).

[30] Katagiri, H. *et al.* Development of thin film solar cell based on Cu2ZnSnS4 thin films. *Solar Energy Materials and Solar Cells* **65**, 141–148 (2001).

[31] Shah, A. V. *et al.* Thin-film silicon solar cell technology. *Progress in photovoltaics: Research and applications* **12**, 113–142 (2004).

[32] Lee, T. D. & Ebong, A. U. A review of thin film solar cell technologies and challenges. *Renewable and Sustainable Energy Reviews* **70**, 1286–1297 (2017).

[33] Park, S.-H. K. *et al.* 42.3: Transparent ZnO thin film transistor for the application of high aperture ratio bottom emission AM-OLED display. In *SID Symposium Digest of Technical Papers*, vol. 39, 629–632 (Wiley Online Library, 2008).

[34] Haitz, R. & Tsao, J. Y. Solid-state lighting:'The case'10 years after and future prospects. *physica status solidi (a)* **208**, 17–29 (2011).

[35] Dinelli, F. *et al.* Spatially correlated charge transport in organic thin film transistors. *Physical Review Letters* **92**, 116802 (2004).

[36] Iino, H., Usui, T. & Hanna, J.-i. Liquid crystals for organic thin-film transistors. *Nature communications* **6**, 1–8 (2015).

[37] Senanayak, S. P. *et al.* Understanding charge transport in lead iodide perovskite thin-film field-effect transistors. *Science advances* **3**, e1601935 (2017).

[38] Pfeiffer, L. *et al.* Cleaved edge overgrowth for quantum wire fabrication. *Journal of Crystal Growth* **127**, 849–857 (1993). URL `http://www.sciencedirect.com/science/article/pii/002202489390746J`.

[39] Danek, M., Jensen, K. F., Murray, C. B. & Bawendi, M. G. Synthesis of Luminescent Thin-Film CdSe/ZnSe Quantum Dot Composites Using CdSe Quantum Dots Passivated with an Overlayer of ZnSe. *Chemistry of Materials* **8**, 173–180 (1996). URL `https://doi.org/10.1021/cm9503137`.

[40] Choi, J.-H. *et al.* Bandlike Transport in Strongly Coupled and Doped Quantum Dot Solids: A Route to High-Performance Thin-Film Electronics. *Nano Letters* **12**, 2631–2638 (2012). URL `https://doi.org/10.1021/nl301104z`.

[41] Venables, J. A. & Spiller, G. D. Nucleation and Growth of Thin Films. *NATO ASI Series, Series B: Physics* **86**, 341–404 (1983).

[42] Venables, J. A., Spiller, G. D. T. & Hanbucken, M. Nucleation and growth of thin films. *Reports on Progress in Physics* **47**, 399–459 (1984). URL `https://doi.org/10.1088/0034-4885/47/4/002`.

[43] Essam, J. W. Percolation theory. *Reports on Progress in Physics* **43**, 833–912 (1980). URL `https://doi.org/10.1088/0034-4885/43/7/001`.

[44] Pastor-Satorras, R. & Vespignani, A. Epidemic Spreading in Scale-Free Networks. *Phys. Rev. Lett.* **86**, 3200–3203 (2001). URL `https://link.aps.org/doi/10.1103/PhysRevLett.86.3200`.

[45] Albert, R. & Barabási, A.-L. Statistical mechanics of complex networks. *Rev. Mod. Phys.* **74**, 47–97 (2002). URL `https://link.aps.org/doi/10.1103/RevModPhys.74.47`.

[46] Stauffer, D. & Aharony, A. *Introduction to percolation theory* (CRC press, 2018).

[47] Chowell, G., Viboud, C., Hyman, J. M. & Simonsen, L. The Western Africa ebola virus disease epidemic exhibits both global exponential and local polynomial growth rates. *PLoS currents* **7**, ecurrents.outbreaks.8b55f4bad99ac5c5db3663e9168032 (2015). URL https://pubmed.ncbi.nlm.nih.gov/25685633https://www.ncbi.nlm.nih.gov/pmc/articles/PMC4322058/.

[48] Rizzo, A., Pedalino, B. & Porfiri, M. A network model for Ebola spreading. *Journal of Theoretical Biology* **394**, 212–222 (2016). URL http://www.sciencedirect.com/science/article/pii/S0022519316000485.

[49] Dehning, J. *et al.* Inferring change points in the spread of COVID-19 reveals the effectiveness of interventions. *Science* **369**, eabb9789 (2020). URL http://science.sciencemag.org/content/369/6500/eabb9789.abstract.

[50] Seifert, U. Stochastic thermodynamics: principles and perspectives. *The European Physical Journal B* **64**, 423–431 (2008). URL https://doi.org/10.1140/epjb/e2008-00001-9.

[51] Sekimoto, K. *Stochastic energetics*, vol. 799 (Springer, 2010).

[52] Seifert, U. Stochastic thermodynamics, fluctuation theorems and molecular machines. *Reports on Progress in Physics* **75**, 126001 (2012). URL http://dx.doi.org/10.1088/0034-4885/75/12/126001.

[53] Mermin, N. D. & Wagner, H. Absence of Ferromagnetism or Antiferromagnetism in One- or Two-Dimensional Isotropic Heisenberg Models. *Phys. Rev. Lett.* **17**, 1133–1136 (1966). URL https://link.aps.org/doi/10.1103/PhysRevLett.17.1133.

[54] Hohenberg, P. C. Existence of Long-Range Order in One and Two Dimensions. *Phys. Rev.* **158**, 383–386 (1967). URL https://link.aps.org/doi/10.1103/PhysRev.158.383.

[55] Mermin, N. D. Crystalline Order in Two Dimensions. *Phys. Rev.* **176**, 250–254 (1968). URL https://link.aps.org/doi/10.1103/PhysRev.176.250.

[56] Berezinsky, V. L. Destruction of long range order in one-dimensional and two-dimensional systems having a continuous symmetry group. I. Classical systems. *Sov. Phys. JETP* **32**, 493–500 (1971).

[57] Kosterlitz, J. M. The critical properties of the two-dimensional xy model. *Journal of Physics C: Solid State Physics* **7**, 1046–1060 (1974). URL https://iopscience.iop.org/article/10.1088/0022-3719/7/6/005.

[58] Shiba, H., Yamada, Y., Kawasaki, T. & Kim, K. Unveiling Dimensionality Dependence of Glassy Dynamics: 2D Infinite Fluctuation Eclipses Inherent Structural Relaxation. *Phys. Rev. Lett.* **117**, 245701 (2016). URL https://link.aps.org/doi/10.1103/PhysRevLett.117.245701.

[59] Illing, B. *et al.* Mermin–Wagner fluctuations in 2D amorphous solids. *Proceedings of the National Academy of Sciences* **114**, 1856–1861 (2017). URL https://www.pnas.org/content/114/8/1856.

[60] Vivek, S., Kelleher, C. P., Chaikin, P. M. & Weeks, E. R. Long-wavelength fluctuations and the glass transition in two dimensions and three dimensions. *Proceedings of the National Academy of Sciences* **114**, 1850 LP – 1855 (2017). URL http://www.pnas.org/content/114/8/1850.abstract.

[61] Yeomans, J. M. *Statistical mechanics of phase transitions* (Clarendon Press, 1992).

[62] Brokate, M. & Sprekels, J. *Hysteresis and phase transitions*, vol. 121 (Springer Science & Business Media, 1996).

[63] Domb, C. *Phase transitions and critical phenomena* (Elsevier, 2000).

[64] Sinai, Y. G. *Theory of phase transitions: rigorous results*, vol. 108 (Elsevier, 2014).

[65] Kern_1995.Pdf.

[66] Li, Y. & Tanaka, T. Study of the universality class of the gel network system. *The Journal of chemical physics* **90**, 5161–5166 (1989).

[67] Kallosh, R. & Linde, A. Universality class in conformal inflation. *Journal of Cosmology and Astroparticle Physics* **2013**, 2 (2013).

[68] Sarma, S. D. & Tamborenea, P. A new universality class for kinetic growth: One-dimensional molecular-beam epitaxy. *Physical review letters* **66**, 325 (1991).

[69] Rossi, M., Pastor-Satorras, R. & Vespignani, A. Universality class of absorbing phase transitions with a conserved field. *Physical review letters* **85**, 1803 (2000).

[70] Corwin, I. The Kardar–Parisi–Zhang equation and universality class. *Random matrices: Theory and applications* **1**, 1130001 (2012).

[71] Campostrini, M., Hasenbusch, M., Pelissetto, A., Rossi, P. & Vicari, E. Critical behavior of the three-dimensional XY universality class. *Physical Review B* **63**, 214503 (2001).

[72] den Broeck, C., Parrondo, J. M. R. & Toral, R. Noise-induced nonequilibrium phase transition. *Physical review letters* **73**, 3395 (1994).

[73] Ódor, G. Universality classes in nonequilibrium lattice systems. *Reviews of Modern Physics* **76**, 663–724 (2004). 0205644.

[74] Marro, J. & Dickman, R. *Nonequilibrium phase transitions in lattice models* (Cambridge University Press, 2005).

[75] Henkel, M., Hinrichsen, H., Lübeck, S. & Pleimling, M. *Non-equilibrium phase transitions*, vol. 1 (Springer, 2008).

[76] Schöll, E. *Nonequilibrium phase transitions in semiconductors: self-organization induced by generation and recombination processes*, vol. 35 (Springer Science & Business Media, 2012).

[77] Partridge, B. & Lee, C. F. Critical Motility-Induced Phase Separation Belongs to the Ising Universality Class. *Phys. Rev. Lett.* **123**, 68002 (2019). URL https://link.aps.org/doi/10.1103/PhysRevLett.123.068002.

[78] Mityashin, A. *et al.* Unraveling the mechanism of molecular doping in organic semiconductors. *Advanced Materials* **24**, 1535–1539 (2012).

[79] Walukiewicz, W. Intrinsic limitations to the doping of wide-gap semiconductors. *Physica B: Condensed Matter* **302**, 123–134 (2001).

[80] Janotti, A. & de Walle, C. G. Native point defects in ZnO. *Physical Review B* **76**, 165202 (2007).

[81] Lany, S. & Zunger, A. Assessment of correction methods for the band-gap problem and for finite-size effects in supercell defect calculations: Case studies for ZnO and GaAs. *Physical Review B* **78**, 235104 (2008).

[82] Marder, S. R., Beratan, D. N. & Cheng, L.-T. Approaches for optimizing the first electronic hyperpolarizability of conjugated organic molecules. *Science* **252**, 103–106 (1991).

[83] Garnier, F. *et al.* Molecular engineering of organic semiconductors: design of self-assembly properties in conjugated thiophene oligomers. *Journal of the American Chemical Society* **115**, 8716–8721 (1993).

[84] Koch, N. Energy levels at interfaces between metals and conjugated organic molecules. *Journal of Physics: Condensed Matter* **20**, 184008 (2008).

[85] Hlawacek, G. & Teichert, C. Nucleation and growth of thin films of rod-like conjugated molecules. *Journal of physics: Condensed matter* **25**, 143202 (2013).

[86] Podzorov, V. *et al.* Intrinsic charge transport on the surface of organic semiconductors. *Physical review letters* **93**, 86602 (2004).

[87] Yuan, Y. *et al.* Ultra-high mobility transparent organic thin film transistors grown by an off-centre spin-coating method. *Nature communications* **5**, 1–9 (2014).

[88] Rolin, C. *et al.* Charge carrier mobility in thin films of organic semiconductors by the gated van der Pauw method. *Nature Communications* **8**, 14975 (2017). URL https://doi.org/10.1038/ncomms14975.

[89] Forgerini, F. L. & Figueiredo, W. Random deposition of particles of different sizes. *Phys. Rev. E* **79**, 41602 (2009). URL https://link.aps.org/doi/10.1103/PhysRevE.79.041602.

[90] Kleppmann, N. & Klapp, S. H. L. A scale-bridging modeling approach for anisotropic organic molecules at patterned semiconductor surfaces. *The Journal of Chemical Physics* **142**, 64701 (2015). URL https://doi.org/10.1063/1.4907037.

[91] Kleppmann, N. & Klapp, S. H. Nonequilibrium surface growth in a hybrid inorganic-organic system. *Physical Review B* **94**, 1–15 (2016). 1511.00587.

[92] Oettel, M. *et al.* Monolayers of hard rods on planar substrates. I. Equilibrium. *The Journal of Chemical Physics* **145**, 74902 (2016). URL https://doi.org/10.1063/1.4960618.

[93] Klopotek, M. *et al.* Monolayers of hard rods on planar substrates. II. Growth. *The Journal of Chemical Physics* **146**, 84903 (2017). URL https://doi.org/10.1063/1.4976308.

[94] Dixit, M., Schilling, T. & Oettel, M. Growth of films with anisotropic particles: Simulations and rate equations. *The Journal of Chemical Physics* **149**, 64903 (2018). URL https://doi.org/10.1063/1.5031217.

[95] Martynec, T. & Klapp, S. H. L. Impact of anisotropic interactions on nonequilibrium cluster growth at surfaces. *Phys. Rev. E* **98**, 42801 (2018). URL https://link.aps.org/doi/10.1103/PhysRevE.98.042801.

[96] Martynec, T. & Klapp, S. H. Modeling of nonequilibrium surface growth by a limited-mobility model with distributed diffusion length. *Physical Review E* **100**, 33307 (2019). URL https://doi.org/10.1103/PhysRevE.100.033307. 1903.08439.

[97] Das Sarma, S. & Tamborenea, P. A new universality class for kinetic growth: One-dimensional molecular-beam epitaxy. *Phys. Rev. Lett.* **66**, 325–328 (1991). URL https://link.aps.org/doi/10.1103/PhysRevLett.66.325.

[98] Das Sarma, S., Lai, Z. W. & Tamborenea, P. I. Crossover effects in models of kinetic growth with surface diffusion. *Surface Science* **268** (1992).

[99] Lookman, T., Eidenbenz, S., Alexander, F. & Barnes, C. *Materials Discovery and Design. By Means of Data Science and Optimal Learning*, vol. 280 (2018). URL http://www.springer.com/series/856{%}0Ahttp://link.springer.com/10.1007/978-3-319-99465-9.

[100] Ryan, K., Lengyel, J. & Shatruk, M. Crystal structure prediction via deep learning. *Journal of the American Chemical Society* **140**, 10158–10168 (2018).

[101] Graser, J., Kauwe, S. K. & Sparks, T. D. Machine Learning and Energy Minimization Approaches for Crystal Structure Predictions: A Review and New Horizons. *Chemistry of Materials* **30**, 3601–3612 (2018).

[102] Seko, A., Hayashi, H., Nakayama, K., Takahashi, A. & Tanaka, I. Representation of compounds for machine-learning prediction of physical properties. *Physical Review B* **95**, 1–11 (2017). 1611.08645.

[103] Xie, T. & Grossman, J. C. Crystal Graph Convolutional Neural Networks for an Accurate and Interpretable Prediction of Material Properties. *Physical Review Letters* **120**, 145301 (2018). URL https://doi.org/10.1103/PhysRevLett.120.145301. 1710.10324.

[104] Zheng, X., Zheng, P. & Zhang, R. Z. Machine learning material properties from the periodic table using convolutional neural networks. *Chemical Science* **9**, 8426–8432 (2018).

[105] Faber, F. A., Lindmaa, A., Von Lilienfeld, O. A. & Armiento, R. Machine Learning Energies of 2 Million Elpasolite (ABC2D6) Crystals. *Physical Review Letters* **117**, 2–7 (2016).

[106] Isayev, O. *et al.* Universal fragment descriptors for predicting properties of inorganic crystals. *Nature Communications* **8**, 1–12 (2017). URL http://dx.doi.org/10.1038/ncomms15679.

[107] Martynec, T., Klapp, S. H. & Kowarik, S. Prediction of energetics in nucleation and non-equilibrium growth using machine learning (2020).

[108] Crochik, L. & Tomé, T. Entropy production in the majority-vote model. *Phys. Rev. E* **72**, 57103 (2005). URL https://link.aps.org/doi/10.1103/PhysRevE.72.057103.

[109] Tomé, T. & de Oliveira, M. J. Entropy Production in Nonequilibrium Systems at Stationary States. *Phys. Rev. Lett.* **108**, 20601 (2012). URL https://link.aps.org/doi/10.1103/PhysRevLett.108.020601.

[110] Nardini, C. *et al.* Entropy Production in Field Theories without Time-Reversal Symmetry: Quantifying the Non-Equilibrium Character of Active Matter. *Phys. Rev. X* **7**, 21007 (2017). URL https://link.aps.org/doi/10.1103/PhysRevX.7.021007.

[111] Noa, C. E. F., Harunari, P. E., de Oliveira, M. J. & Fiore, C. E. Entropy production as a tool for characterizing nonequilibrium phase transitions. *Phys. Rev. E* **100**, 12104 (2019). URL https://link.aps.org/doi/10.1103/PhysRevE.100.012104.

[112] Martynec, T., Klapp, S. H. L. & Loos, S. A. M. Entropy production at criticality in a nonequilibrium Potts model. *New Journal of Physics* **22**, 093069 (2020). URL https://iopscience.iop.org/article/10.1088/1367-2630/abb5f0.

[113] Kemeny, J. G. & Snell, J. L. *Markov chains* (Springer-Verlag, New York, 1976).

[114] Rabiner, L. & Juang, B. An introduction to hidden Markov models. *ieee assp magazine* **3**, 4–16 (1986).

[115] Geyer, C. J. Practical markov chain monte carlo. *Statistical science* 473–483 (1992).

[116] Norris, J. R. & Norris, J. R. *Markov chains*. 2 (Cambridge university press, 1998).

[117] Brooks, S., Gelman, A., Jones, G. & Meng, X.-L. *Handbook of markov chain monte carlo* (CRC press, 2011).

[118] Bäuerle, N. & Rieder, U. *Markov decision processes with applications to finance* (Springer Science & Business Media, 2011).

[119] Prinz, J.-H. *et al.* Markov models of molecular kinetics: Generation and validation. *The Journal of chemical physics* **134**, 174105 (2011).

[120] Gu, K., Chen, J. & Kharitonov, V. L. *Stability of time-delay systems* (Springer Science & Business Media, 2003).

[121] Richard, J.-P. Time-delay systems: an overview of some recent advances and open problems. *automatica* **39**, 1667–1694 (2003).

[122] Loos, S. A. M. & Klapp, S. H. L. Force-linearization closure for non-Markovian Langevin systems with time delay. *Phys. Rev. E* **96**, 12106 (2017). URL `https://link.aps.org/doi/10.1103/PhysRevE.96.012106`.

[123] Loos, S. A. M. & Klapp, S. H. L. Heat flow due to time-delayed feedback. *Scientific Reports* **9**, 2491 (2019). URL `https://doi.org/10.1038/s41598-019-39320-0`.

[124] Dugard, L. & Verriest, E. I. *Stability and control of time-delay systems*, vol. 228 (Springer, 1998).

[125] Shi, P., Boukas, E.-K. & Agarwal, R. K. Control of Markovian jump discrete-time systems with norm bounded uncertainty and unknown delay. *IEEE Transactions on Automatic Control* **44**, 2139–2144 (1999).

[126] Xu, S., Lam, J. & Yang, C. Quadratic stability and stabilization of uncertain linear discrete-time systems with state delay. *Systems & control letters* **43**, 77–84 (2001).

[127] Zhang, Y., Sun, J. & Feng, G. Impulsive control of discrete systems with time delay. *IEEE Transactions on Automatic Control* **54**, 830–834 (2009).

[128] Andrieux, D. *et al.* Entropy production and time asymmetry in nonequilibrium fluctuations. *Physical review letters* **98**, 150601 (2007).

[129] Parrondo, J. M. R., den Broeck, C. & Kawai, R. Entropy production and the arrow of time. *New Journal of Physics* **11**, 73008 (2009).

[130] Zwanzig, R. *Nonequilibrium statistical mechanics* (Oxford University Press, 2001).

[131] Kubo, R., Toda, M. & Hashitsume, N. *Statistical physics II: nonequilibrium statistical mechanics*, vol. 31 (Springer Science & Business Media, 2012).

[132] Prigogine, I. *Non-equilibrium statistical mechanics* (Courier Dover Publications, 2017).

[133] Andrieu, C., Doucet, A. & Holenstein, R. Particle markov chain monte carlo methods. *Journal of the Royal Statistical Society: Series B (Statistical Methodology)* **72**, 269–342 (2010).

[134] Fisher, D. S. Scaling and critical slowing down in random-field Ising systems. *Physical review letters* **56**, 416 (1986).

[135] Berg, B. A. & Neuhaus, T. Multicanonical ensemble: A new approach to simulate first-order phase transitions. *Physical Review Letters* **68**, 9 (1992).

[136] Djurberg, C. *et al.* Dynamics of an interacting particle system: evidence of critical slowing down. *Physical review letters* **79**, 5154 (1997).

[137] Peierls, R. On Ising's model of ferromagnetism. In *Mathematical Proceedings of the Cambridge Philosophical Society*, vol. 32, 477–481 (Cambridge University Press, 1936).

[138] Aharoni, A. & Others. *Introduction to the Theory of Ferromagnetism*, vol. 109 (Clarendon Press, 2000).

[139] Curie, P. *Propriétés magnétiques des corps a diverses températures*. 4 (Gauthier-Villars et fils, 1895).

[140] Van Leeuwen, H.-J. Problemes de la théorie électronique du magnétisme (1921).

[141] Van Vleck, J. H. *The theory of electric and magnetic susceptibilities* (Clarendon Press, 1932).

[142] Pauli, W. Über den Zusammenhang des Abschlusses der Elektronengruppen im Atom mit der Komplexstruktur der Spektren. *Zeitschrift für Physik* **31**, 765–783 (1925). URL `https://doi.org/10.1007/BF02980631`.

[143] Heisenberg, W. Mehrkörperproblem und Resonanz in der Quantenmechanik. *Zeitschrift für Physik* **38**, 411–426 (1926). URL `https://doi.org/10.1007/BF01397160`.

[144] Dirac, P. A. M. On the theory of quantum mechanics. *Proceedings of the Royal Society of London. Series A, Containing Papers of a Mathematical and Physical Character* **112**, 661–677 (1926).

[145] Galam, S. What is sociophysics about? In *Sociophysics*, 3–19 (Springer, 2012).

[146] de Oliveira, M. J. Isotropic majority-vote model on a square lattice. *Journal of Statistical Physics* **66**, 273–281 (1992).

[147] Pereira, L. F. C. & Moreira, F. G. B. Majority-vote model on random graphs. *Physical Review E* **71**, 16123 (2005).

[148] Cates, M. E. & Tailleur, J. When are active Brownian particles and run-and-tumble particles equivalent? Consequences for motility-induced phase separation. *EPL (Europhysics Letters)* **101**, 20010 (2013).

[149] Cates, M. E. & Tailleur, J. Motility-induced phase separation. *Annu. Rev. Condens. Matter Phys.* **6**, 219–244 (2015).

[150] Madras, N. & Slade, G. *The self-avoiding walk* (Springer Science & Business Media, 2013).

[151] Heisenberg, W. Zur Theorie des Ferromagnetismus. *Zeitschrift für Physik* **49**, 619–636 (1928). URL `https://doi.org/10.1007/BF01328601`.

[152] Jayaprakash, C., Riedel, E. K. & Wortis, M. Critical and thermodynamic properties of the randomly dilute Ising model. *Physical Review B* **18**, 2244 (1978).

[153] Lima, F. W. S. & Stauffer, D. Ising model simulation in directed lattices and networks. *Physica A: Statistical Mechanics and its Applications* **359**, 423–429 (2006). URL `http://www.sciencedirect.com/science/article/pii/S0378437105005728`.

[154] Lenz, W. Beitrag zum Verständnis der magnetischen Erscheinungen in festen Körpern. *Z. Phys.* **21**, 613–615 (1920).

[155] BRUSH, S. G. History of the Lenz-Ising Model. *Rev. Mod. Phys.* **39**, 883–893 (1967). URL `https://link.aps.org/doi/10.1103/RevModPhys.39.883`.

[156] Ising, E. Beitrag zur Theorie des Ferromagnetismus. *Zeitschrift für Physik* **31**, 253–258 (1925). URL `https://doi.org/10.1007/BF02980577`.

[157] Baxter, R. J. *Exactly solved models in statistical mechanics* (Elsevier, 2016).

[158] Newell, G. F. & Montroll, E. W. On the theory of the Ising model of ferromagnetism. *Reviews of Modern Physics* **25**, 353 (1953).

[159] Kramers, H. A. & Wannier, G. H. Statistics of the two-dimensional ferromagnet. Part I. *Physical Review* **60**, 252 (1941).

[160] Onsager, L. Crystal statistics. I. A two-dimensional model with an order-disorder transition. *Physical Review* **65**, 117 (1944).

[161] Baxter, R. J. Potts model at the critical temperature. *Journal of Physics C: Solid State Physics* **6**, L445 (1973).

[162] Wu, F.-Y. The potts model. *Reviews of modern physics* **54**, 235 (1982).

[163] Van Himbergen, J. E. & Chakravarty, S. Helicity modulus and specific heat of classical XY model in two dimensions. *Phys. Rev. B* **23**, 359–361 (1981). URL `https://link.aps.org/doi/10.1103/PhysRevB.23.359`.

[164] Hasenbusch, M. The two-dimensional XY model at the transition temperature: a high-precision Monte Carlo study. *Journal of Physics A: Mathematical and General* **38**, 5869 (2005).

[165] Wolff, U. Collective Monte Carlo Updating for Spin Systems. *Phys. Rev. Lett.* **62**, 361–364 (1989). URL https://link.aps.org/doi/10.1103/PhysRevLett.62.361.

[166] Swendsen, R. H. & Wang, J.-S. Nonuniversal critical dynamics in Monte Carlo simulations. *Phys. Rev. Lett.* **58**, 86–88 (1987). URL https://link.aps.org/doi/10.1103/PhysRevLett.58.86.

[167] Metropolis, N., Rosenbluth, A. W., Rosenbluth, M. N., Teller, A. H. & Teller, E. Equation of state calculations by fast computing machines. *The journal of chemical physics* **21**, 1087–1092 (1953).

[168] Hastings, W. K. Monte Carlo sampling methods using Markov chains and their applications (1970).

[169] Glauber, R. J. Time-dependent statistics of the Ising model. *Journal of mathematical physics* **4**, 294–307 (1963).

[170] Andersen, M., Panosetti, C. & Reuter, K. A practical guide to surface kinetic Monte Carlo simulations. *Frontiers in chemistry* **7**, 202 (2019).

[171] Bommel, S. *et al.* Unravelling the multilayer growth of the fullerene C 60 in real time. *Nature Communications* **5** (2014).

[172] Pollak, E. Theory of activated rate processes: A new derivation of Kramers' expression. *The Journal of chemical physics* **85**, 865–867 (1986).

[173] Hänggi, P., Talkner, P. & Borkovec, M. Reaction-rate theory: fifty years after Kramers. *Reviews of modern physics* **62**, 251 (1990).

[174] Eyring, H. & Polanyi, M. On Simple Gas Reactions. *Zeitschrift für Physikalische Chemie* **227**, 1221–1246. URL https://www.degruyter.com/view/journals/zpch/227/11/article-p1221.xml.

[175] Evans, M. G. & Polanyi, M. Some applications of the transition state method to the calculation of reaction velocities, especially in solution. *Transactions of the Faraday Society* **31**, 875–894 (1935).

[176] Hlawacek, G. *et al.* Characterization of step-edge barriers in organic thin-film growth. *Science* **321**, 108–111 (2008).

[177] Goose, J. E., First, E. L. & Clancy, P. Nature of step-edge barriers for small organic molecules. *Physical Review B* **81**, 205310 (2010).

[178] Della Sala, F., Blumstengel, S. & Henneberger, F. Electrostatic-field-driven alignment of organic oligomers on ZnO surfaces. *Physical review letters* **107**, 146401 (2011).

[179] Palczynski, K. & Dzubiella, J. Anisotropic Electrostatic Friction of para-Sexiphenyl on the ZnO $(10\bar{1}0)$ Surface. *The Journal of Physical Chemistry C* **118**, 26368–26376 (2014). URL https://doi.org/10.1021/jp507776h.

[180] Miletic, M. *et al.* Impact of Polarity on Anisotropic Diffusion of Conjugated Organic Molecules on the $(10\bar{1}0)$ Zinc Oxide Surface. *The Journal of Physical Chemistry C* **123**, 6549–6559 (2019). URL https://doi.org/10.1021/acs.jpcc.8b12112.

[181] Ehrlich, G. & Hudda, F. G. Atomic view of surface self-diffusion: tungsten on tungsten. *The Journal of Chemical Physics* **44**, 1039–1049 (1966).

[182] Schwoebel, R. L. & Shipsey, E. J. Step motion on crystal surfaces. *Journal of Applied Physics* **37**, 3682–3686 (1966).

[183] Gillespie, D. T. A general method for numerically simulating the stochastic time evolution of coupled chemical reactions. *Journal of computational physics* **22**, 403–434 (1976).

[184] Gillespie, D. T. Exact stochastic simulation of coupled chemical reactions. *The journal of physical chemistry* **81**, 2340–2361 (1977).

[185] Bortz, A. B., Kalos, M. H. & Lebowitz, J. L. A new algorithm for Monte Carlo simulation of Ising spin systems. *Journal of Computational Physics* **17**, 10–18 (1975).

[186] Liu, J. S. & Chen, R. Sequential Monte Carlo Methods for Dynamic Systems. *Journal of the American Statistical Association* **93**, 1032–1044 (1998). URL https://doi.org/10.1080/01621459.1998.10473765.

[187] Voter, A. F. Introduction to the kinetic Monte Carlo method. In *Radiation effects in solids*, 1–23 (Springer, 2007).

[188] Hohage, M. *et al.* Atomic processes in low temperature Pt-dendrite growth on Pt(111). *Physical Review Letters* **76**, 2366–2369 (1996).

[189] Michely, T. & Krug, J. *Islands, mounds and atoms*, vol. 42 (Springer Science & Business Media, 2012).

[190] Reinken, H., Heidenreich, S., Bär, M. & Klapp, S. H. L. Anisotropic mesoscale turbulence and pattern formation in microswimmer suspensions induced by orienting external fields. *New Journal of Physics* **21**, 13037 (2019).

[191] Goossens, K. & De Winter, H. Molecular Dynamics Simulations of Membrane Proteins: An Overview. *Journal of Chemical Information and Modeling* **58**, 2193–2202 (2018). URL https://doi.org/10.1021/acs.jcim.8b00639.

[192] Clarke, S. & Vvedensky, D. D. Growth kinetics and step density in reflection high-energy electron diffraction during molecular-beam epitaxy. *Journal of applied physics* **63**, 2272–2283 (1988).

[193] Jarzynski, C. Nonequilibrium equality for free energy differences. *Physical Review Letters* **78**, 2690 (1997).

[194] Seifert, U. Entropy Production along a Stochastic Trajectory and an Integral Fluctuation Theorem. *Phys. Rev. Lett.* **95**, 40602 (2005). URL `https://link.aps.org/doi/10.1103/PhysRevLett.95.040602`.

[195] Esposito, M. Stochastic thermodynamics under coarse graining. *Physical Review E* **85**, 41125 (2012).

[196] Van Den Broeck, C. *Stochastic thermodynamics: A brief introduction*, vol. 184 (2012).

[197] den Broeck, C. & Esposito, M. Ensemble and trajectory thermodynamics: A brief introduction. *Physica A: Statistical Mechanics and its Applications* **418**, 6–16 (2015).

[198] Van Wylen, G. J., Sonntag, R. E. & Borgnakke, C. *Fundamentals of classical thermodynamics* (Wiley New York, 1976).

[199] Maxwell, J. C. & Pesic, P. *Theory of heat* (Courier Corporation, 2001).

[200] Kittel, C. & Kroemer, H. Thermal physics (1998).

[201] Clausius, R. Über die bewegende Kraft der Wärme und die Gesetze, welche sich daraus für die Wärmelehre selbst ableiten lassen. *Annalen der Physik* **155**, 368–397 (1850).

[202] Carnot, S. *Reflections on the motive power of fire: And other papers on the second law of thermodynamics* (Courier Corporation, 2012).

[203] Wilks, J. *The third law of thermodynamics* (Oxford University Press, 1961).

[204] De Groot, S. R. & Mazur, P. *Non-equilibrium thermodynamics* (Courier Corporation, 2013).

[205] Zhang, Y. & Barato, A. C. Critical behavior of entropy production and learning rate: Ising model with an oscillating field. *Journal of Statistical Mechanics: Theory and Experiment* **2016**, 113207 (2016).

[206] Shannon, C. E. A mathematical theory of communication. *The Bell system technical journal* **27**, 379–423 (1948).

[207] Schnakenberg, J. Network theory of microscopic and macroscopic behavior of master equation systems. *Reviews of Modern Physics* **48**, 571–585 (1976).

[208] Crooks, G. E. Entropy production fluctuation theorem and the nonequilibrium work relation for free energy differences. *Phys. Rev. E* **60**, 2721–2726 (1999). URL `https://link.aps.org/doi/10.1103/PhysRevE.60.2721`.

[209] Ma, S.-K. *Modern theory of critical phenomena* (Routledge, 2018).

[210] Robinson, G. W. *Water in biology, chemistry, and physics: experimental overviews and computational methodologies*, vol. 9 (World Scientific, 1996).

[211] Denny, M. *Air and water: the biology and physics of life's media* (Princeton University Press, 1993).

[212] Cowley, R. A. Structural phase transitions I. Landau theory. *Advances in physics* **29**, 1–110 (1980).

[213] Toledano, P. & Toledano, J.-c. *Landau Theory Of Phase Transitions, The: Application To Structural, Incommensurate, Magnetic And Liquid Crystal Systems*, vol. 3 (World Scientific Publishing Company, 1987).

[214] Chen, H. *et al.* First-order phase transition in a majority-vote model with inertia. *Physical Review E* **95**, 42304 (2017).

[215] Kosterlitz, J. M. & Thouless, D. J. Ordering, metastability and phase transitions in two-dimensional systems. *Journal of Physics C: Solid State Physics* **6**, 1181 (1973).

[216] Thouless, D. J., Kohmoto, M., Nightingale, M. P. & den Nijs, M. Quantized Hall conductance in a two-dimensional periodic potential. *Physical review letters* **49**, 405 (1982).

[217] Haldane, F. D. M. Fractional quantization of the Hall effect: a hierarchy of incompressible quantum fluid states. *Physical Review Letters* **51**, 605 (1983).

[218] Tinkham, M. *Introduction to superconductivity* (Courier Corporation, 2004).

[219] Wagner, H. Long-wavelength excitations and the Goldstone theorem in many-particle systems with "broken symmetries". *Zeitschrift für Physik* **195**, 273–299 (1966). URL `https://doi.org/10.1007/BF01325630`.

[220] Alexander, S. & McTague, J. Should all crystals be bcc? Landau theory of solidification and crystal nucleation. *Physical Review Letters* **41**, 702 (1978).

[221] Ginzburg, V. L. & Landau, L. D. On the theory of superconductivity. In *On Superconductivity and Superfluidity*, 113–137 (Springer, 2009).

[222] Landau, L. D. *et al. Electrodynamics of continuous media*, vol. 8 (elsevier, 2013).

[223] Ginzburg, V. L. Nobel Lecture: On superconductivity and superfluidity (what I have and have not managed to do) as well as on the "physical minimum" at the beginning of the XXI century. *Reviews of Modern Physics* **76**, 981 (2004).

[224] Gor'kov, L. P. Microscopic derivation of the Ginzburg-Landau equations in the theory of superconductivity. *Sov. Phys. JETP* **9**, 1364–1367 (1959).

[225] Wilson, K. G. & Kogut, J. The renormalization group and the ϵ expansion. *Physics reports* **12**, 75–199 (1974).

[226] Wilson, K. G. The renormalization group and critical phenomena. *Reviews of Modern Physics* **55**, 583 (1983).

[227] Goldenfeld, N. *Lectures on phase transitions and the renormalization group* (CRC Press, 2018).

[228] Binder, K. Finite size scaling analysis of Ising model block distribution functions. *Zeitschrift für Physik B Condensed Matter* **43**, 119–140 (1981).

[229] Privman, V. *Finite size scaling and numerical simulation of statistical systems* (World Scientific Singapore, 1990).

[230] Livi, R. & Politi, P. *Nonequilibrium statistical physics: a modern perspective* (Cambridge University Press, 2017).

[231] Family, F. & s Vicsek, T. *Dynamics of fractal surfaces* (World scientific, 1991).

[232] Family, F. & Vicsek, T. Scaling of the active zone in the Eden process on percolation networks and the ballistic deposition model. *Journal of Physics A: Mathematical and General* **18**, L75 (1985).

[233] Meakin, P., Ramanlal, P., Sander, L. M. & Ball, R. C. Ballistic deposition on surfaces. *Physical Review A* **34**, 5091 (1986).

[234] Evans, J. W. Random-deposition models for thin-film epitaxial growth. *Physical Review B* **39**, 5655 (1989).

[235] Vicsek, T. & Family, F. Dynamic scaling for aggregation of clusters. *Physical Review Letters* **52**, 1669 (1984).

[236] Lai, Z.-W. & Das Sarma, S. Kinetic growth with surface relaxation: Continuum versus atomistic models. *Phys. Rev. Lett.* **66**, 2348–2351 (1991). URL `https://link.aps.org/doi/10.1103/PhysRevLett.66.2348`.

[237] Edwards, S. F. & Wilkinson, D. R. The surface statistics of a granular aggregate. *Proceedings of the Royal Society of London. A. Mathematical and Physical Sciences* **381**, 17–31 (1982).

[238] Kardar, M., Parisi, G. & Zhang, Y.-C. Dynamic Scaling of Growing Interfaces. *Phys. Rev. Lett.* **56**, 889–892 (1986). URL `https://link.aps.org/doi/10.1103/PhysRevLett.56.889`.

[239] Herring, C. Diffusional viscosity of a polycrystalline solid. *Journal of applied physics* **21**, 437–445 (1950).

[240] Mullins, W. W. Theory of thermal grooving. *Journal of Applied Physics* **28**, 333–339 (1957).

[241] Takeuchi, K. A. & Sano, M. Universal Fluctuations of Growing Interfaces: Evidence in Turbulent Liquid Crystals. *Phys. Rev. Lett.* **104**, 230601 (2010). URL https://link.aps.org/doi/10.1103/PhysRevLett.104.230601.

[242] Takeuchi, K. A., Sano, M., Sasamoto, T. & Spohn, H. Growing interfaces uncover universal fluctuations behind scale invariance. *Scientific Reports* **1**, 34 (2011). URL https://doi.org/10.1038/srep00034.

[243] Takeuchi, K. A. & Sano, M. Evidence for Geometry-Dependent Universal Fluctuations of the Kardar-Parisi-Zhang Interfaces in Liquid-Crystal Turbulence. *Journal of Statistical Physics* **147**, 853–890 (2012). URL https://doi.org/10.1007/s10955-012-0503-0.

[244] Wakita, J.-i., Itoh, H., Matsuyama, T. & Matsushita, M. Self-affinity for the growing interface of bacterial colonies. *Journal of the Physical Society of Japan* **66**, 67–72 (1997).

[245] Maunuksela, J. *et al.* Kinetic Roughening in Slow Combustion of Paper. *Phys. Rev. Lett.* **79**, 1515–1518 (1997). URL https://link.aps.org/doi/10.1103/PhysRevLett.79.1515.

[246] Deegan, R. D. *et al.* Capillary flow as the cause of ring stains from dried liquid drops. *Nature* **389**, 827–829 (1997).

[247] Wolf, D. E. & Villain, J. Growth with surface diffusion. *EPL (Europhysics Letters)* **13**, 389 (1990).

[248] Ferrando, R., Hontinfinde, F. & Levi, A. C. Morphologies in anisotropic cluster growth: A Monte Carlo study on Ag(110). *Phys. Rev. B* **56**, R4406—-R4409 (1997). URL https://link.aps.org/doi/10.1103/PhysRevB.56.R4406.

[249] Liu, Z.-J. & Shen, Y. G. Temperature-dependent morphology evolution of the submonolayer clusters grown on fcc metal (110) surfaces. *Journal of Vacuum Science & Technology A* **23**, 177–183 (2004). URL https://doi.org/10.1116/1.1834617.

[250] Lu, C. *et al.* One-dimensional Growth of Zinc Crystals on a Liquid Surface. *Scientific Reports* **6**, 19870 (2016). URL https://doi.org/10.1038/srep19870.

[251] Palczynski, K., Herrmann, P., Heimel, G. & Dzubiella, J. Characterization of step-edge barrier crossing of para-sexiphenyl on the ZnO $(10\bar{1}0)$ surface. *Physical Chemistry Chemical Physics* **18**, 25329–25341 (2016). URL http://dx.doi.org/10.1039/C6CP05251G.

[252] Sparenberg, M. *et al.* Controlling the growth mode of para-sexiphenyl (6P) on ZnO by partial fluorination. *Physical Chemistry Chemical Physics* **16**, 26084–26093 (2014). URL http://dx.doi.org/10.1039/C4CP04048A.

[253] Kleppmann, N. & Klapp, S. H. L. Particle-resolved dynamics during multilayer growth of C_60. *Physical Review B* **91**, 45436 (2015). URL https://link.aps.org/doi/10.1103/PhysRevB.91.045436.

[254] Khokhar, F. S. *et al.* The influence of substrate temperature on growth of para-sexiphenyl thin films on Ir{111} supported graphene studied by LEEM. *Surface Science* **606**, 475–480 (2012). URL http://www.sciencedirect.com/science/article/pii/S0039602811004456.

[255] Kolb, M., Botet, R. & Jullien, R. Scaling of Kinetically Growing Clusters. *Physical Review Letters* **51**, 1123–1126 (1983). URL https://link.aps.org/doi/10.1103/PhysRevLett.51.1123.

[256] Plischke, M. & Rácz, Z. Active zone of growing clusters: Diffusion-limited aggregation and the Eden model. *Physical review letters* **53**, 415 (1984).

[257] Yao, Z. & Olvera de la Cruz, M. Ordered Self-Similar Patterns in Anisotropic Stochastic Growth. *The Journal of Physical Chemistry B* **120**, 5960–5965 (2016). URL https://doi.org/10.1021/acs.jpcb.6b01789.

[258] Heinson, W. R., Sorensen, C. M. & Chakrabarti, A. Does Shape Anisotropy Control the Fractal Dimension in Diffusion-Limited Cluster-Cluster Aggregation? *Aerosol Science and Technology* **44**, i–iv (2010). URL https://doi.org/10.1080/02786826.2010.516032.

[259] Sorensen, C. M. & Roberts, G. C. The Prefactor of Fractal Aggregates. *Journal of Colloid and Interface Science* **186**, 447–452 (1997). URL http://www.sciencedirect.com/science/article/pii/S0021979796946640.

[260] Schaefer, D. W., Martin, J. E., Wiltzius, P. & Cannell, D. S. Fractal Geometry of Colloidal Aggregates. *Physical Review Letters* **52**, 2371–2374 (1984). URL https://link.aps.org/doi/10.1103/PhysRevLett.52.2371.

[261] Vymětal, J. & Vondrášek, J. Gyration- and Inertia-Tensor-Based Collective Coordinates for Metadynamics. Application on the Conformational Behavior of Polyalanine Peptides and Trp-Cage Folding. *The Journal of Physical Chemistry A* **115**, 11455–11465 (2011). URL https://doi.org/10.1021/jp2065612.

[262] Theodorou, D. N. & Suter, U. W. Shape of unperturbed linear polymers: polypropylene. *Macromolecules* **18**, 1206–1214 (1985). URL https://doi.org/10.1021/ma00148a028.

[263] Fry, D., Chakrabarti, A., Kim, W. & Sorensen, C. M. Structural crossover in dense irreversibly aggregating particulate systems. *Physical Review E* **69**, 61401 (2004). URL https://link.aps.org/doi/10.1103/PhysRevE.69.061401.

[264] Fry, D., Mohammad, A., Chakrabarti, A. & Sorensen, C. M. Cluster Shape Anisotropy in Irreversibly Aggregating Particulate Systems. *Langmuir* **20**, 7871–7879 (2004). URL https://doi.org/10.1021/la0494369.

[265] Venables, J. A. Rate equation approaches to thin film nucleation kinetics. *The Philosophical Magazine: A Journal of Theoretical Experimental and Applied Physics* **27**, 697–738 (1973). URL https://doi.org/10.1080/14786437308219242.

[266] Daccord, G., Nittmann, J. & Stanley, H. E. Radial viscous fingers and diffusion-limited aggregation: Fractal dimension and growth sites. *Physical Review Letters* **56**, 336–339 (1986). URL https://link.aps.org/doi/10.1103/PhysRevLett.56.336.

[267] Vicsek, T. Pattern Formation in Diffusion-Limited Aggregation. *Physical Review Letters* **53**, 2281–2284 (1984). URL https://link.aps.org/doi/10.1103/PhysRevLett.53.2281.

[268] Meakin, P. Formation of Fractal Clusters and Networks by Irreversible Diffusion-Limited Aggregation. *Physical Review Letters* **51**, 1119–1122 (1983). URL https://link.aps.org/doi/10.1103/PhysRevLett.51.1119.

[269] Witten, T. A. & Sander, L. M. Diffusion-limited aggregation. *Physical Review B* **27**, 5686–5697 (1983). URL https://link.aps.org/doi/10.1103/PhysRevB.27.5686.

[270] Witten, T. A. & Sander, L. M. Diffusion-Limited Aggregation, a Kinetic Critical Phenomenon. *Physical Review Letters* **47**, 1400–1403 (1981). URL https://link.aps.org/doi/10.1103/PhysRevLett.47.1400.

[271] Körner, M., Einax, M. & Maass, P. Island size distributions in submonolayer growth: Prediction by mean field theory with coverage dependent capture numbers. *Physical Review B* **82**, 201401 (2010). URL https://link.aps.org/doi/10.1103/PhysRevB.82.201401.

[272] Amar, J. G., Family, F. & Popescu, M. N. Kinetics of submonolayer epitaxial growth. *Computer Physics Communications* **146**, 1–8 (2002). URL http://www.sciencedirect.com/science/article/pii/S0010465502004289.

[273] Amar, J. G., Popescu, M. N. & Family, F. Rate-Equation Approach to Island Capture Zones and Size Distributions in Epitaxial Growth. *Physical Review Letters* **86**, 3092–3095 (2001). URL https://link.aps.org/doi/10.1103/PhysRevLett.86.3092.

[274] Jackson, K. A. On the theory of crystal growth: The fundamental rate equation. *Journal of Crystal Growth* **5**, 13–18 (1969). URL http://www.sciencedirect.com/science/article/pii/0022024869900712.

[275] Krug, J., Politi, P. & Michely, T. Island nucleation in the presence of step-edge barriers: Theory and applications. *Physical Review B* **61**, 14037–14046 (2000). URL https://link.aps.org/doi/10.1103/PhysRevB.61.14037.

[276] Caflisch, R. E., E, W., Gyure, M. F., Merriman, B. & Ratsch, C. Kinetic model for a step edge in epitaxial growth. *Physical Review E* **59**, 6879–6887 (1999). URL https://link.aps.org/doi/10.1103/PhysRevE.59.6879.

[277] Castellano, C. & Politi, P. Spatiotemporal Distribution of Nucleation Events during Crystal Growth. *Physical Review Letters* **87**, 56102 (2001). URL https://link.aps.org/doi/10.1103/PhysRevLett.87.056102.

[278] Politi, P. & Castellano, C. Process of irreversible nucleation in multilayer growth. I. Failure of the mean-field approach. *Physical Review E* **66**, 31605 (2002). URL https://link.aps.org/doi/10.1103/PhysRevE.66.031605.

[279] Politi, P. & Castellano, C. Process of irreversible nucleation in multilayer growth. II. Exact results in one and two dimensions. *Physical Review E* **66**, 31606 (2002). URL https://link.aps.org/doi/10.1103/PhysRevE.66.031606.

[280] Bupathy, A., Banerjee, V. & Puri, S. Disordered dipolar solids: Anisotropic growth laws and their slowing-down. *EPL (Europhysics Letters)* **122**, 36002 (2018).

[281] Cheon, M. & Chang, I. Anisotropic Domain Growth of the Axial Next-Nearest-Neighbor Ising Model at Low Temperatures. *Physical Review Letters* **86**, 4576–4579 (2001). URL https://link.aps.org/doi/10.1103/PhysRevLett.86.4576.

[282] Chen, S. *et al.* A Level Set Method for Thin Film Epitaxial Growth. *Journal of Computational Physics* **167**, 475–500 (2001). URL http://www.sciencedirect.com/science/article/pii/S0021999100966890.

[283] Ratsch, C. *et al.* Level-set method for island dynamics in epitaxial growth. *Physical Review B* **65**, 195403 (2002). URL https://link.aps.org/doi/10.1103/PhysRevB.65.195403.

[284] Li, M., Bartelt, M. C. & Evans, J. W. Geometry-based simulation of submonolayer film growth. *Physical Review B* **68**, 121401 (2003). URL https://link.aps.org/doi/10.1103/PhysRevB.68.121401.

[285] Gilmore, C. M. & Sprague, J. A. Molecular-dynamics simulation of the energetic deposition of Ag thin films. *Physical Review B* **44**, 8950–8957 (1991). URL https://link.aps.org/doi/10.1103/PhysRevB.44.8950.

[286] Gilmore, C. M. & Sprague, J. A. Molecular-dynamics study of film growth with energetic Ag atoms. *Journal of Vacuum Science & Technology A* **10**, 1597–1599 (1992). URL https://doi.org/10.1116/1.578050.

[287] Haberland, H., Insepov, Z. & Moseler, M. Molecular-dynamics simulation of thin-film growth by energetic cluster impact. *Physical Review B* **51**, 11061–11067 (1995). URL https://link.aps.org/doi/10.1103/PhysRevB.51.11061.

[288] Dong, L., Smith, R. W. & Srolovitz, D. J. A two-dimensional molecular dynamics simulation of thin film growth by oblique deposition. *Journal of Applied Physics* **80**, 5682–5690 (1996). URL https://doi.org/10.1063/1.363621.

[289] Baletto, F., Mottet, C. & Ferrando, R. Molecular dynamics simulations of surface diffusion and growth on silver and gold clusters. *Surface Science* **446**, 31–45 (2000). URL http://www.sciencedirect.com/science/article/pii/S0039602899010584.

[290] Haselwandter, C. A. & Vvedensky, D. D. Renormalization of stochastic lattice models: Epitaxial surfaces. *Physical Review E* **77**, 61129 (2008). URL https://link.aps.org/doi/10.1103/PhysRevE.77.061129.

[291] Haselwandter, C. A. & Vvedensky, D. D. Multiscale Theory of Fluctuating Interfaces: Renormalization of Atomistic Models. *Physical Review Letters* **98**, 46102 (2007). URL https://link.aps.org/doi/10.1103/PhysRevLett.98.046102.

[292] Haselwandter, C. A. & Vvedensky, D. D. Stochastic equation for the morphological evolution of heteroepitaxial thin films. *Physical Review B* **74**, 121408 (2006). URL https://link.aps.org/doi/10.1103/PhysRevB.74.121408.

[293] Chua, A. L.-S., Haselwandter, C. A., Baggio, C. & Vvedensky, D. D. Langevin equations for fluctuating surfaces. *Physical Review E* **72**, 51103 (2005). URL https://link.aps.org/doi/10.1103/PhysRevE.72.051103.

[294] Maksym, P. A. Fast Monte Carlo simulation of MBE growth. *Semiconductor Science and Technology* **3**, 594 (1988).

[295] Kotrla, M. Numerical simulations in the theory of crystal growth. *Computer Physics Communications* **97**, 82–100 (1996). URL http://www.sciencedirect.com/science/article/pii/0010465596000239.

[296] Levi, A. C. & Kotrla, M. Theory and simulation of crystal growth. *Journal of Physics: Condensed Matter* **9**, 299 (1997).

[297] Chatraphorn, P. P., Toroczkai, Z. & Das Sarma, S. Epitaxial mounding in limited-mobility models of surface growth. *Phys. Rev. B* **64**, 205407 (2001). URL https://link.aps.org/doi/10.1103/PhysRevB.64.205407.

[298] Das Sarma, S., Chatraphorn, P. P. & Toroczkai, Z. Universality class of discrete solid-on-solid limited mobility nonequilibrium growth models for kinetic surface roughening. *Physical Review E* **65**, 36144 (2002). URL https://link.aps.org/doi/10.1103/PhysRevE.65.036144.

[299] Chatraphorn, P. P. & Das Sarma, S. Layer-by-layer epitaxy in limited mobility nonequilibrium models of surface growth. *Physical Review E - Statistical Physics, Plasmas, Fluids, and Related Interdisciplinary Topics* **66**, 10 (2002). 0203105.

[300] Pereira, A. J., Alves, S. G. & Ferreira, S. C. Effects of a kinetic barrier on limited-mobility interface growth models. *Physical Review E* **99**, 42802 (2019). URL https://link.aps.org/doi/10.1103/PhysRevE.99.042802.

[301] Punyindu, P. & Das Sarma, S. Noise reduction and universality in limited-mobility models of nonequilibrium growth. *Physical Review E* **57**, R4863–R4866 (1998). URL https://link.aps.org/doi/10.1103/PhysRevE.57.R4863.

[302] Mandreoli, L., Neugebauer, J., Kunert, R. & Schöll, E. Adatom density kinetic Monte Carlo: A hybrid approach to perform epitaxial growth simulations. *Physical Review B* **68**, 155429 (2003). URL https://link.aps.org/doi/10.1103/PhysRevB.68.155429.

[303] DeVita, J. P., Sander, L. M. & Smereka, P. Multiscale kinetic Monte Carlo algorithm for simulating epitaxial growth. *Physical Review B* **72**, 205421 (2005). URL https://link.aps.org/doi/10.1103/PhysRevB.72.205421.

[304] Opplestrup, T., Bulatov, V. V., Gilmer, G. H., Kalos, M. H. & Sadigh, B. First-Passage Monte Carlo Algorithm: Diffusion without All the Hops. *Physical Review Letters* **97**, 230602 (2006). URL https://link.aps.org/doi/10.1103/PhysRevLett.97.230602.

[305] Chou, C.-C. & Falk, M. L. Multiscale diffusion Monte Carlo simulation of epitaxial growth. *Journal of Computational Physics* **217**, 519–529 (2006). URL http://www.sciencedirect.com/science/article/pii/S0021999106000210.

[306] Tokar, V. I. & Dreyssé, H. Accelerated kinetic Monte Carlo algorithm for diffusion-limited kinetics. *Physical Review E* **77**, 66705 (2008). URL https://link.aps.org/doi/10.1103/PhysRevE.77.066705.

[307] Villain, J. Continuum models of crystal growth from atomic beams with and without desorption. *Journal de physique I* **1**, 19–42 (1991).

[308] Das Sarma, S., Chatraphorn, P. P. & Toroczkai, Z. Universality class of discrete solid-on-solid limited mobility nonequilibrium growth models for kinetic surface roughening. *Physical Review E - Statistical Physics, Plasmas, Fluids, and Related Interdisciplinary Topics* **65** (2002). 0106495.

[309] Das Sarma, S., Punyindu, P. & Toroczkai, Z. Non-universal mound formation in non-equilibrium surface growth. *Surface Science* **457**, L369–L375 (2000). URL http://www.sciencedirect.com/science/article/pii/S0039602800004015.

[310] Family, F. Dynamic scaling and phase transitions in interface growth. *Physica A: Statistical Mechanics and its Applications* **168**, 561–580 (1990).

[311] Mal, B., Ray, S. & Shamanna, J. Revisiting surface diffusion in random deposition. *The European Physical Journal B* **82**, 341 (2011). URL https://doi.org/10.1140/epjb/e2011-10949-8.

[312] Aarão Reis, F. D. A. Dynamic scaling in thin-film growth with irreversible step-edge attachment. *Physical Review E* **81**, 41605 (2010). URL https://link.aps.org/doi/10.1103/PhysRevE.81.041605.

[313] To, T. B. T., de Sousa, V. B. & Aarão Reis, F. D. A. Thin film growth models with long surface diffusion lengths. *Physica A: Statistical Mechanics and its Applications* **511**, 240–250 (2018). URL http://www.sciencedirect.com/science/article/pii/S0378437118308884.

[314] Kim, J. M. & Kosterlitz, J. M. Growth in a restricted solid-on-solid model. *Physical Review Letters* **62**, 2289–2292 (1989). URL https://link.aps.org/doi/10.1103/PhysRevLett.62.2289.

[315] Wolf, D. E. & Kertész, J. Growth: Noise reduction and universality. *Physical Review Letters* **63**, 1191 (1989). URL https://link.aps.org/doi/10.1103/PhysRevLett.63.1191.

[316] Schwoebel, R. L. Step Motion on Crystal Surfaces. II. *Journal of Applied Physics* **40**, 614–618 (1969). URL https://doi.org/10.1063/1.1657442.

[317] Bartelt, M. C. & Evans, J. W. Scaling analysis of diffusion-mediated island growth in surface adsorption processes. *Physical Review B* **46**, 12675–12687 (1992). URL https://link.aps.org/doi/10.1103/PhysRevB.46.12675.

[318] Amar, J. G. & Popescu, M. N. Asymptotic capture number and island size distributions for one-dimensional irreversible submonolayer growth. *Physical Review B* **69**, 33401 (2004). URL https://link.aps.org/doi/10.1103/PhysRevB.69.033401.

[319] Amar, J. G. & Family, F. Critical Cluster Size: Island Morphology and Size Distribution in Submonolayer Epitaxial Growth. *Physical Review Letters* **74**, 2066–2069 (1995). URL https://link.aps.org/doi/10.1103/PhysRevLett.74.2066.

[320] Amar, J. G., Popescu, M. N. & Family, F. Self-consistent rate-equation approach to irreversible submonolayer growth in one dimension. *Surface Science* **491**, 239–254 (2001).

[321] Körner, M., Einax, M. & Maass, P. Capture numbers and island size distributions in models of submonolayer surface growth. *Physical Review B* **86**, 85403 (2012). URL https://link.aps.org/doi/10.1103/PhysRevB.86.085403.

[322] Evans, J. W., Thiel, P. A. & Bartelt, M. C. Morphological evolution during epitaxial thin film growth: Formation of 2D islands and 3D mounds. *Surface Science Reports* **61**, 1–128 (2006). URL http://www.sciencedirect.com/science/article/pii/S0167572906000021.

[323] Chame, A. & Aarão Reis, F. D. A. Scaling of local interface width of statistical growth models. *Surface Science* **553**, 145–154 (2004). URL http://www.sciencedirect.com/science/article/pii/S0039602804000950.

[324] Richards, P. M. Equilibrium interface width for epitaxial growth with step-height-independent hopping of adatoms. *Physical Review B* **43**, 6750–6753 (1991). URL https://link.aps.org/doi/10.1103/PhysRevB.43.6750.

[325] Krug, J. & Spohn, H. Universality classes for deterministic surface growth. *Physical Review A* **38**, 4271–4283 (1988). URL https://link.aps.org/doi/10.1103/PhysRevA.38.4271.

[326] Krug, J., Plischke, M. & Siegert, M. Surface diffusion currents and the universality classes of growth. *Physical Review Letters* **70**, 3271–3274 (1993). URL https://link.aps.org/doi/10.1103/PhysRevLett.70.3271.

[327] Bertini, L. & Giacomin, G. Stochastic Burgers and KPZ Equations from Particle Systems. *Communications in Mathematical Physics* **183**, 571–607 (1997). URL https://doi.org/10.1007/s002200050044.

[328] Burioni, R. Symmetry properties in surface growth models. *Physical Review E* **51**, 5426–5434 (1995). URL https://link.aps.org/doi/10.1103/PhysRevE.51.5426.

[329] Park, S.-C., Kim, D. & Park, J.-M. Derivation of continuum stochastic equations for discrete growth models. *Physical Review E* **65**, 15102 (2001). URL https://link.aps.org/doi/10.1103/PhysRevE.65.015102.

[330] Aarão Reis, F. D. A. Numerical study of discrete models in the class of the nonlinear molecular beam epitaxy equation. *Physical Review E* **70**, 31607 (2004). URL https://link.aps.org/doi/10.1103/PhysRevE.70.031607.

[331] Neave, J. H., Joyce, B. A., Dobson, P. J. & Norton, N. Dynamics of film growth of GaAs by MBE from Rheed observations. *Applied Physics A Solids and Surfaces* **31**, 1–8 (1983).

[332] Alexandre, F. *et al.* Investigation of surface roughness of molecular beam epitaxy Ga1–xAlxAs layers and its consequences on GaAs/Ga1–xAlxAs heterostructures. *Journal of Vacuum Science & Technology B: Microelectronics Processing and Phenomena* **3**, 950–955 (1985). URL https://avs.scitation.org/doi/abs/10.1116/1.583020.

[333] Kunkel, R., Poelsema, B., Verheij, L. K. & Comsa, G. Reentrant layer-by-layer growth during molecular-beam epitaxy of metal-on-metal substrates. *Physical Review Letters* **65**, 733–736 (1990). URL https://link.aps.org/doi/10.1103/PhysRevLett.65.733.

[334] Šmilauer, P., Wilby, M. R. & Vvedensky, D. D. Reentrant layer-by-layer growth: A numerical study. *Physical Review B* **47**, 4119–4122 (1993). URL https://link.aps.org/doi/10.1103/PhysRevB.47.4119.

[335] de Assis, T. A. & Reis, F. D. A. A. Dynamic scaling and temperature effects in thin film roughening. *Journal of Statistical Mechanics: Theory and Experiment* **2015**, P06023 (2015).

[336] Kanjanaput, W., Limkumnerd, S. & Chatraphorn, P. Growth instability due to lattice-induced topological currents in limited-mobility epitaxial growth models. *Physical Review E* **82**, 41607 (2010). URL https://link.aps.org/doi/10.1103/PhysRevE.82.041607.

[337] Luis, E. E. M., de Assis, T. A. & Ferreira, S. C. Optimal detrended fluctuation analysis as a tool for the determination of the roughness exponent of the mounded surfaces. *Physical Review E* **95**, 42801 (2017). URL https://link.aps.org/doi/10.1103/PhysRevE.95.042801.

[338] Luis, E. E. M., de Assis, T. A., Ferreira, S. C. & Andrade, R. F. S. Local roughness exponent in the nonlinear molecular-beam-epitaxy universality class in one dimension. *Physical Review E* **99**, 22801 (2019). URL https://link.aps.org/doi/10.1103/PhysRevE.99.022801.

[339] Draxl, C. & Scheffler, M. NOMAD: The FAIR concept for big data-driven materials science. *MRS Bulletin* **43**, 676–682 (2018).

[340] Draxl, C. & Scheffler, M. The NOMAD laboratory: from data sharing to artificial intelligence. *Journal of Physics: Materials* **2**, 036001 (2019).

[341] Carleo, G. *et al.* Machine learning and the physical sciences. *Reviews of Modern Physics* **91**, 45002 (2019). URL https://link.aps.org/doi/10.1103/RevModPhys.91.045002.

[342] Goh, G. B., Hodas, N. O. & Vishnu, A. Deep learning for computational chemistry. *Journal of computational chemistry* **38**, 1291–1307 (2017).

[343] Ramakrishnan, R., Dral, P. O., Rupp, M. & von Lilienfeld, O. A. Big data meets quantum chemistry approximations: The Δ-machine learning approach. *Journal of chemical theory and computation* **11**, 2087–2096 (2015).

[344] Tarca, A. L., Carey, V. J., Chen, X.-w., Romero, R. & Dr\uaghici, S. Machine learning and its applications to biology. *PLoS Comput Biol* **3**, e116 (2007).

[345] Broecker, P., Carrasquilla, J., Melko, R. G. & Trebst, S. Machine learning quantum phases of matter beyond the fermion sign problem. *Scientific Reports* **7**, 1–10 (2017). URL http://dx.doi.org/10.1038/s41598-017-09098-0. 1608.07848.

[346] Lian, W. *et al.* Machine Learning Topological Phases with a Solid-State Quantum Simulator. *Physical Review Letters* **122**, 210503 (2019). URL https://link.aps.org/doi/10.1103/PhysRevLett.122.210503.

[347] Ch'Ng, K., Carrasquilla, J., Melko, R. G. & Khatami, E. Machine learning phases of strongly correlated fermions. *Physical Review X* **7**, 1–9 (2017). 1609.02552.

[348] Brunton, S. L., Noack, B. R. & Koumoutsakos, P. Machine Learning for Fluid Mechanics. *Annual Review of Fluid Mechanics* **52**, 477–508 (2020). URL https://doi.org/10.1146/annurev-fluid-010719-060214.

[349] Deng, D. L., Li, X. & Das Sarma, S. Machine learning topological states. *Physical Review B* **96**, 1–11 (2017). 1609.09060.

[350] Behler, J. Perspective: Machine learning potentials for atomistic simulations. *The Journal of Chemical Physics* **145**, 170901 (2016). URL https://doi.org/10.1063/1.4966192.

[351] Noé, F., Tkatchenko, A., Müller, K.-R. & Clementi, C. Machine Learning for Molecular Simulation. *Annual Review of Physical Chemistry* **71**, 361–390 (2020). URL https://doi.org/10.1146/annurev-physchem-042018-052331.

[352] Lecun, Y., Bengio, Y. & Hinton, G. Deep learning. *Nature* **521**, 436–444 (2015).

[353] Schmidhuber, J. Deep learning in neural networks: An overview. *Neural networks* **61**, 85–117 (2015).

[354] Noé, F., Olsson, S., Köhler, J. & Wu, H. Boltzmann generators: Sampling equilibrium states of many-body systems with deep learning. *Science* **365** (2019).

[355] Bishop, C. M. *Pattern recognition and machine learning* (springer, 2006).

[356] Goodfellow, I., Bengio, Y., Courville, A. & Bengio, Y. *Deep learning*, vol. 1 (MIT press Cambridge, 2016).

[357] Mehta, P. *et al.* A high-bias, low-variance introduction to machine learning for physicists. *Physics reports* **810**, 1–124 (2019).

[358] Hastie, T., Tibshirani, R. & Friedman, J. *The elements of statistical learning: data mining, inference, and prediction* (Springer Science & Business Media, 2009).

[359] Bottou, L. Large-scale machine learning with stochastic gradient descent. In *Proceedings of COMPSTAT'2010*, 177–186 (Springer, 2010).

[360] Simonyan, K. & Zisserman, A. Very Deep Convolutional Networks for Large-Scale Image Recognition (2014). URL http://arxiv.org/abs/1409.1556. 1409.1556.

[361] Abadi, M. *et al.* Tensorflow: A system for large-scale machine learning. In *12th ${$USENIX$}$ symposium on operating systems design and implementation (${$OSDI$}$ 16)*, 265–283 (2016).

[362] Krizhevsky, A., Sutskever, I. & Hinton, G. E. Imagenet classification with deep convolutional neural networks. *Communications of the ACM* **60**, 84–90 (2017).

[363] Alber, M. *et al.* INNvestigate neural networks! *Journal of Machine Learning Research* (2019).

[364] Nagelkerke, N. J. D. & Others. A note on a general definition of the coefficient of determination. *Biometrika* **78**, 691–692 (1991).

[365] Janke, W. & Speck, T. Modeling of epitaxial film growth of C60 revisited. *Physical Review B* **101**, 1–11 (2020).

[366] Karma, A. & Plapp, M. Spiral Surface Growth without Desorption. *Physical Review Letters* **81**, 4444–4447 (1998). URL `https://link.aps.org/doi/10.1103/PhysRevLett.81.4444`.

[367] Jacobsen, J., Jacobsen, K. W. & Nørskov, J. K. Island shapes in homoepitaxial growth of Pt(111). *Surface Science* **359**, 37–44 (1996). URL `http://www.sciencedirect.com/science/article/pii/0039602896003652`.

[368] Hinrichsen, H. Non-equilibrium critical phenomena and phase transitions into absorbing states. *Advances in Physics* **49**, 815–958 (2000). `0001070`.

[369] Amar, J. G. & Family, F. Phase transition in a restricted solid-on-solid surface-growth model in 2+ 1 dimensions. *Physical review letters* **64**, 543 (1990).

[370] Kim, J. M., Kosterlitz, J. M. & Ala-Nissila, T. Surface growth and crossover behaviour in a restricted solid-on-solid model. *Journal of Physics A: Mathematical and General* **24**, 5569 (1991).

[371] Klümper, A. Free energy and correlation lengths of quantum chains related to restricted solid-on-solid lattice models. *Annalen der Physik* **504**, 540–553 (1992).

[372] Kim, J. M. & Kim, S.-W. Restricted solid-on-solid model with a proper restriction parameter N in 4+ 1 dimensions. *Physical Review E* **88**, 34102 (2013).

[373] Hinrichsen, H., Livi, R., Mukamel, D. & Politi, A. Model for Nonequilibrium Wetting Transitions in Two Dimensions. *Physical Review Letters* **79**, 2710–2713 (1997). URL `https://link.aps.org/doi/10.1103/PhysRevLett.79.2710`.

[374] Barato, A. C. & Hinrichsen, H. Entropy production of a bound nonequilibrium interface. *Journal of Physics A: Mathematical and Theoretical* **45** (2012).

[375] Ferrenberg, A. M. & Swendsen, R. H. New Monte Carlo technique for studying phase transitions. *Physical Review Letters* **61**, 2635–2638 (1988). URL `https://link.aps.org/doi/10.1103/PhysRevLett.61.2635`.

[376] Wu, F. Y. & Lin, K. Y. Two phase transitions in the Ashkin-Teller model. *Journal of Physics C: Solid State Physics* **7**, L181 (1974).

[377] Domany, E. & Riedel, E. K. Two-dimensional anisotropic N-vector models. *Physical Review B* **19**, 5817–5834 (1979). URL https://link.aps.org/doi/10.1103/PhysRevB.19.5817.

[378] de Felício, J. R. D. & Köberle, R. Critical exponents of the Ashkin-Teller model. *Physical Review B* **25**, 511–514 (1982). URL https://link.aps.org/doi/10.1103/PhysRevB.25.511.

[379] Tobochnik, J. Properties of the q-state clock model for $q=4, 5$ and 6$. *Physical Review B* **26**, 6201–6207 (1982). URL https://link.aps.org/doi/10.1103/PhysRevB.26.6201.

[380] Kadanoff, L. P. Scaling laws for ising models near ${T}_{c}$. *Physics Physique Fizika* **2**, 263–272 (1966). URL https://link.aps.org/doi/10.1103/PhysicsPhysiqueFizika.2.263.

[381] Hasenbusch, M. The Binder cumulant at the Kosterlitz–Thouless transition. *Journal of Statistical Mechanics: Theory and Experiment* **2008**, P08003 (2008).

[382] Komura, Y. & Okabe, Y. Large-scale Monte Carlo simulation of two-dimensional classical XY model using multiple GPUs. *Journal of the Physical Society of Japan* **81**, 113001 (2012).

[383] Hsieh, Y.-D., Kao, Y.-J. & Sandvik, A. W. Finite-size scaling method for the Berezinskii–Kosterlitz–Thouless transition. *Journal of Statistical Mechanics: Theory and Experiment* **2013**, P09001 (2013).

[384] Sánchez, A. D., López, J. M. & Rodríguez, M. A. Nonequilibrium Phase Transitions in Directed Small-World Networks. *Physical Review Letters* **88**, 48701 (2002). URL https://link.aps.org/doi/10.1103/PhysRevLett.88.048701.

[385] Castellano, C., Fortunato, S. & Loreto, V. Statistical physics of social dynamics. *Reviews of Modern Physics* **81**, 591–646 (2009). URL https://link.aps.org/doi/10.1103/RevModPhys.81.591.

[386] Dorogovtsev, S. N., Goltsev, A. V. & Mendes, J. F. F. Critical phenomena in complex networks. *Reviews of Modern Physics* **80**, 1275–1335 (2008). URL https://link.aps.org/doi/10.1103/RevModPhys.80.1275.

[387] Dorogovtsev, S. N. & Mendes, J. F. F. Evolution of networks. *Advances in physics* **51**, 1079–1187 (2002).

[388] Schwartz, N., Cohen, R., Ben-Avraham, D., Barabási, A.-L. & Havlin, S. Percolation in directed scale-free networks. *Physical Review E* **66**, 15104 (2002). URL https://link.aps.org/doi/10.1103/PhysRevE.66.015104.

[389] Ivlev, A. *et al.* Statistical Mechanics where Newton's Third Law is Broken. *Physical Review X* **5**, 11035 (2015). URL https://link.aps.org/doi/10.1103/PhysRevX.5.011035.

[390] Loos, S. A. M. & Klapp, S. H. L. Irreversibility, heat and information flows induced by non-reciprocal interactions. *New Journal of Physics* **22**, 123051 (2020). URL https://iopscience.iop.org/article/10.1088/1367-2630/abcc1e.

[391] Kryuchkov, N. P., Ivlev, A. V. & Yurchenko, S. O. Dissipative phase transitions in systems with nonreciprocal effective interactions. *Soft Matter* **14**, 9720–9729 (2018). URL http://dx.doi.org/10.1039/C8SM01836G.